

**Highly stable Zr(Hf)-based Surface-anchored Metal-Organic Frameworks
(SURMOFs) for technical application**

Zur Erlangung des akademischen Grades einer
DOKTORIN DER NATURWISSENSCHAFTEN
(Dr. rer. nat.)

von der KIT-Fakultät für Chemie und Biowissenschaften
des Karlsruher Instituts für Technologie (KIT)

genehmigte

DISSERTATION

von

M.Eng. Evgenia Bogdanova

aus

Zheleznogorsk, Siberia, Russia

1. Referent: Prof. Dr. Christof Wöll

2. Referent: Prof. Dr. Stefan Bräse

Tag der mündlichen Prüfung: 23.10.2024

*Dedicated to my parents –
Irina Bogdanova and Alexander Bogdanov*

Diese Arbeit wurde von Juli 2021 bis Juli 2024 unter der Betreuung von Prof. Dr. Christof Wöll (Institut für Funktionelle Grenzflächen, IFG) am Karlsruher Institut für Technologie angefertigt.

I hereby declare that this dissertation represents my original work, composed by my own hand, without the use of any sources other than those explicitly referenced in the main text. (The phrasing and grammar have been reviewed and verified using Google Translate, ChatGPT, and Scite to ensure precision and clarity.) I have followed the regulations of KIT to uphold the principles of good scientific practice.

Abstract

Metal-Organic Frameworks (MOFs), first reported in 1995, are recognized for their unique properties such as high surface area, tunable porosity, and the ability to incorporate a variety of functional groups, which make them promising for numerous applications. However, their practical use in challenging environments is often limited by stability issues. Although Surface-Anchored MOFs (SURMOFs) have been developed to enhance the integration of MOFs into devices, stability remains a significant challenge.

This PhD thesis explores the synthesis, characterization, modification, and application of highly stable Zr(Hf)-based SURMOFs for various technical applications. Zr(Hf)-based MOFs, including the UiO-66 and NU-1000 families, exhibit exceptional stability, making them well-suited for industrial applications. Despite their stability, the preparation of Zr(Hf)-MOFs is complex due to the use of metal clusters rather than metal ions, and the synthesis of SURMOFs involves many parameters that affect thin film growth and orientation.

The research addresses these challenges by employing Liquid-Phase Epitaxial (LPE) Layer-by-Layer (LbL) methods, which offer advantages over traditional solvothermal techniques by enabling the production of defect-free films with precise orientation. The study also investigates post-synthetic modifications to further enhance the properties and functionality of SURMOFs.

The findings provide significant insights into the preparation and application of Zr(Hf)-based SURMOFs, with implications for various industrial and environmental applications. The outcomes could impact fields such as sensing technology, catalysis, and water purification, and promote interdisciplinary collaboration.

Zusammenfassung

Metallorganische Netzwerke (MOFs), erstmals 1995 veröffentlicht, sind bekannt für ihre hohe spezifische Oberfläche, einstellbare Porosität und die Fähigkeit, funktionelle Gruppen zu integrieren, was sie für zahlreiche Anwendungen vielversprechend macht. Ihre praktische Nutzung, insbesondere in herausfordernden Umgebungen, ist jedoch oft durch Stabilitätsprobleme eingeschränkt. Obwohl Oberflächenverankerte MOFs (SURMOFs) entwickelt wurden, um die Integration von MOFs in Geräte zu verbessern, bleibt die Stabilität eine erhebliche Herausforderung.

Diese Doktorarbeit untersucht die Synthese, Charakterisierung, Modifikation und Anwendung von hochstabilen Zr(Hf)-basierten SURMOFs für technische Anwendungen. Zr(Hf)-MOFs wie die UiO-66 und NU-1000 Familien zeigen außergewöhnliche Stabilität und eignen sich daher gut für industrielle Anwendungen. Trotz ihrer Stabilität ist ihre Herstellung komplex, da Metallcluster statt Metallionen verwendet werden und viele Parameter das Wachstum und die Orientierung der Dünnschichten beeinflussen.

Die Forschung verwendet Liquid-Phase Epitaxial (LPE) Layer-by-Layer (LbL) Methoden, die gegenüber traditionellen solvothermalen Techniken Vorteile bieten, indem sie fehlerfreie Filme mit präziser Orientierung ermöglichen. Zudem werden post-synthetische Modifikationen untersucht, um die Eigenschaften und Funktionalität der SURMOFs weiter zu verbessern.

Die Ergebnisse liefern wesentliche Erkenntnisse über die Vorbereitung und Anwendung von Zr(Hf)-SURMOFs mit Auswirkungen auf industrielle und umwelttechnische Anwendungen. Diese Ergebnisse könnten Bereiche wie Sensortechnologie, Katalyse und Wasseraufbereitung beeinflussen und interdisziplinäre Zusammenarbeit fördern.

Table of Contents

1	Chapter I. Introduction.....	12
1.1	General Remarks	12
1.2	Research Objectives	13
1.3	Expected outcomes.....	15
1.4	Significance.....	15
1.5	Layout of the thesis	17
1.6	Summary	18
2	Chapter II. Theoretical background.....	19
2.1	Metal-Organic Frameworks (MOFs)	19
2.1.1	General description of MOFs.....	19
2.1.2	Properties of MOFs	22
2.1.3	Synthesis methods of MOFs	23
2.1.4	Application of MOFs	25
2.2	Surface-Anchored Metal-Organic Frameworks (SURMOFs).....	31
2.2.1	General description and properties of SURMOFs.....	31
2.2.2	Synthesis of SURMOFs	32
2.2.3	Application of SURMOFs	41
2.3	Zr(Hf)-based MOFs/SURMOFs	43
2.3.1	UiO (University of Oslo) family	45
2.3.2	NU (Northwestern University)-1000	49
3	Chapter III. Materials and methods	51
3.1	Materials and techniques.....	51
3.1.1	Surface functionalization	51

3.1.2	Chemicals used for SURMOF/thin films synthesis	52
3.2	General instrumental information of the characterization techniques	53
3.2.1	X-Ray Diffraction (XRD)	53
3.2.2	Fourier transform-Infrared Spectroscopy (FT-IR).....	58
3.2.3	Field-Emission Scanning Electron Microscopy (FE-SEM)	66
3.2.4	Atomic-Force microscopy (AFM)	71
3.2.5	Water contact Angle (WCA) analysis.....	73
3.2.6	Time-of-Flight Secondary Ion Mass Spectrometry (ToF-SIMS)	76
3.2.7	Quartz-crystal microbalance (QCM)	83
4	Chapter IV. Functionalization of Monolithic MOF Thin Films with Hydrocarbon Chains to Achieve Superhydrophobic Surfaces with Tunable Water Adhesion Strength.....	85
4.1	Introduction	85
4.2	Experimental section	87
4.2.1	Synthesis of UiO-66-NH ₂ via dip-coating	87
4.2.2	Surface functionalization with C18-SAM	88
4.2.3	Surface Roughness Reduction Protocol.....	89
4.2.4	Post-synthetic modifications of UiO-66-NH ₂ SURMOF	89
4.2.5	Molecular Dynamics Simulations.....	90
4.2.6	Time-of-Flight Secondary Ion Mass Spectrometry (ToF-SIMS) results...	92
4.2.7	Surface Roughness Consistency before and after Post-Synthetic Modification.....	94
4.2.8	Morphological Consistency before and after Post-Synthetic Modification	95

4.2.9	Flexibility of hydrocarbon chains in dry conditions vs. during wetting	95
4.2.10	Intrinsic entropy of hydrocarbon chains from Ramachandran plots	97
4.2.11	Determination of surface density of C18 and C18F chains in UiO-66-C18(F) SURMOFs	98
4.3	Results and discussion	101
4.4	Conclusion	113
5	Chapter V. Optimized Detection of Volatile Organic Compounds Utilizing Durable and Selective Arrays of Tailored UiO-66-X SURMOF Sensors	114
5.1	Introduction	114
5.2	Experimental section	116
5.2.1	Synthesis of UiO-66-NH ₂ via flow-cell using openQCM-D	116
5.2.2	Post-synthetic modification to UiO-66-N ₃ and UiO-66-Cl	117
5.2.3	Gas Delivery System and VOC Measurements	118
5.2.4	Data analysis	121
5.3	Results and discussion	121
5.3.1	Synthesis of UiO-66-NH ₂ SURMOF Films with the Layer-by-Layer Method Using a High-Temperature QCM-D Liquid Cell	121
5.3.2	Stability test	124
5.3.3	Adsorption Measurements under Saturated VOC Concentrations	126
5.3.4	Adsorption Measurements under Low Concentrations (10–100 ppm)	128
5.3.5	E-Nose Discrimination Analysis	132
5.4	Conclusion	138
6	Chapter VI. SURMOF E-Tongue: Highly Stable Functionalized UiO-66-X Sensor Array for liquid Discrimination	140
6.1	Introduction	140

6.2	Experimental section	141
6.2.1	Synthesis of UiO-66-X SURMOF	141
6.2.2	Liquid delivery system and E-Tongue measurements	141
6.2.3	Data analysis	142
6.3	Results and discussions	142
6.4	Conclusions	151
7	Chapter VII. Advancements in Zr- and Hf-Based UiO-66-NH ₂ SURMOF Membranes: Synthesis, Stability, and Applications	153
7.1	Introduction	153
7.2	Experimental section	155
7.2.1	Synthesis of Zr- and Hf-UiO-66-NH ₂ MOFs.....	155
7.2.2	Synthesis of Zr- and Hf-UiO-66-NH ₂ thin films on different substrates...	155
7.2.3	Chemical Stability Experiments of Hf-UiO-66-NH ₂ @gold in Acidic, Neutral and Alkaline Media.....	156
7.3	Results and discussion.....	157
7.4	Conclusion.....	163
7.5	Outlook.....	163
8	Chapter VIII. NU-1000 SURMOF/thin film for enzymes immobilization	165
8.1	Introduction	165
8.2	Experimental section	167
8.2.1	Synthesis of NU-1000 SURMOF	167
8.2.2	Synthesis of NU-1000 thin films	167
8.2.3	Materials for enzyme immobilization	169

8.2.4 Enzyme immobilization into NU-1000@QCM-D.....	169
8.3 Results and discussion.....	170
8.4 Conclusion.....	176
8.5 Outlook.....	177
9 Chapter IX. Conclusion and Outlook	178
References	180
List of Abbreviations	201
List of Figures	203
List of Schemes	213
List of Tables	216
Acknowledgements.....	217
Curriculum Vitae (CV)	219
List of Publications	221

1 Chapter I. Introduction

1.1 General Remarks

Materials utilized in modern life are in a constant state of evolution, adapting to the diverse requirements of various fields and optimizing performance under specific working conditions. Metal-Organic Frameworks (MOFs), also known as Porous-Coordination Polymers, have emerged as noteworthy candidates, capturing attention for their distinctive properties that enable customization to meet specific needs. Particularly promising is the utilization of Surface-Anchored Metal-Organic Frameworks (SURMOFs), presenting a more accessible and operable approach for a variety of processes.

Despite the promising potential of SURMOFs, their **synthesis** poses a significant challenge. The most prevalent methods involve Liquid-Phase Epitaxial (LPE) Layer-by-Layer (LbL) growth. Achieving high-quality, oriented SURMOFs requires the optimization of numerous conditions, including the selection of chemicals, their concentrations, surface material, surface functionalization, temperature, and timing.

Furthermore, the **stability of MOFs and SURMOFs** is crucial for their suitability in diverse working conditions. Many MOFs exhibit weakness, particularly in aqueous environments, making them less than ideal candidates. In contrast, Zr(Hf)-based MOFs, such as UiO (University of Oslo) and NU (Northwestern University) have demonstrated exceptional stability across different environments. This stability makes them promising candidates for a wide array of applications, including catalysis, drug delivery, gas storage and separation, water treatment, and sensing.

Moreover, the customizability of Zr(Hf)-based SURMOFs can be further enhanced through **modifications**, expanding the scope of potential applications.

Existing literature primarily focuses on the solvothermal preparation method of UiO-66 family MOF thin films. However, this method proves to be inferior to the LbL method concerning thin film orientation and the presence of defects in published works. As we delve into the synthesis and applications of SURMOFs, addressing these challenges becomes crucial for unlocking their full potential in various technological advancements.

This PhD research aims to explore the synthesis, characterization, modification and versatile applications of highly stable Zr(Hf)-based Surface-Anchored Metal-Organic Frameworks and thin films. The study is focused on two prominent MOFs families: UiO-66, (particularly UiO-66-NH₂ and its modifications) and NU-1000. These materials exhibit exceptional stability and offer promising opportunities for various technical applications.

1.2 Research Objectives

There are four main objectives presented in this thesis:

a. **Synthesis and Characterization:** Investigate different preparation techniques and methods for the synthesis of Zr(Hf)-based UiO-66-NH₂ SURMOFs, emphasizing their structural and morphological characterization.

b. **Post-Modifications:** Explore post-modification strategies to tailor the properties and functionality of SURMOFs, enhancing their applicability in diverse technical fields.

c. **Stability Tests:** Conduct rigorous stability tests to assess the long-term performance and robustness of SURMOFs, especially in challenging environments.

d. **Applications:** Investigate and demonstrate the potential applications of Zr(Hf)-based SURMOFs in the following areas:

- **Superhydrophobic Surfaces:** SURMOF films can be applied as coatings on various surfaces to render them superhydrophobic, repelling water and other liquids. This property facilitates self-cleaning surfaces, where dirt and

contaminants are easily washed away by rain or water droplets, reducing the need for manual cleaning and maintenance. Furthermore, the superhydrophobic nature of SURMOF-coated surfaces can be exploited for controlled drug release or encapsulation applications. By loading drugs or therapeutic agents into the porous SURMOF structure, their release can be modulated based on environmental stimuli such as pH or temperature, offering precise control over drug delivery.

- **Sensors:** SURMOFs possess unique chemical and structural properties that make them ideal candidates for sensor development. Electronic-nose and electronic-tongue sensors, designed using SURMOFs as sensing elements, can detect and discriminate between various volatile organic compounds (VOCs) or dissolved analytes based on their interactions with the SURMOF surface. Additionally, the tunable optical properties of SURMOFs make them promising candidates for optical biosensing applications. By functionalizing SURMOF surfaces with specific biomolecules or receptors, they can selectively capture and detect target analytes, offering sensitive and specific detection platforms for medical diagnostics or environmental monitoring.

- **Water Treatment:** SURMOFs can be utilized in membrane filtration systems for water purification. Their high surface area and tunable pore size enable efficient removal of contaminants, including heavy metals, organic pollutants, and microorganisms, from water sources. Moreover, SURMOFs exhibit exceptional adsorption capacities due to their porous structure and high surface area. They can selectively adsorb contaminants from water, including dyes, heavy metals, and organic pollutants, making them effective adsorbents for wastewater treatment applications. Additionally, SURMOFs can be employed in advanced water purification processes such as desalination and decontamination. By selectively adsorbing ions or molecules present in saline or contaminated water, SURMOFs can produce clean and potable water for various industrial and municipal applications.

- **Continuous Catalysis:** MOFs are particularly superior candidates towards enzyme and protein immobilization over other porous materials, comprising sol gels, zeolites, as well as mesoporous silica supports. Such superiority is because MOFs exhibit fine tunability and crystallinity, thus endowing them uniformity as well as long-range order from atomic to microscale regime. The immobilization of enzymes in solid supports with less uniformity usually results in low protein loading performance, limited thermal stability, and/or enzyme leaching. Several preliminary reports demonstrated that some of such obstacles could be solved when MOFs are used towards enzyme immobilization.

1.3 Expected outcomes

This research is expected to contribute significantly to the understanding of Zr(Hf)-based SURMOFs, their preparation methods, stability under different conditions, and a wide range of technical applications. The outcomes may have far-reaching implications in industries such as sensing technology, catalysis, water treatment, and superhydrophobic surface technologies.

1.4 Significance

This thesis investigates the synthesis, characterization, modification, and application of highly stable Zr(Hf)-based SURMOFs and thin films. By focusing on two prominent MOF families, UiO-66 (particularly UiO-66-NH₂ and its modifications) and NU-1000, the research aims to address several critical challenges and open new avenues for technological advancements.

Firstly, the thesis **explores various synthesis techniques**, emphasizing the optimization of conditions for producing high-quality, oriented SURMOFs. By investigating the LPE LbL method, this research aims to overcome limitations associated with other methods, such as the solvothermal preparation of MOF thin films. The findings could lead to more efficient and reproducible synthesis protocols, facilitating the broader adoption of SURMOFs in various applications.

Stability is a crucial factor for the practical deployment of MOFs and SURMOFs. This research focuses on Zr(Hf)-based MOFs, known for their exceptional stability in diverse environments. By enhancing the understanding of stability mechanisms and exploring post-modification strategies, the thesis aims to **expand the applicability of these materials** in demanding conditions, such as water treatment and continuous catalysis.

The thesis investigates a wide range of applications, **demonstrating the versatility of Zr(Hf)-based SURMOFs**. By developing superhydrophobic surfaces, the research aims to create self-cleaning coatings. The exploration of sensor technologies, including electronic-nose and electronic-tongue sensors, highlights the potential for SURMOFs in environmental monitoring and medical diagnostics. Additionally, the application of SURMOFs in water treatment and continuous catalysis showcases their potential to address critical environmental and industrial challenges.

By developing materials with high stability and tunability, this research contributes to innovative solutions in water purification, pollutant adsorption, and energy-efficient catalytic processes. The potential for developing superhydrophobic surfaces and advanced sensor technologies further underscores the broad applicability and impact of this work.

The research **integrates concepts** from materials science, chemistry, environmental science, and engineering, highlighting the interdisciplinary nature of the work. The insights gained from this thesis could inspire further research across these fields, fostering collaboration and innovation. The development of advanced MOF-based technologies has the potential to **influence a wide range of industries**, from pharmaceuticals to environmental engineering, enhancing the societal impact of the research.

In summary, this thesis aims to make significant contributions to the field of Metal-Organic Frameworks **by advancing synthesis techniques, enhancing stability and customizability, and exploring innovative applications**. The

outcomes of this research have the potential to drive technological advancements, and inspire further interdisciplinary collaboration, underscoring the broad significance of this work.

1.5 Layout of the thesis

After the introductory overview in **Chapter I**, **Chapter II** conducts a comprehensive review of existing literature on MOFs, examining their structures, properties, and fabrication techniques, while also exploring their wide-ranging applications. Similarly, SURMOFs are explored, focusing on their properties, synthesis methods, challenges such as surface functionalization, and parameters affecting their application. Special attention is given to Zr(Hf)-based SURMOFs, particularly the UiO family and NU-1000, highlighting their unique characteristics.

Chapter III outlines the chemicals, methodologies, and instrumentation utilized for the characterization of samples in this study, encompassing techniques such as X-ray Diffraction (XRD), Fourier Transform Infrared Spectroscopy (FT-IR), Field Emission Scanning Electron Microscopy (FE-SEM), Atomic Force Microscopy (AFM), Water Contact Angle (WCA) measurements, Time-of-Flight Secondary Ion Mass Spectrometry (TOF-SIMS), and Quartz Crystal Microbalance (QCM).

Chapter IV focuses on the synthesis of UiO-66-NH₂ SURMOF on gold wafers through a dip-coating approach. Additionally, the Post-Synthetic Modification (PSM) to UiO-66-NH-C18, resulting in superhydrophobic surfaces with WCA exceeding 150 °, is discussed.

Chapter V explores the optimized detection of VOCs using tailored UiO-66-X SURMOF sensors. It covers the synthesis of UiO-66-NH₂ SURMOF on QCM sensors, their subsequent PSM to UiO-66-R (where R is -N₃, -Cl), stability tests with hot water vapor, and sensor tests for VOCs.

Chapter VI explores the innovative expansion of UiO-66-X SURMOFs on QCM sensors, used in Electronic Nose (E-Nose) systems (previous chapter) for detecting gases, to their novel application in Electronic Tongue (E-Tongue) systems for detecting molecules in liquid phases.

Chapter VII investigates Zr(Hf)-UiO-66-NH₂ membranes. It details the synthesis of Hf-UiO-66-NH₂ on gold and its stability testing in different pH ranges (pH 2, pH 7.5, pH 11). Furthermore, the synthesis of Zr- and Hf-UiO-66-NH₂ on cellulose for membrane applications such as water treatment is discussed.

Chapter VIII focuses on NU-1000 SURMOF/thin film for enzymes immobilization. It discusses the synthesis of NU-1000 SURMOF on solid substrates (gold, α -alumina, QCM) using the LPE LbL method and one-pot synthesis of NU-1000 thin films on cellulose substrates. Moreover, enzyme immobilization into NU-1000@QCM with different concentrations of the enzymes is presented.

The concluding **Chapter IX** encapsulates the key research findings, draws conclusions based on the study, and highlights the achievements.

1.6 Summary

The introduction of this thesis outlines the research's focus on exploring the synthesis, characterization, modification, and application of Zr(Hf)-based SURMOFs and thin films, with a particular emphasis on the UiO and NU families. It highlights the challenges in SURMOF synthesis, including the optimization of conditions and achieving stability. The objectives include investigating synthesis techniques, post-modification strategies, stability testing, and exploring applications across various domains such as superhydrophobic surfaces, sensors, water treatment, and continuous catalysis. The research is expected to contribute significantly to understanding Zr(Hf)-based SURMOFs and their applications, with implications for technological advancements and interdisciplinary collaboration.

2 Chapter II. Theoretical background

2.1 Metal-Organic Frameworks (MOFs)

The initial usage of the term "metal-organic framework" referred to the general composition involving both metal ions and organic components, as well as the structural nature of the framework. Over time, the term "MOF" gained significance by encompassing further structural characteristics such as rigidity, along with additional properties like porosity [1].

MOFs field has been developing over last 29 years [2]. Over 99,000 different types of MOFs have been synthesized during this period [3] and more than 500,000 predicted [4]. The considerable increase in MOF research can be attributed to the following five advancements [5]:

1. Enhancements in cluster chemistry,
2. Refinement in organic synthesis related to ligand production and post-synthetic modification,
3. Advancements in structure determination, notably in X-ray crystallography, alongside the evolution of tools and software for assessing sorption properties,
4. The interdisciplinary expansion of MOF research, intertwining with adjacent fields,
5. The continuously expanding spectrum of potential applications.

2.1.1 General description of MOFs

Metal-Organic Frameworks are extended structures obtained by linking molecules and clusters by strong bonds [1]. MOFs usually consist of metal-oxide units joined by organic linkers (Figure 1) through strong metal-carboxyl bonds. Employing various combinations of metals and organic linkers, an extensive array of MOF types can be synthesized, offering limitless possibilities for diverse industrial and commercial applications [6]. Metal nodes contribute to the

framework's stability and often dictate the chemical reactivity of the MOF [7], while organic linkers influence pore size and shape [8].

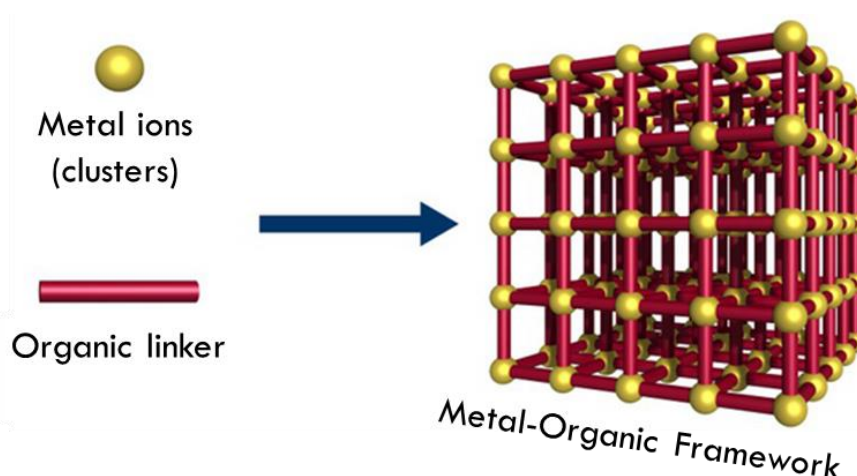


Figure 1 – Structure of MOF

Polynuclear clusters (nodes or secondary building units (SBUs)), can be used in the coordination network instead of single metal-ions to enhance the stability of MOFs. The utilization of SBUs helped in achieving more robust structures: where the metal ions' high coordination number in the polynuclear clusters improved the rigidity and directionality while the bond strength and the formation of neutral frameworks ability was enhanced due to the linker charge [1].

Nearly all metal cations from the Periodic Table, encompassing even radioactive ones, have been employed as inorganic nodes for the construction of MOFs: monovalent (Cu^+ , Ag^+ , etc.), divalent (Mg^{2+} , Mn^{2+} , Fe^{2+} , Co^{2+} , Ni^{2+} , Cu^{2+} , Zn^{2+} , Cd^{2+} , etc.), trivalent (Al^{3+} , Sc^{3+} , V^{3+} , Cr^{3+} , Fe^{3+} , Ga^{3+} , In^{3+} , lanthanides $^{3+}$, etc.), or tetravalent (Ti^{4+} , Zr^{4+} , Hf^{4+} , Ce^{4+} , etc.) [7]. Common types of organic units used as linkers or bridging ligands in MOFs include carboxylates and other organic anions, such as phosphonates, sulfonates, and heterocyclic compounds. [8]. They could be categorized as ditopic, tritopic, tetratopic, hexatopic, octatopic, mixed, desymmetrized, metallo, and N-heterocyclic linkers [8]. Figure 2 demonstrates some examples of SBUs and linkers.

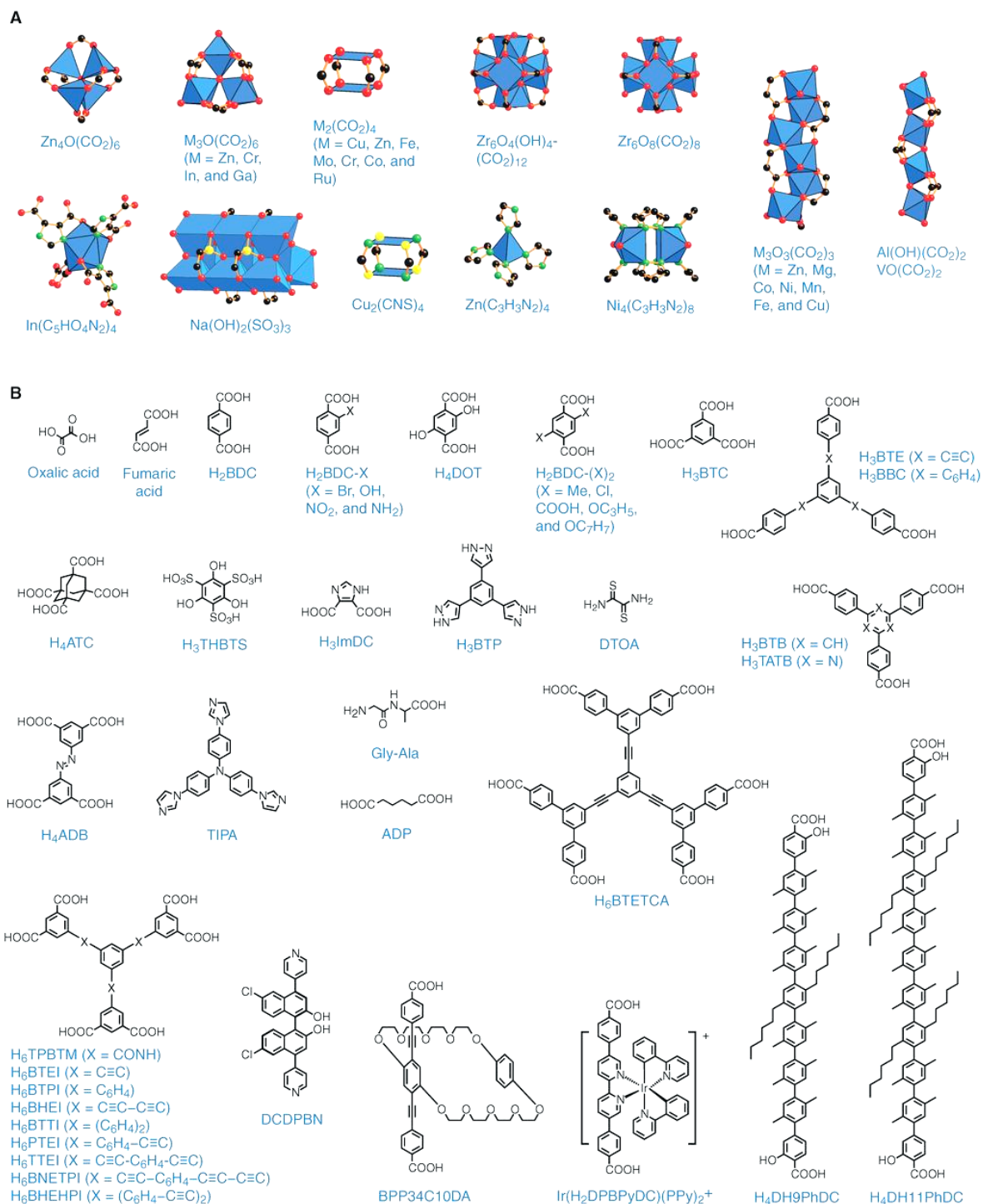


Figure 2 – Examples of inorganic secondary building units (A) and organic linkers (B).
From [9]. Reprinted with permission from AAAS.

Color code: black, C; red, O; green, N; yellow, S; purple, P; light green, Cl; blue polyhedra, metal ions. Hydrogen atoms are omitted for clarity.

2.1.2 Properties of MOFs

Due to the unique structures, MOFs exhibit a wide range of properties, including high surface areas (up to $10000 \text{ m}^2 \text{ g}^{-1}$ [9]) and porosity (up to 90 % [10]); tunability of pore size and shape; structural flexibility; diverse chemical functionalities; and stability:

- **High Surface Area and Porosity:** One of the defining characteristics of MOFs is their exceptionally high surface area, often surpassing traditional porous materials such as zeolites and carbons [9, 11]. The porous structure of MOFs allows for the encapsulation of guest molecules within their framework [12].
- **Tunability of Pore Size and Shape:** The modular nature of MOFs allows for precise control over the size and shape of their pores [1]. The ability to vary the size and nature of MOF structures without changing their underlying topology gave rise to the isorecticular principle and its application in making MOFs with the largest pore aperture (98 Å) and lowest density (0.13 g/cm^3) [9].
- **Structural Flexibility:** MOFs often exhibit structural flexibility [13], a feature known as "breathing". This flexibility arises from the dynamic nature of the metal-ligand coordination bonds, allowing the framework to expand or contract in response to external stimuli such as temperature, pressure, or the presence of guest molecules.
- **Chemical Diversity:** The versatility of MOFs stems from the vast array of metal nodes and organic linkers available for construction. This diversity allows for the creation of MOFs with tailored chemical functionalities [12].
- **Framework Stability:** The stability of MOFs is crucial for their long-term performance. MOFs, in general, demonstrate robust stability; however, variations in stability may arise based on the specific combination of metal and linker [14].
- **Thermal stability:** Because MOFs are composed entirely of strong bonds (e.g., C-C, C-H, C-O, and M-O), they show high thermal stability ranging from

250° to 500°C [9] making them suitable for applications in high-temperature environments.

2.1.3 Synthesis methods of MOFs

The MOFs synthesis process is a crucial factor that determines their structures, properties, and performances. Various methods (Figure 3) have been developed to address specific challenges and achieve desired characteristics in MOF materials.

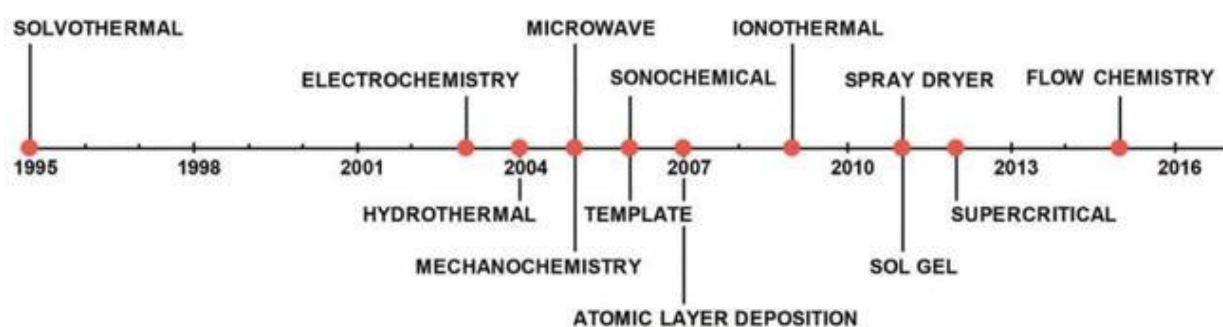


Figure 3 – Timeline of the most common synthesis approaches for MOFs [15]. *Reproduced with permission from Royal Society of Chemistry*

The synthesis usually involves nucleation followed by crystal growth, both of which can be influenced by factors such as temperature, time, solvent type, additives, and reactant concentrations. Controlling these factors enables efficient tuning of the morphology and size of MOF crystals to achieve desired final structures [16]. MOFs are usually prepared at temperatures below 250 °C with a crystallization period range of several hours to several days. Primary solvents used for MOF preparation include water, low molecular weight alcohols such as methanol and ethanol, dialkyl formamides (N,N-dimethylformamide, N,N-diethylformamide), pyridine, acetonitrile [16, 17].

The most widely used synthesis method of MOFs is the solvothermal method [18], which involves the dissolution of metal salts and organic ligands in a solvent, followed by heating in a sealed vessel at a certain temperature and

pressure. The solvothermal method can produce highly crystalline and pure MOFs, but it also has some drawbacks, such as long reaction time, high energy consumption, and difficulty in scaling up [19].

Other synthesis methods include microwave-assisted synthesis [20, 21], sonochemical [22, 23], electrochemical [24, 25], mechanochemical [26] and various others. Short overview of these methods could be found in Table 1.

Table 1 – Different synthetic methods for MOF synthesis [19]. *Reproduced with permission from Springer Nature*

Synthetic method	Characteristics	Advantages	Disadvantages
Solvothermal	Based on a certain temperature (usually above the boiling point of solvents) and consequent pressure	<ul style="list-style-type: none"> • High quality single crystal; • High thermal stability MOF products; • Most widely used; • High phase purity. 	<ul style="list-style-type: none"> • Long reaction time; • Harsh synthetic conditions; • Solvent consumption.
Microwave-assisted	Based on the interaction between electromagnetic radiation and any material containing mobile electric charges	<ul style="list-style-type: none"> • Short reaction time; • High energy efficiency; • Facile morphology control; • Narrow particle size distribution. 	<ul style="list-style-type: none"> • Limited MOF species.
Sonochemical	Very high local temperatures, high pressure, and unique heating/cooling rates by hot spots in the solution	<ul style="list-style-type: none"> • Short reaction time; • High energy efficiency; • Simple manipulation. 	<ul style="list-style-type: none"> • Limited MOF species; • Relatively low yield.
Electrochemical	Utilize electric energy to initiate the redox reaction during MOF synthesis	<ul style="list-style-type: none"> • Mild conditions; • Short reaction time; • Simple manipulation. 	<ul style="list-style-type: none"> • Limited MOF species.
Mechanochemical	Depend on the mechanical force achieved by grinding or milling of precursor solids	<ul style="list-style-type: none"> • Solvent-free; • Green synthesis; • High energy efficiency; 	<ul style="list-style-type: none"> • Limited MOF species;

Synthetic method	Characteristics	Advantages	Disadvantages
		<ul style="list-style-type: none"> • Mild conditions; • Harmless side products; • Short reaction time. 	<ul style="list-style-type: none"> • Relatively poor crystallized MOF products; • Structural defects of MOF products.
Hot-pressing	Pressure and temperature are simultaneously applied onto desired substrates in solvent-free conditions or with a minimal amount of solvents	<ul style="list-style-type: none"> • Solvent-free; • Green synthesis; • High energy efficiency; • Short reaction time. 	<ul style="list-style-type: none"> • Limited MOF species.
Spray-drying	Based on the rapid evaporation of precursors with a hot gas	<ul style="list-style-type: none"> • Low cost; • High energy efficiency; • Short reaction time; • High space time yield (STY). 	<ul style="list-style-type: none"> • Limited MOF species; • Relatively expensive equipment; • Large footprint.
Continuous flow	Reactant solutions are pumped by syringe, HPLC, or peristaltic pumps through microfluidic chips or reactor coils in a continuous process	<ul style="list-style-type: none"> • Low cost; • Less solvent; • High energy efficiency; • Short reaction time; • High STY. 	<ul style="list-style-type: none"> • Limited MOF species.

2.1.4 Application of MOFs

The unique properties of MOFs have led to their exploration in various applications across different scientific fields [17, 27].

2.1.4.1 Gas storage and separation

Initially, MOFs were created with the primary intention of being utilized in the realm of gas storage and separation [28]. Large pores and windows of these materials allows them effectively trap guest molecules [29]. MOF can be used either as an adsorbent or as a membrane material [30].

MOFs exhibit exceptional **gas storage** capabilities owing to their high porosity and large surface area. These materials can adsorb significant amounts of gases such as carbon dioxide [30], hydrogen [31], methane [32], and even more complex molecules like volatile organic compounds (VOCs) [33]. The tunable nature of MOFs allows for the design of materials with specific pore sizes and surface chemistries tailored to enhance gas adsorption [34].

Gas separation processes are vital in industries such as natural gas purification, carbon capture, and air pollution control. MOFs offer advantages in gas separation due to their selective adsorption properties and tailored porosity, enabling the separation of gas mixtures with high efficiency and selectivity.

In carbon capture and storage applications, MOFs can selectively capture carbon dioxide (CO₂) from flue gases emitted by industrial processes or power plants [10]. The high affinity of certain MOFs for CO₂, coupled with their ability to regenerate after adsorption, makes them promising materials for reducing greenhouse gas emissions.

Additionally, MOFs-based membranes have demonstrated potential in separating mixtures of gases such as carbon dioxide/methane and carbon dioxide/nitrogen [35, 36], propylene/propane [36] and others.

The utilization of MOFs in gas storage and separation applications represents a significant advancement in materials science with far-reaching implications. These versatile materials offer solutions to pressing challenges in energy, environmental sustainability, and industrial processes.

2.1.4.2 Catalysis

Another initial purpose proposed for crystalline MOFs materials was catalysis, which was also among the first applications to be practically demonstrated [37].

The high surface areas, tunable pore nature, and high density of active sites in the highly porous structures of MOFs present numerous advantages for their application in catalysis. They have the capacity to facilitate homogeneous

catalysts, stabilize short-lived catalysts, perform size selectivity, and encapsulate catalysts within their pores [9].

MOFs can serve as hosts for **homogeneous catalytic** species [37], providing a stable environment for catalytic reactions. Functional groups within the MOF structure can be tailored to interact with catalytic centers, enhancing catalyst stability and activity. This approach enables the development of efficient catalytic systems for a wide range of reactions, including hydrogenation, oxidation, C-C bond formation, and more.

In **heterogeneous catalysis**, MOFs offer advantages such as high surface area, tunable pore size, and facile modification of active sites. These properties enable the immobilization of catalytic species within the MOF framework [38], leading to enhanced catalytic performance, recyclability, and selectivity. MOF-based heterogeneous catalysts have been employed in various transformations, including olefin metathesis, hydroformylation, Suzuki coupling, and many others.

Moreover, MOFs can **mimic** the structure and functionality of **enzymes**, leading to bioinspired catalytic systems [39]. By incorporating catalytic metal nodes and organic linkers with specific functional groups, MOFs can mimic the active sites of enzymes and catalyze complex reactions with high efficiency and selectivity. This enzyme-like behavior of MOFs opens up new avenues for synthetic catalyst design and biomimetic catalysis.

MOFs possess inherent photochemical properties, making them promising candidates for **photocatalytic applications** [40]. The high surface area and porosity of MOFs facilitate light absorption and efficient charge separation, enabling photocatalytic reactions such as water splitting, pollutant degradation, and organic synthesis under mild conditions. By integrating photosensitive ligands and catalytic metal nodes, MOFs can harness solar energy for sustainable catalysis.

Chiral MOFs have emerged as versatile platforms for **asymmetric catalysis** [41], enabling the synthesis of enantiomerically pure compounds. The chiral environment provided by MOFs facilitates substrate binding and enantioselective transformations, leading to the formation of optically active products with high selectivity. Chiral MOF catalysts have found applications in asymmetric hydrogenation, asymmetric Michael addition, and other enantioselective reactions.

The diverse applications of MOFs in catalysis underscore their versatility and potential to address challenges in synthetic chemistry, environmental remediation, and energy conversion.

2.1.4.3 Drug delivery

MOFs offer an ideal platform for the **encapsulation and storage** of therapeutic agents within their porous structure [42]. Drugs can be loaded into the pores of MOFs through various methods such as physical adsorption, diffusion, or chemical bonding. The high surface area and tailored pore size of MOFs enable efficient loading of a wide range of drugs, including small molecules, proteins, nucleic acids, and imaging agents. Moreover, the encapsulation of drugs within MOFs can protect them from degradation, enhance their stability, and control their release kinetics.

One of the most significant advantages of using MOFs in drug delivery is their ability to **control the release of encapsulated drugs** [43]. The porous nature of MOFs allows for precise modulation of drug release kinetics by adjusting factors such as pore size, surface chemistry, and external stimuli. Stimuli-responsive MOFs, such as those activated by pH, temperature, light, or magnetic fields, enable on-demand drug release at specific target sites within the body. This controlled release capability minimizes systemic toxicity, reduces side effects, and enhances therapeutic efficacy.

MOFs can be functionalized with **targeting ligands** to achieve site-specific drug delivery [44]. By decorating the surface of MOFs with targeting moieties such as antibodies, peptides, or aptamers, selective binding to specific cells or tissues can be achieved. This targeted drug delivery approach enhances drug accumulation at the desired site while minimizing off-target effects, thus improving therapeutic outcomes and reducing dosage requirements.

Theranostic MOFs [45] integrate therapeutic and diagnostic functions into a single platform, enabling simultaneous drug delivery and imaging. By incorporating imaging agents such as fluorescent dyes, magnetic nanoparticles, or contrast agents into the MOF structure, real-time monitoring of drug distribution, release, and therapeutic response can be achieved. Theranostic MOFs hold great potential for personalized medicine, allowing for tailored treatment strategies based on individual patient characteristics and disease profiles.

The utilization of MOFs in drug delivery holds immense promise for advancing the field of medicine by overcoming limitations associated with conventional drug delivery systems. The tunable properties of MOFs enable precise control over drug encapsulation, release, targeting, and imaging, leading to improved therapeutic outcomes and reduced side effects.

2.1.4.4 Water purification

MOFs are utilized for the **removal of heavy metals** from water sources contaminated with pollutants such as mercury, lead, cadmium, and zinc [46]. Functionalized MOFs with specific metal-binding sites or chelating groups can selectively capture heavy metal ions through adsorption or ion exchange processes. The high surface area and tailored pore size of MOFs enhance the accessibility of active sites, leading to efficient removal of heavy metal contaminants from aqueous solutions.

Moreover, MOFs exhibit excellent adsorption capabilities for **organic pollutants** [47, 48], including dyes, pesticides, pharmaceuticals, and industrial chemicals, which are commonly found in wastewater effluents. The porous structure of MOFs provides a large surface area for adsorption, while the tunable pore size allows for selective removal of organic molecules based on their size and polarity. MOF-based adsorbents offer a sustainable and cost-effective solution for removing organic pollutants and improving water quality.

MOFs are also explored **for desalination and ion separation** applications to produce freshwater from saline or brackish water sources [49, 50]. Functionalized MOFs with tailored pore sizes and surface chemistries can selectively adsorb ions while allowing water molecules to pass through, enabling the removal of salts and other dissolved solids from water. MOF-based membranes and adsorbents hold promise for enhancing the efficiency and sustainability of desalination processes [36].

Certain MOFs exhibit **antibacterial and antifouling** properties [51, 52], making them effective materials for disinfection and biofouling control in water treatment systems. MOFs with metal ions or organic ligands that possess inherent antimicrobial activity can inhibit the growth of bacteria, viruses, and other microorganisms in water. Moreover, the porous structure of MOFs can prevent fouling by adsorbing organic matter and biofilms, thereby maintaining the long-term performance of water purification membranes and filters.

Furthermore, MOFs are investigated for **the removal of emerging contaminants** [53], including per- and polyfluoroalkyl substances (PFAS) [54, 55], pharmaceuticals [56], personal care products, and microplastics, which pose challenges to conventional water treatment processes. Functionalized MOFs can selectively adsorb emerging contaminants through specific interactions such as π - π stacking, hydrogen bonding, or electrostatic interactions. MOF-based adsorbents offer a promising solution for mitigating the environmental impact of emerging contaminants and safeguarding water resources.

The versatile properties of MOFs make them attractive materials for water purification applications, addressing various water quality challenges, including heavy metal contamination, organic pollutants, salinity, microbial growth, and emerging contaminants.

2.1.4.5 Others

MOFs also have found application in various fields, including sensors [57], electronics and optoelectronics [58], energy [59] and building [60] applications.

However, despite the numerous advantages offered by MOF powders, their integration into devices poses significant challenges [61]. Emerging applications such as smart membranes, catalytic coatings, and chemical sensors increasingly require MOF thin films or coatings with defined porosity and tunable chemical functionality [62]. However, their utilization is hindered by issues such as low particle orientation and poor substrate adhesion, leading to rough layers and reduced transparency, particularly problematic when coating optical glasses [63]. This technical limitation was partially solved with the development of SURMOFs [61].

2.2 Surface-Anchored Metal-Organic Frameworks (SURMOFs)

The growth of SURMOFs has opened the door for seamless integration of these materials into devices, providing precise control over factors such as crystallographic orientation, film thickness, and interdigitation [61, 64].

2.2.1 General description and properties of SURMOFs

Surface-Anchored Metal-Organic Frameworks are a captivating class of materials that combine the structural versatility of MOFs with surface anchoring. The integration of MOF films onto a solid support provides unique advantages compared to traditional MOF powders which typically yield particles of a few micrometers in size [65]. These anchored MOF films offer novel design possibilities that are not feasible with MOF powders [66].

A variety of substrates and support materials have been utilized depending on the desired applications [67]: porous alumina, graphite, and organic surfaces like self-assembled monolayers (SAMs) on gold, alongside surfaces incorporating silica [62]. The ability to grow SURMOFs with desired orientation has significant implications, e.g., in optimizing membrane systems. Aligning the pore structures parallel to the direction of flow enhances membrane permeance, leading to maximum flux compared to cases where crystallites are randomly oriented on the support [68].

Given the evident need to grow these porous, highly-oriented homogeneous MOF films, various synthesis methods have emerged over recent years [65].

2.2.2 Synthesis of SURMOFs

Growing Surface Mounted Metal-Organic Frameworks presents several challenges due to the intricacies of their synthesis [61, 69].

2.2.2.1 Challenges

2.2.2.1.1 Surface functionalization

To ensure the coordinative attachment of MOFs, it is essential to have the same or similar binding groups on the surface as those present within the MOF material [67]. Various methods are available for modifying the surfaces of different substrates (metal, glass, polymer, etc.) during preparation. Typically, SAMs serve as flexible organic modifiers, spontaneously adsorbing onto substrate surfaces to form ordered monomolecular layers. SAMs typically comprise head groups, tail groups, and functional end groups (Figure 4). Head groups may include thiols, silanes, or phosphonates, while tail groups often consist of alkyl chains $(\text{CH}_2\text{CH}_2)_n$. Functional end groups, such as carboxyl ($-\text{COOH}$), hydroxy ($-\text{OH}$), pyridyl and amino groups ($-\text{NH}_2$), not only offer ideal coordination sites for MOF thin film growth on surfaces but also serve as templates for controlling the growth orientation of MOF thin films [70]. Surface

modification of the substrate is crucial to enable strong bonding with SURMOFs by coordinating the terminal group of the SAM to the metal clusters of the MOF at the interface.

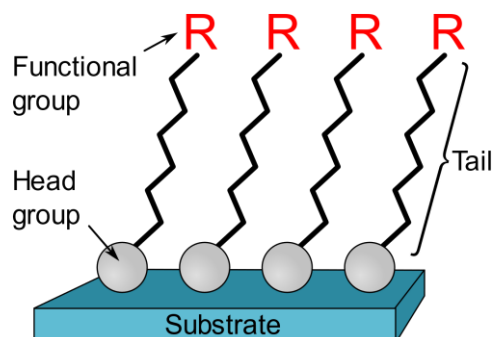


Figure 4 – Components of SAMs [71]

For modification of oxide surfaces (e.g. SiO_2 , Al_2O_3 , TiO_2) acidic conditions, H_2 - and O_2 -plasma are used [68]. It is evident that the growth and density of MOF crystal growth on bare oxide substrates are closely related to surface properties, but which can be adjusted by carefully selecting reaction conditions [68].

2.2.2.1.2 Synthesis parameters

Various types of SURMOFs demand a unique array of synthesis parameters to yield homogeneous, fully-covered films of crystalline structures, owing to the specific chemical interplay among ligands, metals, solvents, and substrates [72]. Different synthetic parameters including concentration, reaction time, solvent choice, temperature, and others, significantly influence the quality and characteristics of the resulting SURMOF films.

Optimizing the **concentrations** of metal salts and organic ligands in the synthesis solution is crucial for achieving desired SURMOF structures. Deviations from the optimal concentration significantly influence SURMOF morphology and surface coverage [61].

The **duration** of the synthesis process plays a critical role in determining the growth kinetics and crystal nucleation of SURMOFs. The quality of the resulting

SURMOF, including its crystallinity, thickness, and orientation, relies heavily on the immersion and rinsing durations [63].

The selection of **solvent** influences the solubility of precursor materials, reaction kinetics, and film morphology. Different solvents exhibit varying affinities towards metal ions and organic linkers, leading to differences in SURMOF growth rates and film quality [73].

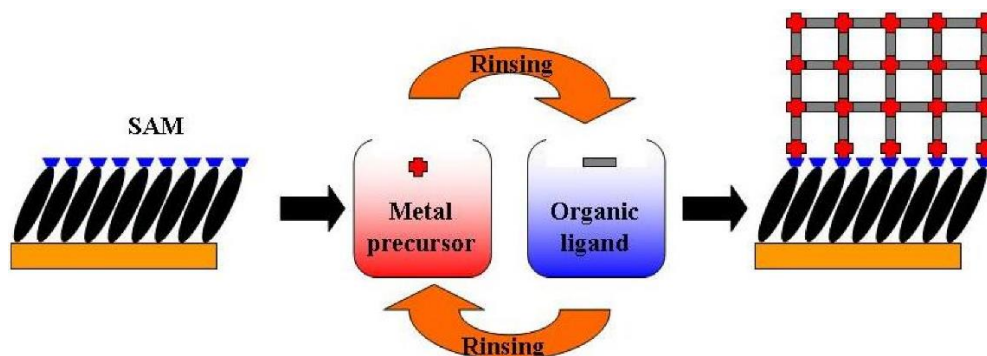
Temperature serves as a key parameter in controlling the nucleation and growth kinetics of SURMOFs. Variations in temperature can impact crystal size, orientation, and structural defects, necessitating precise temperature control throughout the synthesis process. The thin films grown at lower temperatures exhibit inferior coverage [61].

In addition to concentration, time, solvent, and temperature, several other synthesis parameters require careful consideration. These may include pH, stirring rate, precursor ratio, sonication during rinsing step, and the presence of additives or catalysts, each of which can influence SURMOF film properties and performance. Furthermore, the synthesis method itself could also influence the quality of SURMOF films.

2.2.2.2 Synthesis methods of SURMOFs

Liquid-Phase Epitaxy (LPE) is a general term encompassing various submethods, with the layer-by-layer (LbL) synthesis being the most prevalent among them [61]. The stepwise MOFs LbL growth method first was introduced in 2007 [74]. The LPE LbL method is based on the sequential immersion of functionalized substrates in metal ions (MI) and organic linker (L) solutions, immersing them into a washing solution (W) in between steps to remove any unreacted components (Scheme 1) [75-77]. These four sub-steps form one complete deposition cycle [63]. Such an approach allows for accurate thickness control through repeated growth cycles and encourages the formation of highly oriented films on functionalized surfaces [70, 78]. Various methods have been

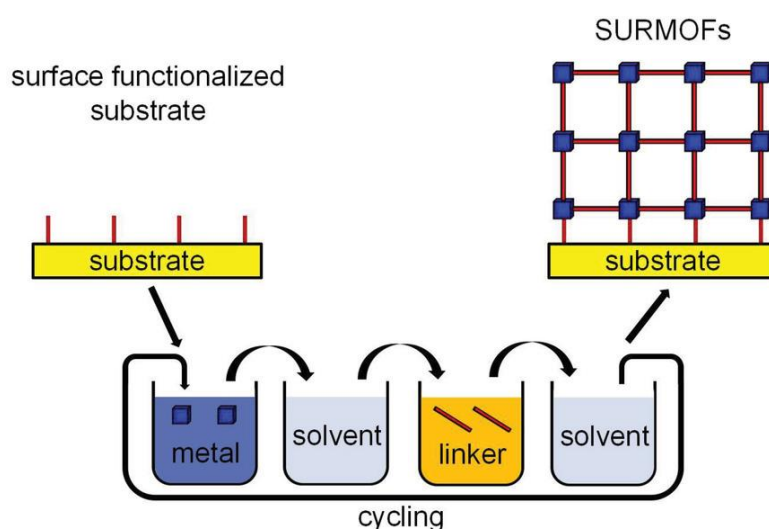
developed for preparing SURMOFs through epitaxial growth, including dip-, spray-, spin-coating, pump and flow cell layer-by-layer techniques [63, 75, 79].



Scheme 1 – Schematic diagram for the step-by-step approach for the growth of the MOFs on substrates functionalized with SAMs [76]

2.2.2.2.1 Dip-coating

The dip-coating method for SURMOF growth is a technique in which a functionalized substrate is secured in a holder and sequentially immersed into a metal ion solution and an organic linker solution (Scheme 2). Between each step, the sample is washed with a solvent. The concentrations, temperature, stirring (yes or no), timing, sonication (yes or no), and amount of cycles vary for different types of SURMOFs and desired properties. Dip-coating can be executed manually or automatically using dipping robots [80-82].

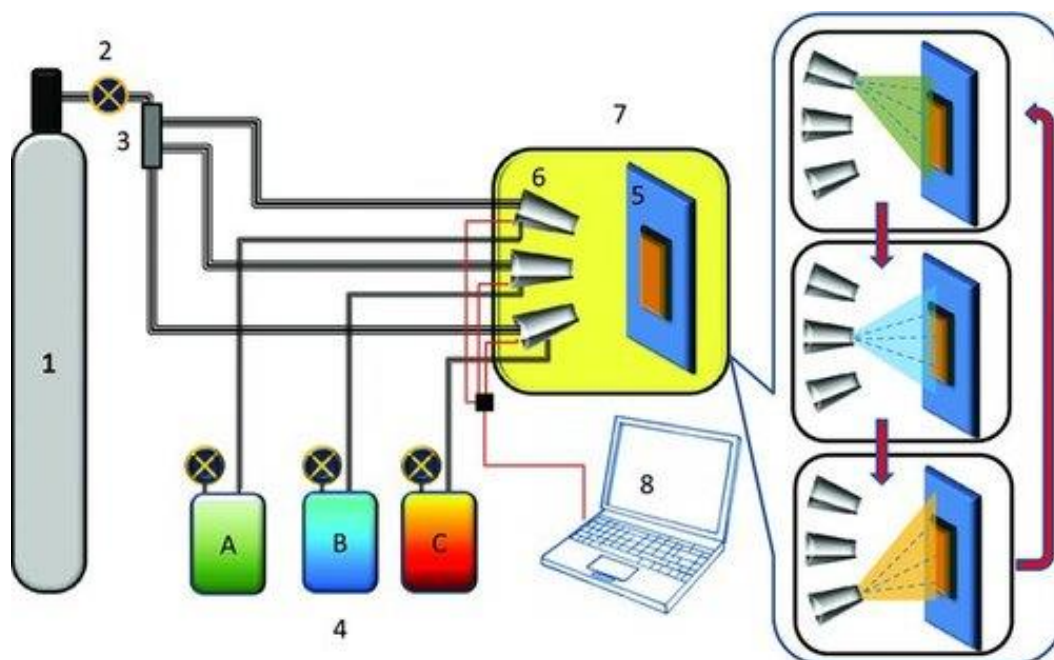


Scheme 2 – Dip-coating approach for SURMOFs synthesis [78]. *Reproduced with permission from Wiley*

Dip-coating enables the production of homogeneous films with the desired thickness. By incorporating heating, stirring, and/or sonication into the preparation process, it allows for the synthesis of different types of SURMOFs and optimization of their film quality through adjustments to a wide range of parameters. However, the sample size is limited due to the volume of glassware.

2.2.2.2.2 Spray-coating

The spray-coating method for SURMOF growth is a technique in which a functionalized substrate is fixed in a holder by a vacuum or glue and sequentially sprayed by solutions of MI and L. In between of depositions, the sample is rinsed with pure solvent. The solutions are drawn into a specifically designed nozzle system (Scheme 3), where they are converted into aerosols for application onto the substrate surface through spraying [83]. The droplets within the aerosol, with sizes as small as 10 μm , strike the substrate, forming a thin film of the reactant on its surface. Material deposition at the solid/liquid interface mirrors the process observed during the LPE process.



Scheme 3 – Setup employed for the fabrication of MOF thin films with the spray method: (1) Gas supply, (2) gas flow controller (3) three-way valve gas distributor (4) (A, B, C) solutions storage containers (5) sample holder (6) dosing valves, (7) spray chamber, (8) PC [83].

Reproduced with permission from Wiley

Spray-coating can be executed manually or automatically. In case of automated spraying three nozzles (MI, washing, L) are aligned side by side as a spraying unit on a programmable moving platform of an x-y-z-axle [84].

Following parameters could be adjusted in order to optimize synthesis conditions for specific applications [84]:

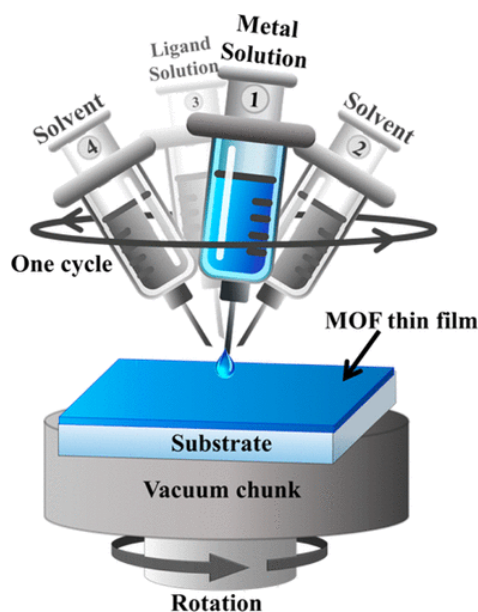
- Working distance relative to the substrate;
- Speed of moving spraying nozzles;
- Type of spraying nozzles: Flat spray nozzles or circular nozzles
- Type of Spray method: Line by line, Frontal Center Spray
- Gas pressure in container;
- Pressure of inert gas in aspirator unit;
- Ratio of liquid and inert gas inside the spraying nozzles;
- Concentration of liquids.

The spray LbL technique offers a high-throughput method for fabricating homogeneous and uniformly coated SURMOFs, significantly faster than dipping or pump LbL approaches [63]. By employing spray-coating, MOF thin films can be grown in a layer-by-layer manner on large samples. The maximum sample size is primarily constrained by the potential traverse paths of the robot arms maneuvering the spray nozzles and could be readily scaled up to achieve industrially relevant membrane sizes (several 1000 m²) [84]. However, this method's applicability is restricted by the types of SURMOFs that can be synthesized, as it lacks heating, stirring, and sonication steps, and offers limited solvent choices.

2.2.2.2.3 Spin-coating

The spin-coating LbL technique is implemented using a spin-coating apparatus, where distinct solutions and rinsing fluids are sequentially deposited onto a chemically functionalized substrate fixed by a vacuum chuck on a rotating rotator operating at a specific angular velocity (Scheme 4) [85]. Droplet

application can be manual or automated using micro syringes. Centrifugal force facilitates uniform spreading of the droplets across the surface. Spin coating offers a straightforward approach for generating SURMOFs with minimal consumption of reactants and solvents. Unlike dipping and pump LbL methods, where immersion times dictate SURMOF quality, spin coating optimizes SURMOF growth through adjustments in drop volumes, rotation speed, and rotation duration [63]. However, similar to the spray-coating method, spin coating lacks heating, stirring, and sonication steps, presenting similar limitations.

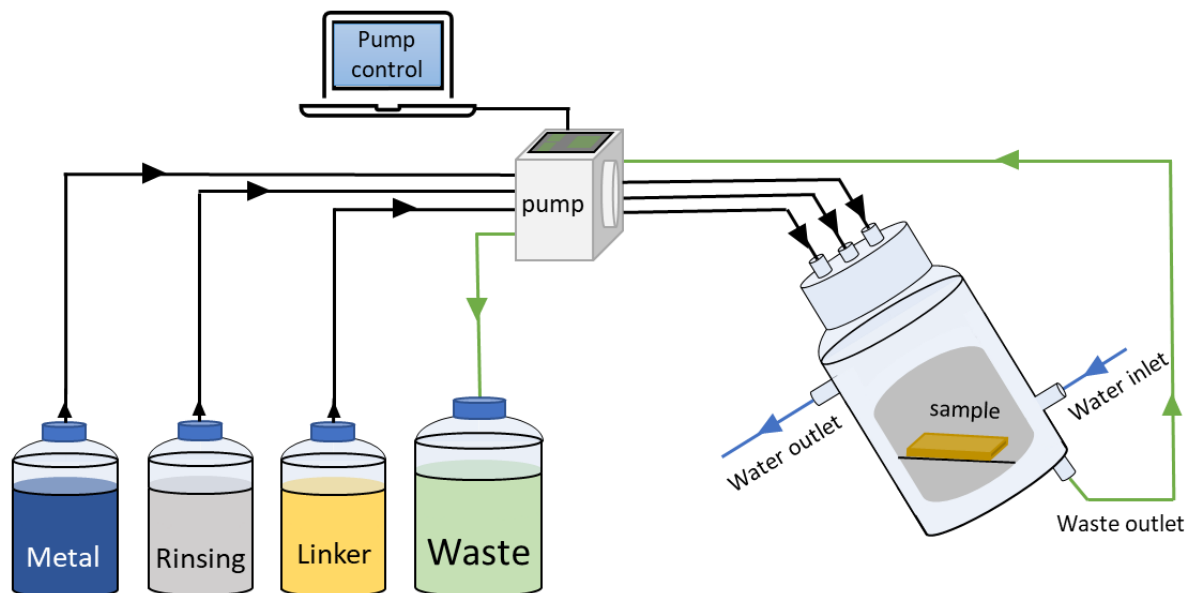


Scheme 4 –Spin Coating approach for SURMOFs synthesis. *Reprinted with permission from [85]. Copyright 2016 American Chemical Society.*

2.2.2.2.4 Pump method

The pump LbL technique follows a similar approach to dip-coating, where a substrate is exposed to different solutions alternately. However, instead of immersing and withdrawing the samples from beakers filled with different solutions, the pump system involves placing functionalized substrates within a temperature-controlled double-walled glass flow reactor (Scheme 5). Within this setup, three channels of the pump introduce a metal ion solution, organic linker solution, and rinsing solvent into the reactor, respectively. A programmable

controller manages the sequence of pump operations along with immersion and rinsing durations. Subsequently, an additional fourth pump channel removes the respective solution before the subsequent solution injection [63]



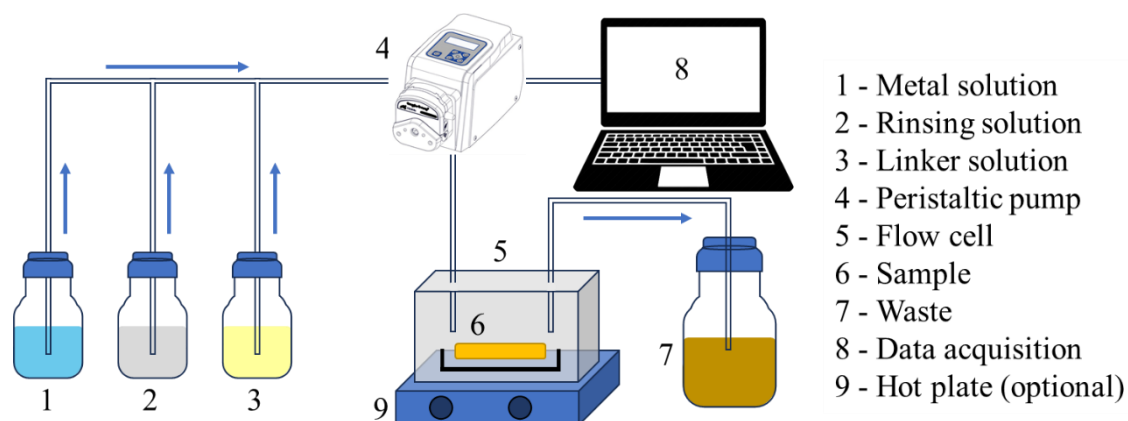
Scheme 5 – Pump approach for SURMOFs synthesis

This method enables the production of homogeneous thin films of SURMOFs and allows for temperature control, thereby expanding the range of SURMOFs that can be synthesized. Additionally, it offers versatility in the choice of solutions. However, stirring and sonication could not be applied. Furthermore, the size of the samples is limited by the geometry of the reactor.

2.2.2.2.5 Flowing method

The flow method, or flow cell technique, presents a dynamic approach to SURMOF synthesis similar to pump method but with the difference that solutions are not sucked out by fourth pump channel. In this method, reactants are continuously flowed over a functionalized substrate surface within a controlled flow cell environment in a subsequent manner. This allows for precise regulation of reaction conditions such as temperature, pressure, and flow rate, facilitating reproducible and uniform SURMOF growth. The continuous flow of reactants also ensures efficient mass transfer and reaction kinetics, leading to

enhanced film quality and thickness control. Additionally, the flow method permits the use of a wide range of precursor solutions and additives, enabling flexibility in SURMOF composition and structure. However, the complexity of flow cell setup and operation may pose challenges, and the method requires careful optimization of flow parameters to achieve desired film characteristics. Furthermore, the size of the samples is constrained by the dimensions of the flow cell, limiting scalability for large-scale production.



Scheme 6 – Flow cell approach for SURMOFs synthesis

A comparable approach involves the utilization of commercially accessible quartz crystal microbalance (QCM) systems (Scheme 6) alongside an auto sampler. This sampler delivers reactant and rinsing solutions to the QCM sensor cell. Real-time monitoring of the LbL growth of the SURMOF thin film is feasible by observing the frequency change of the QCM sensor [63, 86]. The frequency difference is then converted into a mass change using the Sauerbray equation (see details in 3.2.7 Quartz-crystal microbalance (QCM)), providing valuable insights into synthesis kinetics and the total mass of the resulting SURMOF film.

2.2.2.2.6 Summary

When comparing various methods for synthesizing SURMOF-based thin films, each approach offers distinct advantages and drawbacks. In dipping- or pump-based synthesis, each deposition sub-step is time-consuming, but it results

in perfect orientation and precisely one layer increase in SURMOF thickness per deposition cycle. Conversely, the spray method completes one deposition cycle, comprising four sub-steps, within minutes, with an average thickness increase equivalent to about ten SURMOF layers. However, spray-coated SURMOFs exhibit lower orientation compared to those prepared by dipping or pump methods. Additionally, the flow method offers precise regulation of reaction conditions and enhanced film growth control. Spin-coating, on the other hand, facilitates homogeneous SURMOF formation with minimal reactant and solvent consumption.

Synthesis methods for MOF thin films continue to evolve, adapting to specific film properties desired, with recent examples including the vacuum filtration method for 2D MOFs, solution atomic layer deposition, and autoclave synthesis [85].

Ultimately, for each SURMOF type, selecting a specific deposition approach yields optimized quality. High-quality SURMOFs open up numerous new possibilities for MOF applications [65].

2.2.3 Application of SURMOFs

As mentioned in the preceding section, SURMOFs can be synthesized using various methods, resulting in a variety of properties in the resulting thin films. For example, these films can exhibit surface roughness, ranging from separate crystallites to highly uniform surfaces on a nanoscale level. It's evident that different applications require specific types of SURMOFs. SURMOFs offer superior control over surface properties, leading to enhanced performance and durability in practical applications. The ability to immobilize SURMOFs on solid supports provides benefits in terms of ease of handling, scalability, and compatibility with existing technologies.

The optical and structural integrity of SURMOFs holds significant importance across a variety of **optical applications**, including but not limited to light-

emitting materials, optical sensors, nonlinear optical materials, and up-conversion materials [63, 65, 81].

Additionally, SURMOFs have garnered considerable interest for their potential applications in various **sensing technologies**, including QCM sensors, where they can be utilized as selective coatings on the quartz surface [87, 88], enabling the detection of specific analytes through changes in mass or viscoelastic properties.

In **membrane applications** [88], SURMOFs enhance separation performance in gas separation, water purification, and molecular sieving processes, representing a cutting-edge approach in membrane technology.

SURMOFs could be utilized as **coatings** with tailored properties for diverse needs. External surface functionalization allows alteration of surface characteristics such as hydrophilicity/hydrophobicity and affinity while preserving porosity [89].

Furthermore, SURMOFs' crystalline structures enable accurate comparisons with theoretical models, especially since defects can be readily identified and controlled. These porous films have extensive potential for **advanced applications**, including facilitating remote-controlled molecule release, producing membranes with photoswitchable selectivity, developing ion conductors with adjustable conductivity [79], and constructing electrochromic devices [90].

Despite numerous advantages, applications of many MOFs are ultimately limited by their stability in water or under other harsh conditions [91]. Nonetheless, Zr(Hf)-based MOFs families demonstrate high stability in harsh media, making them promising candidates for different applications utilizing such conditions.

2.3 Zr(Hf)-based MOFs/SURMOFs

Initially synthesized in 2008 (Figure 5) Zr-based MOFs (Zr-MOFs) gained significant attention due to their high mechanical (external pressure up to 10.000 kg/cm²), thermal (decomposition temperature above 500 °C) and chemical stability (resistant to water and most chemicals) [92]. The difficulties in synthesizing and characterizing Zr-MOFs following the discovery of UiO-66 led to a lack of new structures reported until 2011 [91]. The innovation of modulated synthesis enabled the creation and characterization of UiO-68-NH₂ single crystals [93], sparking the exploration of new Zr-based MOFs and their applications.

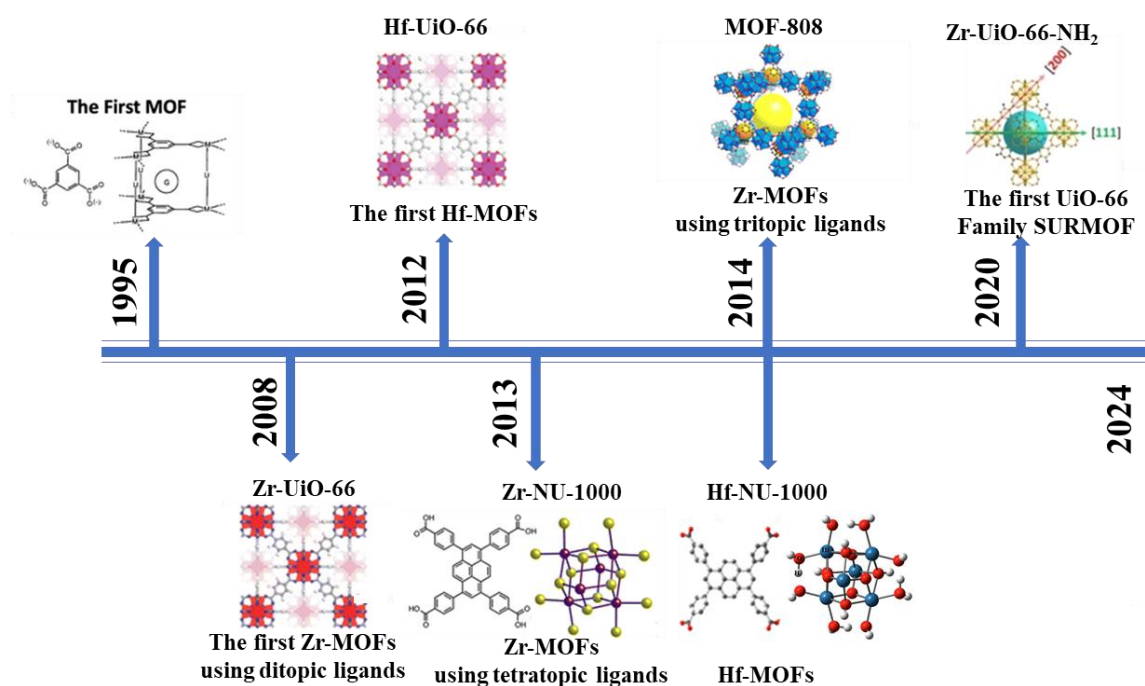


Figure 5 – Timeline of development of stable Zr(Hf)-based MOFs and SURMOFs. Edited from [94]; Copyright 2023 RSC. MOF from [95]; Copyright 1995 Springer Nature. Zr based UiO-66, UiO-67, and UiO-68 from [92]; Copyright 2008 American Chemical Society. Hf-UiO-66 from [96]; Copyright 2012 American Chemical Society. Zr-NU-1000 from [97]; Copyright 2013 American Chemical Society. MOF-808 from [98]; Copyright 2014 American Chemical Society. Hf-NU-1000 from [99]; Copyright 2014 American Chemical Society. Zr-UiO-66-NH₂ SURMOF from [100]; Copyright 2020 Wiley.

Hafnium (Hf) and Zirconium (Zr) are chemical twins due to similar chemical properties and close resemblance in terms of atomic structure and behavior. As a

result, Hafnium-based MOFs (Hf-MOFs) typically exhibit identical structures to Zr-based ones [101]. By employing identical organic linkers and synthesis parameters, the zirconium precursor salt (ZrCl_4 or ZrOCl_2) can be substituted with a hafnium salt (HfCl_4 or HfOCl_2) [102].

Zr(Hf)-MOFs have been demonstrated exceptional thermal and chemical stability in compare to other MOFs [103, 104]. The crystallinity and porosity of many Zr-MOFs remain unaffected when exposed to water, acidic solutions, steam, and even H_2S vapor [105]. The stability can be attributed to the high valence of the metal and the strong interaction between Zr (or Hf) and oxygen, which leads to robust Zr(Hf)-O bonds. High stability make Zr(Hf)-MOFs suitable for applications that require resistance to harsh conditions such as catalysis [99, 106], gas storage [107] and separation [108, 109], drug delivery [110], sensing [87] and water treatment [111-114].

A large variety of Zr-MOFs have been reported (Table 2).

Table 2 – Zr-MOFs [91]. *Reproduced with permission from Wiley*

MOF family	MOF	Clusters/Cores	Linker
UiO	UiO-66	$[\text{Zr}_6(\mu_3\text{-O})_4(\mu_3\text{-OH})_4(\text{COO})_{12}]$	BDC
	UiO-67	$[\text{Zr}_6(\mu_3\text{-O})_4(\mu_3\text{-OH})_4(\text{COO})_{12}]$	BPDC
	UiO-68	$[\text{Zr}_6(\mu_3\text{-O})_4(\mu_3\text{-OH})_4(\text{COO})_{12}]$	TPDC
NU	NU-1000	$[\text{Zr}_6(\mu_3\text{-O})_4(\mu_3\text{-OH})_4(\text{OH})_4(\text{H}_2\text{O})_4(\text{COO})_8]$	TBAPy
	NU-1100	$[\text{Zr}_6(\mu_3\text{-O})_4(\mu_3\text{-OH})_4(\text{COO})_{12}]$	PTBA
	NU-1101	$[\text{Zr}_6(\mu_3\text{-O})_4(\mu_3\text{-OH})_4(\text{COO})_{12}]$	Py-XP
	NU-1102	$[\text{Zr}_6(\mu_3\text{-O})_4(\mu_3\text{-OH})_4(\text{COO})_{12}]$	Por-PP
	NU-1103	$[\text{Zr}_6(\mu_3\text{-O})_4(\mu_3\text{-OH})_4(\text{COO})_{12}]$	Py-PTP
	NU-1104	$[\text{Zr}_6(\mu_3\text{-O})_4(\mu_3\text{-OH})_4(\text{COO})_{12}]$	Por-PTP
PCN	PCN-94	$[\text{Zr}_6(\mu_3\text{-O})_4(\mu_3\text{-OH})_4(\text{COO})_{12}]$	ETTC
	PCN-222	$[\text{Zr}_6(\mu_3\text{-O})_4(\mu_3\text{-OH})_4(\text{OH})_4(\text{H}_2\text{O})_4(\text{COO})_8]$	TCPP
	PCN-223	$[\text{Zr}_6(\mu_3\text{-O})_4(\mu_3\text{-OH})_4(\text{COO})_{12}]$	TCPP
	PCN-224	$[\text{Zr}_6(\mu_3\text{-O})_4(\mu_3\text{-OH})_4(\text{OH})_6(\text{H}_2\text{O})_6(\text{COO})_6]$	TCPP
	PCN-225	$[\text{Zr}_6(\mu_3\text{-O})_4(\mu_3\text{-OH})_4(\text{OH})_4(\text{H}_2\text{O})_4(\text{COO})_8]$	TCPP

	PCN-228	$[\text{Zr}_6(\mu_3\text{-O})_4(\mu_3\text{-OH})_4(\text{COO})_{12}]$	TCP-1
	PCN-229	$[\text{Zr}_6(\mu_3\text{-O})_4(\mu_3\text{-OH})_4(\text{COO})_{12}]$	TCP-2
	PCN-230	$[\text{Zr}_6(\mu_3\text{-O})_4(\mu_3\text{-OH})_4(\text{COO})_{12}]$	TCP-2
	PCN-521	$[\text{Zr}_6(\mu_3\text{-O})_4(\mu_3\text{-OH})_4(\text{OH})_4(\text{H}_2\text{O})_4(\text{COO})_8]$	MTBC
	PCN-700	$[\text{Zr}_6(\mu_3\text{-O})_4(\mu_3\text{-OH})_4(\text{OH})_4(\text{H}_2\text{O})_4(\text{COO})_8]$	Me ₂ BPDC
	PCN-777	$[\text{Zr}_6(\mu_3\text{-O})_4(\mu_3\text{-OH})_4(\text{OH})_6(\text{H}_2\text{O})_6(\text{COO})_6]$	TATB
	PCN-133	$[\text{Zr}_6(\mu_3\text{-O})_4(\mu_3\text{-OH})_4(\text{COO})_{12}]$	BTB, DCDPS
	PCN-134	$[\text{Zr}_6(\mu_3\text{-O})_4(\mu_3\text{-OH})_4(\text{OH})_2(\text{H}_2\text{O})_2(\text{COO})_{10}]$	BTB, TCPP
MIL	MIL-140A	$[\text{ZrO}(\text{COO})_2]_n$	BDC
	MIL-140B	$[\text{ZrO}(\text{COO})_2]_n$	2,6-NDC
	MIL-140C	$[\text{ZrO}(\text{COO})_2]_n$	BPDC
	MIL-140D	$[\text{ZrO}(\text{COO})_2]_n$	Cl ₂ ABDC
MOF	MOF-801	$[\text{Zr}_6(\mu_3\text{-O})_4(\mu_3\text{-OH})_4(\text{COO})_{12}]$	FUM
	MOF-802	$[\text{Zr}_6(\mu_3\text{-O})_4(\mu_3\text{-OH})_4(\text{OH})_2(\text{H}_2\text{O})_2(\text{COO})_{10}]$	PZDC
	MOF-808	$[\text{Zr}_6(\mu_3\text{-O})_4(\mu_3\text{-OH})_4(\text{OH})_6(\text{H}_2\text{O})_6(\text{COO})_6]$	BTC
	MOF-812	$[\text{Zr}_6(\mu_3\text{-O})_4(\mu_3\text{-OH})_4(\text{COO})_{12}]$	MTB
	MOF-841	$[\text{Zr}_6(\mu_3\text{-O})_4(\mu_3\text{-OH})_4(\text{OH})_4(\text{H}_2\text{O})_4(\text{COO})_8]$	MTB
	MOF-525	$[\text{Zr}_6(\mu_3\text{-O})_4(\mu_3\text{-OH})_4(\text{COO})_{12}]$	TCPP
DUT	DUT-51	$[\text{Zr}_6(\mu_3\text{-O})_4(\mu_3\text{-OH})_4(\text{OH})_4(\text{H}_2\text{O})_4(\text{COO})_8]$	DTTDC
	DUT-52	$[\text{Zr}_6(\mu_3\text{-O})_4(\mu_3\text{-OH})_4(\text{COO})_{12}]$	2,6-NDC
	DUT-84	$[\text{Zr}_6(\mu_3\text{-O})_4(\mu_3\text{-OH})_4(\text{OH})_6(\text{H}_2\text{O})_6(\text{COO})_6]$	2,6-NDC
	DUT-67	$[\text{Zr}_6(\mu_3\text{-O})_4(\mu_3\text{-OH})_4(\text{OH})_4(\text{H}_2\text{O})_4(\text{COO})_8]$	TDC
	DUT-68	$[\text{Zr}_6(\mu_3\text{-O})_4(\mu_3\text{-OH})_4(\text{OH})_4(\text{H}_2\text{O})_4(\text{COO})_8]$	TDC
	DUT-69	$[\text{Zr}_6(\mu_3\text{-O})_4(\mu_3\text{-OH})_4(\text{OH})_2(\text{H}_2\text{O})_2(\text{COO})_{10}]$	TDC

Since the UiO-66 type is the main SURMOF in this thesis, more details about the UiO family and NU-1000 are introduced below.

2.3.1 UiO (University of Oslo) family

Recognized as a pivotal Metal-Organic Framework, UiO-66 has attracted considerable attention for its remarkable porous structure and exceptional stability under elevated temperatures, high pressures, and harsh chemical conditions (acidic or basic environments) [16, 115]. The addition of active

functional groups (-NH₂, -NO₂, -Br) to the UiO-66 structure has been found to minimally impact its exceptional thermal and chemical stability [116]. Furthermore, we found that UiO-66-NH₂ SURMOF exhibits high stability across a broad pH range, from pH 2 to pH 10 (Figure 6) [117].

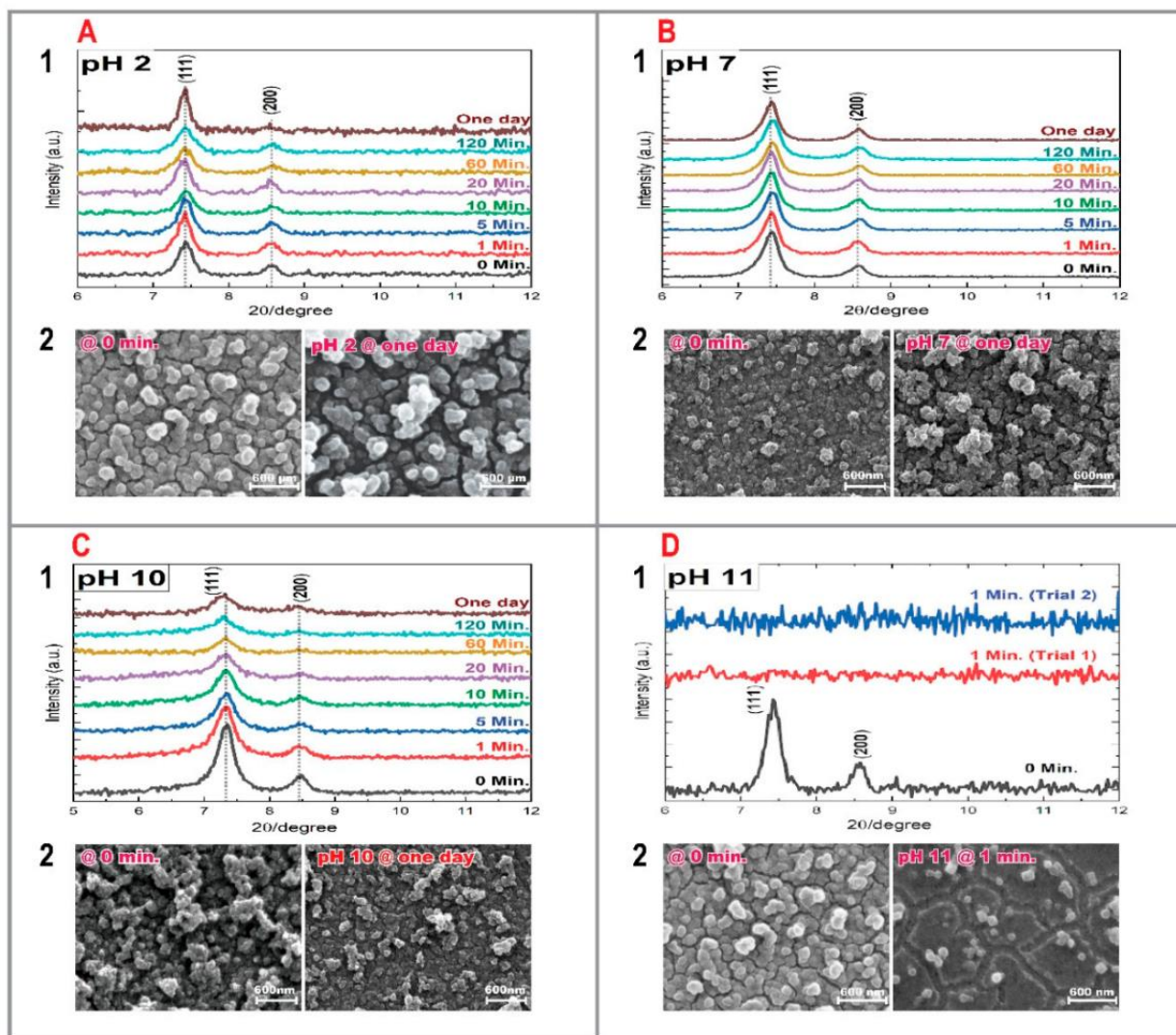


Figure 6 – XRD patterns and SEM images of UiO-66-NH₂ SURMOF films immersed in a: (A) pH 2 solution, (B) pH 7 solution, (C) pH 10 solution, and (D) pH 11 solution [117]

2.3.1.1 Structure of UiO-66 MOF

The UiO-66 framework is constructed from [Zr₆O₄(OH)₄] SBUs, each coordinated with 12 1,4-benzene-dicarboxylate (H₂BDC) linkers in cuboctahedral node, forming a network with fcu topology [101]. Within the

octahedral cluster, six Zr^{4+} ions occupy vertices, while eight triangular faces are alternately adorned with four $\mu_3\text{-OH}$ and four $\mu_3\text{-O}$ groups. The $[\text{Zr}_6(\mu_3\text{-O})_4(\mu_3\text{-OH})_4]$ core is further capped by 12 carboxylates, forming clusters denoted as $[\text{Zr}_6(\mu_3\text{-O})_4(\mu_3\text{-OH})_4(\text{COO})_{12}]$. The cubic structure comprises octahedral cages (11 Å) and tetrahedral cages (8 Å), connected through narrow triangular windows (6 Å) [92], yielding a substantial BET surface area nearing $1200 \text{ m}^2 \text{ g}^{-1}$. Additionally, two isorecticular structures, UiO-67 and UiO-68, were obtained through linker elongation (Figure 7) [91].

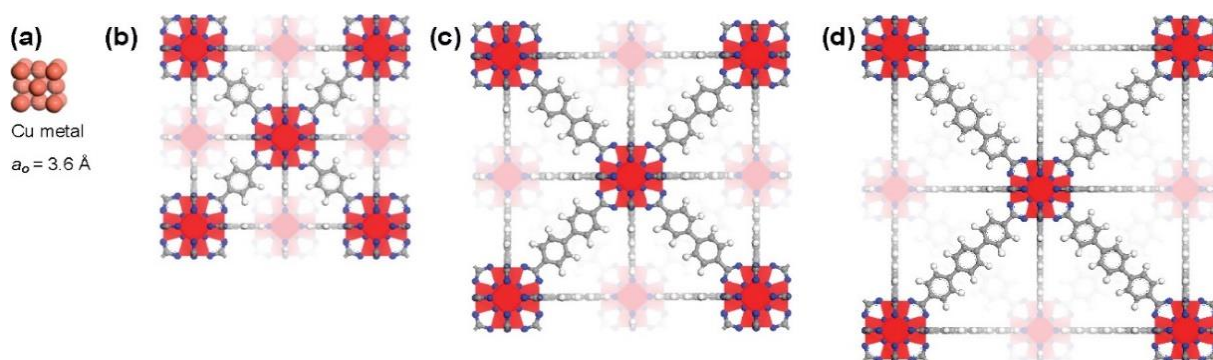


Figure 7 – (a) One unit cell of copper drawn to scale with: (b) Zr–MOF with 1,4-benzene-dicarboxylate (BDC) as linker, UiO-66, (c) Zr–MOF with 4,4' biphenyl-dicarboxylate (BPDC) as linker, UiO-67, (d) Zr–MOF with terphenyl dicarboxylate (TPDC) as linker, UiO-68 [92]. *Reproduced with permission from American Chemical Society.*

Zirconium, oxygen, carbon, and hydrogen atoms are red, blue, gray, and white, respectively.

Most of the reported isostructural analogues of UiO-66, comprising elongated or functionalized linkers, are constructed using the same $[\text{Zr}_6(\mu_3\text{-O})_4(\mu_3\text{-OH})_4(\text{COO})_{12}]$ cluster [91].

Hf-based analogues are commonly obtained and typically exhibit similar structures and properties, with the exception of an increase in molecular weight [91]. Nearly every Zr-based UiO MOF can be synthesized with Hf, incorporating an octahedral $[\text{Hf}_6(\mu_3\text{-O})_4(\mu_3\text{-OH})_4]$ SBU [102]. Examples of known Hf-based UiO MOFs include Hf-UiO-66 [96], Hf-UiO-66-R (where R is $-\text{NH}_2$, $-(\text{OH})_2$, $-(\text{COOH})$, $-(\text{F})_4$) [109], Hf-UiO-67 [118], and Hf-Fum [101, 119].

2.3.1.2 Post-synthetic modification (PSM) of UiO MOF/SURMOF

Post-synthetic modification has emerged as a powerful strategy for tailoring the properties and functionalities of MOFs. PSM offers precise control over the **chemical functionality** of UiO MOFs by introducing functional groups onto the organic linkers or metal nodes. Functionalization can impart specific properties such as catalytic activity, selectivity, or sensing capabilities. PSM techniques can be employed to **improve the stability and robustness** of UiO MOFs under harsh conditions, such as high temperatures or corrosive environments. **Surface modification** through PSM allows for the precise tuning of surface properties, such as hydrophobicity/hydrophilicity or surface charge, which can influence adsorption, catalysis, and biological interactions.

Furthermore, PSM is an essential addition to traditional synthesis methods for MOFs, providing a flexible tool for creating MOFs with diverse functionalities while maintaining stability. Stable MOFs, in particular, have an advantage over less stable ones as they can withstand harsh modification conditions while maintaining their crystallinity and porosity. This durability allows for a broader range of PSM reactions on these stable MOF platforms [91]. For instance, processes like post-synthetic ligand and metal ion exchange have been successfully carried out in several stable MOFs, including the UiO series (Figure 8). Compared to direct solvothermal synthesis, ligand exchange in robust MOFs offers an alternative way to incorporate functional groups, especially sensitive ones, under relatively mild conditions [91].

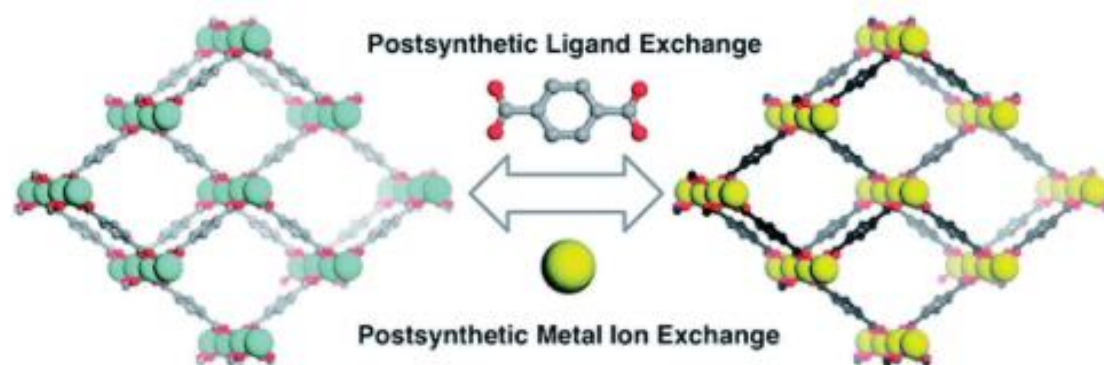


Figure 8 – Postsynthetic ligand and cation exchange in robust MOFs [91]. *Reproduced with permission from Wiley*

Covalent modification is the most common PSM route, allowing MOFs to be functionalized with tailored internal surfaces for specific applications. Functional groups, such as amino groups, are often pre-anchored on the linkers of MOFs to facilitate further modification reactions. PSMs involving amino groups have been performed using anhydrides, isocyanates, aldehydes, acyl chlorides, alkyl bromides, and various complex metal-organic compounds [91, 120, 121]. Additionally, click chemistry between azides and alkynes has been widely used to modify MOFs with desired functional groups. The readily accessible and reactive azide groups in the MOF cavities enable efficient click reactions with alkynes, leading to MOFs with customized pore surfaces [91].

2.3.2 NU (Northwestern University)-1000

NU-1000 is another prominent MOF known for its high stability, large pores, and exceptional water stability, making it suitable for various applications such as catalysis, gas storage, and separation processes.

The structure of NU-1000 (Figure 9) is constructed from $\text{Zr}_6(\mu_3\text{-O})_4(\mu_3\text{-OH})_4(\text{OH})_4(\text{H}_2\text{O})_4$ clusters, and tetatopic 1,3,6,8-tetrakis(p-benzoate)pyrene (TBAPy) linkers, forming a 3D network with an ftw topology.

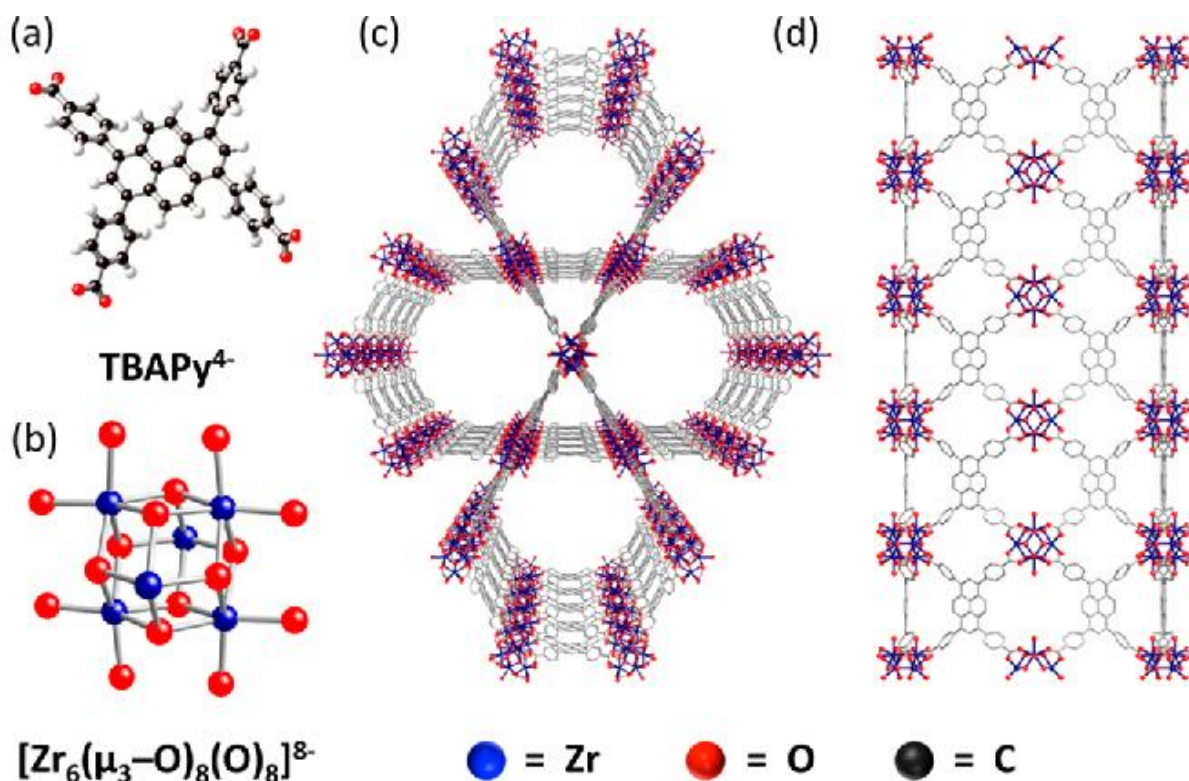


Figure 9 – (a) 1,3,6,8-Tetrakis(p-benzoic acid)pyrene linker, TBAPy⁴⁻ and (b) the $[\text{Zr}_6(\mu_3\text{-O})_8(\text{O})_8]^{8-}$ node of the (c and d) Zr₆-based framework NU-1000. Note that the linkers are not shown in the representation of the node, and the hydrogens are not shown in the framework representations for clarity [122]. *Reproduced with permission from American Chemical Society*

Each Zr₆ SBU is connected to eight TBAPy linkers through the carboxylate groups, forming a highly porous and robust structure. Even though the number of connections is decreased, the stability of Zr-MOFs featuring 8-connected Zr-clusters remains intact. As evidence, NU-1000 demonstrates resilience even in highly concentrated HCl solutions [91].

The framework contains large mesoporous cages, approximately 31 Å in diameter, and microporous channels, approximately 12 Å, contributing to its high surface area (BET surface area > 2000 m²/g). The Zr₆ clusters in NU-1000 contain terminal hydroxyl and water ligands, which can participate in hydrogen bonding and coordination chemistry, enhancing the framework's chemical versatility and stability.

3 Chapter III. Materials and methods

This chapter describes the relevant materials used, as well as the techniques and instruments applied for the characterization of synthesized SURMOFs/thin films in this thesis. These include X-ray Diffraction (XRD), Fourier transform-Infrared Spectroscopy (FT-IR), Scanning Electron Microscopy (SEM), Atomic-Force Microscopy (AFM), Water Contact Angle (WCA), Time-of-Flight Secondary Ion Mass Spectrometry (ToF-SIMS), and Quartz-Crystal Microbalance (QCM).

3.1 Materials and techniques

In the following subchapter, the materials and techniques used for substrate functionalization prior to SURMOF/thin film growth are described. Additionally, the chemicals used for SURMOF/thin film synthesis are presented, while the synthesis methods, as well as materials required for post-synthetic modifications and various tests, are detailed in each relevant chapter.

3.1.1 Surface functionalization

3.1.1.1 Materials

Self-assembled monolayers of 11-mercapto-1-undecanol (MUD, Sigma Aldrich) were employed to functionalize Au-coated silicon wafers and AT-cut quartz sensor crystals (0.3 mm thick) coated with a gold layer QSX 301 (100 nm thick) (Q-Sense, Frölunda, Sweden) with a resonance frequency at 4.95 MHz.

Porous α -Al₂O₃ disks (h = 1 mm, d = 13 mm), consisting of a smooth layer of α -Al₂O₃ (d₅₀ = 70 nm) on the top of an α -Al₂O₃ support (d₅₀ = 2.5 μ m), was obtained from Fraunhofer IKTS. Commercial Filter paper (Ashless circles 90 mm Ø, 2.5 mm), was obtained from Whatman, England, and was used as a substrate. Chloroacetic acid (99%) was purchased from SigmaAldrich, USA.

Sodium hydroxide (NaOH) (99% purity) was obtained from Merck, Germany. All reagents were used without further purification.

3.1.1.2 Techniques

3.1.1.2.1 Au coated Si wafers functionalization

MUD SAM were employed to functionalize Au-coated silicon wafers and AT-cut quartz sensor crystals coated with a gold layer. The substrates were left in the dark at room temperature for 48 h with the gold side up in a 1 mM ethanolic solution of MUD, producing an -OH functionalized surface. To prepare the substrates for immediate use in the synthesis, they were completely washed with pure ethanol and dried in a flow of dry nitrogen.

3.1.1.2.2 Membranes functionalization

For the functionalization of α -alumina, a 20-minute O₂ plasma treatment was applied, after which the substrates were immediately immersed in a metal ion solution.

Cellulose was functionalized using the method previously described by Hashem et al. [123]. To create anchoring sites for the deposition of SURMOFs and thin films, filter paper was carboxymethylated with chloroacetic acid in the presence of sodium hydroxide. This process involved immersing the filter paper in a solution of 1 M chloroacetic acid in 15% w/v sodium hydroxide for 72 hours. After the immersion period, the filter paper was rinsed with distilled water and left to dry overnight.

3.1.2 Chemicals used for SURMOF/thin films synthesis

The following reagents were purchased from Alfa Aesar, Germany and Saudi Arabia to prepare UiO-66-NH₂ SURMOF: zirconium (IV) chloride (ZrCl₄, reactor grade, 99.5%), hafnium (IV) chloride (HfCl₄, reactor grade, 99.5%) and 2-aminoterephthalic acid (99%, NH₂-BDC) were used as metal ions and organic

linker sources, respectively. Hydrochloric acid (HCl, 36 %, Merck, Darmstadt, Germany, analytical grade) was used as modulator.

The reactents for NU 1000 synthesis, zirconyl chloride octahydrate ($\text{ZrOCl}_2 \cdot 8\text{H}_2\text{O}$) and benzoic acid ($\text{C}_6\text{H}_5\text{COOH}$) were provided by Alfa Aesar, Germany. 1,3,6,8tetra(4-carboxylphenyl) pyrene (H_4TBAPy) supplied by Chemsoon LTD, China.

N,N-Dimethylformamide (DMF) was supplied by Emsure Company and was used as a solvent for metal ions and linkers compounds, as well as an intermediate washer for prepared samples. N,N-Diethylformamide (DEF) was supplied by Emsure Company and was applied as a solvent for NU-1000 SURMOF synthesis.

All reagents were used without further purification.

3.2 General instrumental information of the characterization techniques

3.2.1 X-Ray Diffraction (XRD)

Substances consist of atoms organized within crystal microstructures. Solid-state compounds are classified into three main categories: amorphous, single crystalline, and polycrystalline materials (Figure 10), depending on the internal atomic arrangement [124]. Amorphous materials possess isotropic characteristics due to the irregularity in atomic arrangement, resulting in consistent properties regardless of direction. Conversely, crystalline materials feature a regular and repetitive atomic structure, leading to directional variations in properties (known as anisotropy). Polycrystalline materials are formed by the aggregation of multiple crystals varying in sizes and shapes.

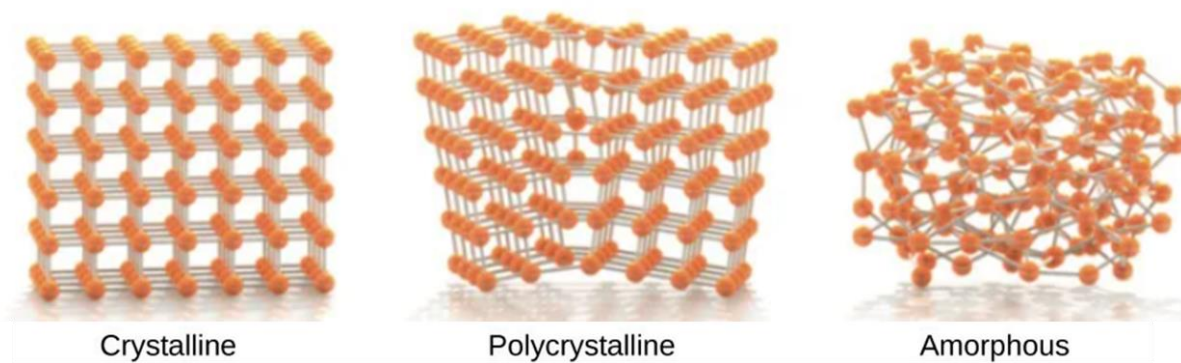


Figure 10 – Solid phases [125]

XRD is a powerful technique that provides valuable insights into the atomic arrangement and crystallographic properties of crystalline materials [126]. X-rays exhibit wavelengths that are on the same order of magnitude as the size of atoms (typically ranging from approximately 10^{-3} nm [127]). Consequently, the intensity of X-ray diffraction techniques and their resulting patterns are utilized to obtain insights into atomic structures [124]. Typically, XRD provides information regarding the crystalline structure, nature of the phase, lattice parameters and crystalline grain size [128].

XRD, a non-destructive testing method, is applicable for examining a wide range of materials, encompassing minerals, polymers, plastics, metals, semiconductors, ceramics, and solar cells. When X-rays interact with solid materials, they scatter due to the movement of electrons around atomic nuclei. These scattered waves, emitted in various directions, undergo interference phenomena – both constructive and destructive. Constructive interference specifically leads to diffraction of the X-rays. It's notable that the orderly arrangement or periodicity of atomic structures within solids induces constructive interference, making the interpretation of XRD graphs for crystalline substances straightforward [124].

The first experiment on X-ray diffraction by a crystal was performed by W. Friedrich, P. Knipping and M. von Laue in 1912 and Bragg's law was derived in 1913 [129]. Bragg's Law is a fundamental principle in X-ray diffraction (Figure

11) that plays a crucial role in understanding the relationship between the angles of incidence, the wavelength of X-rays, and the arrangement of atoms in a crystal lattice. This law, formulated by Sir William Henry Bragg and his son Sir William Lawrence Bragg in 1913, provides a mathematical expression for constructive interference of X-rays scattered by crystal planes.

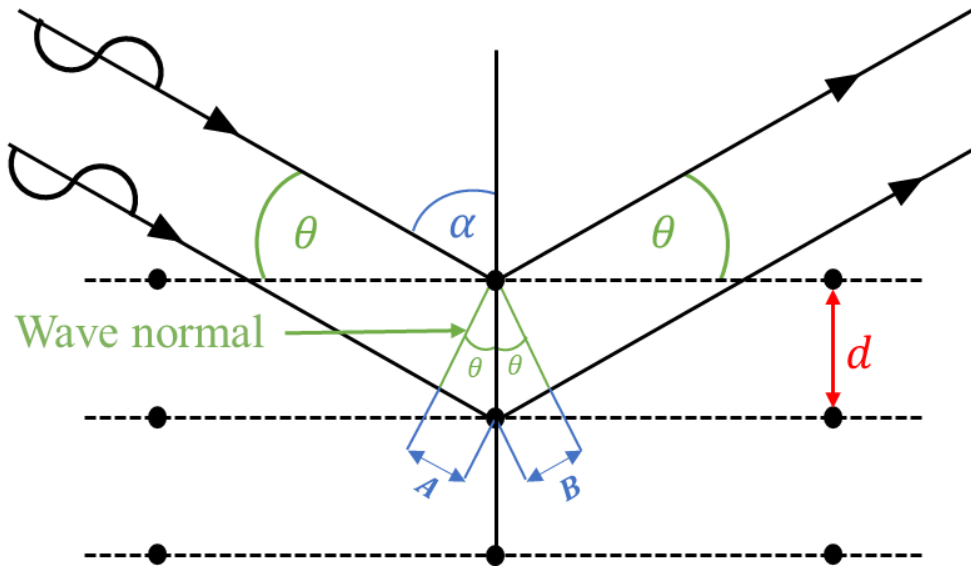


Figure 11 – Visualization of the Bragg's Law

Figure 11 illustrates the diffraction process from two distinct scattering planes separated by a distance d and intersected by X-radiation of wavelength λ at the incident angle Θ . The parameter 2Θ represents the angle formed between the diffracted and undeviated X-ray waves. Although the diagram depicts only two scattering planes, it implies the existence of numerous parallel, identical planes, each spaced apart by the distance d . The positions of these planes are determined by a periodic function, with a "wavelength" associated with the unit cell dimensions and the orientation of the plane hkl . Wave normals connect points of identical phase for both incident and diffracted waves. For total constructive reinforcement to occur between the scattering from these planes, the combined distance $(A + B)$ must equal an integer multiple of wavelengths, necessitating the calculation of the value of Θ , given d , for which $(A + B) = n\lambda$, where n is an integer. The direction of d is perpendicular to the planes, and the wave normal is

perpendicular to the wavelets, so the angles opposite A and B are also Θ . $\sin\Theta = A/d = B/d$, thus $(A + B) = 2d\sin\Theta$. Constructive interference happens when $(A + B) = n\lambda$ [130], leading to the expression of Bragg's Law:

$$n\lambda = 2d \cdot \sin\Theta \quad (1)$$

where:

n is the order of the diffraction peak,

λ is the wavelength of the incident X-ray, Å,

d is the interplanar spacing of crystal lattice planes, Å,

Θ is the angle of incidence of the X-ray.

X-Ray Diffractometer comprises five major components (Figure 12):

- X-Ray Source (typically a sealed X-ray tube that produces X-rays when high-energy electrons strike a metal target (commonly copper));
- Detector (detects the diffracted X-rays at various angles. Modern detectors are often electronic, such as scintillation detectors or solid-state detectors. They convert X-rays into electrical signals for analysis);
- Incident (primary beam) optics (these optics focus and direct the primary X-ray beam onto the sample. They may include components like collimators and mirrors to shape and control the incident X-ray beam before it interacts with the sample);
- Receiving (diffracted beam) optics (after interacting with the sample, the diffracted X-rays scatter in different directions. The receiving optics focus and direct these diffracted beams towards the detector, optimizing their collection for accurate analysis);
- Sample holder/goniometer (the sample holder holds the material being analyzed. The goniometer determines the angles between the source, detector, and sample surface).

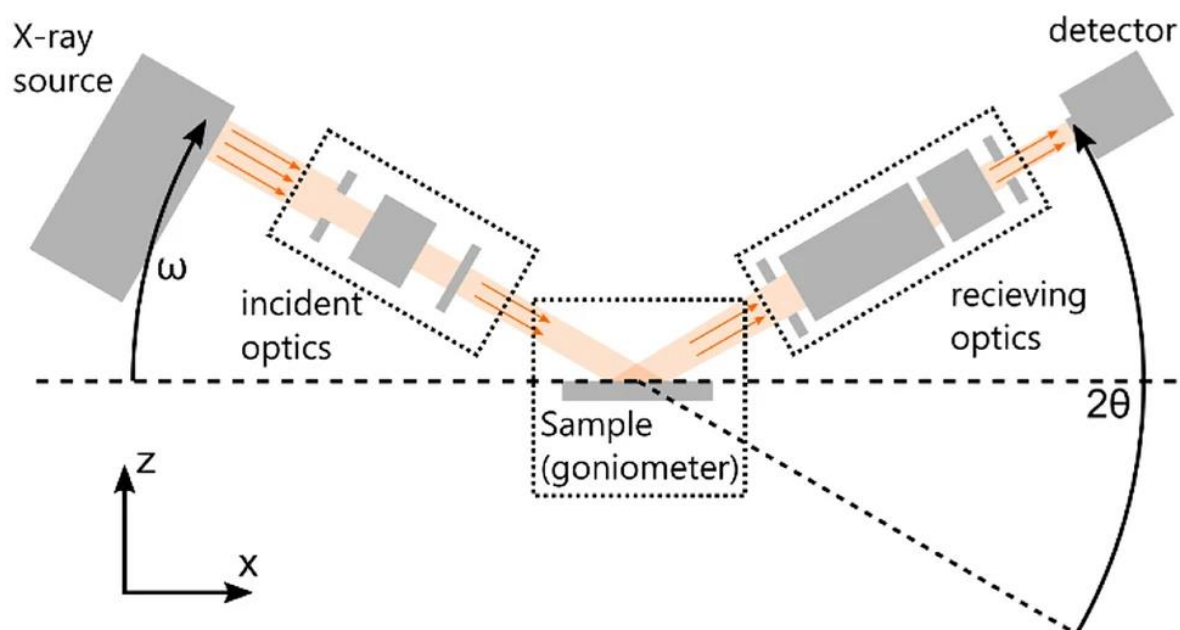


Figure 12 – Components of a diffractometer [131]. *Reproduced with permission from Springer Nature*

In the context of SURMOF XRD patterns, the observed diffraction peaks provide significant insights into the crystallographic orientation of the thin films. Since SURMOFs are typically synthesized through oriented growth on SAMs, the XRD patterns reflect the specific alignment of the crystallites relative to the substrate. For instance, in the case of HKUST-1 SURMOF (Figure 13) [132], which consists of benzenetricarboxylate (BTC) and Cu^{2+} ions, the XRD patterns reveal a selective orientation depending on the termination of the SAM. When the substrate is terminated with carboxylic acid ($-\text{COOH}$) groups, the XRD pattern predominantly shows peaks corresponding to the [100] crystallographic direction, indicating that the crystallites are aligned such that the [100] planes are perpendicular to the substrate. In contrast, when the SAM is terminated with hydroxyl ($-\text{OH}$) groups, the diffraction peaks shift to the [111] direction, suggesting a different orientation where the [111] planes are perpendicular to the substrate. The width of the peaks is indicative of the domain sizes, and in the case of out-of-plane XRD, this can be used to calculate the approximate thickness of the films.

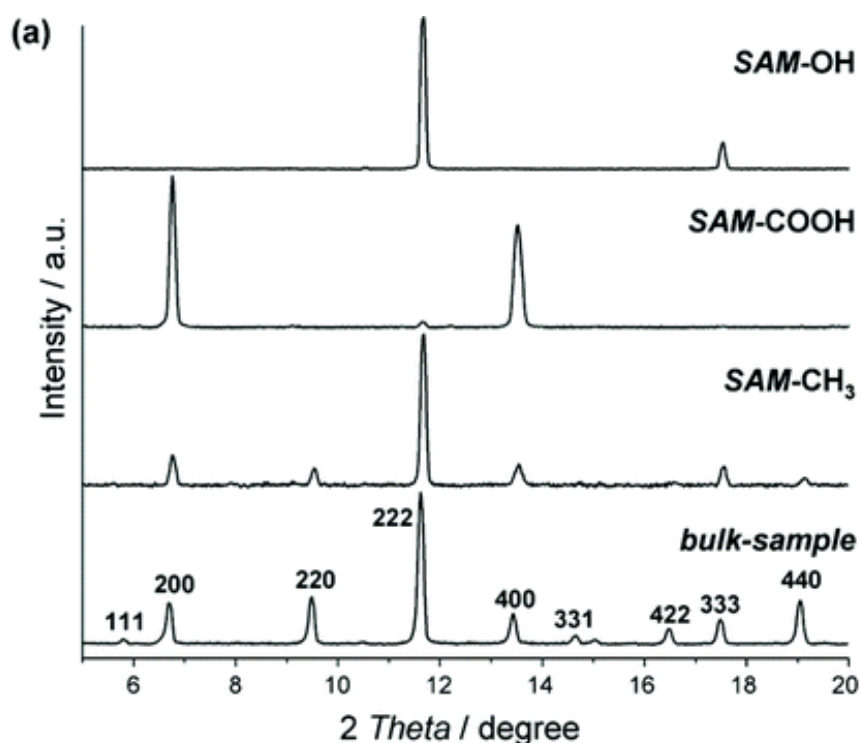


Figure 13 – X-ray diffraction patterns (background corrected) of thin films of $\text{Cu}_3(\text{BTC})_2$ on functionalized gold surfaces, compared with a randomly oriented $\text{Cu}_3(\text{BTC})_2$ powder sample measurement. Each pattern is normalized to the most intensive reflection [132]. *Reproduced with permission from American Chemical Society*

XRD method was used to characterize synthesized UiO-66 family SURMOFs to confirm the crystal structures of samples. The patterns of powder X-ray diffraction (PXRD) were recorded using an X-ray diffractometer Bruker D8-Advance “DaVinci” (Ettlingen, Germany) in Bragg-Brentano Θ - Θ geometry and a 192-stripe Lynxeye detector with Cu $\text{K}\alpha_1$ radiation ($\lambda = 1.54 \text{ \AA}$).

3.2.2 Fourier transform-Infrared Spectroscopy (FT-IR)

FT-IR is a preferred method of infrared (IR) spectroscopy [133]. Infrared spectroscopy is a powerful analytical technique that investigates the interaction of infrared light with molecules. It provides valuable insights into molecular vibrations, functional groups, and chemical structures.

When infrared radiation passes through a sample, some of it is absorbed by molecules, causing them to undergo vibrational transitions, and some of it is

passed through (transmitted) (Figure 14). Different functional groups within the molecules absorb infrared radiation at characteristic frequencies, resulting in unique absorption spectra that can be used to identify and characterize the sample. Due to the distinct composition of each material and the corresponding variation in atomic arrangement, no two compounds yield identical IR spectra [133].

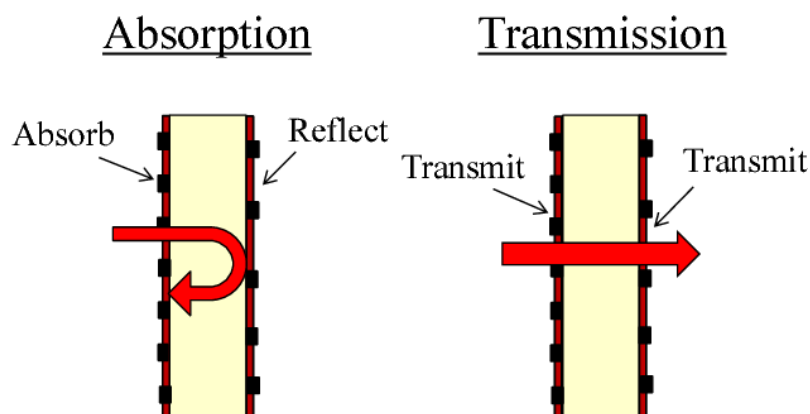


Figure 14 – Infrared radiation: absorption and transmission [134]. *Reproduced with permission from IEEE*

The IR region is commonly divided into three areas [135, 136] (Figure 15): near-IR (short wave IR: $400\text{-}10\text{ cm}^{-1}$), mid-IR (medium wave IR: $4000\text{-}400\text{ cm}^{-1}$), and far-IR (long wave IR: $14,000\text{-}4000\text{ cm}^{-1}$). IR photons possess sufficient energy to induce vibrational motion in groups of atoms relative to their connecting bonds. Similar to electronic transitions, these vibrational shifts correspond to specific energies, and molecules selectively absorb IR radiation at particular wavelengths and frequencies. Chemical bonds exhibit characteristic vibrational frequencies, and when exposed to IR radiation, they absorb energy at frequencies corresponding to their vibrational modes. By measuring the frequency of absorbed radiation, a spectrum is generated, facilitating the identification of functional groups and compounds. The essential condition for IR activity, resulting in the absorption of IR radiation, is the necessity for a net alteration in dipole moment during the vibration of the molecule or functional group under examination [133].

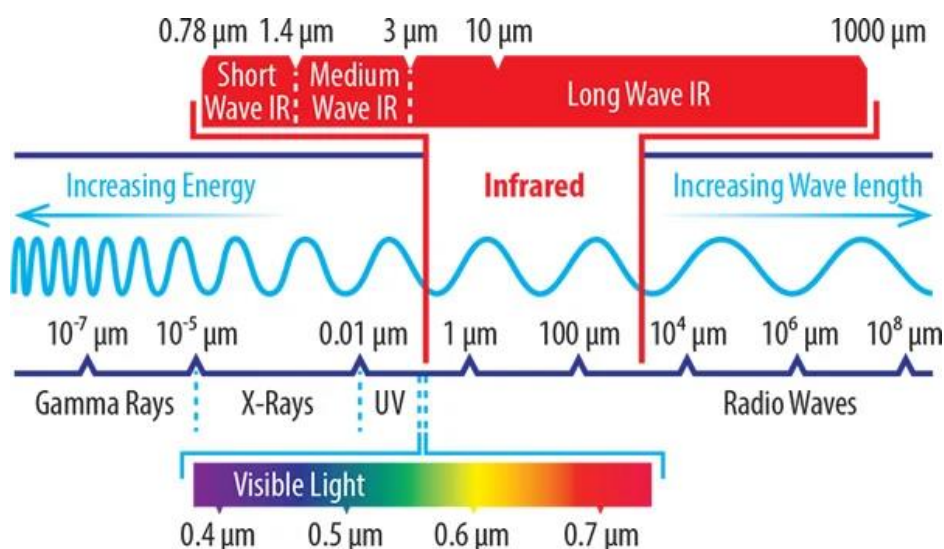


Figure 15 – Electromagnetic spectrum, highlighting the visible and IR regions [137]

Molecules can undergo various types of motion, which are important for understanding their behavior and properties. Three common forms of motion (Figure 16 (a)) in molecules include:

- **Vibrational Motion:** Atoms within a molecule are connected by chemical bonds, and these bonds can vibrate. Vibrational motion involves periodic oscillations of atoms about their equilibrium positions along the bonds. These vibrations can be symmetric, asymmetric, stretching (change in bond length), or bending (change in bond angle) [138], which are often subdivided into scissoring, rocking, wagging, and twisting (Figure 16 (b)).
- **Rotational Motion:** Molecules can rotate around their center of mass. Rotation can occur along single bonds (e.g., internal rotation in ethane) or around the entire molecule (e.g., rotational motion of a diatomic molecule). Allowed rotational states depend on the molecule's shape, mass distribution, and symmetry.
- **Translational Motion:** Molecules can undergo translational motion, where the entire molecule moves through space. This motion is typically observed in gases and liquids, where molecules are free to move past each other.

In solids, translational motion is restricted, but molecules can still exhibit vibrational and rotational motion.

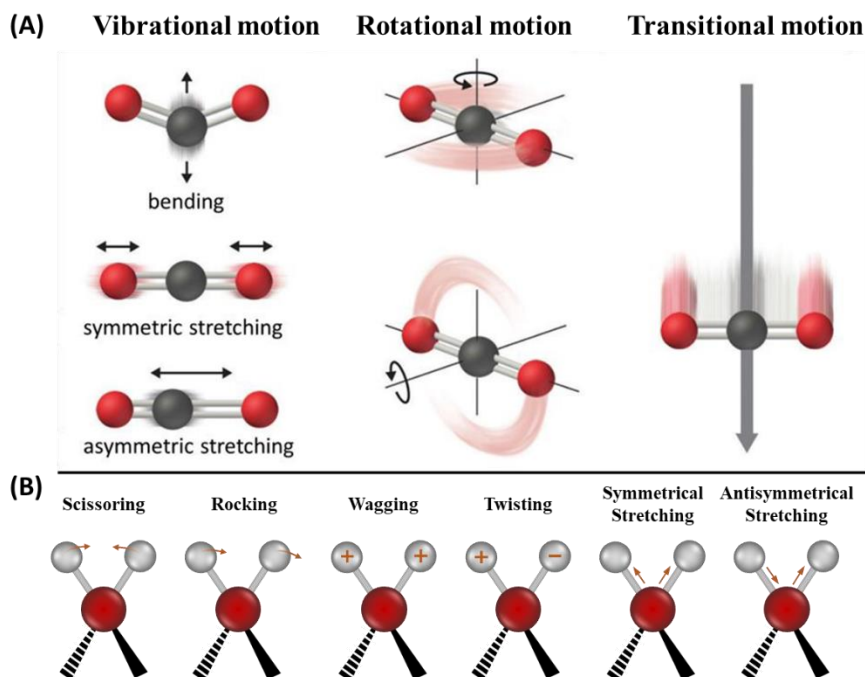


Figure 16 – (a) Three common forms of motions in a molecule [139] and (b) Vibrational bond alignments

In an FT spectrometer, there are three fundamental components: a radiation source, an interferometer, and a detector. The radiation source typically emits infrared light. This light interacts with the analyzing sample, causing specific molecular vibrations that are characteristic of the sample's chemical composition. The interferometer is a crucial component of FTIR spectrometers. It's used to modulate the infrared radiation before it reaches the detector. One common type of interferometer used in FTIR spectrometers is the Michelson interferometer (Figure 17). It splits the incoming radiation into two beams, one of which travels a longer path than the other. The recombination of these beams creates an interference pattern that contains information about the sample's infrared absorption spectrum. The detector in an FTIR spectrometer measures the intensity of the modulated infrared radiation after it has passed through the interferometer. The interferogram produced by the interferometer is converted into a spectrum using Fourier transform mathematics, hence the name "Fourier Transform

Infrared Spectrometer." Common detectors used in FTIR spectrometers include photodiodes, pyroelectric detectors, and mercury-cadmium-telluride (MCT) detectors, depending on the wavelength range and sensitivity required.

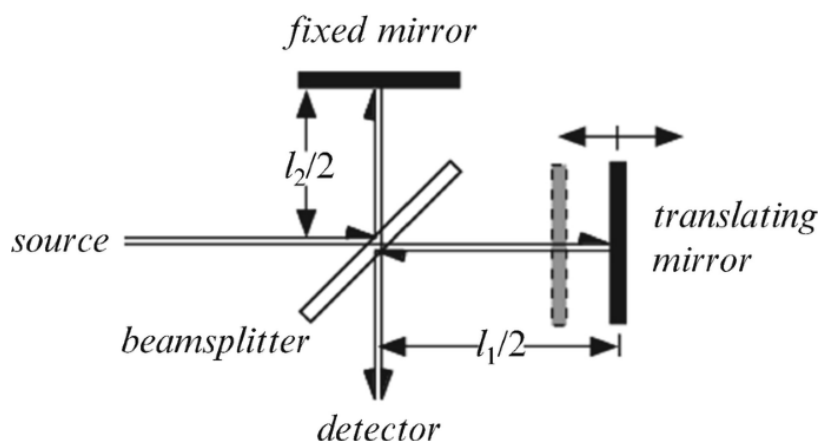
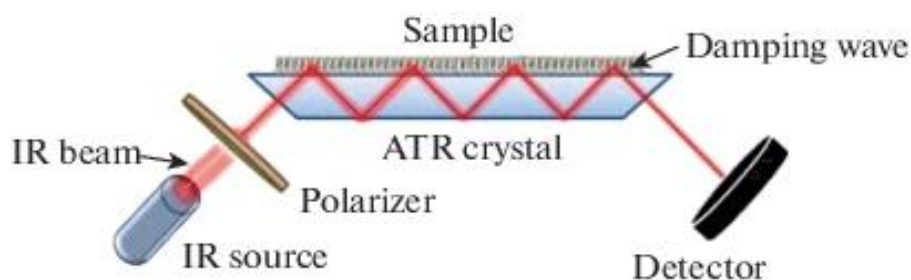


Figure 17 – Michelson interferometer [140]. *Reproduced with permission from Springer Nature*

This subchapter is focus on two specialized techniques within infrared spectroscopy: Attenuated Total Reflection spectroscopy and Infrared Reflection-Absorption Spectroscopy.

3.2.2.1 Attenuated Total Reflection (ATR) spectroscopy

ATR spectroscopy capitalizes on the phenomenon of total internal reflection (TIR) to probe the surface properties of a sample. When IR radiation is directed onto a crystal surface at an angle greater than the critical angle, it undergoes total internal reflection within the crystal (diamond, germanium, or zinc selenide). At the interface between the crystal and the sample, evanescent waves are generated, penetrating a short distance into the sample. As the evanescent waves interact with the sample, they undergo attenuated total reflection, resulting in absorption spectra that provide valuable information about the sample's composition and structure (Scheme 7).



Scheme 7 – Schematic illustration of the ATR -FTIR system [141]. The infrared beam passes through the ATR crystal covered on the top by the sample. The damping wave penetrates into the sample and is absorbed by the sample. The polarizer generates parallel and perpendicular polarized incident beam. *Reproduced with permission from Springer Nature*

Attenuated total reflection infrared spectroscopy (ATR-IR) was utilized to investigate the UiO-66-NH₂ bulk material. ATR-IR was recorded on a Bruker OpticsTensor-27 spectrometer equipped with platinum ATR (diamond crystal, 45°, one reflection) accessory and a deuterated L-alanine doped triglycine sulfate (LaDTGS) detector. The spectra were recorded at room temperature, with a resolution of 4 cm⁻¹, and air is used to record the background.

3.2.2.2 Infrared Reflection-Absorption Spectroscopy (IRRAS)

IRRAS is a surface-sensitive variant of infrared spectroscopy that is particularly useful for studying monolayers or thin films adsorbed onto surfaces. In traditional transmission infrared spectroscopy, the sample is typically analyzed in transmission mode, which limits its applicability to bulk samples. In IRRAS, however, infrared radiation is directed onto the sample surface at an angle, allowing for reflection and absorption by the surface-bound species. IRRAS can provide valuable insights into the structure, orientation, and interactions of molecules at surfaces

IRRAS relies significantly on a highly reflective metal surface to optimize the signal-to-noise ratio. The reflectivity of the substrate covered with adsorbates is contingent upon both the type of metal surface utilized and the angle of incidence. Incident light can be separated into two components: the electric field parallel to

the plane of incidence (E_p) and the electric field perpendicular to the plane of incidence (E_s) (Figure 18) [142].

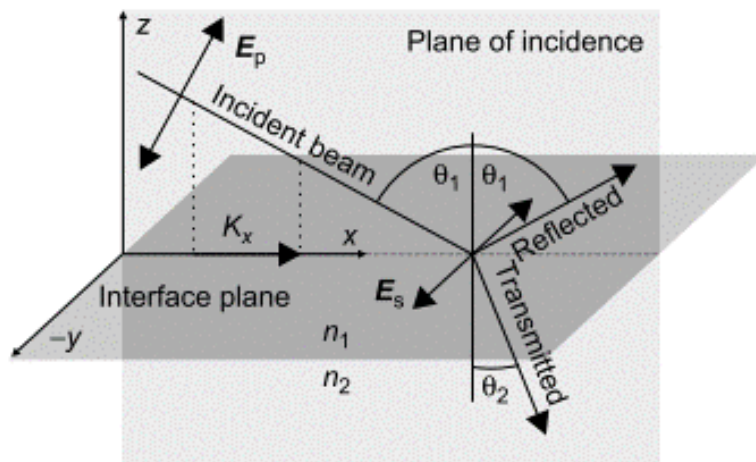


Figure 18 – Beam geometry and polarization of IR radiation at the interface between two optically different media [142]. *Reproduced with permission from Wiley*

Various substrate materials, such as gold, silver, silicon, or glass, demonstrate different levels of reflectivity when covered with an adsorbate, depending on factors such as the angle of incidence (θ_1), polarization, and, to a lesser extent, the energy of the light. Generally, these materials react differently to the component of light parallel to the incident plane compared to the component perpendicular to the plane. When using unpolarized light, the intensity of the vibrational band may be minimal if an incorrect angle of incidence or substrate material is chosen. Gold, for instance, exhibits high reflectivity and eliminates the perpendicular light component. Its maximum reflectivity occurs around 87° , approximately 50 times greater than that of silicon or germanium. To circumvent issues related to interfering polarizations, setting the angle of incidence to the Brewster angle is an effective strategy. This angle, at which the reflectivity of parallel-polarized light is zero, ensures only the perpendicular light component remains. Moreover, the metal surface introduces additional effects, such as the surface selection rule [142], where only the vibration parallel to the incident plane is observable while the perpendicular component vanishes.

The beam initially deflects off a mirror towards the sample, where it penetrates thin films, reflects off the IR-reflecting metal, and ultimately redirects towards the detector.

In the analysis of SURMOF thin films using IRRAS, the data provides key insights into the stepwise growth and structural composition of the layers. For instance, in the case of $\text{Zn}_x(\text{BDC})_y$ multilayers grown on a MHDA SAM [76], the IRRAS spectra reveal that with each deposition cycle, characteristic peaks associated with the asymmetric (1585 cm^{-1}) and symmetric (1404 cm^{-1}) stretching modes of the coordinated carboxylic acid groups become more pronounced, indicating an increase in the film thickness (Figure 19). Additionally, the peak at 1505 cm^{-1} , attributed to the C=C stretching of the aromatic rings, further confirms the presence and growth of the $\text{Zn}_x(\text{BDC})_y$ multilayers. These findings demonstrate the layer-by-layer construction of the SURMOF, with IRRAS serving as a valuable tool for monitoring the molecular structure and thickness evolution during the fabrication process.

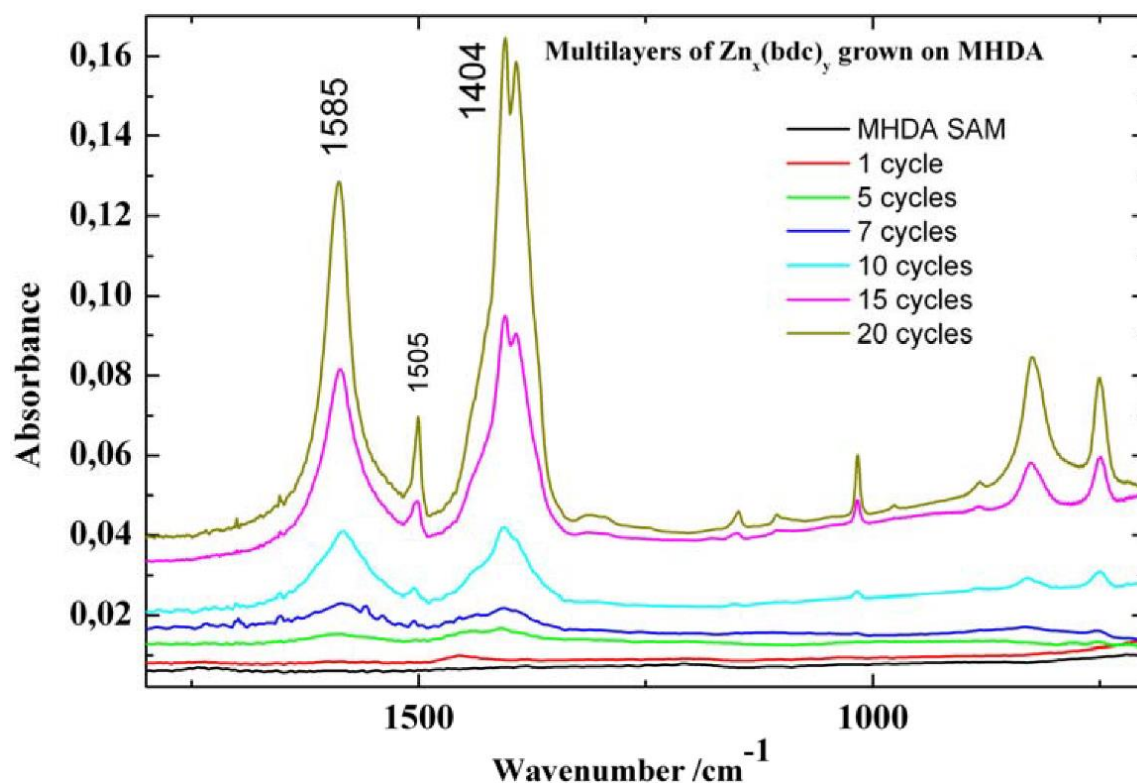


Figure 19 – IRRAS spectra of different cycles of $\text{Zn}_x(\text{BDC})_y$ MOF grown on a MHDA SAM [76]

The IRRAS technique was utilized to investigate the SAMs of C18 and UiO-66-NH-C18 as well as UiO-66-family SURMOFs before and after modifications. IRRAS data was achieved utilizing a Bruker VERTEX 80 (Germany). IRRAS accessory (A518) exhibits a fixed angle of incidence of 80°. The data were collected using a narrow-band liquid-nitrogen-cooled MCT detector. Per-deuterated hexadecanethiol SAM on Au/Ti/Si was utilized for reference measurements.

3.2.3 Field-Emission Scanning Electron Microscopy (FE-SEM)

Scanning electron microscopy is a commonly utilized technique for capturing detailed images of surfaces at high resolutions, which can also be utilized for analyzing nanoscale substances. Like a light microscope utilizes visible light, SEM employs electrons for imaging purposes [128]. SEM has the capability to resolve details as small as 1 nm and can magnify images up to 400,000 times [143]

When the incident electron beam, carrying a negative charge, encounters the material with its distinct electron clouds and arrangement, it generates diverse signals that mirror both the topographic intricacies and the atomic makeup of the examined specimen's surface. This electron beam prompts the release of X-rays from the atoms located on the sample's surface, along with elastically backscattered (or primary) electrons (BSE), secondary inelastic electrons (SE), and Auger electrons (Figure 20) [143].

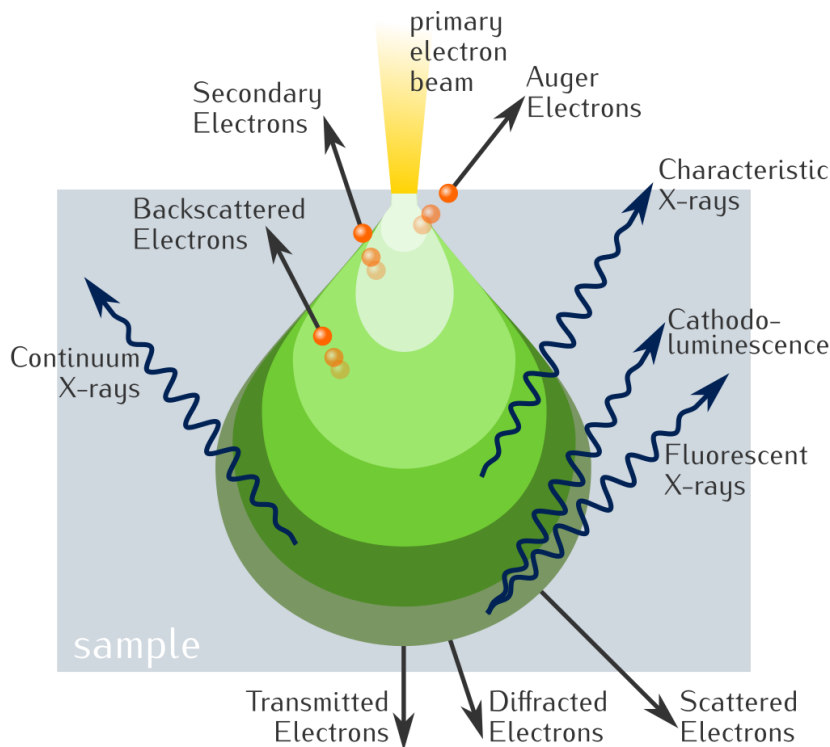


Figure 20 – Electron – matter interactions: the different types of signals generated [144]

Secondary electrons are particularly valuable for capturing the morphology or topography of a sample. These electrons enable the generation of high-resolution images that unveil details within the range of approximately 1 to 5 nanometers. Concurrently, characteristic X-rays are utilized in a technique known as energy dispersive X-ray analysis (EDX) to ascertain the elemental composition, while Auger electrons are employed in surface analytical methods [143]. The SE mode stands as the predominant signal type utilized for SEM image processing. Since incident electrons possess relatively low energy, detection is limited to only a few nanometers beneath the sample's surface. Consequently, SEs are quite effective in producing topological contrast, such as surface texture and roughness, for the sample. It's crucial to note that only the SEs reaching the detector contribute to image formation; obstructed SEs result in dark contrast within the image. Moreover, employing low-voltage electrons in the primary beam will likely generate SEs from the outermost surface layer of the sample, accurately depicting detailed topographic information [145].

The BSE mode of scanning primarily focuses on detecting incident electrons with energies surpassing 50 electron volts (eV). When an electron undergoes an elastic collision resulting in a directional change exceeding 90 degrees, nearly half of these electrons bounce back toward their original direction, conserving much of their initial energy. Elements with higher atomic numbers tend to deflect more electrons due to the greater number of positive ions within their nuclei. For example, elements like gold, with higher atomic numbers, exhibit a BSE yield of approximately 50%, while for carbon, the BSE yield is around 6%. BSE yield refers to the percentage of reflected electrons produced by the sample. BSE electrons carry significant information regarding the structures beneath the surface of the samples [145].

A typical SEM (Figure 21) comprises several key components, including the electron source, column containing electromagnetic lenses, electron detector, sample chamber, and computer display [145]. Positioned at the top of the instrument, the electron gun emits electrons. There are two primary types of electron guns: field emission guns (FEG), which generate a potent electric field to extract electrons from atoms, and thermionic guns, where the filament is heated until electrons are emitted (typically employing tungsten (W) filament or solid-state crystals like CeB_6 or LaB_6) [145]. These emitted electrons are then accelerated to voltages ranging between 1 and 40 kV and focused into a narrow beam for imaging and analysis. Typically, an optimal operating voltage of 20–25 kV is utilized. Lower accelerating voltages (2.5–10 kV) result in high chromatic aberration of the incident beam, leading to poor resolution. Conversely, higher accelerating voltages (30–50 kV) cause the beam spot to enlarge, allowing deeper penetration into the sample and enlarging the zone of internal scattering, which generates backscattered electrons. The sample is positioned near the lower end of the column [143].

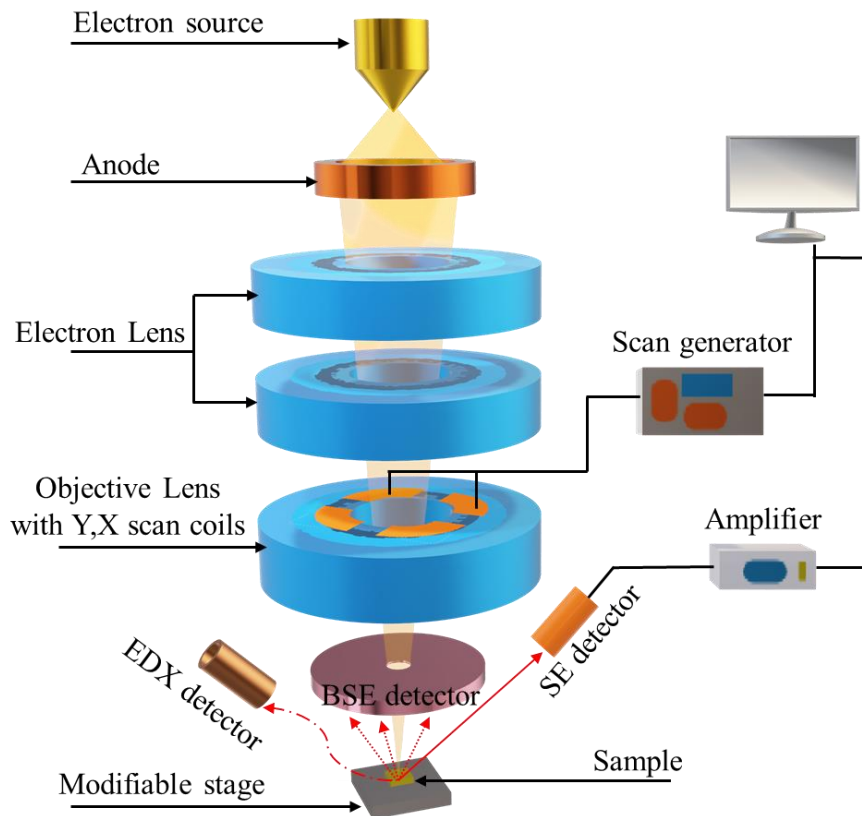


Figure 21 – FE-SEM instrument illustration with all major components

Initially, electrons traverse through two or more electromagnetic lenses that converge the electron beam into a minute spot, crucial for determining instrument resolution (with smaller spots yielding higher resolution). Subsequently, the electron beam, now finely focused, is systematically scanned across the specimen by scan coils, while a detector registers the quantity of low-energy secondary electrons or other emissions emanating from the specimen's surface. Utilizing the raster method, the resultant image is then displayed on a cathode ray tube, showcasing a distribution map of signal intensity emitted from the scanned area of the specimen. Due to the limited distance electrons can travel through air, the instrument operates within a high vacuum to facilitate the high-energy electron beam [143].

In SEM, ensuring the surface of the sample is electrically conductive and grounded is essential to prevent the accumulation of electrostatic charge, which can lead to distorted images and artifacts. To achieve this, non-conductive

samples are coated with an ultrathin layer of an electrically conducting material, such as Au, Au/Pd alloys, or Pt. Additionally, in conventional SEM, it's crucial to eliminate water from the sample as water molecules will evaporate under vacuum conditions, compromising image clarity. The environmental scanning electron microscope (ESEM), a more recent development, is designed to operate under lower vacuum and voltage conditions. ESEM enables the visualization of specimens in their "natural" state with minimal sample preparation, including the examination of moist samples like biological specimens [143].

In a field emission SEM, a FEG generates high-primary electron brightness and a small spot size, even at low accelerating potentials, resulting in minimal charging of the surface. Compared to conventional SEM, FE-SEM produces clearer and less electrostatically distorted images, boasting a spatial resolution as fine as 20 nm, which is three to six times superior to that achieved by conventional SEM [143].

SEM provides information about the shape, size, and size distribution of nanomaterials [143].

Nevertheless, SEM measurements do have limitations. During sample preparation, processes such as drying and contrasting can lead to the shrinkage of nanomaterials, altering their size and shape characteristics. Additionally, due to the small number of particles within the scanning region, biased statistics regarding the size distribution of heterogeneous samples are unavoidable [143].

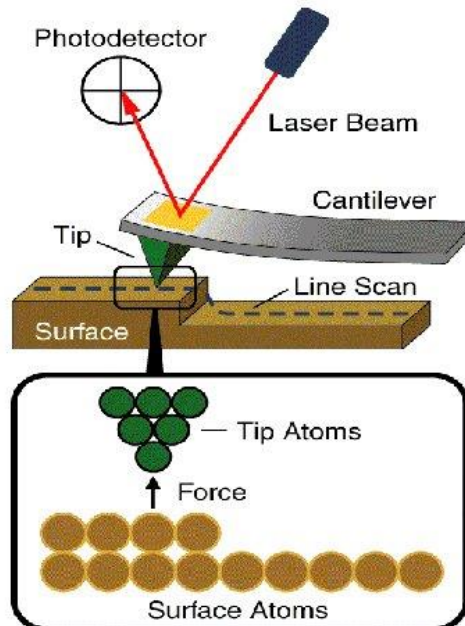
To investigate the morphology of Zr-SURMOFs before and after modification, SEM measurements were conducted using a Field Emission Gun (FEI) Philips XL SERIES 30 ESEM-FEG (FEI Co., Eindhoven, NL). To preclude charging and increase sample's conductivity, all samples were coated with a ~5 nm thick gold/palladium film before recording SEM micrographs. Moreover, all specimens underwent high-vacuum (1.5 Torr) using 20 keV acceleration voltage.

3.2.4 Atomic-Force microscopy (AFM)

Atomic force microscopy, also known as scanning probe microscopy (SPM), is a microscopy technique capable of generating three-dimensional images of surfaces at high magnification [128]. Similar to SEM, AFM can be employed to examine the shape, size, structure, and degree of dispersion of nanomaterials. However, AFM offers several advantages over conventional microscopy techniques. It conducts measurements in three dimensions (x, y, and z), allowing for the creation of 3D images of the sample. The resolution ranges from 0.1 to 1.0 nm in the x-y plane and achieves atomic resolution (0.01 nm) in the z-direction. AFM does not necessitate conductive surfaces or any special sample preparation processes. It can operate under ambient conditions or in a liquid environment [143].

The topographic image is acquired by scanning a probe over the surface of a specimen using a sharp tip (probe) situated at the free end of a cantilever, typically composed of silicon or silicon nitride. This process relies on interatomic forces between the sample and the tip. AFM can detect various tip-surface interactions, depending on the distance between the tip and the sample. At short distances, the tip primarily encounters interatomic forces: very short-range (~ 0.1 nm) Born repulsive forces and longer-range (up to 10 nm) van der Waals forces. At greater distances from the surface (100–500 nm above the surface), long-range electric, magnetic, and capillary forces can be probed [143]. During scanning, the cantilever deflects due to attractive or repulsive forces between the tip and the sample surface (Scheme 8). This deflection is measured by a laser beam reflected on the backside of the cantilever. The forces are subsequently determined by combining the information from the laser variation with the known cantilever stiffness [128]. In most instances, a feedback mechanism is utilized to regulate the tip-sample distance and maintain a constant force between them. The sample

is mounted on a piezoelectric scanner, which moves it in the z-direction, thereby ensuring a constant force or height above the sample [143].



Scheme 8 – Schematic of AFM imaging technique [146]. *Reproduced with permission from AIP Publishing*

AFM can be operated in various modes, depending on the application. Typically, imaging modes are categorized into contact modes and non-contact modes, with the cantilever either in continuous contact or vibrated during scanning. Contact mode entails the probe being drawn across the surface, scanning progressively in rows. However, direct contact with the surface may risk causing damage. Tapping modes (also referred to as intermediate or oscillating mode [128]) involve intermittent contact as the probe oscillates vertically towards and away from the surface during scanning. Other modes include non-contact modes, where interactions or currents occur between the probe tip and the surface [143].

In addition to analyzing the shape and size of nanomaterials, AFM excels at characterizing surface features, surface roughness, and the dynamics of nanomaterials in real-time, such as in biological systems. It can image biomaterials without significantly damaging their surfaces and can measure

various position-related properties like surface friction, hardness, electrical, and thermal conductivity. A key advantage of AFM is its ability to image a wide range of nanomaterials at the subnanometer scale under environmental conditions or even in fluid environments. However, a notable disadvantage of AFM is that the size of the cantilever tip is typically larger than the dimensions of the nanomaterials being examined, leading to an overestimation of the lateral dimensions of the sample. Furthermore, AFM is limited in its capability to detect or locate specific molecules. Nevertheless, recent advancements in single-molecule force spectroscopy have addressed this limitation by employing an AFM cantilever tip modified with small molecules, cell adhesion molecules, or chemical groups, enabling the probing or detection of single functional molecules on a surface [143].

AFM offers the advantage of not requiring any surface modification or coating before imaging. It is capable of characterizing low-density materials that exhibit poor contrast in electron microscopy. Additionally, AFM provides the capability to image samples in three dimensions, enabling the characterization of nanoparticle height. Moreover, it offers resolution comparable to SEM and TEM while being more cost-effective and requiring less laboratory space. However, it's worth noting that AFM typically entails slower scanning times compared to electron microscopes [128].

AFM measurements were carried out with a Bruker Icon atomic force microscope operating in tapping mode. NSC15/Al-BS cantilevers were used at a scan rate of 0.295 Hz, with 256 samples per line.

3.2.5 Water contact Angle (WCA) analysis

The water contact angle serves as the primary data obtained from wettability studies, indicating the degree of wetting in the interaction between a solid and a liquid. This angle is formed at the juncture of the liquid under consideration and

the specific solid surface, thereby reflecting the properties and structure of the material's surface in contact with the droplet [147].

Geometrically, the contact angle is defined by drawing a tangent line from the contact point along the liquid-vapor interface in the droplet profile (Figure 22). In simpler terms, WCA is the angle formed by the intersection of the liquid-solid interface and the liquid-vapor interface, often referred to as a water-in-air contact angle [147].

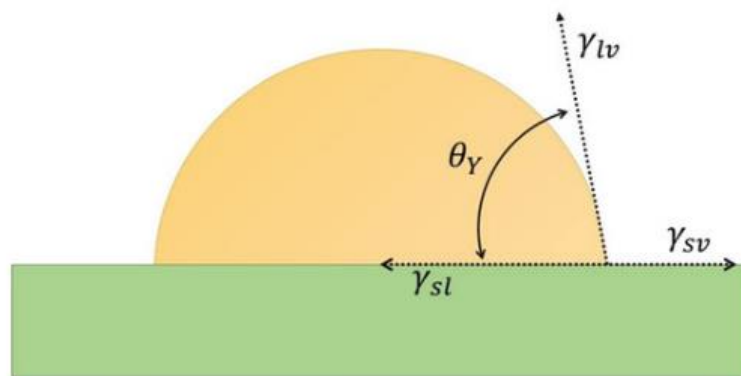
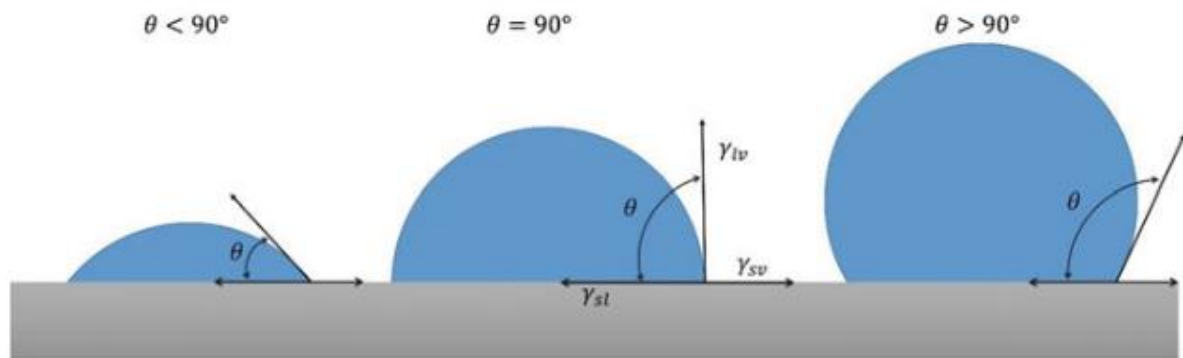


Figure 22 – Illustration of three-phase contact line, where γ_{lv} , γ_{sv} and γ_{sl} represent the liquid-vapor, solid-vapor and solid-liquid intermolecular tension, and Θ_Y is the contact angle [147].

Reproduced with permission from Springer Nature

A large contact angle is observed when the liquid forms beads on the surface, while a small contact angle indicates that the liquid spreads across the surface. When the contact angle is less than 90° , it signifies that the surface is hydrophilic, and the fluid spreads over a larger area of the surface (Scheme 9). Conversely, contact angles greater than 90° suggest that the surface is hydrophobic, causing the fluid to minimize contact with the surface and form a compact droplet. Complete wetting occurs when the droplet transforms into a flat puddle, resulting in a contact angle of approximately 0° , indicating a superhydrophilic surface. Conversely, for superhydrophobic surfaces, water contact angles are often greater than 150° , signifying minimal contact between the surface and the liquid, a phenomenon known as the lotus effect. The lotus effect is a self-cleaning phenomenon observed in nature, where water droplets rolling on the surface

collect particles due to the interaction between the water droplet and the nanoscale architecture of the surface [147].



Scheme 9 – Schematic representation of different measured contact angles where less than 90° surface is hydrophilic and more than 90° surface is hydrophobic [147]. *Reproduced with permission from Springer Nature*

The surface tension of a liquid naturally forms it into a droplet shape. This is because, for a fixed volume, a spherical droplet provides the least surface area, driven by the intermolecular force that contracts the liquid surface to minimize its area, known as surface tension. Consequently, the shape of liquid droplets is determined by this surface tension. However, external forces such as gravity can influence and distort the droplet's shape, impacting the contact angle, which is defined by a combination of surface tension and these external forces [147].

The sessile drop method is a well-known technique for analyzing contact angles and involves directly measuring the tangent angle at the three-phase equilibrium interfacial position. By observing the drop profile on flat surfaces, the wetting property can be determined by directly recording the contact angle (Figure 23). To measure the contact angle, the sample stage needs to be flattened to prevent the droplet from moving during deposition. Subsequently, a droplet of liquid is dispensed onto the surface, and a light source illuminates the droplet from behind. An image of the droplet is then projected onto a screen and recorded by a camera for further analysis using software. The software conducts the contact angle analysis, while the images and/or recordings of the phenomenon are stored on the connected computer. Using relatively high magnifications improves the

accuracy of the method and allows for detailed exploration of the intersection between the solid surface and the drop profile. This technique is simple and straightforward to execute and requires only a small surface area of substrates and small quantities of liquid for analysis. However, impurities and irregularities on the surface can significantly influence the analysis outcomes [147].

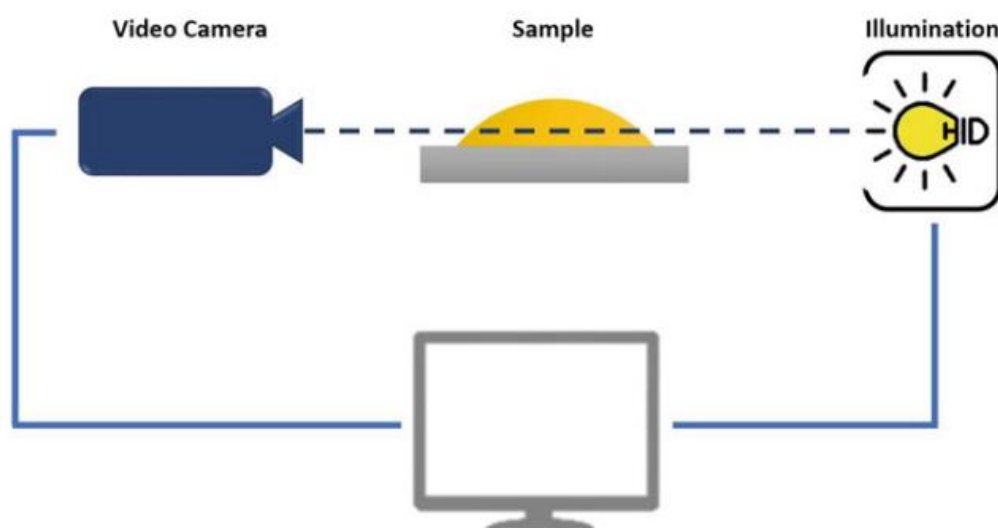


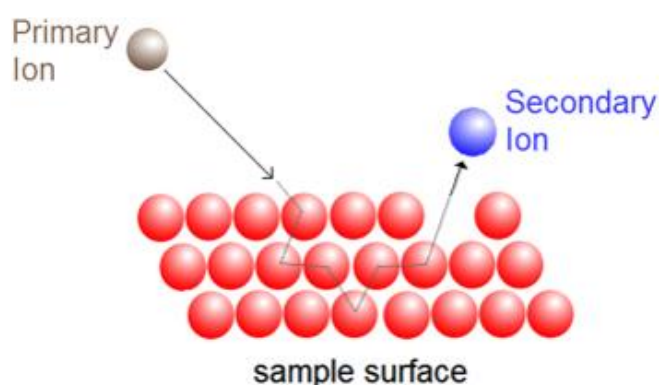
Figure 23 – Graphical illustration of sessile drop technique. The camera takes images of the droplet, while the light is in the background and the contact angle is assessed by the software [147]. *Reproduced with permission from Springer Nature*

In order to investigate the presence of Cassie-Baxter states, the modified UiO-66-NH-C18 sample was evaluated using water contact angle measurement. The static WCA was measured using a Data physics contact angle meter with a droplet of distilled water (5 μL) at ambient temperature.

3.2.6 Time-of-Flight Secondary Ion Mass Spectrometry (ToF-SIMS)

Time of Flight Secondary Ion Mass Spectrometry is a material characterization technique known for its high chemical sensitivity, surface sensitivity (probing the upper 2–3 nm), and molecular specificity [128]. ToF-SIMS is widely employed for characterizing nanostructures within larger components, including electronic devices, as well as thin to ultrathin films of both organic and inorganic compositions [128].

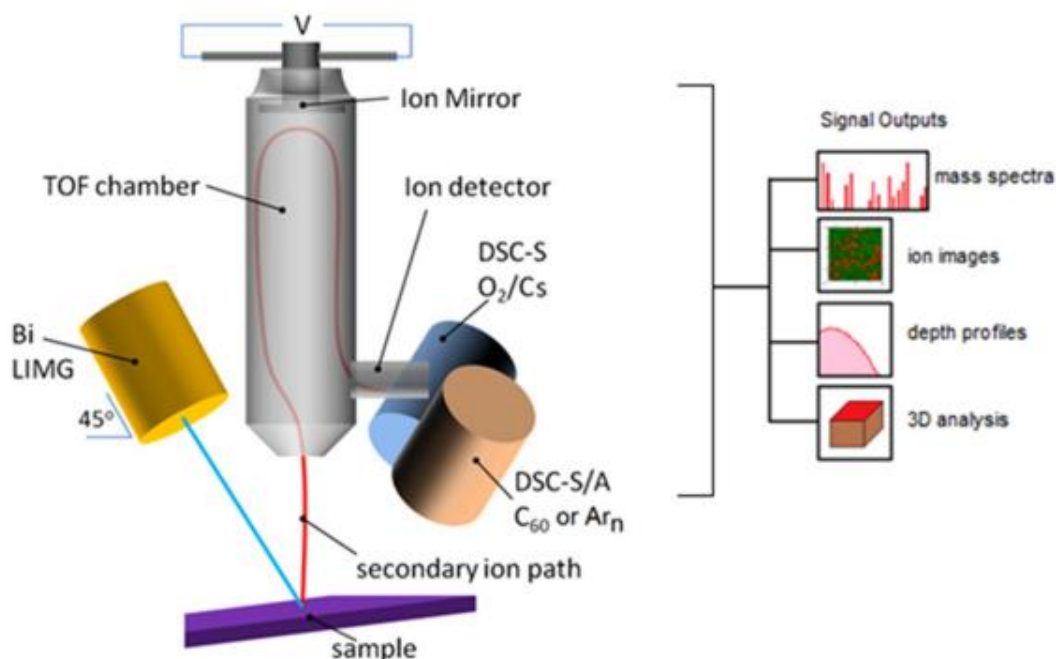
A beam of primary ions with high energy (ranging from 0.1 to 20 kiloelectron volts, keV) is directed at the surface of the sample. Upon bombarding the sample surface, the primary ions cause a variety of sputtered particles to be emitted (Scheme 10), including monatomic and polyatomic particles derived from the sample, as well as electrons, photons, and re-sputtered primary ions. The secondary ions that are generated possess negative, positive, and neutral charges. The desired secondary ions are selectively extracted and detected using mass spectrometry techniques [148].



Scheme 10 – Schematic representation of the collision of a primary ion (grey) with a sample surface (red). Energy is transferred onto the surface and distributed through several atoms (grey lines) until a secondary ion (blue) is ejected [148]. *Reproduced with permission from Morgan & Claypool Publishers*

A schematic diagram illustrating the components of a dual- ToF-SIMS system is depicted in Scheme 11. In a dual-beam system, a primary ion gun is utilized to generate the secondary ions for analysis under static ion beam conditions, facilitating high-resolution surface mass spectrometry. The second ion beam, referred to as the sputter gun, can be employed for the controlled erosion of the sample, a process known as sputter depth profiling. This controlled removal of material enables the analysis of composition from the surface to the bulk [148]. The sample is positioned beneath the ToF analyzer and can be scanned with various ion sources, depending on the sample material and the required information. ToF-SIMS not only generates mass spectra from the surface, which can be translated into ion maps, but it also allows for depth profiling by sputtering.

During depth profiling, selected species and their intensities can be observed throughout the sputtering process. Moreover, the combination of depth profiling and ion maps enables the generation of 3D maps of the analyzed volume.



Scheme 11 – Schematic representation of the main components of dual-beam time-of-flight secondary mass spectrometer. Secondary ions are sputtered from a target/sample by primary ion gun. The sputtered secondary ions are extracted by an extraction potential into the flight tube and detector electronically, typically with a microchannel plate. Depending on the mode of operation of the instrument, a range of signal outputs can be obtained: mass spectra, ion images, depth profiles and 3D analyses [148]. *Reproduced with permission from Morgan & Claypool Publishers*

The primary ion beam in a dual-beam ToF-SIMS instrument is typically a liquid metal ion gun/source (LMIG/S), known for producing a highly focused ion beam, resulting in high lateral resolutions during secondary ion mapping. Initially based on gallium and gold, LMIGs have now shifted to bismuth ion sources, particularly in the form of small clusters of Bi³⁺, due to their improved secondary ion yields. Additionally, large cluster sources based on carbon fullerenes have shown potential for characterizing bio-molecular structures [148].

Once the secondary ions are generated, they need to be separated based on their mass-to-charge ratio (m/z) to record the mass spectrum. Among the available analyzers such as quadrupole, magnetic sector, time-of-flight, ion trap,

and orbitrap, the ToF system is the most common and simplest. In this system, secondary ions are separated based on their flight time in a flight tube without the use of an electric or magnetic field. The primary ion beam is pulsed in extremely short pulses as it is rastered over the sample surface, creating a pulse of secondary ions from the sample surface. These ions are accelerated through an extraction plate into the ToF analyzer [148].

In the ToF analyzer, the lightest ions travel the fastest and arrive first at the detector, while heavier ions arrive later. The arrival times of the ions at the detector are dependent on their mass, allowing the arrival times to be transformed into respective m/z ratios, generating a mass spectrum from each pulse of the ion beam [148]. After passing through the mass analyser, the secondary ions are detected and amplified by a microchannel plate.

Different types of analyses that can be obtained with ToF-SIMS include high-resolution mass spectra, ion images (chemical maps), and depth profiles (including 3D analysis). High-resolution mass spectra are acquired from sample surfaces solely using the primary ion beam. Very short pulses of the primary ion beam (on the order of nanoseconds) are used to irradiate a predefined spot on the sample surface (Figure 24 (a)). The resulting secondary ions are then extracted and accelerated into the time-of-flight analyzer (Figure 24 (b)). Subsequently, the secondary ions are separated according to their mass-to-charge ratio (m/z), and the mass spectrum is recorded along with the coordinates of the ion beam spot. The primary ion beam is then moved to an adjacent pixel, and the process is repeated until the desired area (x, y) has been scanned and analyzed, producing a mass spectrum (Figure 24 (c) and (d)). Due to the very short pulses of the primary ion beam, the mass resolution of the mass spectra is very high, typically reaching a mass resolution ($M/\Delta M$) of 10,000 routinely [148].

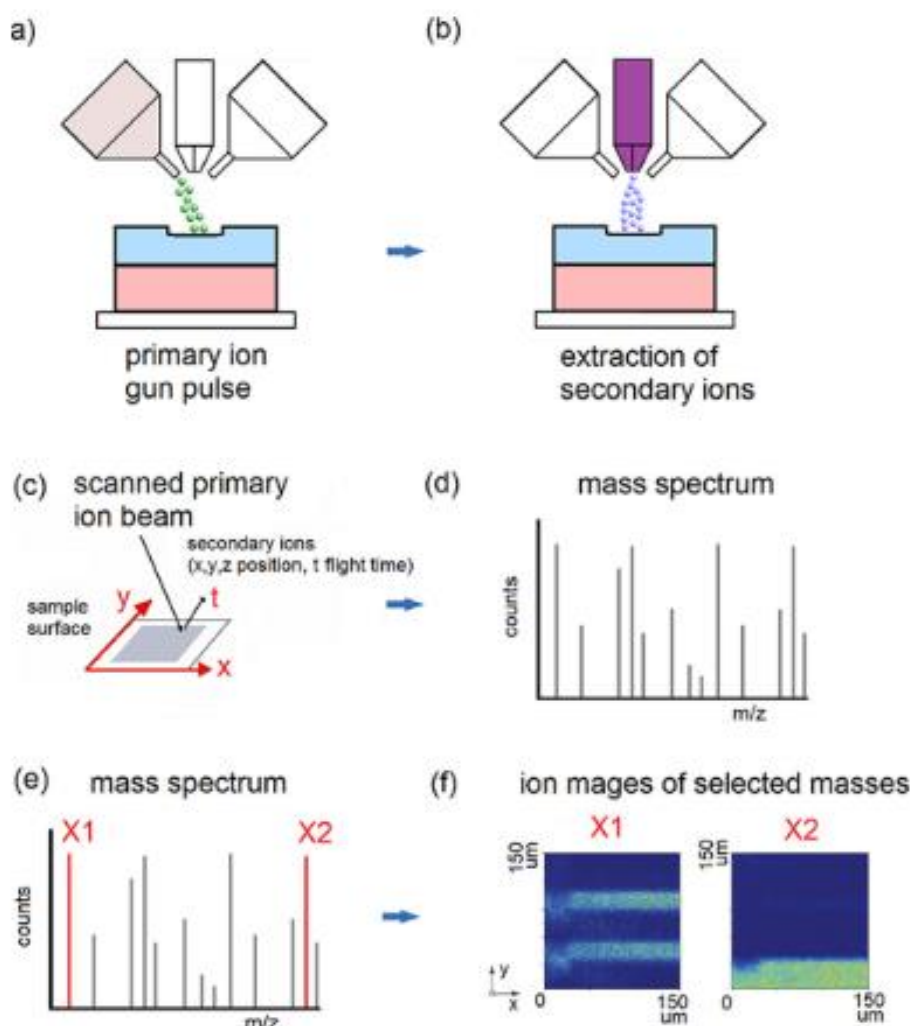


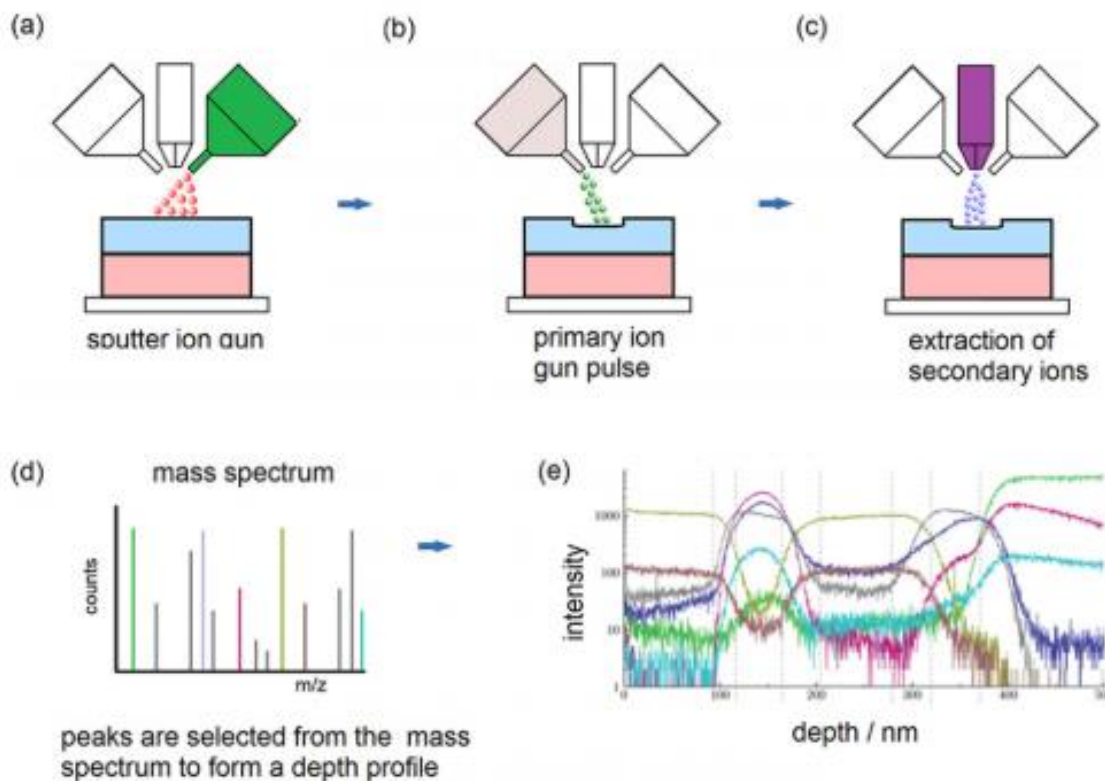
Figure 24 – The steps needed to obtain mass spectra and ion images [148]. (a) A short pulse from the primary ion beam irradiates a spot and sputters secondary ions. (b) These are collected in the analyser, and separated according to (m/z). (c) The process is repeated on the neighboring pixel, until a specified area has been analysed. (d) Mass spectra are produced as the detector collects the sputtered secondary ions. (e) By selecting specific peaks from the mass spectrum, (f) the spatial distribution of the selected peaks can be generated to give ion images as the spatial co-ordinates for the secondary ion signals are known. *Reproduced with permission from Morgan & Claypool Publishers*

During analysis, the ion beam dose must be strictly controlled to prevent excessive sputtering of the surface, a method known as "static SIMS." Static SIMS minimizes the interaction of the primary ion beam with the surface atoms or molecules, ensuring less than 1% of the surface is removed. Depending on the pulse time of the primary ion beam, the lateral resolution can reach up to approximately 250 nm [148].

For many systems, understanding how composition varies with depth is essential. Depth profiling is achieved through the use of a sputter ion beam/gun, allowing for the measurement of mass spectra as a function of depth. In this method, the ion beam dose exceeds the static limit, and layers of material are "peeled away" by the sputter gun to expose further layers of atoms or molecules for analysis. This type of analysis, known as "dynamic SIMS," is more destructive compared to static SIMS, with ion beam doses greatly exceeding the static limit. Dynamic SIMS is typically used to characterize interfaces, compositional changes through a material due to a processing step, and features beyond the surface region [148].

The process of depth profiling in a dual-beam ToF-SIMS system involves three key steps, as outlined in Scheme 12. The first step is to raster the sputter beam over the predefined sputter area, typically a square with a side length between 250 and 500 μm (Scheme 12 (a)). The sputter ion beam is generally of a much higher current than the analytical ion beam, typically tens to hundreds of nanoamperes. This higher ion beam dose allows for the controlled removal of material, and it's crucial to maintain a stable current to ensure a constant sputter rate during the analysis. It's worth noting that besides removing material, the sputter beam may alter the surface chemistry of the sample, affecting ion yields. Therefore, careful selection of the sputter beam is essential to optimize measurement accuracy. After sputtering, the primary ion beam is applied to a smaller area within the larger sputter crater, forming a sub-crater (Scheme 12 (b)). This results in the emission of secondary ions, as described previously. The use of a sub-crater minimizes interference from material on the edge of the sputter crater, known as the 'edge effect'. Once the secondary ions have been collected in the analyzer, the process of sputtering and primary ion beam analysis is repeated sequentially until the desired depth of the sample has been measured. Again, the detected secondary ions produce a mass spectrum. Peaks of interest are selected from the mass spectra (Scheme 12 (d)), and a depth profile of those species is

generated (Scheme 12 (e)). Finally, to prevent any charge buildup that may occur on an insulating sample, a flood of low-energy electrons can be irradiated onto the surface [148]



Scheme 12 – Schematic representation of the three main steps used in depth profile ToF-SIMS [148]. (a) A high energy sputter beam is rastered over the sputter area. (b) The analytical beam is applied to the analysis area which is centered within the sputter area. (c) The secondary ions generated by the analysis beam are collected and accelerated into the analyser, and a mass spectrum produced. (d) By selecting certain peaks a depth profile of the species can be obtained (e). *Reproduced with permission from Morgan & Claypool Publishers*

The location of each generated mass spectrum, and thus the selected peaks, are known, allowing for the generation of 2D ion maps. This also applies to chemical information obtained during depth profiling, but now includes the z-axis. With secondary ions registered on all three axes, 3D chemical plots can be constructed [148].

ToF-SIMS was employed to study the surface modification of UiO-66-NH₂ SURMOF via ion maps and depth-profiling.

3.2.7 Quartz-crystal microbalance (QCM)

The Quartz Crystal Microbalance operates on the principle of piezoelectricity exhibited by quartz crystals. Quartz, a crystalline form of silica (SiO_2), demonstrates piezoelectric behavior, where mechanical stress induces an electric charge and vice versa. Quartz crystal is then sandwiched between two metal electrodes (Figure 25).

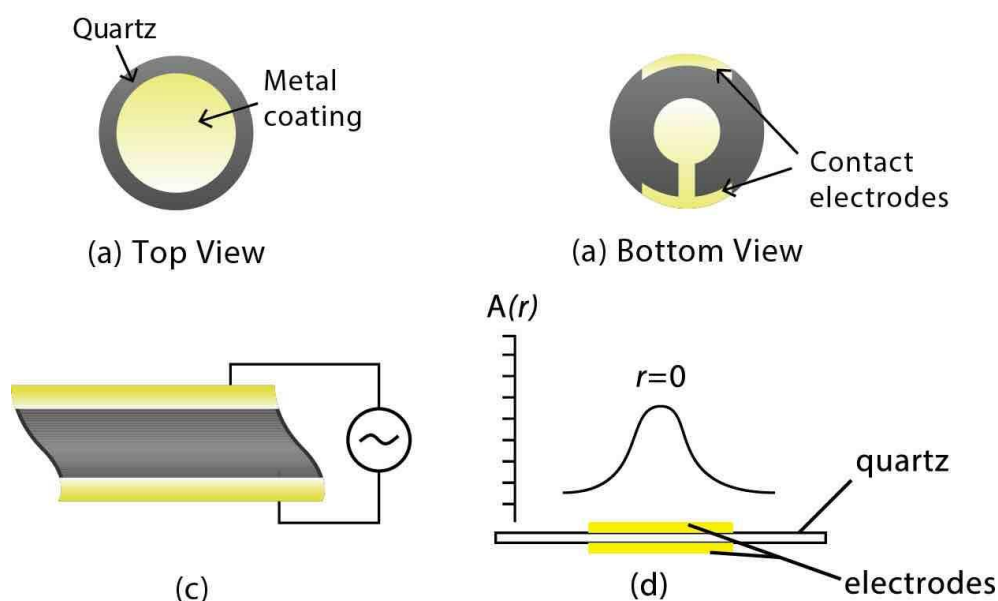


Figure 25 – Design of quartz crystal (grey) with electrodes (yellow); (a) top view (b) bottom view. (c) A schematic illustration of the strain induced in an AT cut crystal on application of AC voltage. (d) A schematic illustration of how amplitude of vibration ($A(r)$) varies with the distance (r) from the center of the sensor. The area of vibration is called the active surface area and is sensitive to mass changes [149].

When an alternating voltage is applied to the electrodes, the quartz crystal undergoes mechanical deformation, resulting in oscillations at its resonant frequency. This frequency, determined by the crystal's dimensions and material properties, remains stable under ideal conditions. Any change in the mass adhering to the crystal's surface alters its resonant frequency due to the added inertia, providing a sensitive measure of mass changes.

The mass sensing mechanism of the QCM relies on the relationship between the frequency shift (Δf) and the mass change (Δm) according to the Sauerbrey equation [150]:

$$\Delta m = -\frac{A \sqrt{\rho \mu}}{2f_0^2} \frac{\Delta f}{n} = -C \frac{\Delta f}{n} \quad (2)$$

where A is the active area of the crystal; ρ is the density of quartz; μ is the shear modulus of quartz; f_0 is the fundamental frequency of the quartz crystal before a mass change; as a result, C is usually defined as the mass sensitivity constant related to the structural and physical properties of the oscillating quartz QCM substrate and the driving fundamental resonance frequency [150, 151]. For a 5 MHz crystal, $C = 17.7 \text{ ng}/(\text{cm}^2 \cdot \text{Hz})$. The parameter n is the number of the odd harmonic and can be 1, 3, 5, 7, etc.

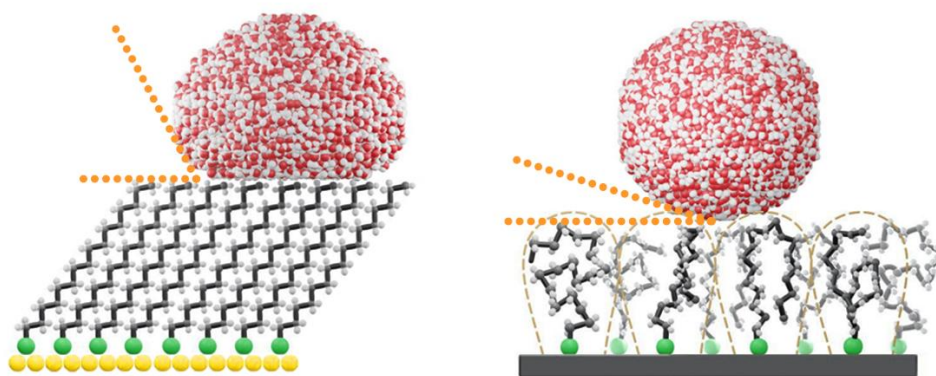
The QCM has the capacity to offer valuable insights into both the quantity of mass deposited and the speed at which films are deposited or removed, achieved through continuous monitoring of frequency changes in real-time [152]. Moreover, QCM-D additionally furnishes immediate data concerning the viscoelastic characteristics of the adhered film, encompassing parameters such as viscosity, elasticity, and density.

4 Chapter IV. Functionalization of Monolithic MOF Thin Films with Hydrocarbon Chains to Achieve Superhydrophobic Surfaces with Tunable Water Adhesion Strength

4.1 Introduction

The external surfaces of metal-organic frameworks have recently emerged as intriguing subjects of study due to their unique characteristics and potential applications. While MOFs are well-known for their versatile properties and diverse applications in fields such as gas capture and catalysis, the attention to their surface properties has been relatively limited until recent advancements in thin film fabrication techniques, particularly the development of high-quality MOF thin films using layer-by-layer methods. Development of these films has unlocked new applications by enabling the integration of MOF thin films into (opto)electronic devices [153]. An especially intriguing aspect of SURMOF outer surfaces is that they reveal anchoring sites with significantly greater spacing compared to other substrates.

One crucial aspect of MOF surface properties is their wettability, particularly by solvents like water. Grafting hydrocarbon chains onto SURMOF surfaces can lead to the formation of SAMs with brush-like structures, similar to polymer brushes [154]. This structural modification can significantly alter the surface properties, including increasing the WCA and reducing water adhesion strength, leading to superhydrophobic surfaces. The formation of brush-like SAMs hinges on achieving increased spacing between hydrocarbon chains, as illustrated in Scheme 13. Conventional substrates with closely spaced anchoring sites typically result in low-entropy hydrophilic states. In contrast, to achieve the brush-like configuration, a larger spacing between the chains is necessary.



Scheme 13 – The WCA on a hydrocarbon monolayer is shown to be substantially increased when instead of the normal close packing (left) the chains adopt a brush-like structure (right). The C18 hydrocarbon chains have an end-to-end distance of ~ 2 nm [155, 156], which is much larger than the separation of grafting sites in the SURMOF grid (~ 0.8 nm), such that the grafted hydrocarbons form a polymer brush.

In this context, UiO-66-NH₂, a member of highly water-stable MOF family, presents an attractive platform for surface modification due to its well-defined structure and functionalizable amino groups of the linker sites. By grafting hydrocarbon chains onto UiO-66-NH₂ thin films, we could reach low-roughness, crystalline and porous superhydrophobic surfaces. A modest elevation in roughness, from as low as 31.4 nm to larger values, results in a significant decrease in water adhesion force. These surfaces, characterized by low adhesion, hold considerable promise for enhanced self-cleaning capabilities. Coupled with their low roughness, these interfaces are poised to deter the buildup of submicron-sized solid particles, unlike traditional high-roughness superhydrophobic surfaces [157].

Additionally, superhydrophobic UiO-66-NH-C18 was also achieved on the highly porous material – α -alumina substrates. XRD and WCA measurements confirm the retention of crystal structure as well as superhydrophobicity. These membranes show potential for water treatment applications, such as cleaning water from oils, and will be tested in future studies.

The aim of this study is to synthesize UiO-66-NH₂ SURMOF on gold-coated substrates with low roughness and to achieve superhydrophobic surfaces through

Post-Synthetic Modification by grafting hydrocarbon chains onto the thin films. This research aims to investigate the feasibility and mechanisms of creating such surfaces for self-cleaning applications. Through comprehensive experimental characterization and theoretical analysis, we aim to advance our understanding of MOF surface modification and its potential implications for surface science and technology.

4.2 Experimental section

This section outlines the experimental methods used in this study. It covers the layer-by-layer synthesis of UiO-66-NH₂, surface roughness reduction protocols, and post-synthetic modifications into UiO-66-NH-C18 and UiO-66-NH-C18F SURMOFs.

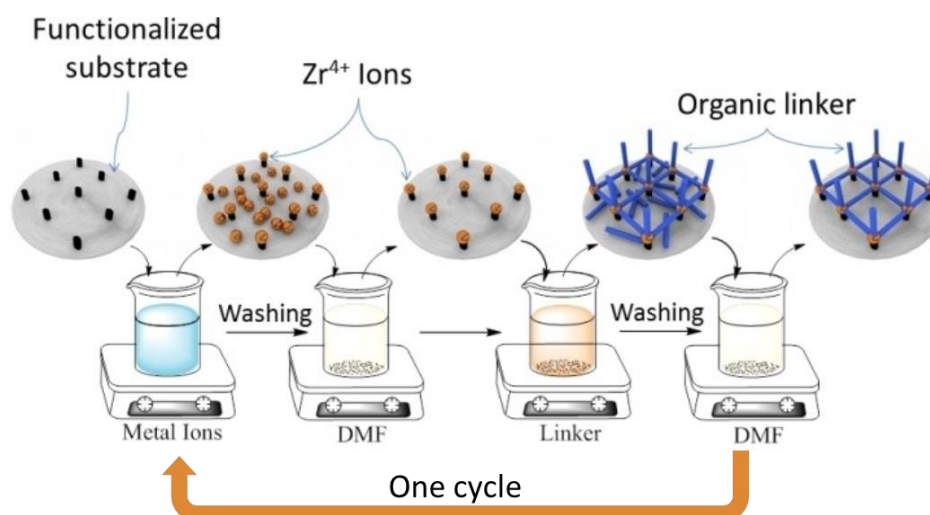
Additionally, molecular dynamic simulations provide structural insights, while ToF-SIMS results confirm chemical composition. AFM and SEM analyses ensure surface and morphological consistency before and after modifications.

Discussions also focus on flexibility variations between SAM and hydrocarbons, with summaries provided via Ramachandran plots. Furthermore, surface density determination of C18 and C18F chains in UiO-66-C18(F) SURMOFs offers quantitative insights.

4.2.1 Synthesis of UiO-66-NH₂ via dip-coating

UiO-66-NH₂ was synthesized following a previously described by Dr. Hashem (KIT, IFG) et al. method [100]. The synthesis involves an automated dip coating technique using a silar coating system (Holmarc, HO-TH-03B1, India) to form LPE SURMOF of UiO-66-NH₂ on a functionalized gold-coated substrate (FGCS) and α -alumina membranes (Scheme 14). Two solutions were prepared for this process. Solution A, which serves as the metal ion source, consisted of 90 mM ZrCl₄ in 100 mL DMF and 20 mL HCl. Solution B, which provides the organic linker, was made by dissolving 150 mM BDC-NH₂ in 100 mL DMF.

Both solutions were heated and maintained at 80 °C throughout the preparation. The substrates were first immersed in solution A, stirred at 500 rpm for 90 minutes, and then washed with DMF. Next, the substrates were immersed in solution B for 120 minutes under the same stirring conditions, followed by another DMF wash. This cycle of immersion in solutions A and B, along with washing, was repeated 30 times to build up 30 layers of UiO-66-NH₂ on the FGCS. To ensure thorough exchange of guest molecules, the resultant SURMOF was washed with ethanol six times and then soaked in ethanol for 24 hours. After this washing step, the samples were allowed to dry in air overnight.



Scheme 14 – Schematic diagram for the synthesis of UiO-66-NH₂ SURMOF through LPE using dip-coating. *Edited from [100] with permission from Wiley*

4.2.2 Surface functionalization with C18-SAM

4.2.2.1 Materials

Self-assembled monolayers of Octadecanethiol (ODT, Sigma Aldrich) was used to obtain C18 SAM@Au without further purification.

4.2.2.2 Technique

ODT SAM were employed to functionalize Au-coated silicon wafers. The substrates were left in the dark at room temperature for 48 h with the gold side up in a 0.1 mM ethanolic solution of ODT. After that the SAM@Au was completely

washed with pure ethanol and dried in a flow of dry nitrogen and then used for IRRAS and WCA.

4.2.3 Surface Roughness Reduction Protocol

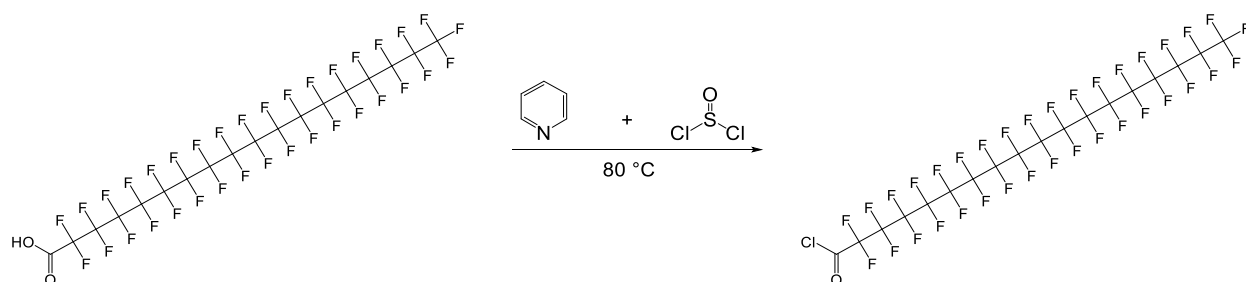
The surface roughness of the prepared SURMOF samples was addressed through a treatment process as follows: initially, the prepared SURMOF samples were immersed in DMF for one hour at 90 degrees Celsius. Subsequently, the samples were immersed in ethanol and subjected to sonication for a duration of four hours. Throughout this period, the ethanol was refreshed every hour. This treatment protocol effectively contributed to the reduction of surface roughness in the UiO-66-NH₂ SURMOF samples.

4.2.4 Post-synthetic modifications of UiO-66-NH₂ SURMOF

4.2.4.1 Chemicals

Triethylamine (TEA, 99.0%) was obtained from Merck, USA, octadecanoyl chloride (97%) was provided by Sigma-Aldrich, USA, and tetrahydrofuran (THF, 99%) was supplied by VWR, EC.

Perfluorooctadecanoyl chloride was synthesized (Scheme 15) by Prof. Dr. S. Bräse (KIT, IBCS-FMS & IOC), Dr. P. Hodapp (KIT, IBG3-SML) and M.Sc. A. Jung (KIT, IBCS-FMS), using the following chemicals: perfluorooctadecanoic acid (95%) from abcr, Germany, pyridine (99.5%, United Kingdom) and thionyl dichloride (+99.5%, BE) were supplied by Acros Organics.



Scheme 15 – Schematic illustration of perfluorooctadecanoyl chloride preparation

To a flask containing a mixture of perfluorooctadecanoic acid (501 mg) and thionyl chloride (5 mL), a catalytic amount of pyridine (5 μ L) was added under stirring. The flask was fitted with a reflux condenser, and the reaction mixture was heated in an oil bath at 80 °C for three days. After one day, an additional 5 mL of thionyl chloride was added to the mixture.

Once the reaction cooled to room temperature, the volatiles were removed using a rotavap under reduced pressure (180 mbar, 40 °C water bath). The resulting white/yellow powder (perfluorooctadecanoyl chloride) was stored under argon until further use.

4.2.4.2 Modification to UiO-66-NH-C18 SURMOF

To synthesize UiO-66-NH-C18 (C18@SURMOF), we immersed the prepared UiO-66-NH₂ SURMOF in a glass container containing a mixture of 5 mL of TEA solution and 5 mL of DMF. The container was placed in an ice bath and gently shaken for one hour. Following this, a solution of 0.5 g of octadecanoyl chloride in 5 mL of THF was added to the sample. The reaction mixture containing the SURMOF was then heated to 45 °C for 24 hours. After cooling, C18@SURMOF was collected and washed five times with DMF and methanol.

4.2.4.3 Modification to UiO-66-NH-C18F SURMOF

To prepare UiO-66-NH-C18F (C18F@SURMOF), we followed the same procedure as for C18@SURMOF, with the exception of using perfluorooctadecanoyl chloride in place of octadecanoyl chloride.

4.2.5 Molecular Dynamics Simulations

Molecular dynamics (MD) simulations were carried out by Dr. M. Liu (KIT, IFG) and Prof. Dr. W. Wenzel (KIT, INT).

All-atom MD simulations were performed to determine the structure of C18 chains grafted to the outer surface of the SURMOF and to investigate the wetting behavior of both pristine and modified substrates. To validate this theoretical

approach, the wetting behavior of thiolate-based SAMs on Au substrates was simulated using OPLS-AA force field parameters for C18 chains, following previously reported protocols [158]. For the SURMOF simulations, the UFF4MOF force field was used to describe the flexible UiO-66-NH₂ SURMOF [159]. The C18 chains were modeled using the OPLS-AA force field [160, 161] with parametrization refined from LigParGen [162]. Water molecules in the wetting simulations were parametrized according to the SPC/E model [163].

MD simulations for grafting and wetting processes were conducted using the LAMMPS package [164]. In the grafting simulations, the timestep was set to $\tau = 0.01$ fs in the canonical ensemble under a Nose-Hoover thermostat [165] at $T = 300$ K. During the wetting simulations, the timestep was set to $\tau = 0.25$ fs under a Nose-Hoover thermostat [165] and Nose-Hoover-Andersen barostat [166] to model NPT conditions at ambient pressure ($p = 1$ atm) and temperature ($T = 300$ K).

The initial molecular configuration consisted of a 4x4x2 supercell of UiO-66-NH₂ SURMOF. During the simulated grafting, C18 chains were tilted by 5° and artificially placed in the MOF, with the hydrophilic head of the chain within 0.3 nm of the nitrogen on the -NH₂ group of the MOF linker. One hydrogen atom from the head of the C18 chain and one hydrogen from the -NH₂ group in the SURMOF linker were removed to allow bond formation to occur as a stochastic process. If the carbon from the C18 chain was within 0.4 nm of the nitrogen atom in the -NH₂ group, an 80% probability was applied for forming a C–N bond, linking the hydrocarbon chain to the SURMOF and removing the extra hydrogen atoms. Chains that failed to anchor to the SURMOF were removed. For successfully grafted chains, partial charges on the -NH- group and the head of the C18 chain were reassigned using the Hartree-Fock method via MOPAC [167].

For the wetting simulation on a pristine UiO-66-NH₂ MOF, a water "cube" consisting of 1074 water molecules was placed on top of the SURMOF. For the grafted UiO-66-NH-C18, a water "ball" consisting of 3604 water molecules was

placed on top of the grafted chains. The water droplet on the SURMOF system was relaxed for 3 ns in the MD simulation. After this time, the water contact angle was determined from the geometrical profile of the water droplets in MD snapshots using a previously established method [168].

4.2.6 Time-of-Flight Secondary Ion Mass Spectrometry (ToF-SIMS) results

Time-of-Flight Secondary Ion Mass Spectrometry (ToF-SIMS) results were obtained with the help of Dr. A. Welle (KIT, IFG).

ToF-SIMS was utilized to examine the surface modification of UiO-66-NH₂ SURMOF. Figure 26 shows a blank sample (in black) representing the pristine SURMOFs before modification and two surface-modified SURMOF samples (in blue and red). The modified samples are identical to ensure test result repeatability.

The results revealed that Zr⁴⁺ and Cl⁻ were easily detected in the blank sample of pristine UiO-66-NH₂ SURMOF (Figure 26 (a, b)). However, after post-treatment, their signal intensities significantly decreased. These elements are present due to the hydrolysis of the ZrCl₄ precursor used in MOF synthesis, forming ZrOCl₂ trapped within the MOF structure. Following the modification process, several washes removed ZrOCl₂ from the MOF structure. In Figure 26 (c), the C–N bond was fully detected (100%) in the pristine SURMOF (blank sample). However, post-synthetic treatment of the amino groups in the pristine SURMOF (blank sample) with stearic acid chloride led to their partial conversion into -NH-C18 groups, as shown by the appearance of CNO bonds alongside CN bonds (red and blue peaks, Figure 26 (d)). Figure 26 (e) illustrates the residual part of stearic acid chloride after reacting with the amino groups in the pristine SURMOF, confirming their successful conversion into the amide form.

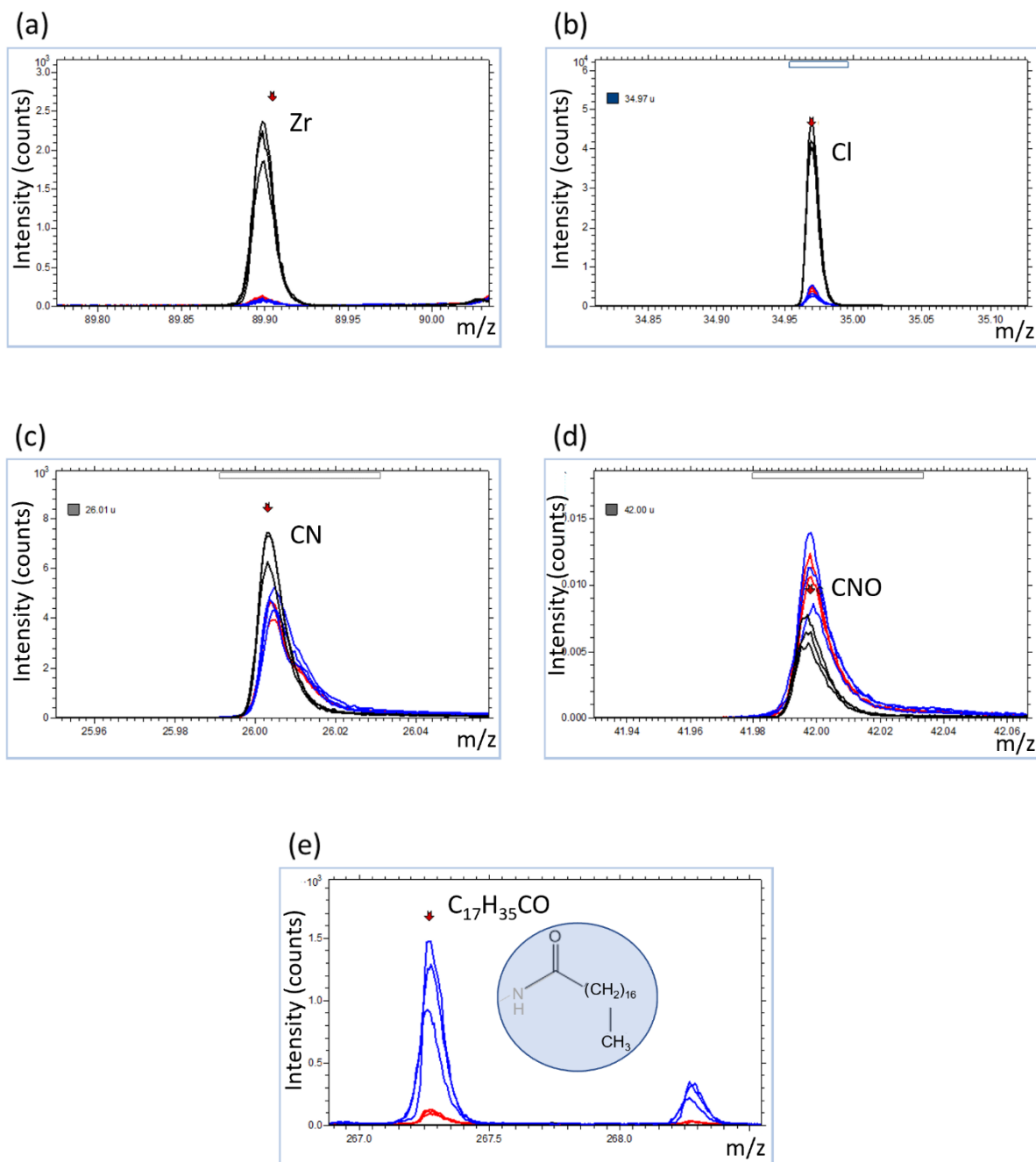


Figure 26 – ToF-SIMS results for pristine UiO-66-NH₂ SURMOF (blank sample in black) and its surface-modified counterpart (modified samples in blue and red), demonstrating (a-b) the high prevalence of Zr⁴⁺ and Cl⁻ in the blank sample before modification, which are washed away with (c) higher appearance of amino groups in the blank sample, followed by (d) concurrent appearance of amino and amido groups in the modified samples in addition to (e) full proof of the amidation reaction by the existence of the residual part of stearic acid chloride.

4.2.7 Surface Roughness Consistency before and after Post-Synthetic Modification

The atomic force microscope analysis was performed to evaluate the surface roughness of UiO-66-NH₂, C18F@SURMOF, and C18@SURMOF samples. The AFM results (Figure 27) showed no significant differences in roughness values among the three samples. This suggests that the post-synthetic modification (PSM) did not cause notable changes in the surface roughness of the SURMOF samples. The consistent roughness values indicate that the structural integrity and surface characteristics remained largely unaffected by the PSM process. These results highlight the robustness and stability of the synthesized SURMOF materials, which is crucial for their potential applications in various fields.

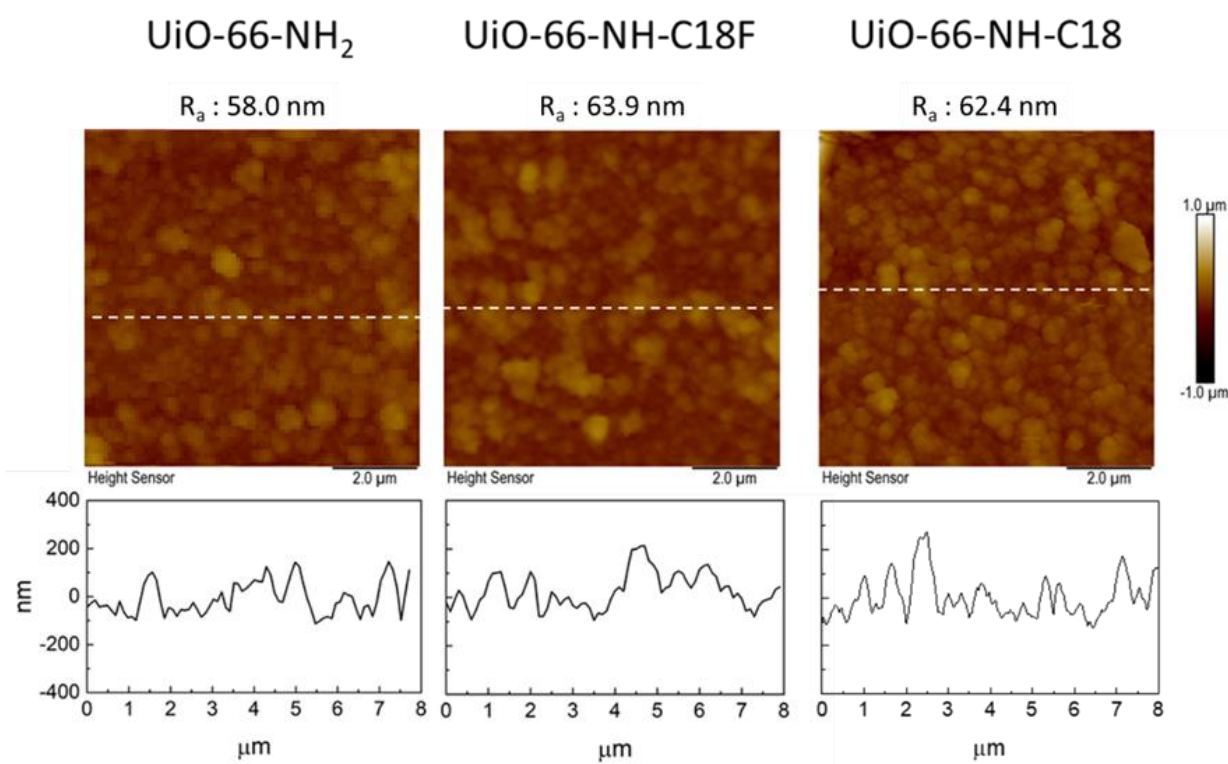


Figure 27 – AFM comparison of UiO-66-NH₂, UiO-66-C18F and UiO-66-C18 SURMOFs

4.2.8 Morphological Consistency before and after Post-Synthetic Modification

The scanning electron microscope analysis was performed to examine the morphology of UiO-66-NH₂, C18F@SURMOF, and C18@SURMOF samples. The SEM images (Figure 28) showed remarkable similarities in the morphology of the three samples, with no noticeable differences observed. This observation aligns with the AFM analysis results. The similar morphology across all samples indicates a high degree of structural uniformity and stability, which are advantageous for potential applications in various fields. Furthermore, the consistent morphology suggests that the surface structure of the SURMOF remained unchanged after the PSM.

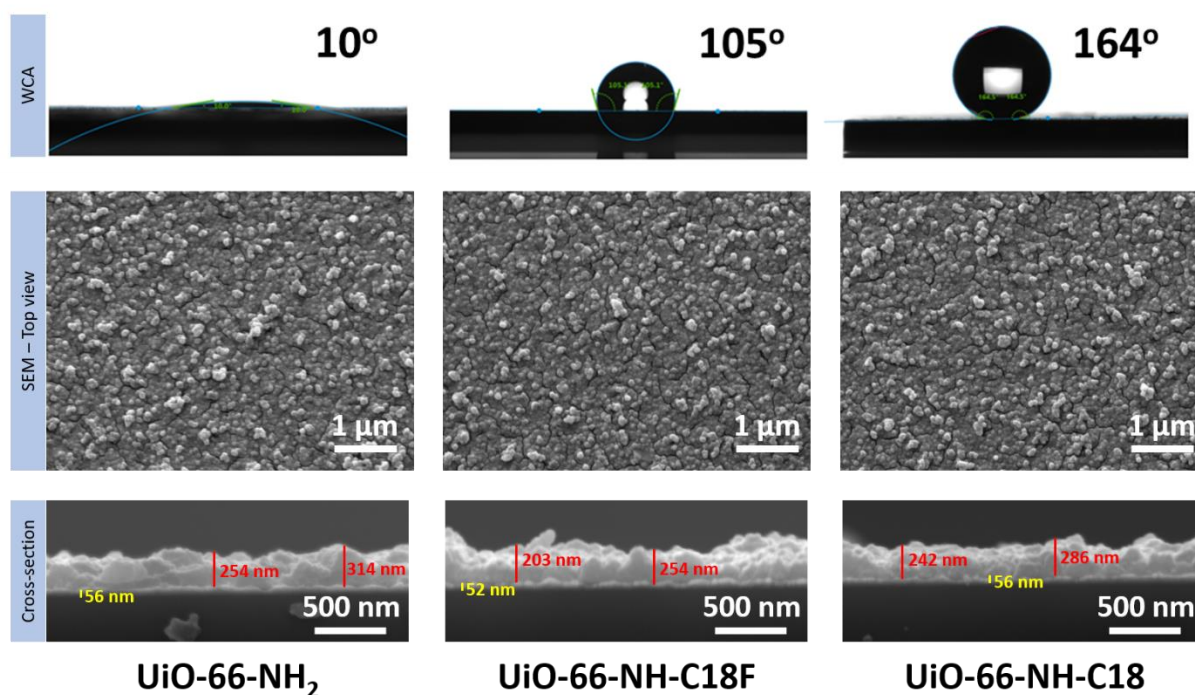


Figure 28 – SEM images and WCA of UiO-66-NH₂, UiO-66-C18F and UiO-66-NH-C18

4.2.9 Flexibility of hydrocarbon chains in dry conditions vs. during wetting

The flexibility of hydrocarbon chains in SAM@Au, C18F@SURMOF, and C18@SURMOF is evident from their chain conformations. In SAM@Au (Figure

29 (a)), the densely packed all-trans hydrocarbon chains are stretched and tilted. In contrast, the increased spacing among grafted anchor points in C18F@SURMOF (Figure 29 (b)) and C18@SURMOF (Figure 29 (c)) allows for greater flexibility of the chains.

In case of the perfluorinated chains, the stronger repulsion of fluorine atoms in $-\text{CF}_2-$ groups compared to hydrogen in $-\text{CH}_2-$ groups effectively stretches the hydrocarbon chains, resulting in enhanced rigidity. This increased rigidity of the CF chains leads to a greater film thickness of 0.4 nm.

When a water droplet contacts SAM@Au (Figure 30 (a)), the hydrocarbons of SAM form a dense insulating layer, while the pristine SURMOF (Figure 30 (b)) adsorbs water. In the case of C18F@SURMOF (Figure 30 (c)), the perfluorinated hydrocarbon chains mix with water "pins" that penetrate the polymer brush. In contrast, C18@SURMOF (Figure 30 (d)) exhibits a clear separation between water and hydrocarbon chains, resulting in a much higher water contact angle.

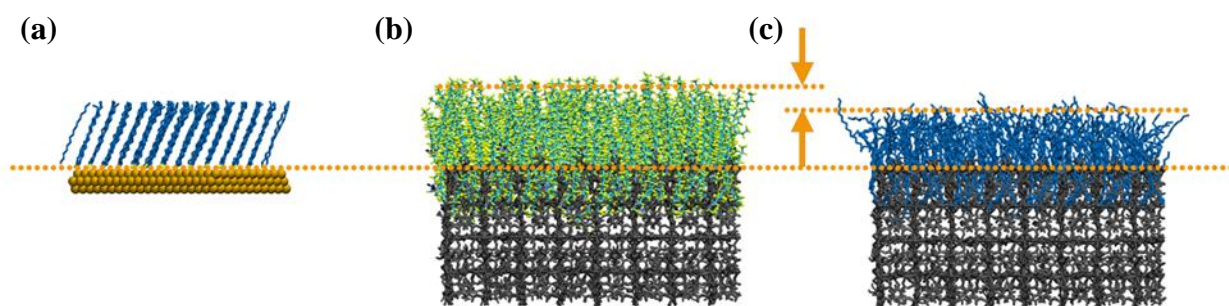


Figure 29 – The stretching of hydrocarbon chains in the dry conditions for (a) SAM@Au, (b) C18F@SURMOF, and (c) C18@SURMOF. The substrates are aligned, marked by the orange dotted line across the three systems, whereas the distinguished thicknesses between C18F@SURMOF and C18@SURMOF are illustrated by orange arrows. This difference in chain stretching is measured at 0.4 nm due to the stronger repulsion among fluorine atoms in CF chains, exemplifying a lower entropy in CF chains. The fluorine atoms are explicitly shown in bright yellow, whereas hydrogen atoms on hydrocarbon chains are omitted for clarity

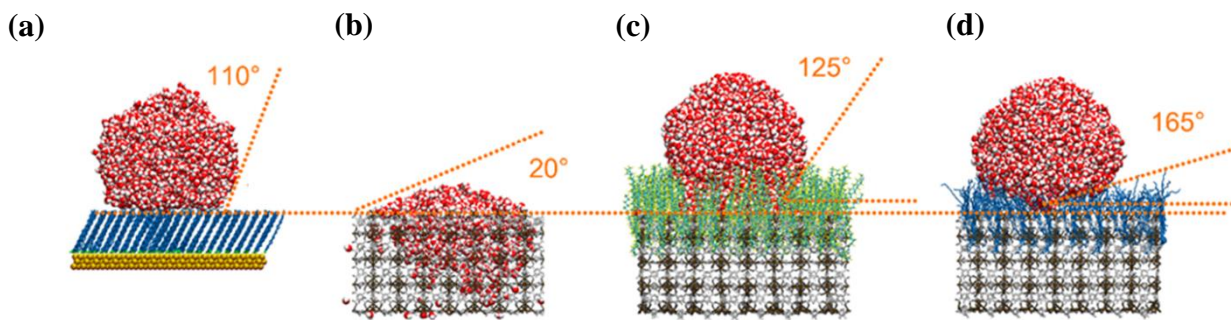


Figure 30 – Water contact angles in the wetting simulations for (a) SAM@Au, (b) SURMOF, (c) C18F@SURMOF, and (d) C18@SURMOFs. The substrates are aligned, marked by the orange dotted line across the four systems. The water contact angles are marked by orange dotted lines. Particularly, in the case of C18F@SURMOF and C18@SURMOFs, the water droplet cannot react to the reference surface on the substrate, where additional baselines are indicated by horizontal orange dotted lines. For better clarity, MOF linkers are shown in light gray.

4.2.10 Intrinsic entropy of hydrocarbon chains from Ramachandran plots

The intrinsic entropy for SAM@Au, C18F@SURMOF, and C18@SURMOF was calculated from the conformational phase space by Dr. U. Manna and Dr. A. Borbora, a member of Dr. Manna's research group at IITG. The torsional angles on the hydrocarbon C-C backbone statistically fall into the categories of trans-trans (180° – 180°), trans-gauche (60° – 180°), and gauche-gauche (60° – 60°) conformations. In dry conditions, SAM is predominantly in an all-trans conformation, as indicated by the concentrated distribution at the 180° – 180° extremities in the Ramachandran plot (Figure 31), with gauche defects being very rare. In contrast, the conformers in C18F@SURMOF and C18@SURMOF cover larger areas of the phase space with a reduced trans-trans density.

Entropy was then estimated based on the probability of individual states across the phase space using the formula:

$$S = -k_b \sum_i p_i \ln p_i, \quad (3)$$

where p_i is the estimated kernel density over all conformers.

The estimated entropy values were ranked as SAM@Au ($5.3k_b$), C18F@SURMOF ($6.47k_b$), and C18@SURMOF ($6.97k_b$), indicating increasing

disorder. The number of gauche defects per chain was also calculated based on occurrence probability, averaging 0.04 gauche defects per hydrocarbon chain in SAM@Au, 1.42 per chain for C18F@SURMOF, and 2.89 per chain for C18@SURMOF

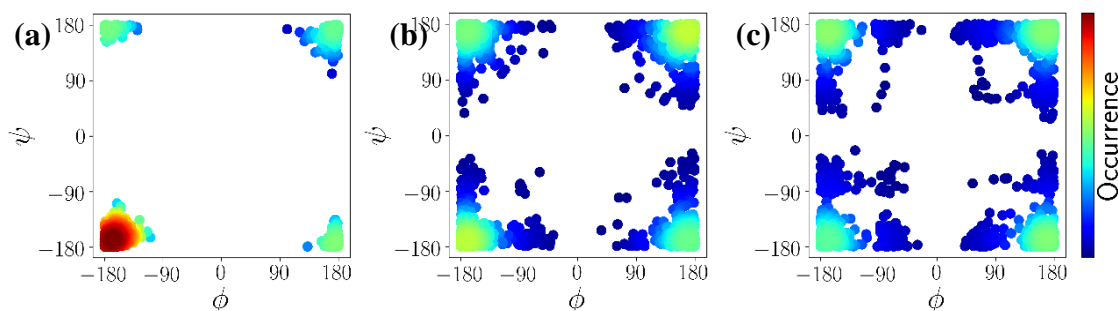


Figure 31 – Ramachandran plots for the torsional angles of the C-C backbone in the dry conditions for (a) SAM@Au, (b) C18F@SURMOF, and (c) C18@SURMOF. Color-coded is the occurrence frequencies of individual states. The SAM is in all-trans states where the torsional angles are constrained to the π - π corners in all quadrants, whereas for C18F@SURMOF and C18@SURMOF, there exist numerous gauche defects. The entropy calculated based on the state occurrence frequencies ranks the SAM as the least entropic at 5.3, the C18F@SURMOF in the middle with an entropy reference at 6.47, and C18@SURMOF with the highest entropy at 6.97. In dry conditions, the number of gauche defects per chain is 0.04 for SAM, 1.42 for C18F@SURMOF, and 2.89 for C18@SURMOF

4.2.11 Determination of surface density of C18 and C18F chains in UiO-66-C18(F) SURMOFs

To assess the grafted density in C18F@SURMOFs, the CH₂ stretching vibration intensity at 2929 cm⁻¹, originating from the MUD-SAM used to functionalize the Au substrate prior to SURMOF deposition, was compared with the C-F stretching vibration intensity at 1151 cm⁻¹, which is associated with the grafted hydrocarbons (Figure 32).

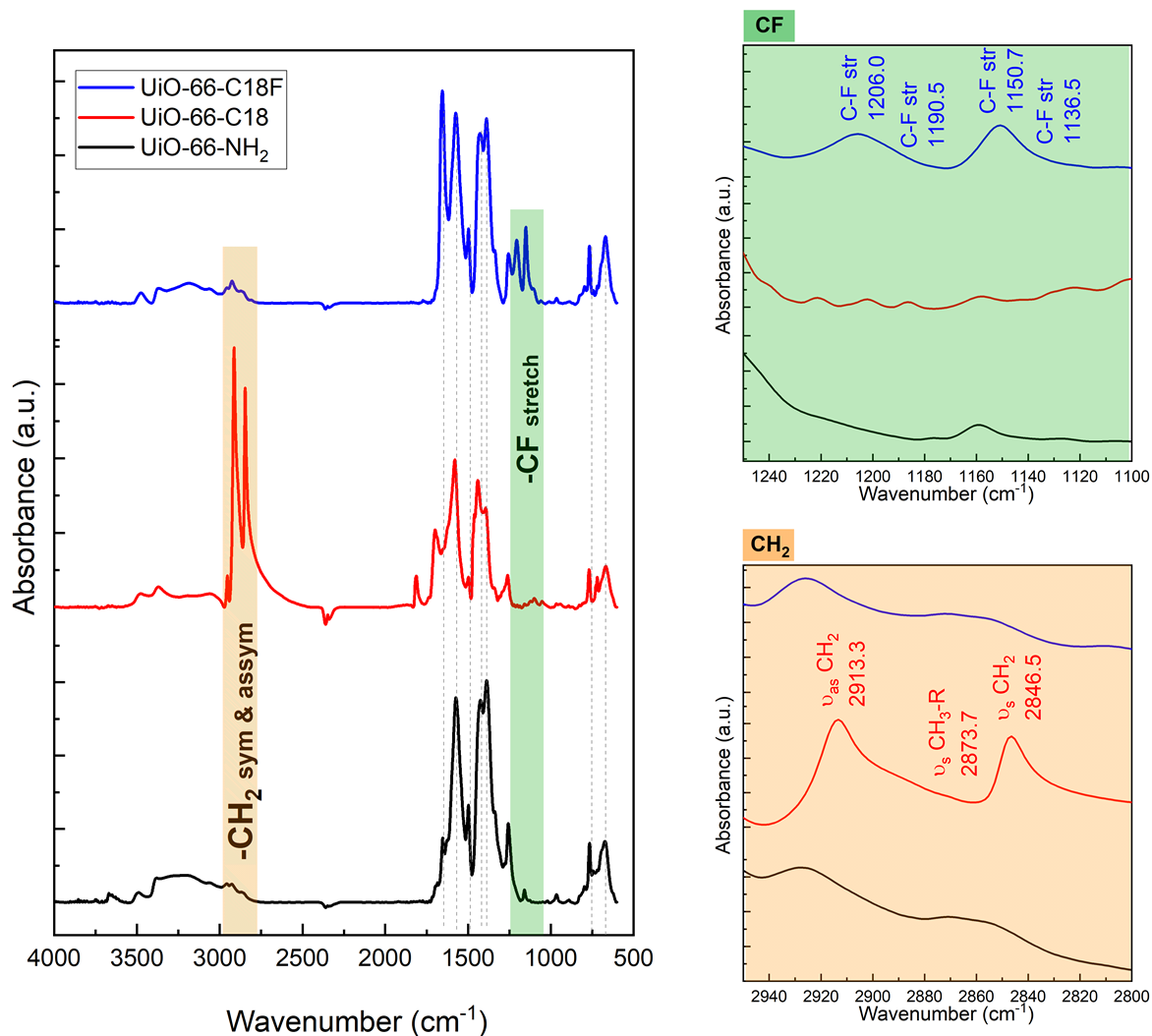


Figure 32 – IRRAS data of UiO-66-NH₂, C18@SURMOF and C18F@SURMOF

Using theoretical results on the IR vibrational modes (Figure 33) obtained by Dr. M. Liu (KIT, IFG) and Prof. Dr. W. Wenzel (KIT, INT), the ratio of monomer coverage in MUD-SAM to C18F was determined to be 0.7:1, indicating that the surface density of C18F is comparable to that in the MUD-SAM. It is important to note that this is a semiquantitative estimate, as other factors (e.g., scattering of IR light passing through the SURMOF) could introduce errors. Nevertheless, the calculated surface density of C18F aligns with the density observed in partially fluorinated SAM [169].

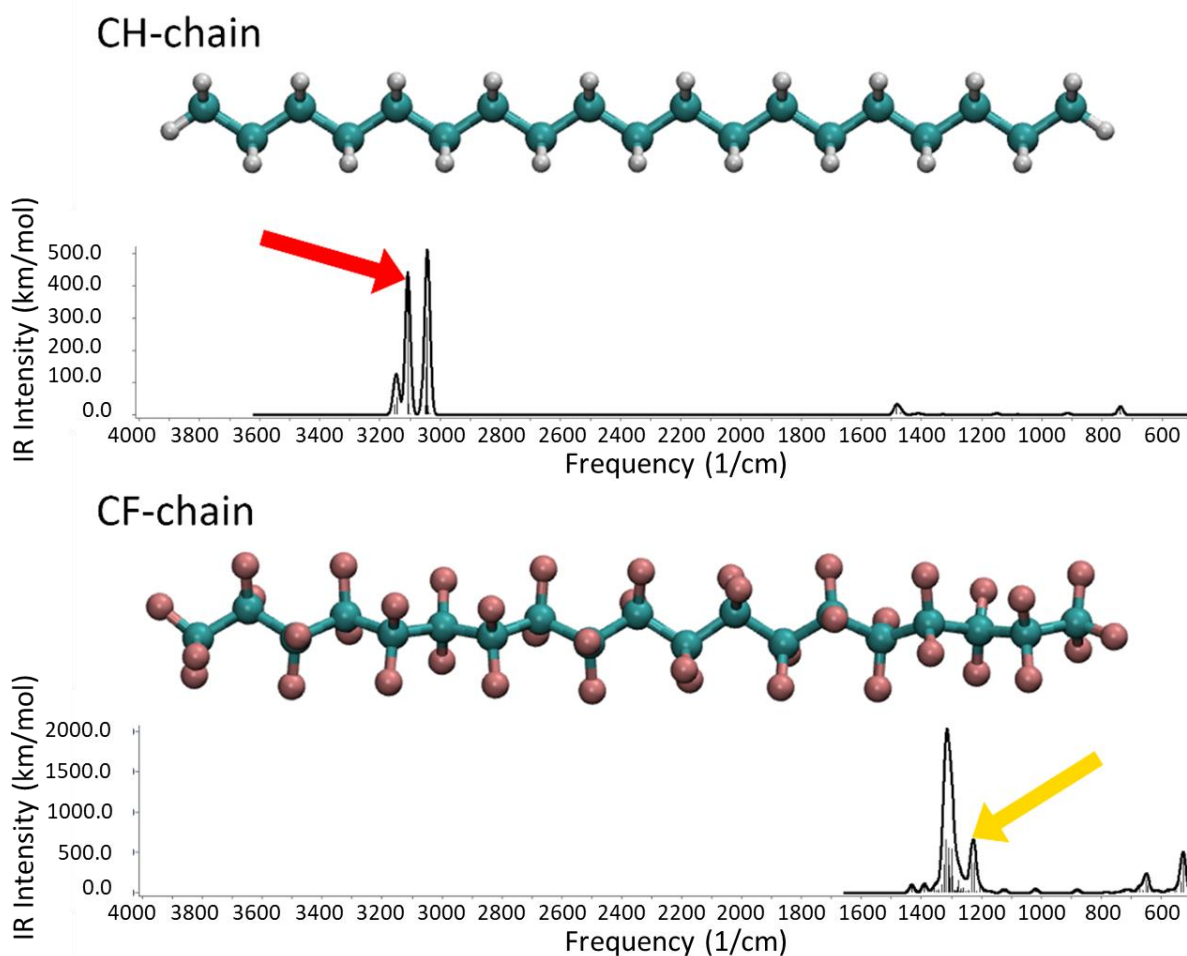


Figure 33 – DFT optimized molecular geometries and corresponding calculated IR spectra for isolated chains.

Determining the surface density in C18@SURMOF is more challenging because the CH₂ signals in the MUD-SAM and the C18 chains overlap. Additionally, surface selection rules [170] complicate the estimation of CH chain densities, as the C18 chains are coiled. Considering these factors, we conclude that the surface densities of grafted C18F and C18 are consistent with the setup in the MD simulations.

For reference, isolated C18 and C18F chains in the linear (trans) conformation were structurally optimized using density functional theory (DFT) before calculating the vibrational intensities corresponding to their unique peaks in the IR spectrum. Geometry optimizations were conducted with the PBE0 hybrid functional under a tight convergence criterion (tightSCF) using Orca version

5.0.4. The optimized CH chain represents the all-trans configuration, while the optimized C18F adopts the helical configuration (Figure 33).

After reaching the global minimum, the vibrational modes were determined using numerical Hessian calculations. To align with experimental IRRAS data, discrete IR peaks from DFT were integrated with Gaussian broadening with a bandwidth of 20 cm^{-1} . The unique peaks at 3144 cm^{-1} for CH (indicated by the red arrow) and at 1227 cm^{-1} for CF (indicated by the yellow arrow) were chosen for calculating the surface densities of CH and CF.

4.3 Results and discussion

XRD analysis performed on UiO-66-NH₂ and UiO-66-NH-C18 SURMOFs indicated high film quality. The XRD peak positions and intensities align with simulations (Figure 34 (a)) based on the previously reported UiO-66-NH₂ bulk structure [171]. The samples retained their crystallinity after PSM, however the signal-to-noise (S/N) ratio decreased. This decrease could be related to the reaction conditions, particularly the acidic environment at a slightly elevated temperature (45°C) for an extended period (24 h).

Successful grafting of alkyl chains to the SURMOF surface was confirmed using FT-IR spectroscopy. The IRRAS data of C18@SURMOF (Figure 34 (b)) clearly revealed symmetric (2920 cm^{-1}) and asymmetric (2850 cm^{-1}) stretching vibrations of alkyl -CH₂- groups, which were missing in pristine UiO-66-NH₂ SURMOF.

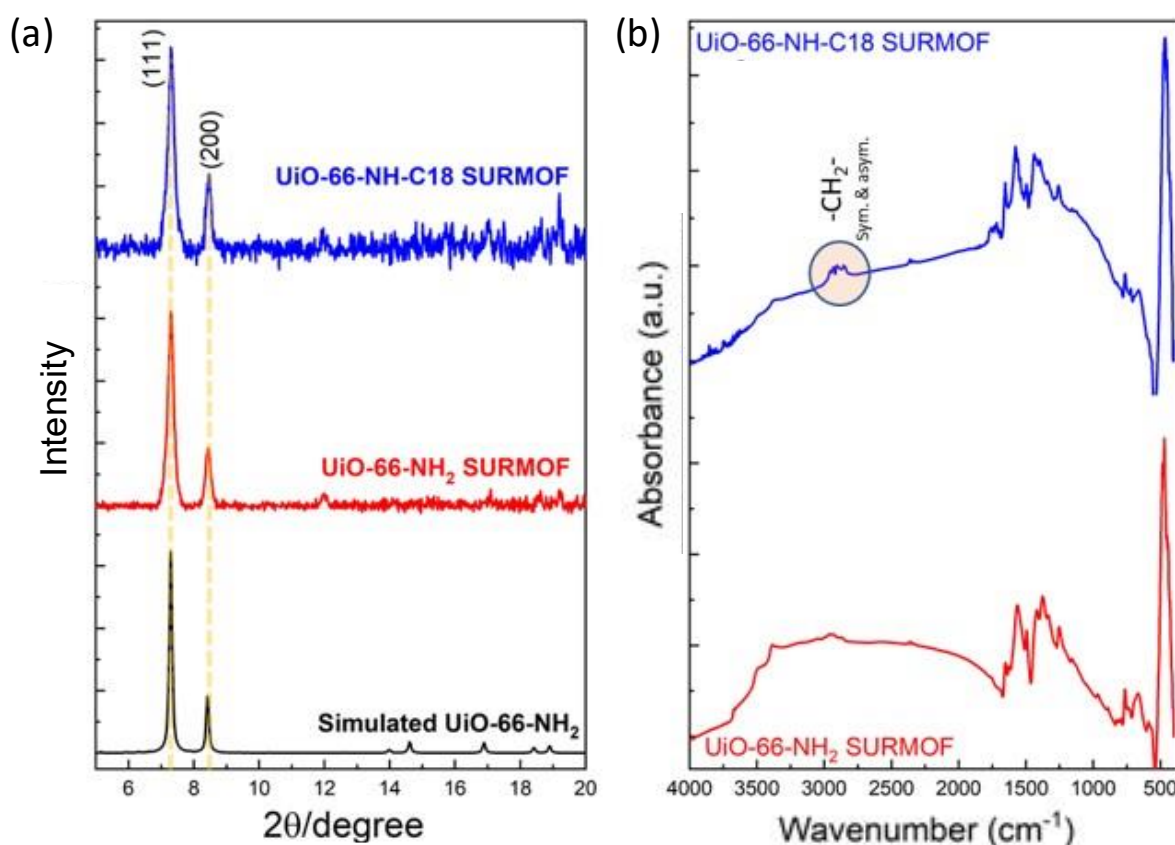


Figure 34 – (a) XRD patterns and (b) IRRAS data for the pristine SURMOF UiO-66-NH₂ and the modified UiO-66-NH-C18.

The surface selection rule in IR spectroscopy is well-known for determining the chemical composition of films and the orientation of molecules near metal surfaces, such as the tilt of alkane chains relative to the surface [158]. IRRAS was also used to compare the IR spectra of C18 SAM (SAM@Au) and C18@SURMOF. Notably, the asymmetric and symmetric methylene peaks of C18@SURMOF are shifted by 5 cm⁻¹ compared to those of SAM@Au (Figure 35), indicating the presence of a substantial amount of gauche-conformations in the SAM-forming monomers [172-174]. This shift confirms the disorder of C18 chains in the modified SURMOF. Thus, the IRRAS technique strongly supports the proposed entropy effect discussed in this study.

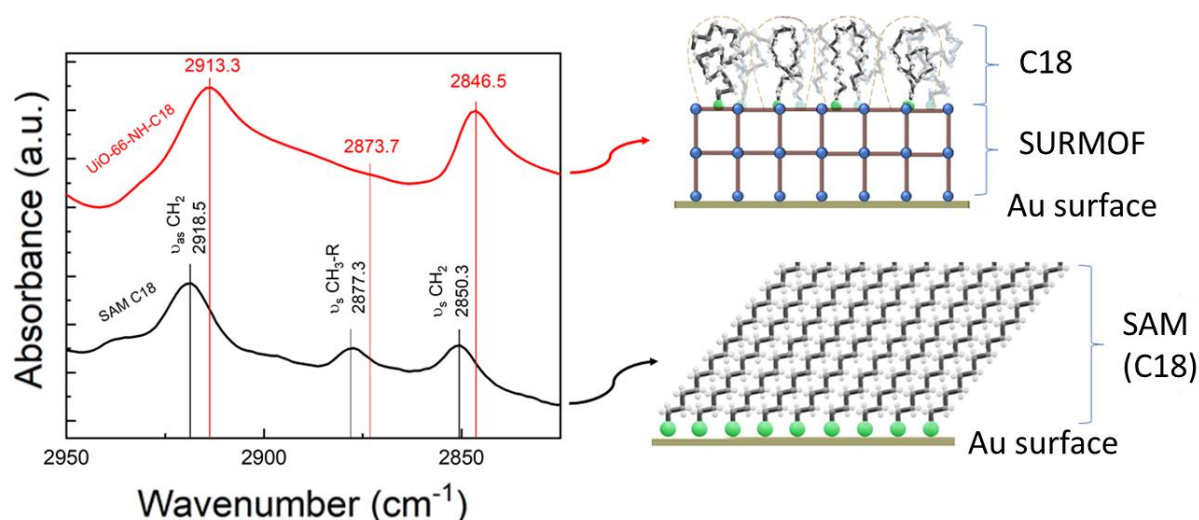


Figure 35 – The IRRAS results demonstrate the shift in the CH-region of self-assembled monolayers (SAM@Au) and C18@SURMOF. The spectrum shows a noticeable shift in the CH stretching vibration for both samples, confirm the disorder of the C18 on the surface of C18@SURMOF.

As evident from Figure 36 (a), the static water contact angle for the pristine SURMOF is quite small, less than 11° , which is similar to that of metal oxides [175]. Drastic changes in wetting properties are observed after grafting C18 alkyl chains to the crystalline array of anchoring sites on the outer surface of the porous SURMOF substrate. As shown in Figure 36 (c), the surface becomes superhydrophobic, with a static WCA exceeding 160° . Notably, when fluorinated hydrocarbon chains were used in place of standard ones, the WCA values unexpectedly decreased from 161° to 101° , as shown in Figure 36 (b). This outcome is remarkably different from that of conventional alkanethiolate-based SAMs, where fluorination enhances hydrophobicity [176].

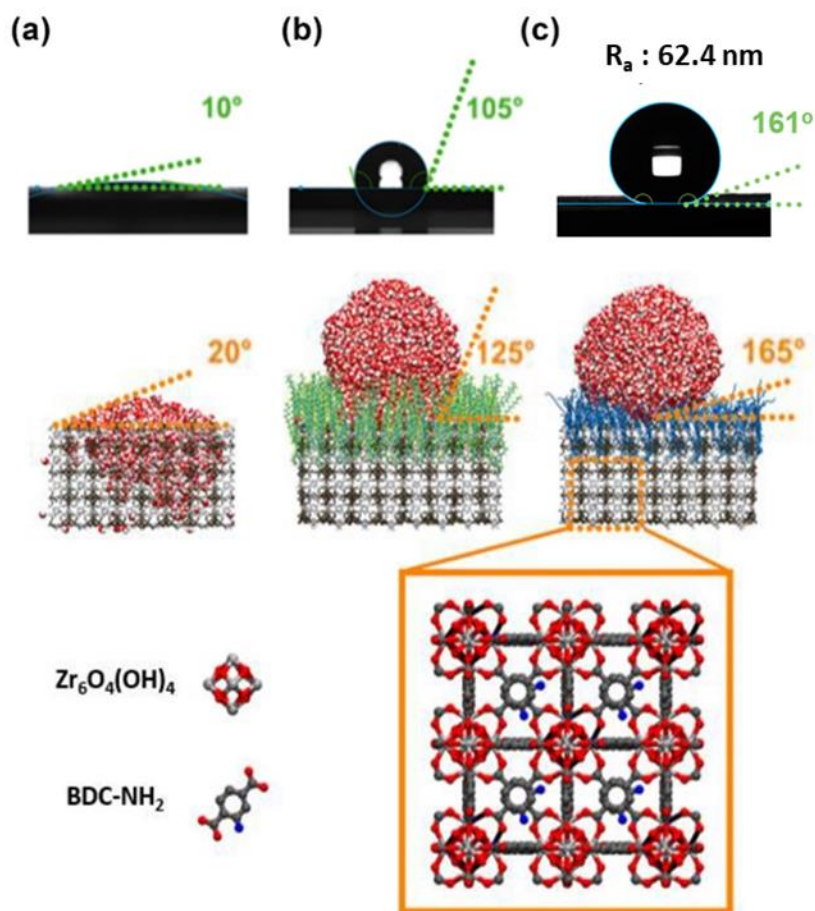


Figure 36 – Static water contact angle, snapshots taken from equilibrated MD-simulations for water droplets and enlarged structure of UiO-66-NH₂. **Top:** Static water contact angle of (a) pristine UiO-66-NH₂ SURMOF, (b) SURMOF grafted with perfluorinated chains, UiO-66-NH-CF and (c) SURMOF grafted with C18 hydrocarbon chains from the experiment and the simulation. **Center:** Snapshots taken from equilibrated MD-simulations for water droplets on pristine (a) UiO-66-NH₂ SURMOF, (b) SURMOF grafted with perfluorinated hydrocarbon chains, and (c) SURMOF grafted with C18 hydrocarbon chains. **Bottom:** Enlarged structure of UiO-66-NH₂ (C₄₈H₃₄N₆O₃₂Zr₆) SURMOF, formed by linking Zr-clusters (Zr₆O₄(OH)₄) with organic linkers BDC-NH₂ (C₈H₇NO₄). Explicit hydrogen atoms are omitted for clarity.

The roughness (arithmetic average, R_a) of C18@SURMOF, measured by AFM, is approximately 30 nm (Figure 37 (a) and Figure 27). The WCA value is around 154°, indicating the superhydrophobic character of these substrates. To fully characterize surface wetting, the contact angle hysteresis (difference between advancing and receding contact angles) was measured for C18@SURMOF substrates. Significant hysteresis was observed, with advancing

angles around 163° and receding at 151° . Notably, a sample with higher R_a roughness (62.4 nm compared to 31.4 nm) showed hysteresis below 5° , suggesting a notable decrease in water adhesion strength with increasing roughness (Figure 37 (b), (c)) [177], [178].

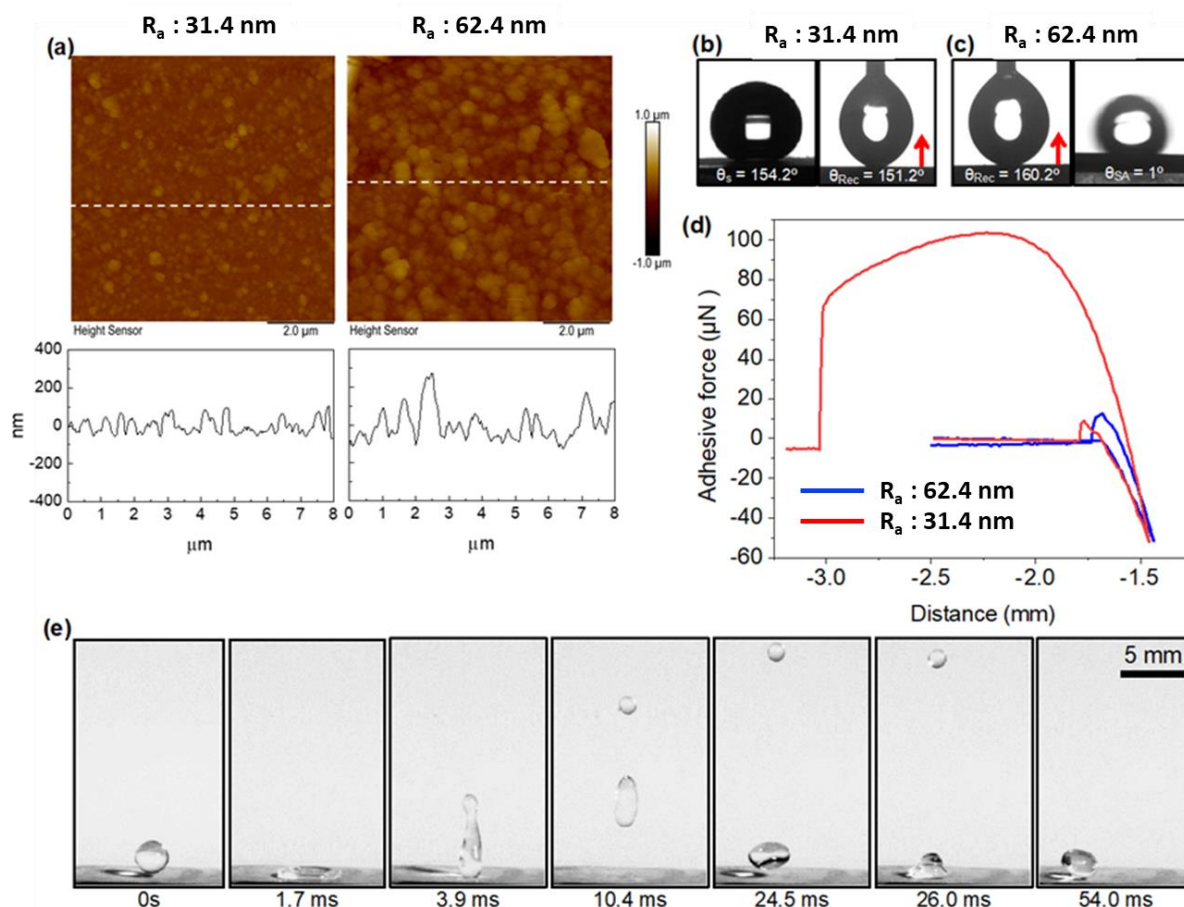


Figure 37 – (a) AFM images comparing the surface roughness of two different SURMOF surfaces. (b) Sequential images showing static and receding water contact angles on C18@SURMOF with arithmetic average roughness (R_a) of 31.4 nm. (c) Sequential images showing receding contact angle and sliding angle on C18@SURMOF with R_a of 62.4 nm. (d) Adhesion force measurement of the water droplet on adhesive and non-adhesive superhydrophobic surfaces. (e) High-speed images depict the bouncing behavior of a water droplet dropped on the non-adhesive superhydrophobic SURMOF surface. (b)-(e) results were obtained by Dr. U. Manna and Dr. A. Borbora (IITG)

An independent confirmation of roughness-induced reduction in adhesion strength of water droplets (volume = $5\ \mu\text{L}$; (Figure 37 (d)) was provided using a force-tensiometer-based system equipped with a micro-electromechanical balance [179]. When the sample with higher roughness (62 nm) was tested, a

decrease in adhesion from $106.3 \pm 5.4 \mu\text{N}$ to $16.4 \pm 4.2 \mu\text{N}$ was observed. Moreover, the sample surface demonstrated extremely low sliding angle ($\theta_{\text{SA}} = 1^\circ$, Figure 37 (c)), ensuring effortless and lossless rolling of water droplets. Furthermore, the dynamics of water droplets impinging on the SURMOF surface showed almost complete bouncing back (Figure 37 (e)). These results demonstrate the presence of a superhydrophobic, non-sticky surface. Notably, such non-adhesive superhydrophobicity usually indicates the presence of high-roughness ($> 100 \text{ nm}$, Table 3) substrates with micro- or nanostructures, where air pockets form between the rough surface and liquid, creating the Cassie-Baxter state [180-183].

Table 3 – WCA comparisons for hydrophobic thin films. WCA colored in red correspond to mediocrehydrophobicity and the rest corresponds to superhydrophobicity [184-194]

No.	Fabrication approach	Chemistry	Topography	Roughness (R_a/R_q)		WCA ($^\circ$)	Ref.
				$> 100 \text{ nm}$	$< 100 \text{ nm}$		
1	Dip coating of PDMS@MOF@Cu mesh	Hydrocarbon	Micro-/nanohierarchical	$8.94 \mu\text{m}$		151.8	[184]
2	Octadecylamine (ODA) modification in electrodeposited MOF (Zn-BTC)-film	Hydrocarbon	Micro-/nanohierarchical	$\sim 3 \mu\text{m}$		153	[185]
3	Soot-templated fluorosilica protected with silicon microarmor prepared using photolithography	Fluorocarbon	Nano-structures within microstructure armor	Micro-roughness		> 170	[186]
4	Zn-MOF film, subsequent fluoroalkylsilane coating	Fluorocarbon	Micro-/nanohierarchical	857 nm		155	[187]
5	Polymer multilayers coating	Hydrocarbon	Micro-/nanohierarchical	$\sim 275 \text{ nm}$		138.0 ± 1.9	[188]
6	Polymer & SiO ₂ nanoparticle crosslinked films	Hydrocarbon	Nanohierarchical	$\sim 175 \text{ nm}$		> 160	[189]
				$\sim 113 \text{ nm}$		~ 148	
7	Octyltrichlorosilane (OTS) SAM	Hydrocarbon	i) Micrometer-sized spikes of	Micro-roughness		> 160	[190]

			black silicon (bSi)				
			ii) Nanostructured SiO ₂ surface		0.21 nm	109	
8	Spin coating of silica particle with epoxy resin	Fluorocarbon	Nanohierarchical		96.5 nm	162 ± 3	[191]
9	Boehmite and aluminum acetylacetonate film with fluoroalkylsilane coating	Fluorocarbon	Nanohierarchical		93 nm	152.5 ± 1.6	[192]
10	Solidification-induced phase separation of polysiloxane (PSO)/poly(dimethylsiloxane) (PDMS)	Hydrocarbon	Nanoporous		87.7 nm	155	[193]
11	Alkylsilane functionalized MOF (UiO-66-OH) films	Hydrocarbon	Nanohierarchical		73.9 nm	~ 112	[194]
12	Alkyl-modified SURMOF (UiO-66-NH ₂) films	Hydrocarbon	Nanohierarchical		31.4 nm	154.2	This work
					62.4 nm	155.3	
				~ 1 μm		164	
						~ 166.7	

The WCA values observed for C18@SURMOF samples are significantly higher than those found on other hydrocarbon-terminated surfaces, such as polyethylene (96°) [195], self-assembled monolayers on Au-substrates (Au-SAMs) made from alkanethiols (109°–112°) [196], alkylsilanes (80°–120°) [197], and polysiloxanes (107°) [198], which are commonly used to achieve hydrophilic and hydrophobic surfaces [199-201]. Despite the higher roughness of the present samples (30 nm) compared to other systems (sub-10 nm), the WCA values are larger than any other substrate with low roughness (below 100 nm) reported in the literature. This strongly suggests an unusual mechanism yielding superhydrophobicity.

This conclusion is supported by comparisons with two similar, recently studied similar substrates. First, an alkylsilane-modified MOF thin film with a

roughness of 73.9 nm exhibited only moderate hydrophobicity, with a WCA of 112° [194]. Second, superhydrophobic films made from MOF powder with significantly higher roughness, in the micrometer range, achieved WCA values of 156° [202]. While this is comparable to the 154.7° observed for our low-roughness films, it is notably lower than the 165°, which was observed in our rough (1 micrometer roughness) C18@SURMOF substrate.

Additionally, the WCA values of C18@SURMOF thin films exceeded those of fluoroalkylsilane-coated boehmite transparent thin films, which have roughness (R_a) of approximately 100 nm and reported WCAs of 150° [192].

The findings consistently suggest an unusual microscopic origin of superhydrophobicity observed for the C18@SURMOF substrates. A key difference from conventional SAM/Au systems is the spacing of the hydrocarbon chain anchoring sites. As indicated schematically in Scheme 13, for SAMs on Au(111), this spacing is approximately 0.4 nm [172], resulting in tight packing that forces the chains into an all-trans conformation. In contrast, the SURMOF outer surfaces have nearly double the chain spacing, which provides greater flexibility for the individual hydrocarbon chains. This suggests that the unexpected superhydrophobicity observed is likely due to entropic effects rather than static energy, a hypothesis supported by MD simulations.

To verify the hypothesis that entropic effects are responsible for the superhydrophobicity observed, we conducted a comprehensive series of MD simulations, following previously established protocols [158, 168, 203]. For the SURMOF-based system, the simulations involved anchoring C18 hydrocarbons to the grid points defined by the NH_2 groups exposed on the [001] surface of the SURMOF. Wetting simulations were then carried out by placing a water droplet on various substrates. For the C18@SURMOF substrate, the theoretical results showed strong hydrophobic interactions with WCA values of 165°, fully aligning with the experimental findings.

To validate our theoretical approach, a number of additional MD simulations were performed for reference systems. For alkanethiolate-based SAMs on Au(111), we obtained a contact angle of 108° , consistent with previously reported experimental and theoretical values [172]. For the pristine, bare SURMOF, a low WCA angle of 16° was observed in the simulations, in line with the expected behavior for a metal oxide cluster-terminated surface (Figure 36 (a)). In this case, snapshots of the wetting simulations showed that parts of the water droplet actually penetrate into the UiO-66-NH₂ SURMOF, whereas for C18@SURMOF the droplet was repelled from the surface, maintaining its spherical shape (Figure 38).

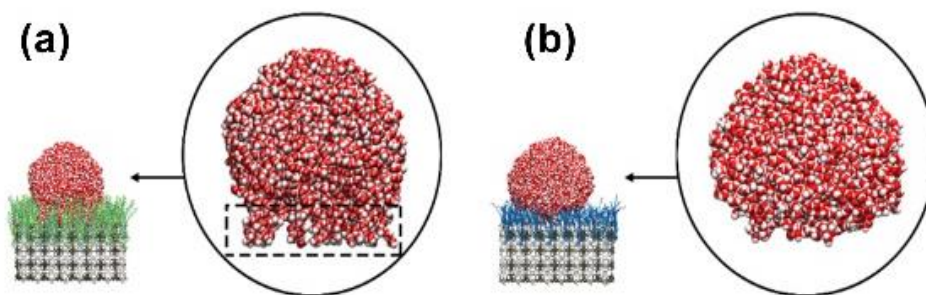


Figure 38 – Snapshot of conformations of the water droplets on the grafted SURMOF with (a) perfluorinated hydrocarbons and (b) C18 hydrocarbons. The dashed region corresponding to the wetting on perfluorinated hydrocarbons exhibits pin-and-plug patterns, mixing with CF chains, whereas in the case of CH chains, the water droplet maintains its spherical shape.

After confirming that the simulations accurately reproduce the experimental findings, we turned our attention to understanding the microscopic origins of this unusual hydrophobicity. A detailed analysis confirmed earlier findings for SAM@Au case, showing that the lowest energy state features alkyl chains rigidly packed into an array of all-trans chains tilted by 30° , with a low density of gauche conformations. Interestingly, in such SAMs on Au, an order-disorder transition occurs in the outermost segments at elevated temperatures above 80°C [204]. This pre-melting can be described by the introduction of gauche defects at the ends of the chains.

In pronounced contrast, for the case of C18@SURMOF, the simulations reveal that the hydrocarbon chains adopt a coiled structure with an increased density of gauche defects, reaching 2.89 per hydrocarbon chain. This value is nearly as high as in the high entropy state of free C18 hydrocarbon tangles solvated in a poor solvent like ethanol [204]. Due to the repulsive interaction with the water droplet, these grafted C18 "brushes" become distorted, forming dimples. This structural deformation upon contact with water leads the hydrocarbon chains to adopt a more stretched configuration, incurring an entropy penalty. In this process, the coil-like hydrocarbon chains sacrifice their flexibility to accommodate the water droplet. Such dimples were not observed in the SAM@Au films, as the hydrocarbon chains there are already fully stretched and tightly packed before water droplet deposition.

Therefore, we concluded that entropy contributions are responsible for the significant difference in wetting behavior between the spaced-out hydrocarbon chain arrays on SURMOF substrates and the rigidly packed arrays on SAMs on Au. This conclusion is supported by the observation that fluorination reduces the large WCA angles. In the case of C18F@SURMOF, the energy cost of forming gauche defects in perfluorinated chains is high, preventing the coiling necessary for the superhydrophobicity seen in C18@SURMOF.

Entropic penalties associated with the stretching of hydrocarbon chains have been previously discussed for polymer brushes in non-aqueous environments [205-207]. Notably, Dimitrov *et al.* observed dimple formation when chains in a high entropy state interacted with a poor solvent. The protrusions seen here with water (a poor solvent) align well with their findings. The significant role of entropy in the wetting of similar systems, such as large polymer brushes, was also highlighted by Mensink *et al.* [154]. Although their simulations involved significantly more segments (~1000) compared to ours (18), the key conclusions from their study are applicable to our system as well. As illustrated in Figure 29 and Figure 30, despite being a poor solvent, water partially penetrates the arrayed

hydrocarbons, thereby limiting the conformational space available to the polymer chains.

To enable a quantitative comparison, we calculated the conformational entropy for SAM@Au, C18@SURMOFs, and C18F@SURMOFs applying the formula $S = -\sum_i p_i \ln p_i$, where p_i corresponds to the occurrence frequencies of conformers in Ramachandran plots (Figure 31). The entropies were found to be $S = 5.3k_b$, $6.47k_b$, and $6.97k_b$ for the SAM, C18F@SURMOF, and C18@SURMOF, respectively. The highest conformational entropy was observed for C18F@SURMOF films, consistent with the fact that the interaction with the “poor solvent” water leads to the largest water contact angles. In the case of C18F@SURMOF, forming gauche defects in CF chains incurs a significantly higher energy penalty than in CH chains, aligning most CF groups into a trans conformation. Consequently, the entropic influence is much smaller, as shown in Figure 38 and Figure 31. The lower density of gauche defects also results in an increased adlayer thickness (+ 0.4 nm) for the perfluorinated case (Figure 36 and Figure 29). Unlike the Cassie-Baxter wetting state, water molecules can penetrate between CF chains to reach the underlying SURMOF, resulting in wetting in the Wenzel state [208]. Here, water forms pin-like structures that plug into CF bushes (Figure 38), consistent with previous reports on a planar substrate [168]. As a result, the less flexible CF chains, with lower intrinsic entropy, mix better with water, leading to a contact angle reduction to around 120° on the fluorinated SAM on the SURMOF surface.

In addition to the described experiments, superhydrophobic UiO-66-NH-C18 was also synthesized on highly porous α -alumina substrates to explore its potential application in water treatment, particularly for cleaning water from oils. This preparation aimed to assess the robustness and effectiveness of the superhydrophobic films on a porous support. XRD analysis (Figure 39 (a)) indicated that there were no changes in crystallinity during the PSM from UiO-66-NH₂ SURMOF to UiO-66-NH-C18 SURMOF, suggesting that the structural

integrity of the MOF was maintained throughout the modification process. WCA measurements (Figure 39 (b)) demonstrated a significant transformation, with the surface of the membrane transitioning from superhydrophilic to superhydrophobic. This marked change in wettability is crucial for the intended application, as it indicates that the modified membrane can effectively repel water while potentially allowing for the separation and removal of oil contaminants, showcasing its promise for future water treatment technologies.

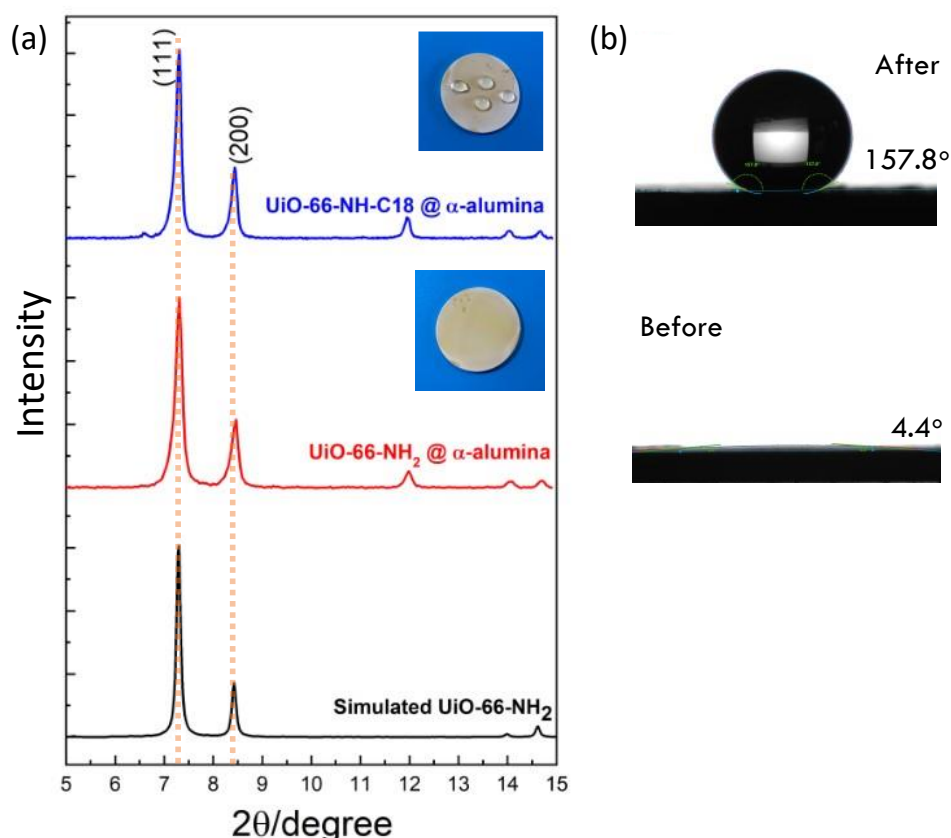


Figure 39 – (a) XRD patterns and (b) WCA data for the pristine SURMOF UiO-66-NH₂ and the modified UiO-66-NH-C18 on α -alumina substrate.

In summary, MD simulations demonstrate the hydrophilic, hydrophobic characteristics of pristine SURMOF, C18F@SURMOF, and C18@SURMOF, respectively. The non-adhesive superhydrophobic behavior of C18@SURMOF arises from the high intrinsic entropy of the C18 hydrocarbon chains grafted at distances defined by the MOF lattice. Long-term experiments showed that this

non-adhesive superhydrophobicity remained stable on a low-roughness interface, with no significant changes in contact angle observed even after 90 days.

4.4 Conclusion

This study reports the successful fabrication of low-roughness superhydrophobic substrates by grafting C18 hydrocarbon chains onto UiO-66-NH₂ MOF thin films. The original SURMOFs, which exhibited strong wetting (contact angles under 11°), transformed into superhydrophobic surfaces after post-functionalization, displaying water contact angles exceeding 150°. The current approach allowed to combine superhydrophobicity with low water adhesion forces while maintaining nanometer roughness. Molecular dynamics simulations revealed that the high entropy state of the coiled C18 hydrocarbons is the primary factor behind this remarkable water repellency. This entropic effect is absent in UiO-66-NH₂ substrates functionalized with less flexible fluorinated compounds, resulting in significantly lower water contact angles of 123° [176].

Additionally, the study found that adjusting the roughness of the SURMOFs could control water adhesion strength. Low roughness levels (31.4 nm) led to higher adhesion strengths, evidenced by significant differences between advancing and receding contact angles and in the water adhesion forces ($16.4 \pm 4.2 \mu\text{N}$ vs $106.3 \pm 5.4 \mu\text{N}$). Conversely, increasing roughness within the nanometric range significantly reduced contact angle hysteresis and decreased adhesion strength by nearly an order of magnitude.

Given the variety of surface structuring techniques available for SURMOFs, such as photo- and e-beam lithography, these newly functionalized surfaces are well-positioned to significantly influence the development of hydrophilic/hydrophobic nano- or micro-structured surfaces [209]. Moreover, the emergence of superhydrophobic substrates with low adhesion strength suggests numerous potential applications, particularly in the fabrication of self-cleaning surfaces [157, 210].

5 Chapter V. Optimized Detection of Volatile Organic Compounds Utilizing Durable and Selective Arrays of Tailored UiO-66-X SURMOF Sensors

5.1 Introduction

Porous materials have emerged as highly effective for the development of sensors targeting volatile organic compounds (VOCs). The adsorption of gas-phase molecules by these materials can be monitored using a variety of techniques, including gravimetric, optical, and electrical methods [211-214]. Among these porous materials, MOFs stand out due to their exceptional surface areas, significant pore sizes and volumes, and versatile structural properties [66, 215, 216]. These attributes, coupled with their relatively straightforward theoretical modeling, make MOFs attractive for numerous applications, notably in sensing.

For sensor applications, the use of monolithic MOF thin films with well-defined structures is particularly advantageous. Surface-anchored MOFs produced via layer-by-layer (LbL) techniques offer notable benefits [63, 217]. Prior research has demonstrated the efficacy of single compound MOF films and MOF arrays in detecting and distinguishing pure single-component gases, vapors, and liquids [218-220]. Nonetheless, the reliable detection of complex multicomponent gas mixtures remains a challenge.

Electronic nose (E-Nose) systems, which utilize sensor arrays made from various MOF types, have shown promise in this area. These arrays' multidimensional responses can be analyzed using machine learning (ML) methods such as principal component analysis, linear discriminant analysis (LDA), and k-nearest neighbor (k-NN) [221]. E-Nose sensors are molecular systems capable of distinguishing several similar molecules, including enantiomers [195-197].

This chapter explores the use of gravimetric E-Nose sensors based on QCM arrays to differentiate various VOCs. The QCM not only serves as a sensor

readout but also plays a role in monitoring and optimizing the synthesis of UiO-66-NH₂ SURMOF within a Teflon liquid cell equipped with a pump system at elevated temperatures [100]. Machine learning techniques are then applied to interpret the multidimensional sensor responses and quantify the relative concentrations of different VOCs.

Previous studies on QCM-based sensor arrays using various MOFs have achieved notable results in detecting odor molecules, essential oils, and VOCs [222-226]. However, real-world applications often encounter issues related to MOF instability under humid conditions [227-231]. For instance, MOFs like HKUST-1 exhibit changes in morphology and framework integrity when exposed to moisture [232], which can detrimentally affect their performance in applications such as CO₂ gas separation.

UiO-66-NH₂ MOFs are particularly well-suited for these applications due to their remarkable chemical, thermal, and architectural stability, attributed to robust Zr–O bonds. Traditional MOF forms, such as powders, are not ideal for fabricating gravimetric sensors and other application fields [63]. Our research group has pioneered the deposition of structurally well-defined UiO-66-NH₂ SURMOFs on various substrates, followed by stability assessments and their application in hydrogen separation [108, 117]. The primary amine group in UiO-66-NH₂ facilitates postsynthetic modification [233], allowing for conversion to functional groups like azide (N₃) or chloride (Cl), thereby creating a wide array of multifunctional SURMOFs with high sensing performance for specific target gases or liquids.

In this study, we synthesized three highly stable UiO-66-X (X = NH₂, Cl, and N₃) SURMOFs for E-Nose applications and employed them to distinguish eight VOCs in the gas phase. Utilizing three statistical models – LDA, k-NN, and neural network analysis (NNA) – we achieved discrimination accuracies exceeding 95% for concentrations between 50 and 100 ppm, with near-perfect accuracy at higher concentrations.

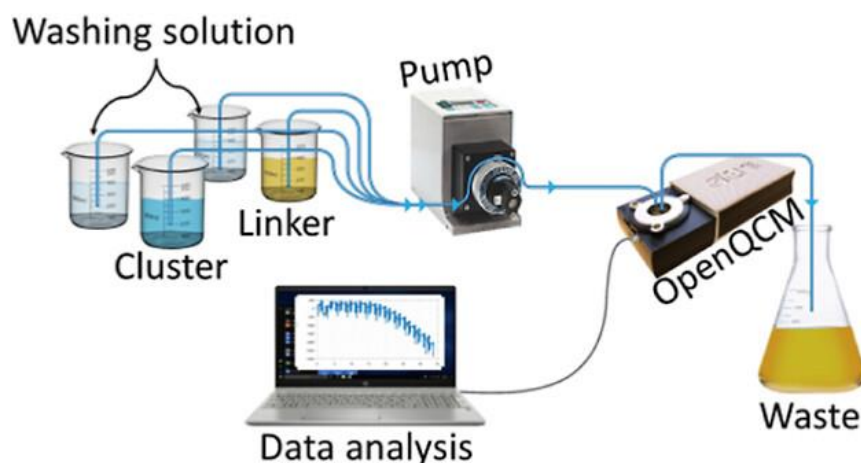
5.2 Experimental section

All operations and control using the openQCM system were performed by Dr. S. Okur (KIT, IFG).

5.2.1 Synthesis of UiO-66-NH₂ via flow-cell using openQCM-D

The UiO-66-NH₂ SURMOF was grown on the functionalized gold-coated QCM sensor substrates using a LbL method. A commercial openQCM-D (Novatech, Italy) equipped with a Teflon liquid cell and DMF-stable Kalrez-type O-rings (DuPont, USA) served as the reactor. An integrated temperature sensor within the sensor module was used to monitor the temperature, while a homemade on/off heater installed beneath the sensor allowed for precise temperature control during operation. A peristaltic pump (Ismatec, Wertheim, Germany) facilitated the flow of solutions.

Initially, 1 mL of metal ion solution was introduced into the liquid cell, allowing a one-hour reaction period with the functionalized surface. Subsequently, the cell was flushed with 5 mL of DMF to remove any unreacted metal ion clusters. Following this, the cell was filled with 1 mL of MOF linker solution, with a 45-minute interval for the linker molecules to interact with the remaining reacted Zr clusters on the surface, completing the reaction and functionalizing the surface. The SURMOF layer deposition cycle concluded with a final rinse of pure DMF to clear out any unreacted linker molecules (Scheme 16). A total of 26 deposition cycles were performed to grow the SURMOFs. The entire synthesis process and data acquisition were managed by a MATLAB 2021B software in combination with Python.



Scheme 16 – A schematic illustration of the working principle of the one-channel openQCM for SURMOF synthesis. *Reprinted with permission from [234]. Copyright 2024 American Chemical Society*

5.2.2 Post-synthetic modification to UiO-66-N₃ and UiO-66-Cl

A Sandmeyer reaction-type [235-237] two-step procedure was applied to refunctionalize the amino groups in UiO-66-NH₂ SURMOF-coated QCM sensors, converting them into the corresponding azide (UiO-66-N₃) or chloride (UiO-66-Cl) versions. Reaction parameters were optimized by Dr. P. Hodapp (KIT, IBG3-SML) and Prof. Dr. S. Bräse (KIT, IBCS-FMS & IOC).

First Step: Diazonium Salt Formation.

The diazonium salt-functionalized SURMOF was synthesized through the diazotization of a UiO-66-NH₂ SURMOF-coated QCM crystal sensor. Initially, a solution of 500 mg of sodium nitrite (7.23 mmol) in 15 mL of deionized water was cooled to 0 °C, followed by the gradual addition of 3 mL of 6 M HCl. While maintaining a temperature of 0 °C and continuous slow stirring, the UiO-66-NH₂ SURMOF-coated QCM crystal was immersed in the solution for 15 minutes using a custom-machined PTFE holder. This holder ensured the SURMOF-coated surface was exposed to the solution while keeping the QCM crystal steady and preventing mechanical damage to the SURMOF layer. After immersion, the SURMOF-coated QCM sensor was carefully rinsed with deionized water and

then placed in a beaker with deionized water for 1 minute. Following a second rinse with deionized water, the diazonium salt-functionalized SURMOF was immediately used for the subsequent reaction step without further treatment or drying.

Second step: A. Modification to UiO-66-N₃

The diazonium-salt-functionalized SURMOF-coated QCM sensor was placed in a solution containing 1.30 g of sodium azide (20.0 mmol) in 20 mL of deionized water cooled to 0 °C, using PTFE holder, for 5 minutes under slow stirring. The ice bath was then removed, allowing the solution to gradually warm to room temperature. After two hours, the QCM sensor was taken out of the solution, rinsed with deionized water, immersed in a beaker of deionized water for 2 minutes, and then rinsed again. Excess water was carefully removed using a nitrogen gas stream, and the sensor was dried in an oven at 40 °C overnight.

Second step: B. Modification to UiO-66-Cl

The diazonium-salt-functionalized SURMOF-coated QCM sensor was placed in a suspension containing 1.98 g of copper(I) chloride (1 mol/L) in 20 mL of deionized water cooled to 0 °C, using PTFE holder, under slow stirring. The ice bath was removed, allowing the solution to gradually warm to room temperature. After two hours, the QCM sensor was taken out of the solution, rinsed with deionized water, immersed in a beaker of deionized water for 2 minutes, and then rinsed again. Excess water was carefully removed using a nitrogen gas stream, and the sensor was dried in an oven at 40 °C overnight.

5.2.3 Gas Delivery System and VOC Measurements

The Teflon liquid cells from the openQCM-D system, initially utilized for high-temperature SURMOF synthesis, were also utilized for VOC testing in gaseous environments. Figure 40 illustrates our custom-made four-channel

QCM-type E-Nose experimental setup for VOC measurements, featuring three functionalized UiO-66-X SURMOFs and a gas delivery setup.

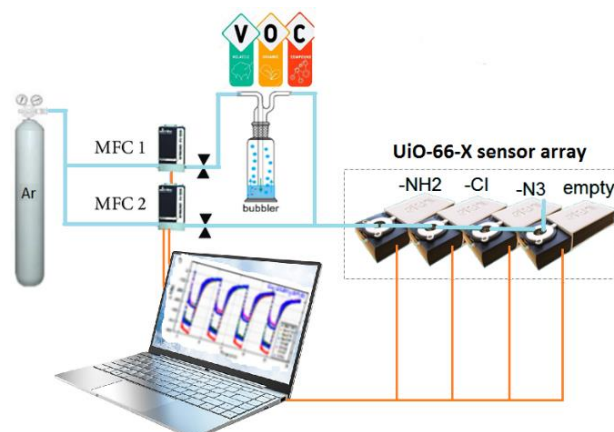


Figure 40 – QCM type E-Nose experimental setup for VOC measurements with three functionalized UiO-66-X SURMOFs (X: NH₂, N₃, and Cl). *Reprinted with permission from [234]. Copyright 2024 American Chemical Society*

The test setup comprised four interconnected openQCM Teflon cells using Teflon tubes (1 mm diameter). Three of these units were allocated for the functional UiO-66-X sensors (X: NH₂, N₃, and Cl), while the fourth unit housed a bare QCM sensor with a gold surface, serving as a control channel. Two mass flow controllers were connected in parallel between the argon (Ar) source and the test cell. One controller purged the test cell with Ar to remove VOC residue and regulated the Ar flow during VOC concentration dilution. The other controller determined the flow rate passing through the liquid inside the VOC bubbler, transporting saturated VOC gas just above the surface into the test cell. The VOC concentration inside the test cell was calculated by multiplying the saturated concentration value with the ratio of the flow rates from these two mass flow readings. The saturated concentrations of each gas were determined using well-established Antoine parameters [238] at room temperature (20 °C). Throughout the VOC test measurements, the temperature remained constant to minimize small temperature fluctuations.

To assess the QCM data, including SURMOF deposition and sensing, the Sauerbrey equation was employed. This equation enables the calculation of the mass change of the thin film during UiO-66-NH₂ synthesis or the quantity of VOC gas absorbed by the SURMOF when exposed to the respective gases.

Two sets of gas phase adsorption measurements were conducted for eight VOCs, including water vapor, ethanol, cyclohexane, 2-propanol, methanol, p-xylene, toluene, n-hexane. The first measurement involved high concentrations of eight targeted VOC analytes at their respective saturated pressures, as detailed in Table 4. Each VOC gas was introduced into the gas test cell for 10 minutes for adsorption, followed by a 10-minute purge with inert Ar gas for desorption. These adsorption and desorption cycles were repeated four times to assess repeatability. For the second measurement, six different low VOC concentrations (10, 15, 25, 50, 75, and 100 ppm) were utilized to determine the detection limit of the functional UiO-66-X SURMOF sensor films. In this instance, the gas injection time remained at 10 minutes for adsorption, but the Ar rinsing time was extended to 20 minutes for desorption to evaluate the sensor response time.

Table 4 – Calculated concentrations under saturated pressures of eight VOCs used for gas adsorption measurements at room temperature (25 ° C)

VOCs	C _{sat} (ppm)
Ethanol	68,776.3
Water	23,531.6
Cyclohexane	117,210.5
2-propanol	50,684.2
Methanol	150,328.9
p-xylene	12,907.9
Toluene	27,631.6
n-hexane	182,381.6

5.2.4 Data analysis

The entire setup control, data acquisition, and analysis of E-Nose data were managed using a MATLAB 2021B by Dr. S. Okur (KIT, IFG). Two standard supervised ML algorithms: LDA [239, 240] and k-NN [224, 241], as described in previous work [224, 240, 241], were utilized for classifying the sensing data in E-Nose discrimination analysis. Specifically, data points in the saturated region (highest response region) of the adsorption-desorption curves were utilized to enhance accuracy during data analysis. A 10-fold cross-validation procedure was implemented for the classification analysis, with 90% of the total observations allocated to the training set and the remaining 10% for testing discrimination accuracies. The results were presented as a confusion matrix to illustrate the discrimination analysis outcomes of LDA, k-NN, and NNA models.

5.3 Results and discussion

5.3.1 Synthesis of UiO-66-NH₂ SURMOF Films with the Layer-by-Layer Method Using a High-Temperature QCM-D Liquid Cell.

The synthesis parameters, including temperature, injection and exposure times, flow rates, metal ion/cluster concentration, organic linker, and rinsing solutions, have a direct impact on the growth kinetics of UiO-66-NH₂ SURMOF films. The growth of these films on MUD SAMs was monitored using a QCM. Figure 41 illustrates the typical time-dependent synthesis kinetics of UiO-66-NH₂ SURMOF films employing the LBL method with a high-temperature QCM-D liquid cell at 100 °C. For this setup, a brief injection time of 7.5 seconds was utilized for both the solutions of Zr metal clusters and linker with continuous flow. Between cycles, a 2-minute DMF rinsing was conducted through the MUD-coated QCM substrate inside the liquid cell to expedite SURMOF film formation. Typically, a mass upload of -2100 Hz (37 µg/cm², equivalent to 57.5 µg with a 1.54 cm² Q-Sense QCM substrate surface area) of UiO-66-NH₂ SURMOF was

achieved with 26 cycles. Throughout this synthesis, the temperature remained constant at 100 °C. An incrementally increasing upload was observed during synthesis with each additional LBL cycle. A linear fit yielded a synthesis upload speed of -19.2 Hz/min, totaling -2100 Hz over 26 cycles.

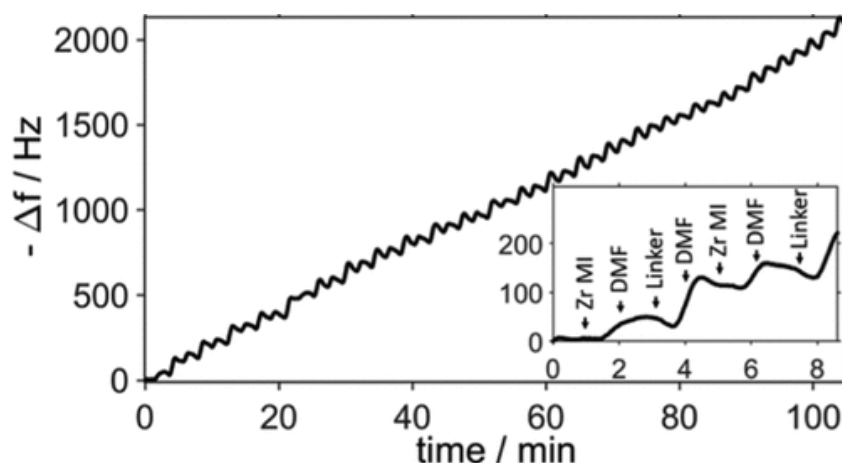


Figure 41 – Typical temperature and time-dependent synthesis kinetics of UiO-66-NH₂ SURMOF films with the LBL method using a high-temperature QCM-D liquid cell.
Reprinted with permission from [234]. Copyright 2024 American Chemical Society

Figure 42 illustrates the structural analysis. In Figure 42 (a), the XRD pattern of the functional UiO-66-X after post-modification shows the exchange of functional groups among NH₂, N₃, and Cl. The XRD peak positions at 7.4° (representing (111)) and at 8.5° (representing (200)) are in complete agreement with the simulations of the previously reported UiO-66-NH₂ bulk structure [100, 117, 123]. SEM imaging was performed to examine the topography of the synthesized sensors. Figure 42 (b) presents SEM images of the top surface, while Figure 42 (c) provides a cross-sectional view for the structural analysis of UiO-66-NH₂ SURMOF films. The SEM surface topography reveals smooth crystalline UiO-66-NH₂ SURMOF films covering the entire QCM surface, with thicknesses approximately between 300 and 500 nm.

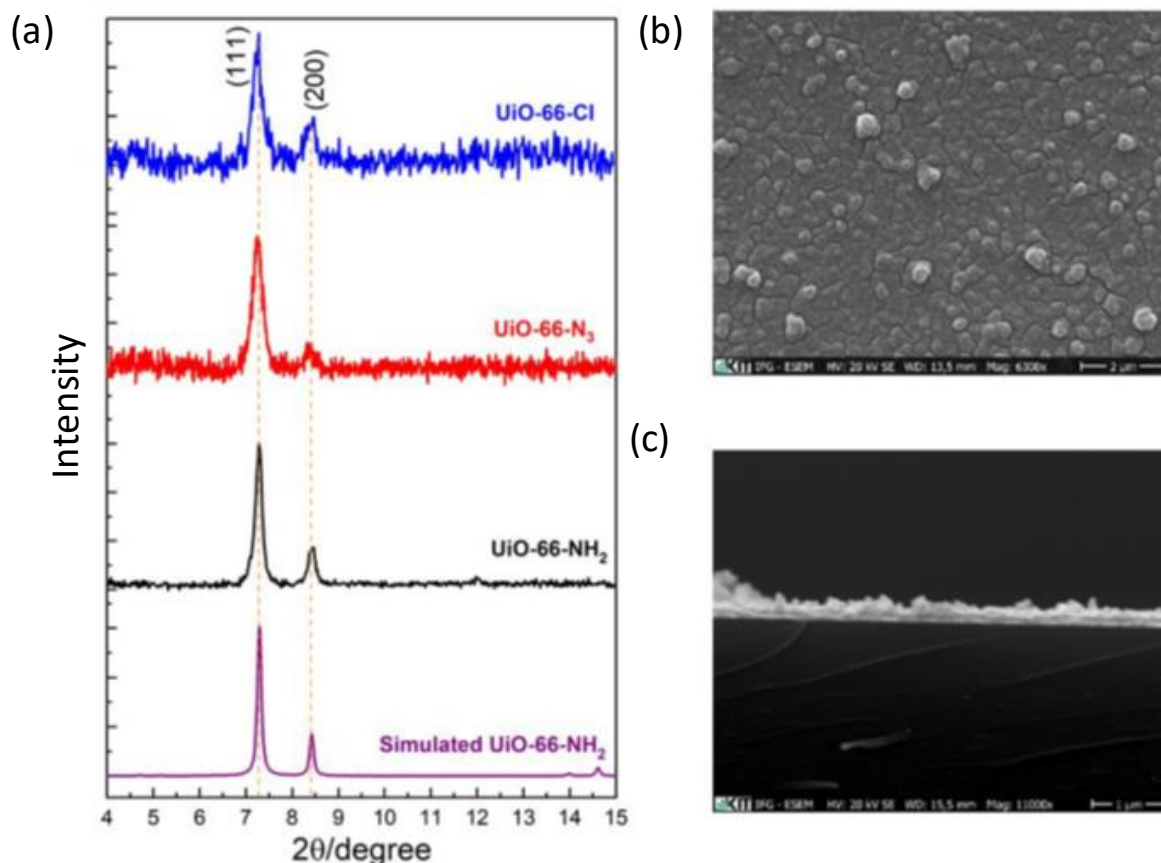


Figure 42 – The structural analysis: (a) XRD pattern, (b) SEM surface topography, and (c) SEM cross section of the functional UiO-66-X after post-modification process. *Reprinted with permission from [234]. Copyright 2024 American Chemical Society*

To verify the effectiveness of the modification process the modified SURMOFs were subjected to a comprehensive characterization utilizing IRRAS. The results clearly confirm the success of the modifications (Figure 43).

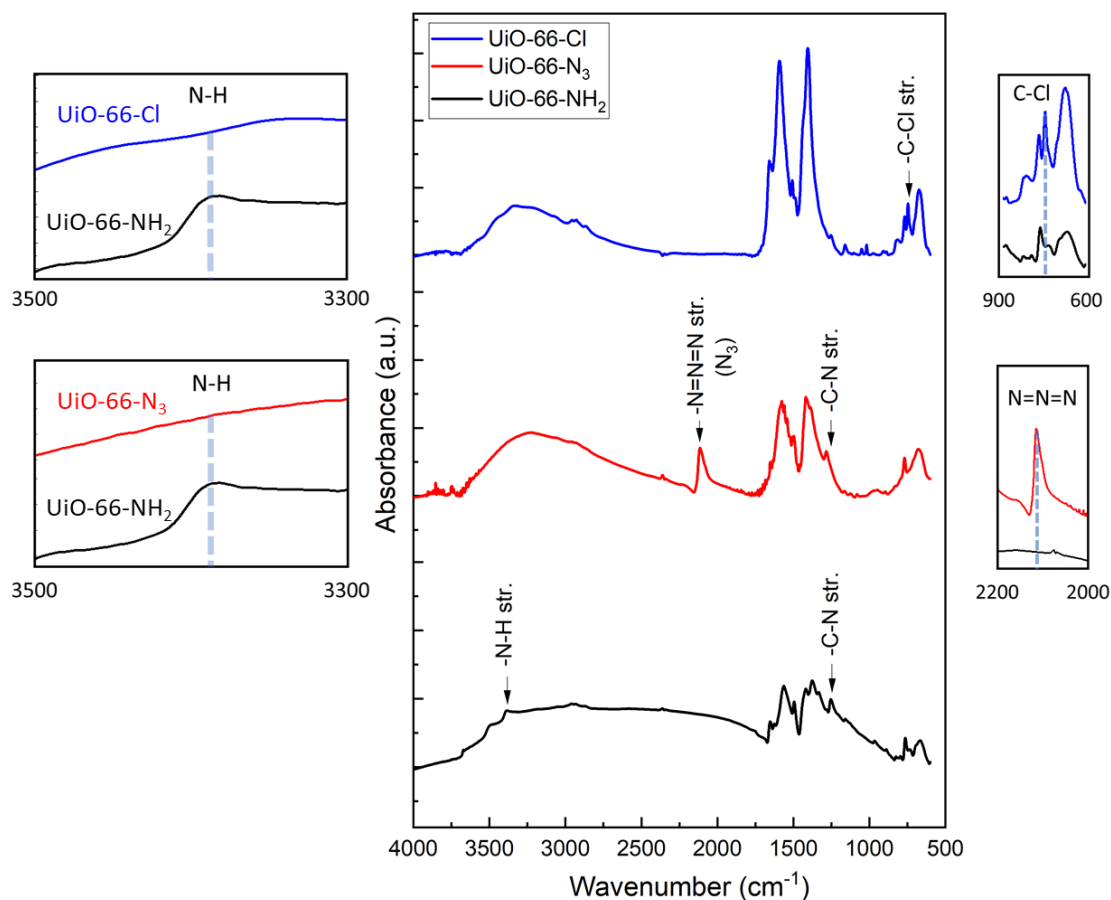


Figure 43 – IRRAS data of UiO-66-NH₂, UiO-66-N₃ and UiO-66-Cl. *Reprinted with permission from [234]. Copyright 2024 American Chemical Society*

5.3.2 Stability test

To assess the stability of our sensors, the modified system was analyzed before and after exposure to saturated hot water vapor under controlled conditions of 90 °C for 120 minutes (Figure 44 (a) and (b)). The results indicate that the system maintains high stability. Although minor changes were observed after exposure, this is attributed to hot water molecules diffusing through the empty pores during prolonged exposure, which are not easily recoverable in a short time. To fully recover the water molecules, the films need to be heated above 100 °C and annealed for a sufficient duration in a nitrogen environment.

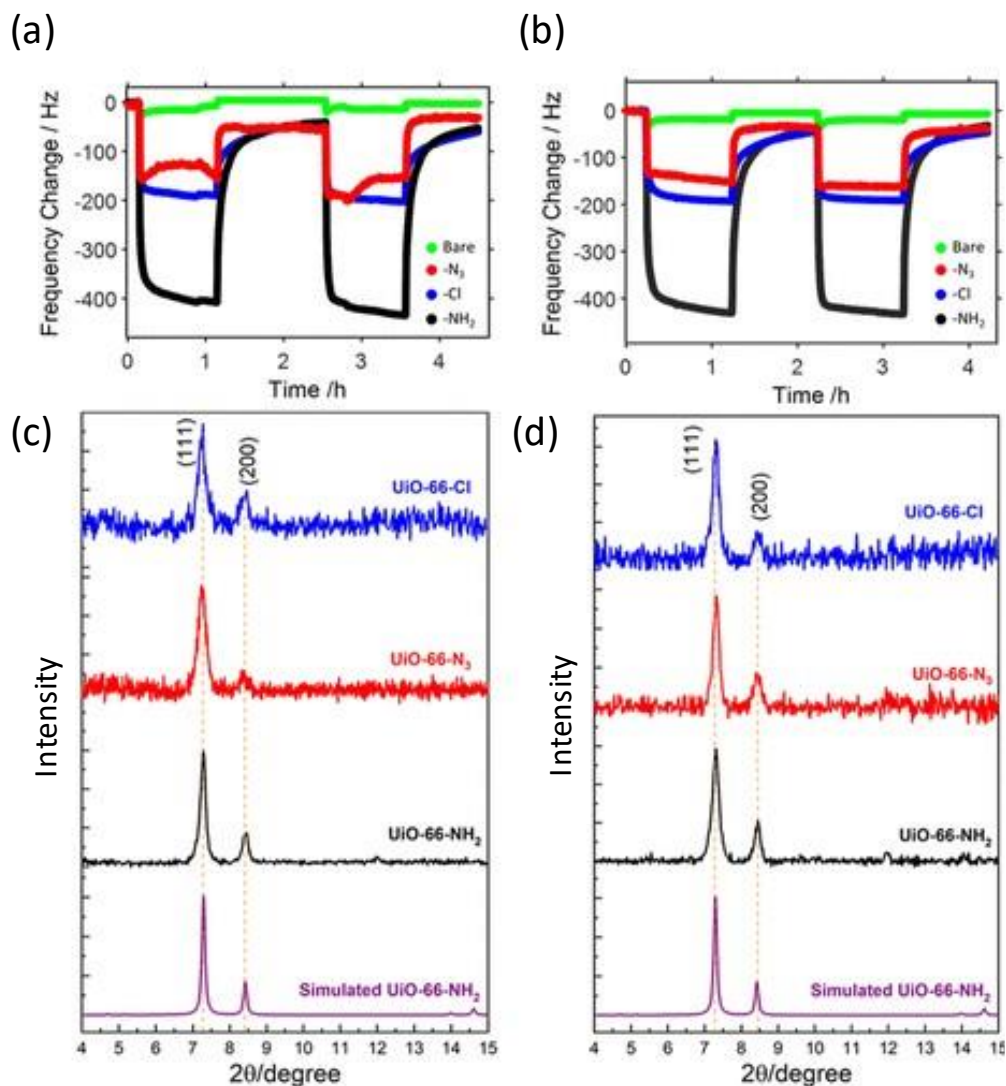


Figure 44 – Ethanol uptake results (a) before and (b) after saturated hot water vapor at relative humidity conditions at 90 °C. XRD results of UiO-66-X (c) before and (d) after a high-humidity test (100% RH at 90 °C). *Reprinted with permission from [234]. Copyright 2024 American Chemical Society*

The mass uptake decreases as the temperature rises due to a lower concentration of water molecules within the cell. This occurs because the relative humidity inside the cell is proportionally linked to the water molecule concentration, which, according to the general gas law, is inversely related to the environmental temperature when pressure and volume remain constant. QCM sensor adsorption tests demonstrate consistent cycles even at elevated temperatures up to 90 °C and under high-humidity conditions up to 100% relative humidity. XRD results before and after high humidity tests (Figure 44 (c),(d))

show that the functionalized UiO-66-X sensors maintain structural stability at high humidity levels. Figure 45 ((a)-(c)) presents uptake results for saturated hot water vapor for UiO-66-X. Additionally, SURMOF retains its crystallinity after exposure to 100% relative humidity at various temperatures as well as HCl/water vapor at 25 °C (Figure 45 (d)).

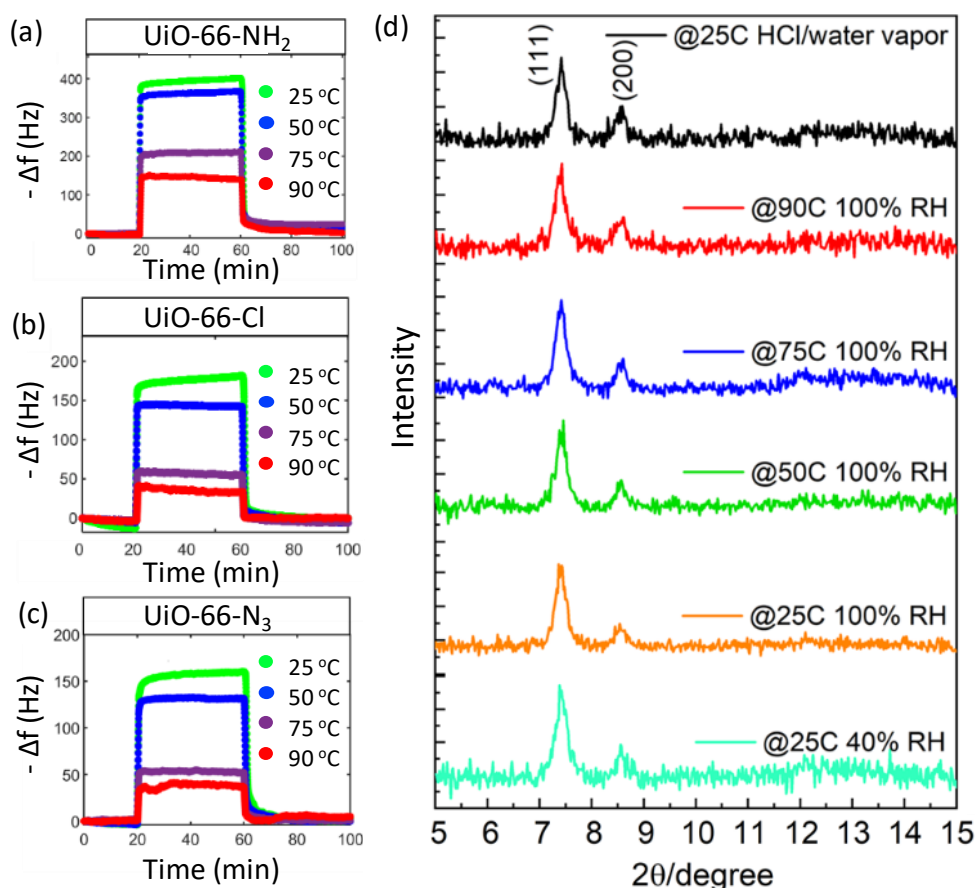


Figure 45 – Uptake results at saturated hot water vapor at relative humidity conditions between 25 and 90 °C for (a) UiO-66-NH₂, (b) UiO-66-Cl, (c) UiO-66-N₃. XRD results of (d) UiO-66-NH₂@QCM sensor after high humidity/HCl test. *Reprinted with permission from [234]. Copyright 2024 American Chemical Society*

5.3.3 Adsorption Measurements under Saturated VOC Concentrations

Eight VOCs were tested at both high and low concentrations. The initial adsorption measurement was conducted at high concentrations under their saturated pressures (Table 4). Each VOC was injected into the gas test cell for 10 min for adsorption, followed by a 10 min flush with inert argon gas for

desorption. This adsorption-desorption cycle was repeated four times to assess repeatability. The second measurement aimed to determine the limit of detection (LOD) [242] for the functional UiO-66-X SURMOF sensor films at low concentrations (10, 15, 25, 50, 75, and 100 ppm). The gas injection time for adsorption was maintained at 10 min for quick testing suitable for practical applications, while the desorption phase involved a 20 min argon rinse.

Figure 46 illustrates the negative QCM frequency changes due to mass uptake on the three functional UiO-66-X SURMOF sensors when exposed to the eight VOCs: X = NH₂ (Figure 46 (a)), X = Cl (Figure 46 (b)), and X = N₃ (Figure 46 (c)). Each analyte underwent four cycles with 10 min adsorption and 10 min desorption phases. The UiO-66-X sensors exhibited a response time of less than 1 min, and the radar plot in Figure 46 (d) shows the maximum sensor responses to each VOC gas.

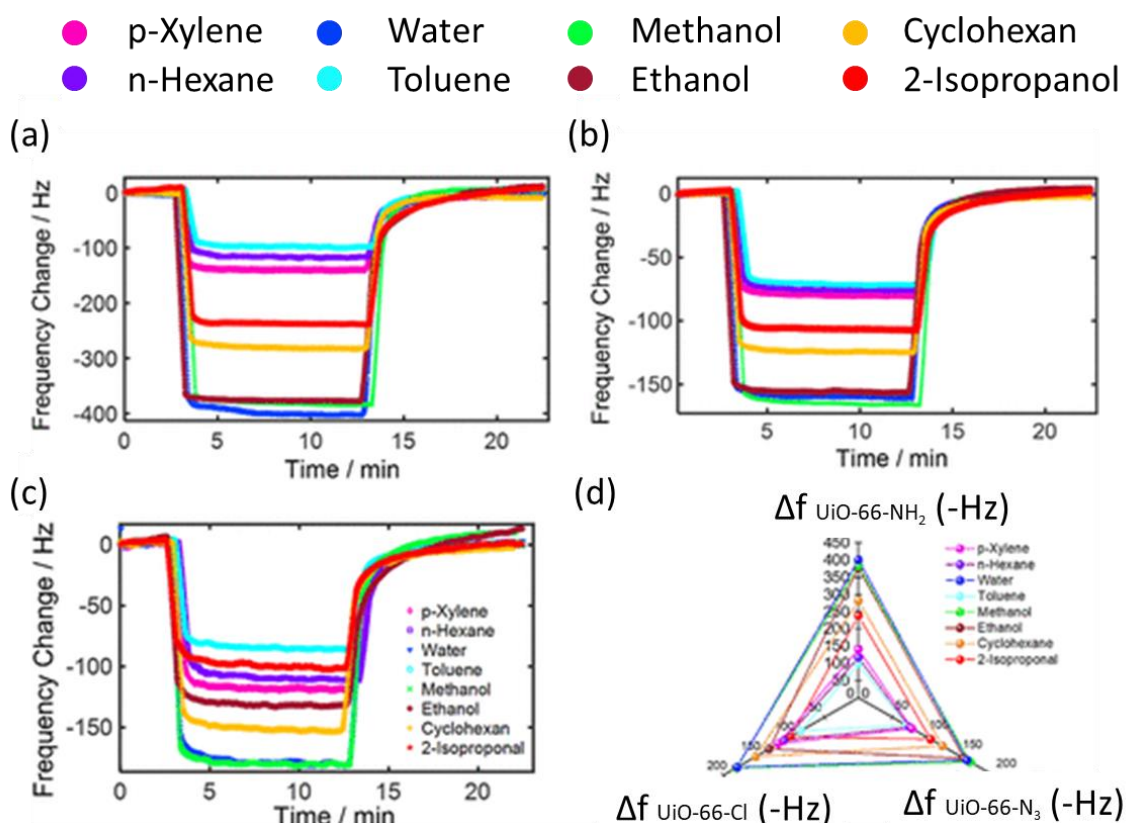
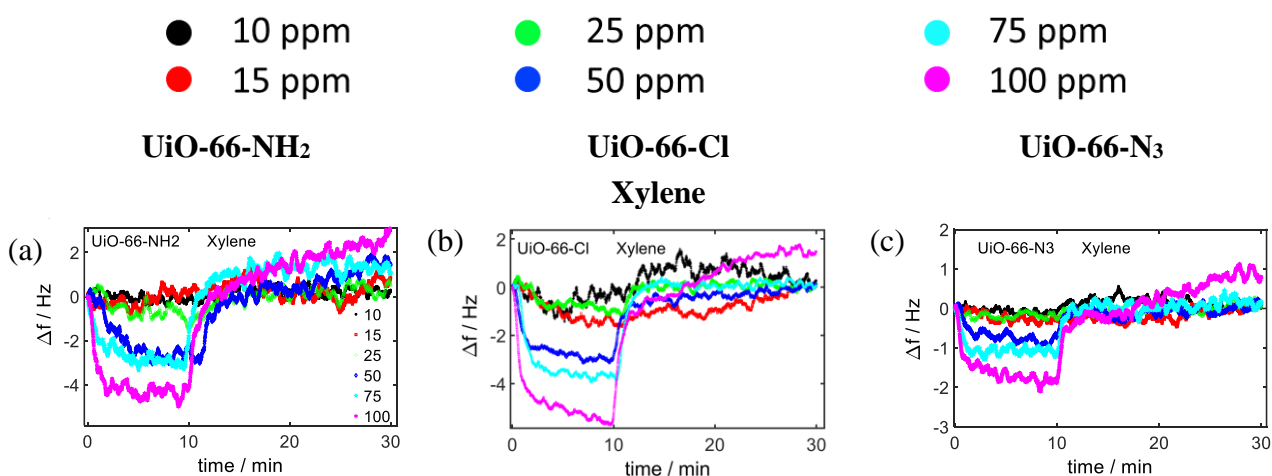


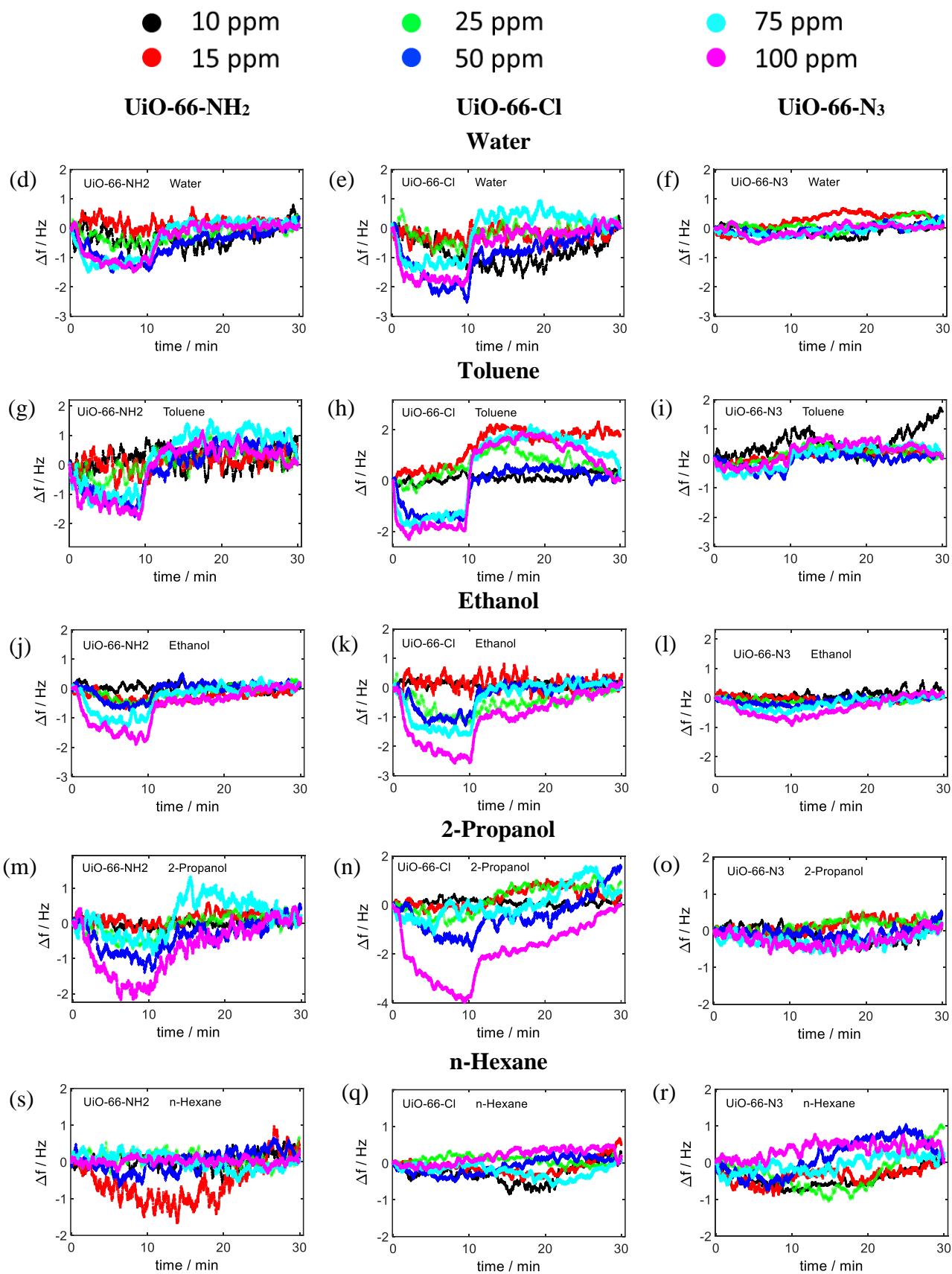
Figure 46 – Negative QCM frequency changes observed due to mass uploads on three functional UiO-66-X SURMOF sensors with X = NH₂ (a), X = Cl (b), and X = N₃ (c) when exposed to VOCs. The radar plot (d) illustrates the maximum sensor responses against each VOC gas. Reprinted with permission from [234]. Copyright 2024 American Chemical Society

The adsorption tests conducted at high concentrations revealed that the sensors had response times of less than 1 min, reaching saturation rapidly and returning to their initial background values within 10 min. The NH₂-functionalized UiO-66-X sensor exhibited responses more than twice as high as those of the N₃- and Cl-functionalized sensors. Among the Cl-functionalized sensors, slightly higher responses were observed compared to the N₃-functionalized sensor. All three sensors showed their strongest responses to water and methanol, while they exhibited lower responses to toluene.

5.3.4 Adsorption Measurements under Low Concentrations (10–100 ppm)

The second set of measurements involved testing the functional UiO-66-X SURMOF sensor films at six low concentrations (10, 15, 25, 50, 75, and 100 ppm) to determine their lowest sensing limit. Gas injection for adsorption was again set at 10 min, while the desorption phase involved an extended 20 min rinse with argon to evaluate sensor response times. Figure 47 depicts the QCM responses of three functional UiO-66-X variants (X = NH₂, X = Cl, and X = N₃) to p-xylene (Figure 47 (a)–(c)), water (Figure 47 (d)–(f)), toluene (Figure 47 (g)–(I)), ethanol (Figure 47 (i)–(k)), 2-propanol (Figure 47 (l)–(n)), *n*-hexane (Figure 47 (o)–(r)), and cyclohexane (Figure 47 (v)–(z)) at concentrations ranging from 10 to 100 ppm.





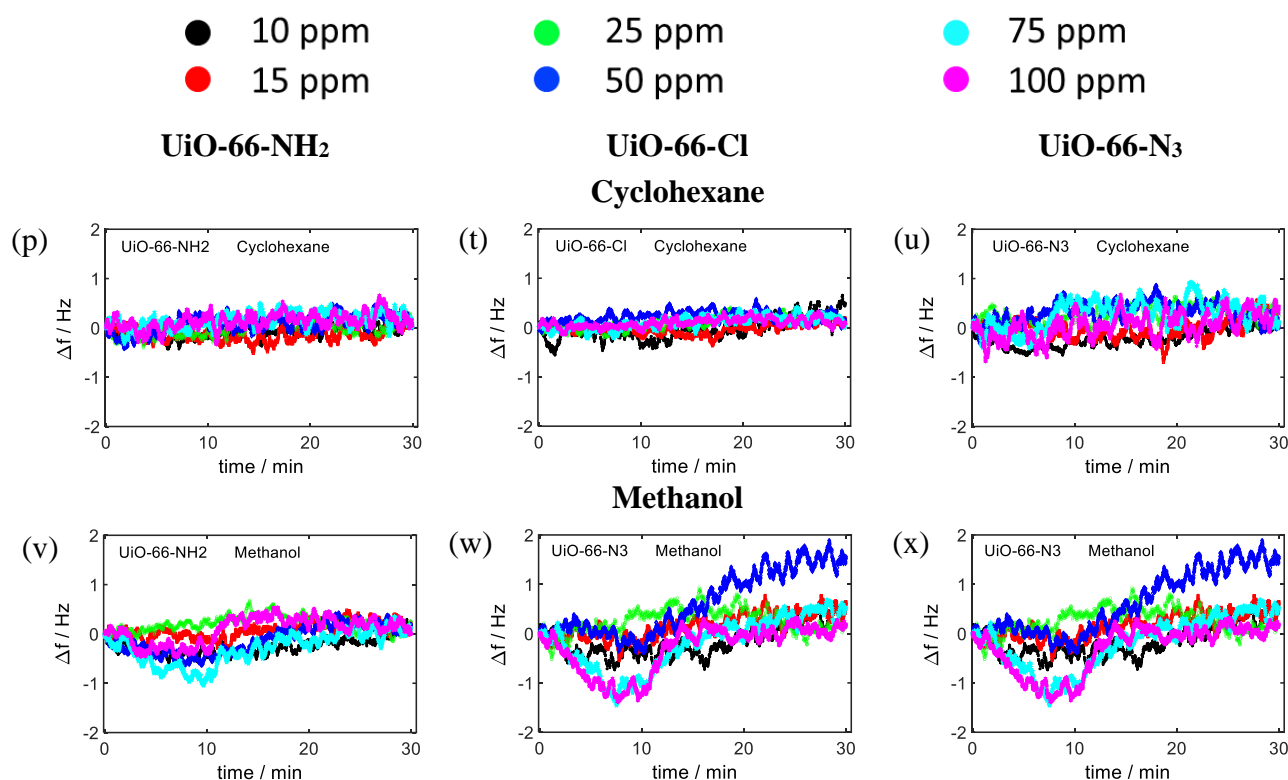


Figure 47 – QCM responses of three functional UiO-66-X with X=NH₂, X=Cl, and X=N₃, against p-xylene (a-c), water (d-f), toluene (g-i), ethanol (j-l), 2-propanol (m-o), n-hexane (p-r), cyclohexane (s-u), and methanol (v-x) at different low concentrations between 10 and 100 ppm. Reprinted with permission from [234]. Copyright 2024 American Chemical Society

The sensitivities of each UiO-66-X sensor are represented by the slopes of the plots depicting QCM frequency changes versus concentration for each sensor's response (Table 5). The slopes varied for each sensor depending on the gas molecules tested and the specific concentrations and functional groups present in the SURMOF material.

Table 5 – The sensor names, the calculated sensitivity (a), and limit of detections (b) of individual sensors

a)	Sensitivity in Hz/ppm							
	<i>2-propanol</i>	<i>Cyclohexane</i>	<i>Ethanol</i>	<i>n-Hexane</i>	<i>Methanol</i>	<i>Toluene</i>	<i>Water</i>	<i>p-Xylene</i>
S1 UiO-66-NH ₂	0.0028	0.0024	0.0055	0.0007	0.0025	0.0036	0.0169	0.0108
S2 UiO-66-Cl	0.0021	0.0011	0.0023	0.0004	0.0011	0.0026	0.0067	0.0060

S 3	UiO-66- N ₃	0.0020	0.0013	0.0019	0.0006	0.0012	0.0031	0.0076	0.0090
b)		Limit of Detection (LOD) in ppm							
		<i>2-propanol</i>	<i>Cyclohexane</i>	<i>Ethanol</i>	<i>n-Hexane</i>	<i>Methanol</i>	<i>Toluene</i>	<i>Water</i>	<i>p-Xylene</i>
S 1	UiO-66- NH ₂	96.0	79.5	105.4	439.3	66.1	131.7	19.0	58.3
S 2	UiO-66- Cl	79.1	115.7	50.7	331.1	287.3	47.3	24.0	25.0
S 3	UiO-66- N ₃	190.8	148.5	191.1	715.7	200.4	82.5	35.5	44.4

The sensitivities of the UiO-66-NH₂ sensor to 2-propanol, cyclohexane, ethanol, n-hexane, methanol, toluene, water, and p-xylene were 0.0028, 0.0024, 0.0055, 0.0007, 0.0025, 0.0036, 0.0169, and 0.0108 Hz/ppm, respectively. Water showed the highest sensitivity at 0.0169 Hz/ppm among all functional UiO-66-X sensors (Table 5 (a)). UiO-66-NH₂ exhibited greater sensitivity compared to other functionalized sensors. The second highest sensitivity was observed for p-xylene (0.0108 Hz/ppm). Sensitivities ranged from 0.0004 to 0.0067 Hz/ppm for UiO-66-Cl sensors and from 0.0006 to 0.0090 Hz/ppm for UiO-66-N₃ sensors. The lowest sensitivity was found for n-hexane (0.0004 Hz/ppm), followed by cyclohexane (0.0011 Hz/ppm) among the UiO-66-Cl sensors. The same UiO-66-X sensor exhibited varying sensitivities depending on the analyte due to different affinities stemming from diverse functional groups. This variability is crucial for distinguishing analytes using machine learning methods such as LDA, k-NN, and NNA.

The LOD for each sensor (Table 5 b) were calculated as three times the standard deviation divided by the sensitivity. The standard deviations of the signals were determined from the baseline values before exposure to analytes began. The average standard deviations were 0.23 Hz for the UiO-66-NH₂ sensor, 0.10 Hz for the UiO-66-Cl sensor, and 0.28 Hz for the UiO-66-N₃ sensor. The UiO-66-Cl sensor achieved the lowest LOD primarily due to its minimal standard deviation. Detection limits varied depending on the type of analyte and were generally around 50 ppm for most VOCs. The LOD values obtained with these

sensors are comparable to those reported for alcohol vapors in Table 6. As mentioned earlier, the mass sensitivity constant C is determined by the fundamental resonance frequency f_0 and the material properties of the quartz crystal. Therefore, LOD not only relies on the affinity of the functional groups in UiO-66-X films but also on the resonance frequency of the underlying QCM oscillator sensors [150, 151]. Thinner QCM oscillator sensors with higher resonance frequencies can potentially lower the LOD to below the ppm level for lower concentrations.

Table 6 – Comparison of LOD of the present sensor with some published sensors for alcohol vapors

Type	Analytes	LOD	Ref.
SURMOF-QCM UiO-66-X E-Nose	MeOH	66-287 ppm	This work
	EtOH	50-191 ppm	
SURMOF inverse opal film	MeOH	10~60 ppm	[243]
	EtOH		
	1-PrOH		
	1-BuOH		
Magnetic nanoemulsion	MeOH	100 ppm	[244]
MOF crystal	MeOH	NA	[245]
Cellulose photonic crystal	EtOH	250 ppm	[246]
	PrOH		
	BuOH		
Porous silicon fiber	PrOH	160 ppm	[247]
QCM HKUST-1	MeOH	158.0 ppm	[248]
	EtOH	140.6 ppm	

5.3.5 E-Nose Discrimination Analysis

The response patterns of functionalized UiO-66-X sensors vary for each VOC, making them distinctive identifiers for different gases suitable for electronic nose

(E-Nose) applications. Discrimination analysis employed three models: LDA [224, 241], which maximizes the ratio of variances between classes and within classes; k -NN [225], utilizing a $k = 10$ nearest neighbor approach where an unknown data point is classified based on its proximity to its 10 nearest neighbors; and NNA [249-252], employing a single hidden layer neural network with 25 nodes, lambda zero, rectified linear unit (ReLU) activation function, and standardized data. E-Nose discrimination analysis was conducted using both adsorption data under VOCs' saturated vapor pressures and at six low concentrations ranging from 10 to 100 ppm.

Data extracted from the saturated region of the adsorption/desorption curves (Figure 48) were utilized for discriminating VOCs in the analysis. A 10-fold cross-validation method was applied for classification, involving 4638 individual observations. Typically, 10% of these observations were reserved for testing, leaving 4175 for the training set and 463 for comparing discrimination accuracies achieved by LDA, k -NN, and NNA models separately.

Figure 48 (a) presents a two-dimensional discriminant plot from LDA analysis, showing a 95% confidence ellipse for eight VOCs, including water, at their saturated vapor pressure concentrations. The LDA model achieved a discrimination of 96.3% in the first component and 3.1% in the second component. Confusion matrix results for the LDA model with 100% test discrimination accuracy are displayed in Figure 48 (b). Similarly, the k -NN model achieved 100% discrimination accuracy, illustrated in Figure 48 (c). The NNA model also demonstrated 100% discrimination accuracy, with its confusion matrix depicted in Figure 48 (d).

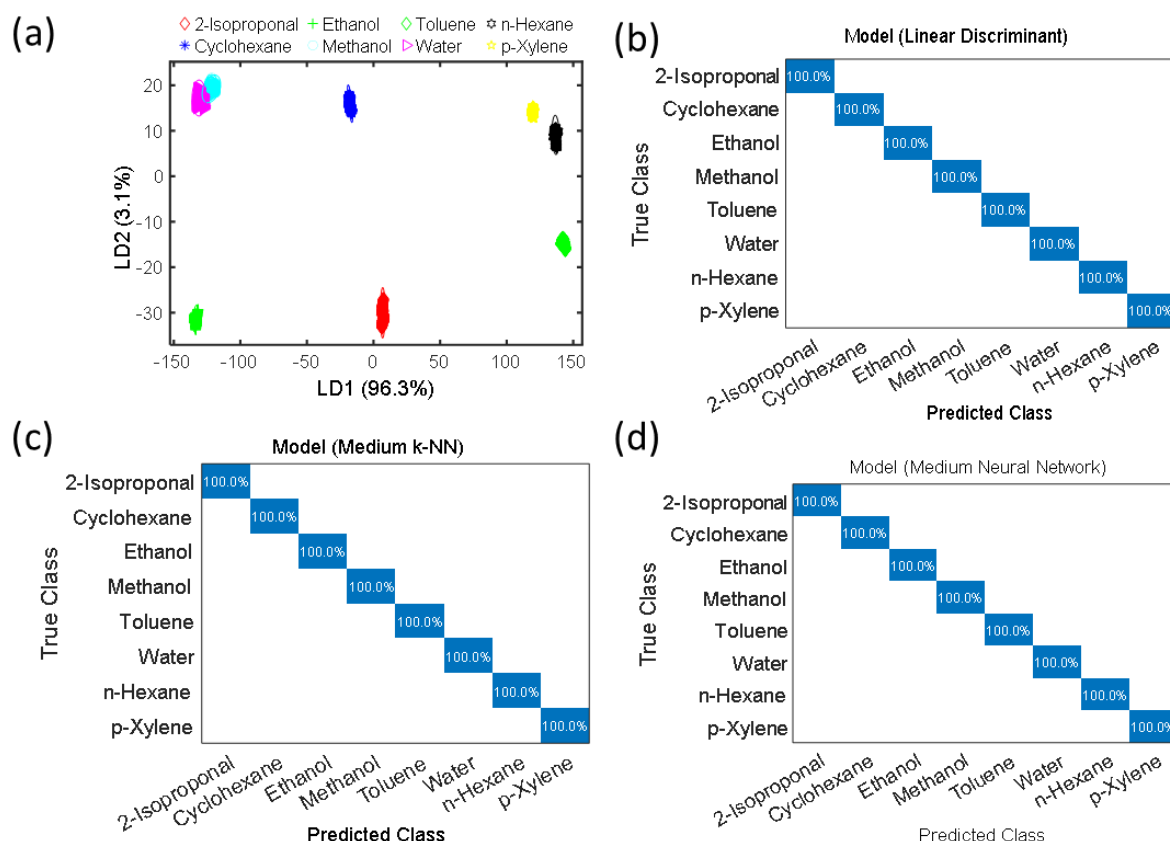


Figure 48 – E-Nose analysis results. (a) Two-dimensional plot of LDA with a 95% confidence ellipse of eight VOCs, including water, at their saturated vapor pressure concentrations. The confusion matrix results of the (b) LDA, (c) k-NN, and (d) NNA models. True classes (Y-axis) represent the already trained (labeled) values introduced to the models and predicted classes (X-axis) are the calculated results by the model. The discrimination accuracy is 100% for all three models. *Reprinted with permission from [234]. Copyright 2024 American Chemical Society*

The functional UiO-66-X sensors ($X = \text{NH}_2$, Cl, and N_3) were also evaluated under six low concentrations (10, 15, 25, 50, 75, and 100 ppm). E-Nose analysis using all three models (LDA, k-NN, and NNA) employed a 10-fold cross-validation method across all concentrations ranging from 10 to 100 ppm. Specifically, each analysis utilized 10 test sets consisting of 1780 observations (1602 for training and 178 for testing). Here, only the analysis results for the E-Nose measurements at 25 ppm and 100 ppm are presented for comparison.

Figure 49 presents the E-Nose analysis of the functional UiO-66-X sensor array at 25 ppm using three models: LDA, k-NN (with $k = 10$), and NNA (with a single hidden layer of size 25 and ReLU activation). In Figure 49 (a), two-

dimensional plots from LDA depict the 95% confidence ellipse of frequency changes for the three functional UiO-66-X sensors across all eight VOC analytes, including water vapor, at 25 ppm. LDA achieved a discrimination accuracy of 88.7%, as shown in the confusion matrix in Figure 49 (b).

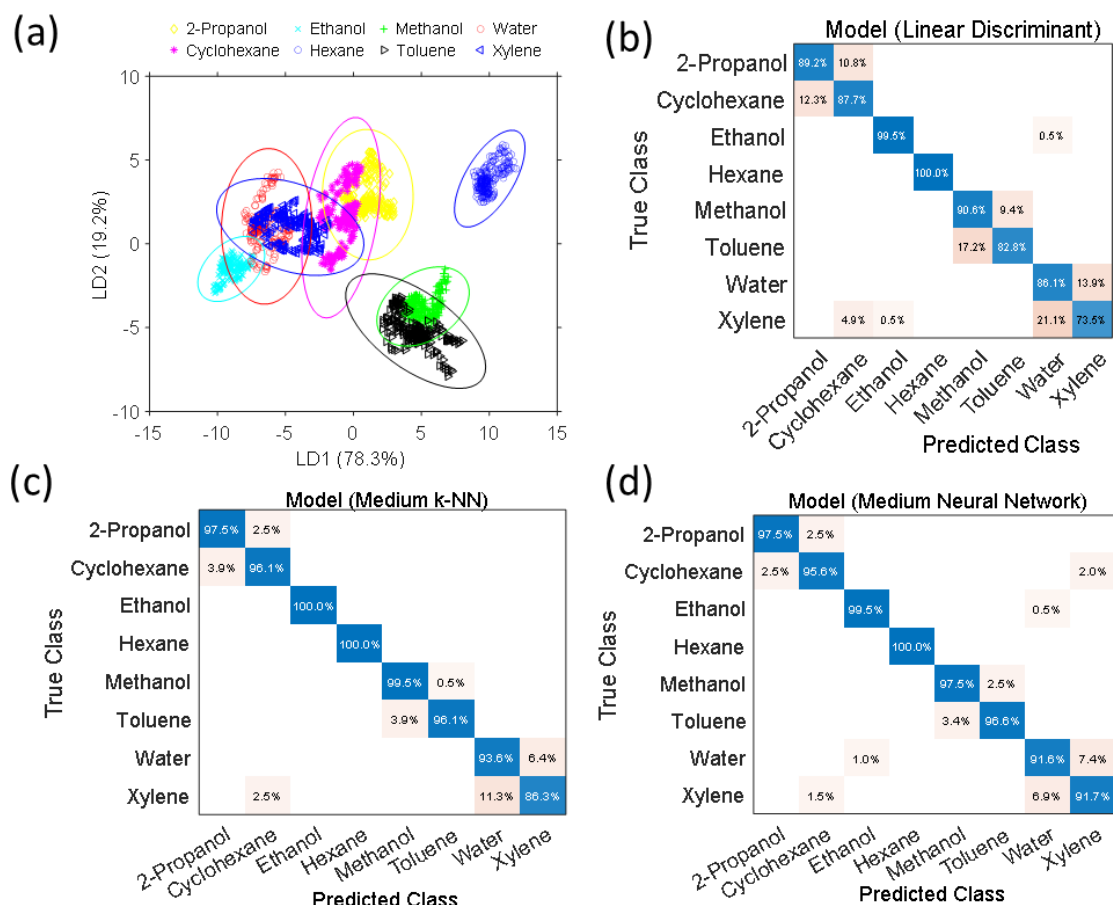


Figure 49 – E-Nose analysis results at 25 ppm concentrations. (a) Two-dimensional plot of LDA with a 95% confidence ellipse of eight VOCs, including water. The confusion matrix results of (b) LDA model with 88.7% discrimination accuracy, (c) k-NN model with 96.1% test discrimination accuracy, and (d) NNA model with 96.2% test discrimination accuracy.

Reprinted with permission from [234]. Copyright 2024 American Chemical Society

The k-NN model achieved a discrimination accuracy of 96.1%, as illustrated by the confusion matrix in Figure 49 (c). Meanwhile, the NNA model performed slightly better with a discrimination accuracy of 96.2%, and its confusion matrix is displayed Figure 49 (d). Notably, the NNA model demonstrated the highest discrimination accuracy among the three models tested.

Figure 50 showcases the E-Nose analysis of the functional UiO-66-X sensor array at 100 ppm using three models: LDA, k-NN (with $k = 10$), and NNA (with a single hidden layer of size 100 and ReLU activation). In Figure 50 (a), the two-dimensional plots from LDA depict the 95% confidence ellipse of frequency changes for the three functional UiO-66-X sensors across all eight VOC analytes, including water vapor, at 100 ppm. LDA achieved a discrimination accuracy of 90.0%, as indicated by the confusion matrix in Figure 50 (b).

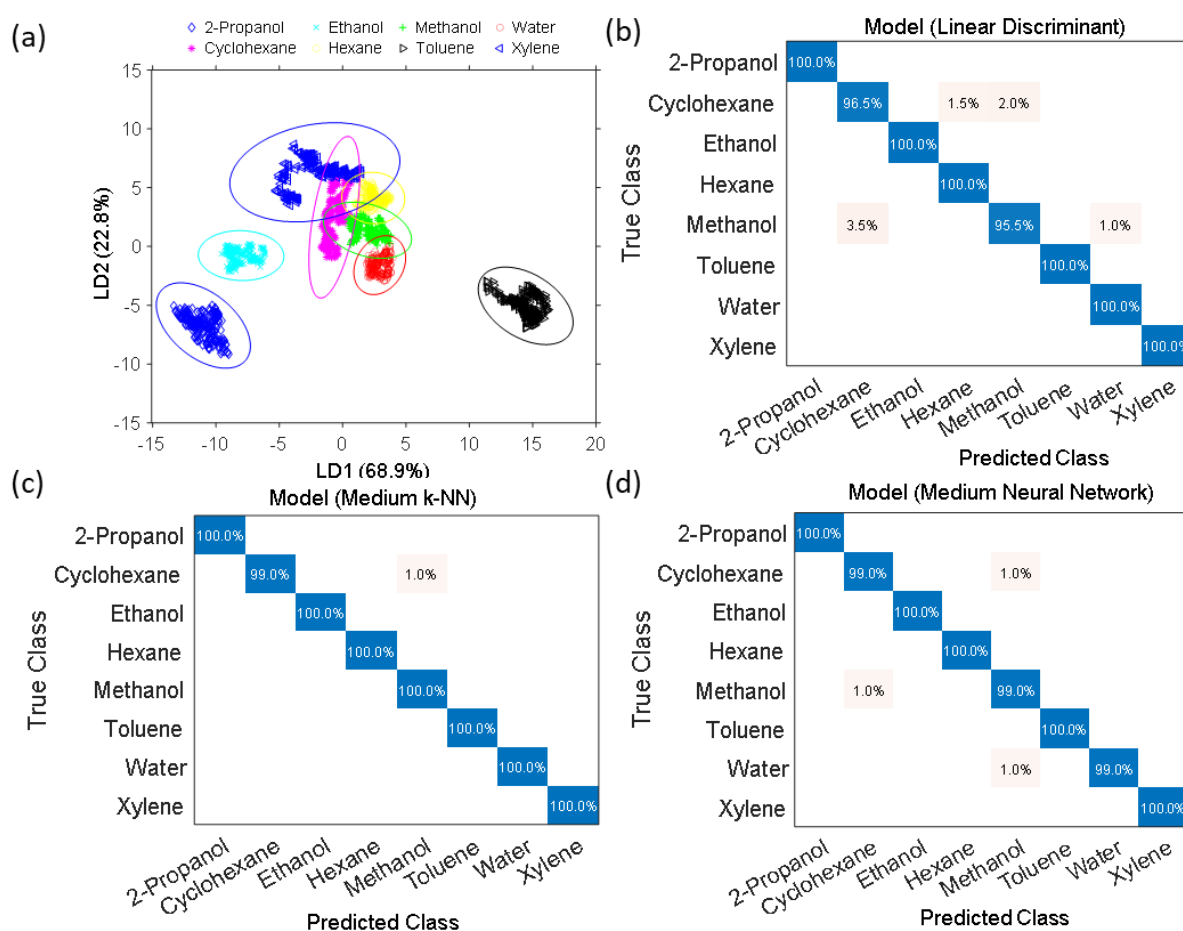


Figure 50 – E-Nose analysis results at 100 ppm. (a) Two-dimensional plot of LDA with a 95% confidence ellipse of eight VOCs, including water. The confusion matrix results of (b) LDA model with 90% discrimination accuracy, (c) k-NN model with 99.9% test discrimination accuracy, and (d) NNA model with 99.6% test discrimination accuracy.

Reprinted with permission from [234]. Copyright 2024 American Chemical Society

The k-NN model demonstrated superior discrimination accuracy with 99.9%, as shown in the confusion matrix in Figure 50 (c). Similarly, the NNA model

performed well with a discrimination accuracy of 99.6%, and its confusion matrix is displayed in Figure 50 (d). Among the models tested, the k-NN model achieved the highest discrimination accuracy at 100 ppm.

Figure 51 illustrates the variation in discrimination accuracy of the three models as concentrations increase from 10 to 100 ppm. The discrimination accuracy of LDA increased from 74.8% to 98.4%, while that of k-NN increased from 89.9% to 100%. This upward trend in accuracy was observed across all models as concentrations increased up to 100 ppm. However, both k-NN and NNA consistently demonstrated higher discrimination accuracies compared to LDA throughout the concentration range.

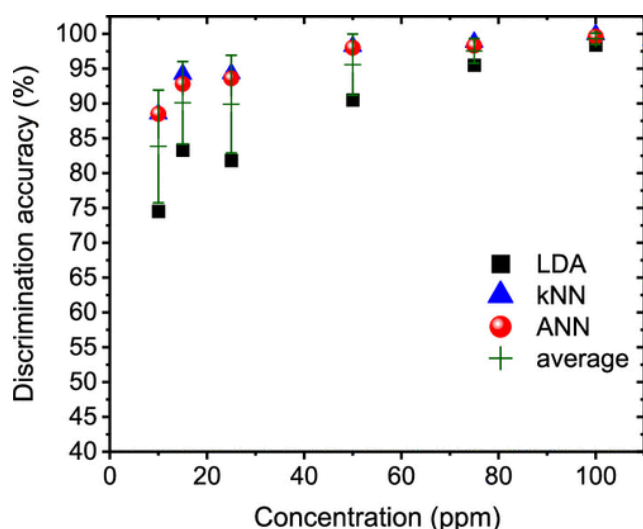


Figure 51 – Change in the discrimination accuracy of LDA, k-NN, and NNA models with increasing concentration from 10 to 100 ppm. *Reprinted with permission from [234]. Copyright 2024 American Chemical Society*

Classification models such as LDA, k-NN, and NNA are instrumental in discerning the responses of a sensor array to various VOC vapors, including low concentrations up to 10 ppm in this study. UiO-66-X, known for its stability, features a prominent zirconia cluster with a large central pore and eight smaller pores, enabling selective interaction with VOC molecules based on their size and affinity. The efficacy of these classification models in QCM-type E-Nose

applications is demonstrated using just three distinct functional groups within the robust UiO-66 SURMOF sensor array.

The degree of differentiation in sensing responses to the same VOC odor correlates directly with selectivity. Thus, enhancing the selectivity of the SURMOF sensor array for E-Nose applications can be readily achieved by incorporating additional functional groups into the sensor array using the PMS techniques proposed in this research. By introducing other types of functional groups, the sensor's selectivity and discrimination accuracy in E-Nose applications can be further enhanced.

Highly stable UiO-66-X SURMOFs can be easily postmodified for this purpose. Figure 52 illustrates a potential post-modification of UiO-66-NH₂, demonstrating the addition of various functional groups tailored to meet the requirements of industrial applications.

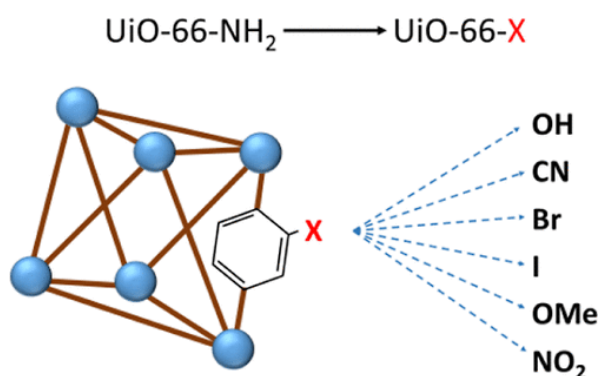


Figure 52 – Possible postmodification of UiO-66-NH₂ to add different functional groups.
Reprinted with permission from [234]. Copyright 2024 American Chemical Society

5.4 Conclusion

We introduced a novel gravimetric sensor platform based on UiO-66-X, a series of MOF thin films known as SURMOFs, obtained through post-synthetic modification of UiO-66-NH₂ SURMOF. As a proof of concept, we developed three sensors with variations X = NH₂, Cl, and N₃, integrated into an array to detect and distinguish eight different VOCs. These UiO-66-based sensors

exhibited exceptional stability, enduring severe conditions such as operation at 100% relative humidity and 90°C.

The sensor array analysis employed three machine learning methods: LDA, *k*-NN, and NNA. Near 100% discrimination accuracy was achieved at saturated vapor pressure, while at lower concentrations ranging from 10 to 100 ppm, discrimination accuracies ranged from 74.8% to 99.9%. Detection limits varied depending on the VOC type, typically falling between 19 and 440 ppm. However, utilizing QCM oscillator sensors with higher resonance frequencies could potentially lower detection limits below the ppm concentration range, given that QCM sensor mass sensitivity depends on the square of the resonant frequency.

Our results demonstrate that QCM-based sensors employing UiO-66-NH₂ SURMOFs represent a very versatile, robust, and sensitive platform for VOC detection. By appropriately functionalizing the NH₂ side groups in UiO-66-NH₂, high sensitivity to target VOCs can be achieved. With just three different side groups, our sensors reliably detected and differentiated eight VOCs. Future applications could explore additional side groups such as Br, I, OH, CN, OMe, and NO₂ to expand the sensor's capability for detecting other VOCs. Furthermore, for chiral VOCs like biomolecules, we envision employing click chemistry [252-254] to attach short peptides to the UiO-66-N₃ MOF, potentially enabling differentiation between different enantiomers [239, 255] using our E-Nose platform.

6 Chapter VI. SURMOF E-Tongue: Highly Stable Functionalized UiO-66-X Sensor Array for liquid Discrimination

6.1 Introduction

The detection and discrimination of liquids in various applications, ranging from environmental monitoring to food quality control [256-260], pose significant challenges due to the diverse chemical properties and concentrations of target analytes.

In response to these challenges, sensor technologies such as QCM sensors have emerged as versatile tools for detecting both gases and liquids [261]. QCM sensors operate by coating the quartz crystal with sensing materials that interact with target analytes (gases/vapors or liquids/ions), resulting in a measurable change in resonant frequency correlated with the mass of the adsorbed/desorbed substances. This approach offers advantages such as low cost, simplicity, high sensitivity and selectivity, low power consumption, compact volume, facile portability, along with the ability to be customized to achieve the highest sensing performance [223]. However, while QCM sensors have shown great promise in gas sensing applications (E-Nose), their application to liquid analysis (electronic tongue, or E-Tongue [262, 263]) remains less developed. Many existing QCM-based E-Tongue sensors rely on non-porous coatings [264-267], which limit their adsorption capacity and selectivity.

To address these limitations, there is a growing interest in utilizing porous materials, particularly MOFs, as coatings for QCM sensors. MOFs offer high surface areas and tunable chemical functionalities, making them ideal for enhancing the sensitivity and selectivity of sensors [223]. Recent advancements have demonstrated the effectiveness of MOF-based coatings in E-Nose devices for gas sensing, including the use of SURMOFs for detecting VOCs [224-226, 240, 241, 255]. However, the application of MOFs to liquid sensing, specifically using QCM sensors, remains underexplored.

In previous work [234], we synthesized three highly stable UiO-66-X (X = NH₂, Cl, and N₃) SURMOFs for E-Nose applications and employed them to distinguish eight VOCs in the gas phase, achieving discrimination accuracies exceeding 95% for concentrations between 50 and 100 ppm, with near-perfect accuracy at higher concentrations. Herein, we employed these functionalized UiO-66-X SURMOFs for E-Tongue applications as coating materials for QCM surfaces to discriminate six liquids, including water and 18% HCl in the liquid phase. The discrimination accuracies were calculated to be over 100% using three statistical models: Linear Discriminant Analysis, k-Nearest Neighbor, and Neural Network Analysis.

This study aims to address the current gaps in liquid detection by leveraging the high stability and versatility of these SURMOFs.

6.2 Experimental section

The contributions to the E-Tongue project are identical to those described for the E-Nose project in the previous chapter.

6.2.1 Synthesis of UiO-66-X SURMOF

The surface preparation, synthesis of UiO-66-NH₂ SURMOF, and PSM of SURMOFs were conducted according to the previous chapter.

6.2.2 Liquid delivery system and E-Tongue measurements

Six pure liquids, comprising water and 36% HCl at their highest concentrations, were subjected to absorption measurements in liquid phase. During liquid phase absorption and desorption, pure ethanol was employed as the reference background solution. In the liquid phase, 10 minutes of pure ethanol were used to bring the sensor to the reference level, clean the liquid cell, and prepare the functional UiO-66-X sensors for absorption measurements, followed by 10 minutes of test liquids for absorption measurements. The test liquid was

then replaced with ethanol for 10 minutes to prepare the sensors for the desorption procedure. This process of absorption and desorption was repeated four times.

6.2.3 Data analysis

The control of the complete system, data acquisition, and E-Tongue data analysis were carried out using MATLAB 2021B-written program code. The sensing data for E-Tongue discrimination analysis were classified using three standard supervised ML algorithms, LDA [239, 240] and k-NN [224, 241]. To improve accuracy, data from the saturated area (highest response region) of adsorption/desorption curves were employed during data analysis. Classification analysis included a 10-fold cross-validation process. Typically, 90% of the total observations were used for the training set, while 10% were used to evaluate the discrimination accuracy. The findings of LDA, k-NN, and NNA models' discrimination analyses were presented as a confusion matrix.

6.3 Results and discussions

Synthesis of UiO-66-X SURMOF

As was mentioned above the synthesis of UiO-66-NH₂ and SURMOF functionalization process were conducted same way as in previous chapter.

The growth kinetics of UiO-66-NH₂ SURMOF films are directly affected by synthesis parameters such as temperature, injection volume and exposure duration, flow rate, metal ion/cluster concentration, as well as organic linker concentration and type of rinsing solution. QCM with dissipation (QCM-D) was employed to follow the growth/deposition rate of such films. A typical time-dependent growth kinetics of UiO-66-NH₂ SURMOF films synthesized with the LbL approach in a high-temperature QCM-D liquid cell at 100 °C demonstrated linear dependence of the deposited SURMOF on the cycle number. In this setup, a 7.5-second injection time was chosen for Zr metal clusters and linkers in continuous flow mode. For rapid SURMOF film generation, a 2-min DMF rinse

was employed, at a pumping speed of 6 rpm in between each cycle. The temperature was maintained in this synthesis at 100 °C. With increased LBL cycle, a linearly rising upload was recorded during synthesis.

The XRD patterns of functional UiO-66-X following post-modification with NH_2 , N_3 , and Cl are shown in Figure 53 (a). The XRD peaks at 7.4° representing (111) and 8.5° at (200) orientation as well as intensities show complete consistency with simulations of the previously published UiO-66- NH_2 bulk structure [117, 123, 268]. By employing SEM imaging, the topography of synthesized sensors was analyzed. Figure 53 (b) depicts SEM images of the top surface, whereas Figure 53 (c) depicts a cross-sectional view of UiO-66- NH_2 SURMOF films for structural investigation. SEM surface topography reveals smooth, crystalline UiO-66- NH_2 SURMOF films with estimated 300–500 nm thicknesses that cover the entire QCM surface.

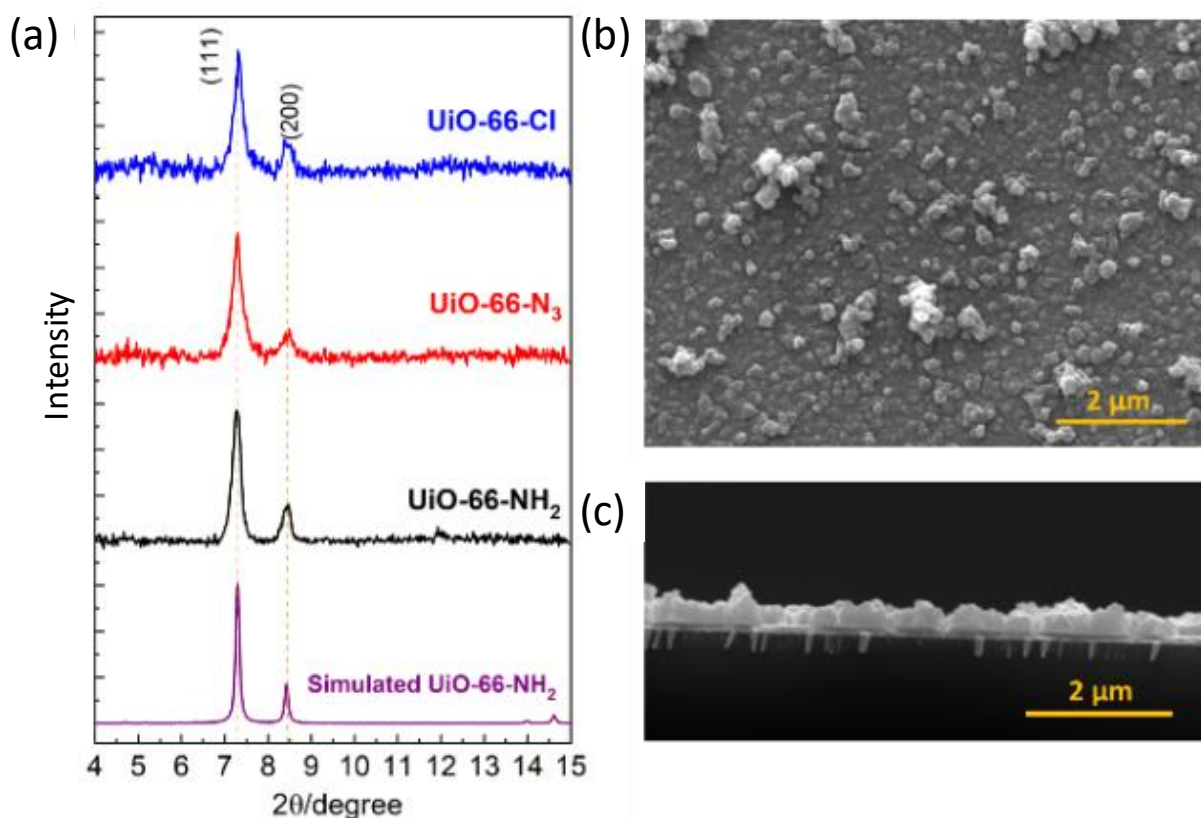


Figure 53 – Structural analysis of the functional UiO-66-X following the post-modification process: (a) XRD pattern, (b) SEM surface topography, and (c) SEM cross-section.

Sensor stability against moisture and HCl

The stability of the surface functionalized QCM sensor was tested in water vapor at temperatures between 25-90 °C for 45 minutes, as well as for exposure to 18% HCl (5.43 M) aqueous solution for 6 hours. The results were discussed in detail in previous chapter.

Adsorption measurements

The enhanced response of the QCM bearing SURMOF layer was evident from comparison of the recorded magnitude of Δf , where the UiO-66-NH₂@QCM demonstrated far enhanced signal as compared to the bare QCM (Figure 54 (a)). This behavior was consistent for the six tested liquids of ethanol, isopropanol, n-hexane, p-xylene, toluene, and water. The sensor was flushed with N₂ gas between tests to regenerate the sensor for subsequent test. In all tests conducted, the signal recovered back to its initial value upon flushing with N₂, indicating the full recovery of the sensing element after exposure to the various liquids.

To attain differential responses for each tested liquid, the array of four QCM sensing elements, namely the bare QCM and the QCM coated with UiO-66-X (X = NH₂, Cl, N₃) were simultaneously tested against the six liquids (Figure 54 (b)). Each sensor demonstrated a different magnitude of Δf for the same tested liquid, as well as dependence of Δf on the kind of liquid tested. Additionally, all sensing elements demonstrated rapid and full recovery after each test when regenerated through exposure to a stream of N₂.

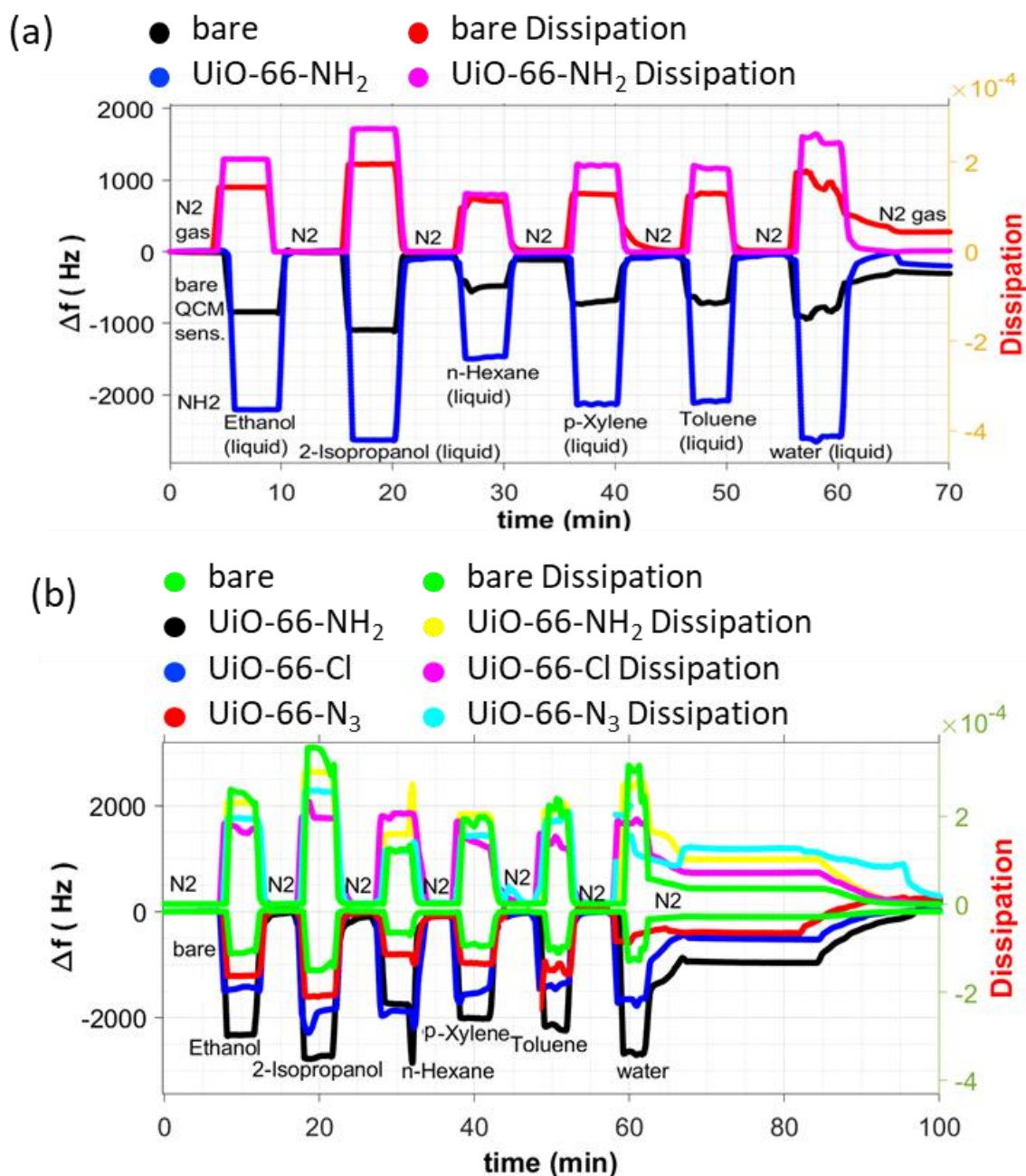


Figure 54 – Changes in resonance frequency of (a) the bare QCM as compared to UiO-66-NH₂@QCM, indicating enhanced response for the MOF-coated QCM towards all the liquids tested; (b) the bare QCM and the three different UiO-66-X@QCM sensors

Moreover, ethanol (in liquid form) was tested as a baseline for liquid sensing (Figure 55). The frequency difference Δf for the UiO-66-NH₂@QCM sample and the bare QCM sample differs depending on the liquid type. Moreover, after washing with ethanol, the sensor signals returned to their initial values,

demonstrating the full recovery of the sensors after tests and showing the possibility of using ethanol as a baseline.

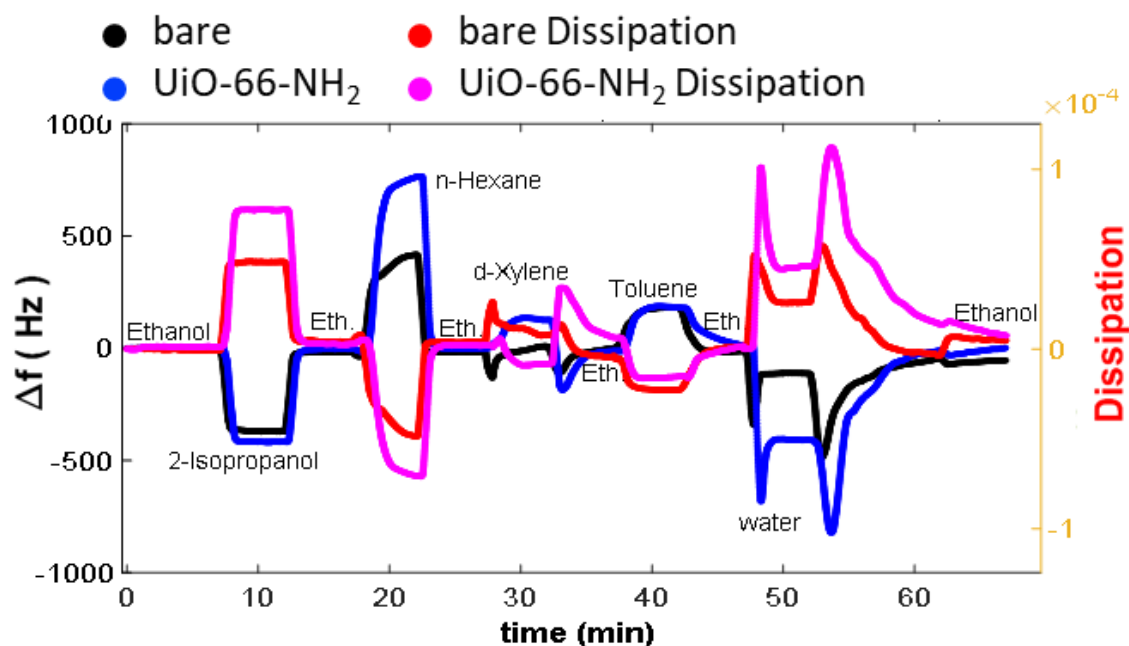


Figure 55 – Frequency difference for the UiO-66-NH₂@QCM sample and the bare QCM sample using ethanol as a baseline

In order to evaluate the sensitivity of the sensors, different concentrations of analytes diluted in the baseline liquid were used. The bare sample and UiO-66-NH₂ with ethanol as a baseline were tested first (Figure 56 (a)). The responses to varying concentrations of 2-isopropanol and n-hexane (C/4, C/2, 3C/4, C) indicate that the Δf depends on both: the type of tested liquid and its concentration. Distinct differences were observed at each concentration level. This test was repeated for all four sensors: the bare QCM, UiO-66-NH₂, UiO-66-Cl, and UiO-66-N₃ (Figure 56 (b)). This comprehensive comparison highlights the differential sensitivity of each sensor type to varying concentrations of 2-isopropanol and n-hexane.

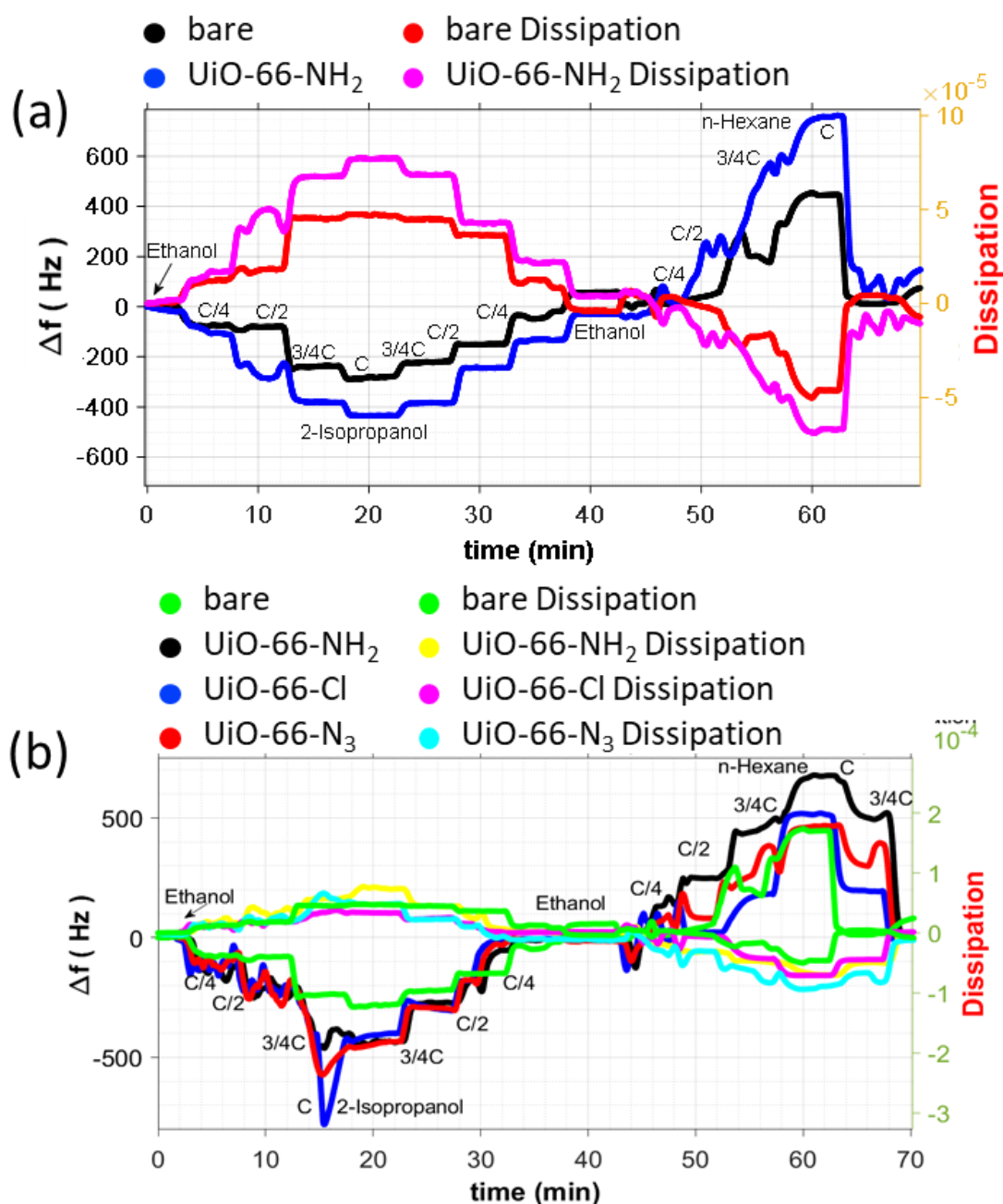


Figure 56 –Response to varying concentrations of 2-isopropanol and n-hexane with ethanol as a baseline for (a) bare QCM and UiO-66-NH₂@QCM; (b) all four sensors: bare QCM, UiO-66-NH₂, UiO-66-Cl, and UiO-66-N₃

To check if the response would change depending on a different baseline material, the experiment was repeated with toluene (Figure 57). The process was repeated several times, cycling between different concentrations of 2-isopropanol and n-hexane, and returning to the toluene baseline between tests. This cyclic testing demonstrates the stability and repeatability of the sensors' responses to

different liquids and concentrations, with clear and consistent recovery to the baseline after each test cycle.

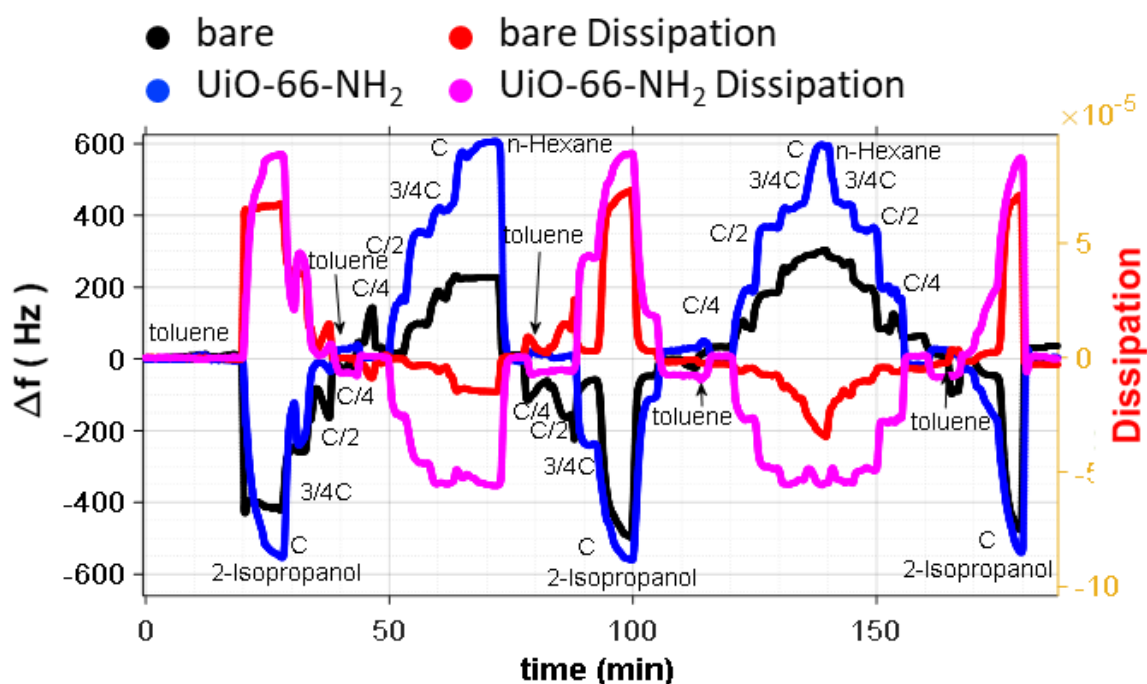


Figure 57 – Response to varying concentrations of 2-isopropanol and n-hexane with toluene as a baseline, demonstrating sensitivity, stability and repeatability

These results underscore the high sensitivity, selectivity, and stability of the UiO-66-X coated QCM sensors across a range of liquids and concentrations, addressing the current gaps in liquid detection technology.

Figure 58 depicts the liquid phase test findings for UiO-66-X when X=NH₂ (Figure 58 (a)), X=Cl (Figure 58 (b)), and X=N₃ (Figure 58 (c)) for 36% HCl, water, n-hexane, 2-isopropanol, toluene, as well as p-xylene relative to pure ethanol in liquid form as a reference. The dissipation changes of UiO-66-X sensors for X=NH₂ (Figure 58 (d)), X=Cl (Figure 58 (e)), and X=N₃ are presented (Figure 58 (f)). During the testing, 5-min liquid analytes were introduced to the liquid cell and washed for 10 minutes with ethanol to determine the adsorption and desorption parameters

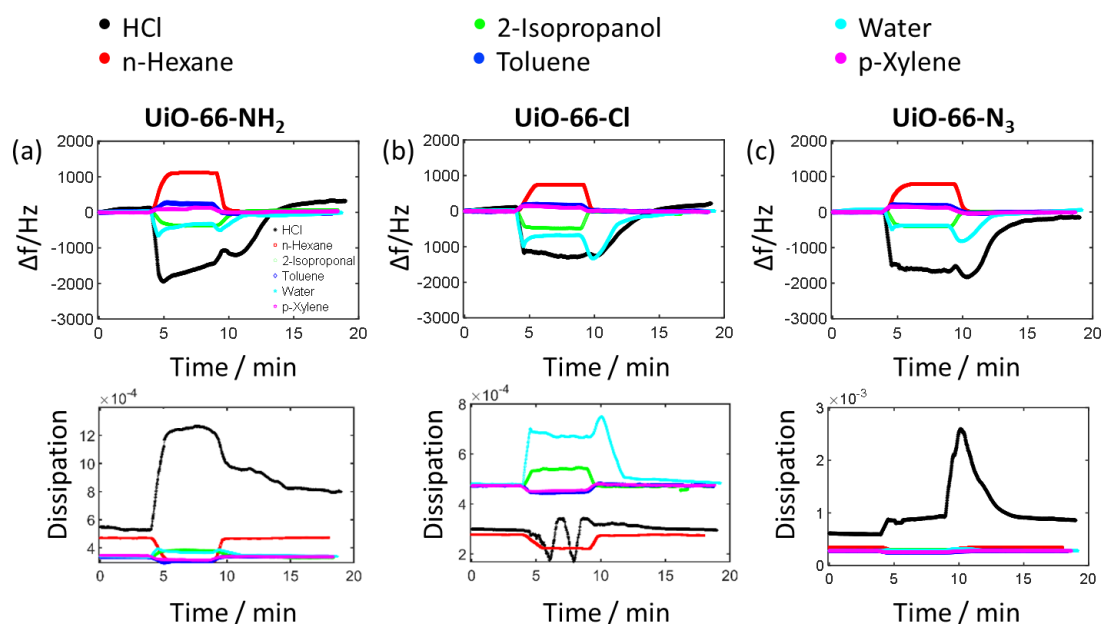


Figure 58 – The liquid phase test results for the (a) UiO-66-X for X=NH₂, (b) X=Cl and (c) X=N₃ for 36% HCl, water, n-hexane, 2-isopropanol, toluene, and p-xylene with respect to pure ethanol in liquid form as a reference solution

To the end, all sensor responses remained constant. HCl and water elicited the strongest absorption responses, whereas toluene and p-xylene elicited the weakest responses. During QCM oscillations, the functional UiO-66-X sensor recorded a positive frequency effect for toluene, n-hexane, and p-xylene due to the distinct viscosity mass effect of each liquid (Table 7).

Table 7 – Viscosity values of liquids

	Isopropanol	Water	HCl	Ethanol	n-Hexane	Toluene	p-Xylene
Viscosity (mPa·s)	2.37	1.67	1.5	1.04	0.3	0.6	0.6

During oscillation, various disturbances in the quartz crystal's mechanical damping characteristics and energy dissipation to the viscous liquid environment lead to the mass effect of a liquid (Kanazawa effect) on the frequency shift or positive shifts in the resonance frequency [269]. According to Figure 58 (d)-(f),

this demonstrates that the recorded dissipation change is a function of the coupling between the oscillating sensor and its environment. Table 7 displays the viscosity values of liquids relative to that of ethanol. The frequency changes of liquids with greater viscosities than ethanol are diametrically opposed to those of liquids with lower viscosities than ethanol.

E-Tongue Discrimination Analysis

For E-Tongue analyses of functional UiO-66-X sensor array in liquid phase, three models were utilized: LDA, k-NN $k = 10$, and NNA. Figure 59 (a) depicts two-dimensional LDA plots of frequency changes of three functional UiO-66-X sensors against n-hexane, 2-isopropanol, toluene, p-xylene, water, as well as 36% HCl (11.65 M), with a 95% confidence ellipse. With LDA and confusion matrix depicted in Figure 59 (b), 99.6% discrimination accuracy was achieved. Figure 59 (c) depicts the 99.5% discrimination accuracy derived from k-NN model with $k=10$ and confusion matrix. Utilizing the NNA model, Figure 59 (d) demonstrate the confusion matrix where 99.9% discrimination accuracy was attained. In this case, the NNA model was the most accurate of the three models.

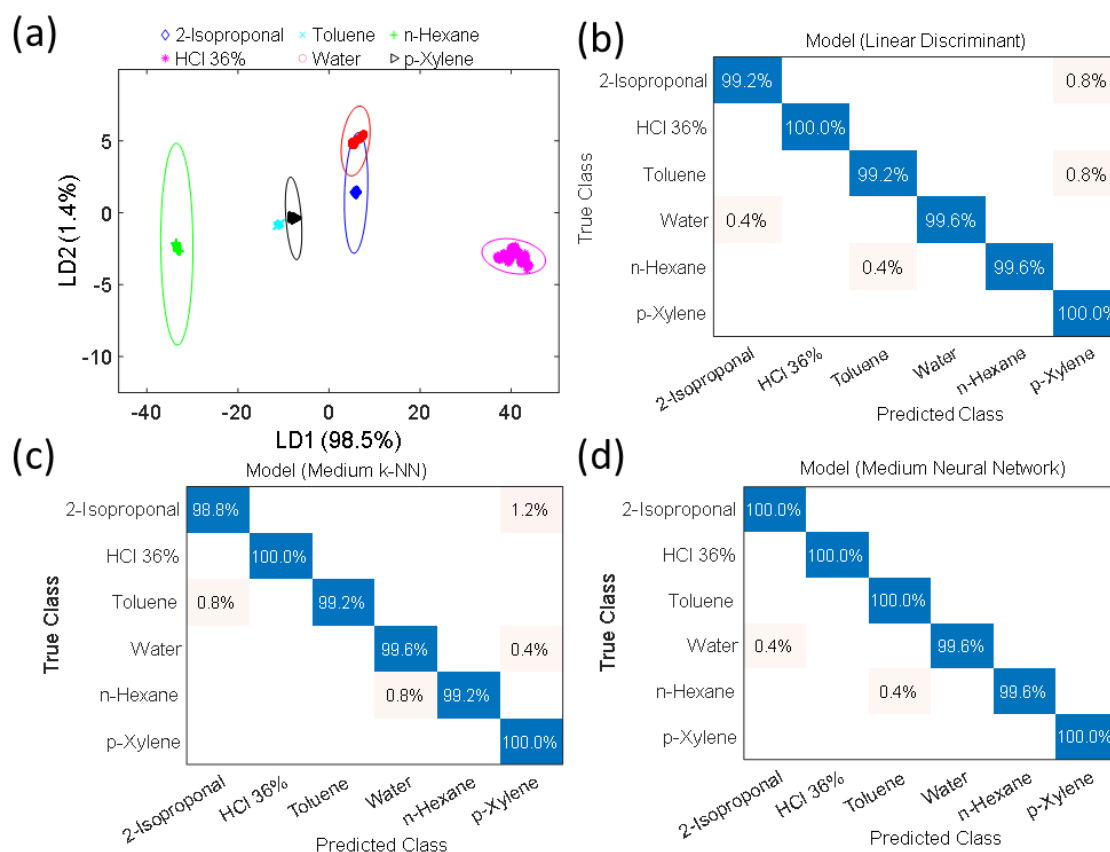


Figure 59 – E-Tongue analysis results: (a) Two-dimensional plot of LDA with a 95% confidence ellipse of six different liquid, e.g. n-hexane, 2-isopropanol, toluene, p-xylene, including water and 36% HCl; (b) the confusion matrix results of LDA model with 99.6% discrimination accuracy, (c) the confusion matrix results of k-NN model with 99.5% test discrimination accuracy; (d) the confusion matrix results of NNA model with 99.9% test discrimination accuracy.

6.4 Conclusions

In this study, we have demonstrated the successful development and application of a highly stable and functionalized selective UiO-66-X SURMOF QCM-sensor array, where the different functional groups within the SURMOF coating (NH_2 , Cl, and N_3) aided differential sensing of six distinct liquids with high accuracy. The performance of the functionalized QCM sensors array is compared to that of the bare QCM element and demonstrated clearly the enhancement in signal and differential response to the tested liquids. Moreover,

the stability of the sensing array was tested in humid conditions and in acidic solution, demonstrating strong stability of the SURMOF functional coating.

The SURMOF E-Tongue's ability to achieve high accuracy in distinguishing between various liquids highlights its potential for a wide range of practical applications, including environmental monitoring, quality control in the food and beverage industry, and medical diagnostics. The robustness, stability, and functionalizability of the UiO-66-X based SURMOFs make them ideal candidates for developing next-generation E-Tongue systems.

In conclusion, the integration of functionalized UiO-66-X SURMOFs with advanced machine learning techniques has enabled the creation of a highly effective and reliable electronic tongue system. Future work could explore the application of this technology to a broader range of analytes and real-world samples, as well as the development of miniaturized and portable E-Tongue devices for on-site analysis. The findings of this study pave the way for further innovations in the field of chemical sensing and liquid discrimination, leveraging the unique properties of metal-organic frameworks.

7 Chapter VII. Advancements in Zr- and Hf-Based UiO-66-NH₂ SURMOF Membranes: Synthesis, Stability, and Applications

7.1 Introduction

Membrane technologies have become indispensable tools across various fields, transforming processes from water treatment to gas separation and catalysis. Their power lies in their ability to selectively separate molecules or particles based on various factors like size, shape, charge, or affinity, providing effective and sustainable solutions to complex challenges. Among the diverse materials used for membranes, MOFs have gained significant attention due to their exceptional properties, including high surface areas, adjustable pore sizes, and customizable chemical functionalities.

Among various MOFs, UiO-66-NH₂, is expected to give promising results across a wide range of applications due to its sturdy structure and adaptable surface chemistry. By adding amino functional groups, its ability to grab onto contaminants from both water and air is greatly enhanced. However, fully leveraging its potential in membrane-based applications requires optimizing its synthesis and integration into functional membranes.

UiO-66-NH₂ usually consist of zirconium (Zr) metal ions and amino-functionalized terephthalic acid (BDC-NH₂) as an organic linker, however, suggestion was made to replace Zr ions with hafnium (Hf), as both Zr-UiO-66-NH₂ and Hf-UiO-66-NH₂ share similar structural properties but are differentiated by their metal nodes.

Hf-MOFs have gained increasing attention due to their superior performance as gas adsorbents compared to Zr-MOFs. This improved performance is attributed to the presence of Brønsted acid sites with a high affinity for adsorbates, coupled with chemical and hydrothermal stability comparable to their Zr counterparts [109]. Additionally, Hf-based UiO-66 MOFs have shown superior catalytic performance compared to Zr-UiO-66, suggesting that the type of metal

center in the MOF structure has a greater impact than the presence of amine functional groups [270]. However, the progress in developing Hf-MOFs has been limited by the lack of efficient synthesis methods [109].

Layer-by-layer (LbL) synthesis techniques provide an excellent way for creating MOF-based membranes with precise control over thickness, pore size, and surface properties. By layering MOFs alternately with compatible materials onto porous substrates, LbL synthesis allows for the development of composite membranes with improved stability, selectivity, and overall performance. In this context, Zr(Hf)-UiO-66-NH₂ membranes synthesized via LbL deposition on cellulose substrates represent a significant leap forward in membrane technology.

However, despite the considerable potential of Zr(Hf)-UiO-66-NH₂ membranes, their synthesis faces several challenges. Achieving optimal parameters like surface functionalization, concentrations of reagents, timing for each step, temperature, and choice of solvents is crucial. Additionally, ensuring compatibility between MOF precursors and cellulose substrates is essential to promote efficient nucleation and growth without compromising membrane integrity.

Despite these challenges, the development of Zr(Hf)-UiO-66-NH₂ membranes holds promise for numerous applications, with water treatment, gas separation, and catalysis emerging as particularly promising areas. These membranes offer the potential to tackle pressing environmental issues such as water scarcity and air pollution, while also driving advancements in industrial processes and healthcare.

In this study, we first present the LPE LbL SURMOF synthesis of Hf-UiO-66-NH₂@gold as well as Zr(Hf)-UiO-66-NH₂@cellulose membranes. Moreover, the stability of Hf-UiO-66-NH₂@gold SURMOF in acidic (pH 2), neutral (pH 7.5) and alkaline (pH 11) media is investigated, demonstrating the practical viability and durability of these innovative membrane technologies.

7.2 Experimental section

7.2.1 Synthesis of Zr- and Hf-UiO-66-NH₂ MOFs

UiO-66-NH₂ MOF was prepared using solvothermal method. The synthesis involved the preparation of two separate solutions. Solution A was prepared by dissolving 0.251 g (90 mM) of ZrCl₄ in 10 mL of DMF, followed by sonication until complete dissolution. Subsequently, 2 mL of 36% HCl was added to solution A, which was further sonicated to ensure homogeneity. Solution B was prepared by dissolving 0.271 g (150 mM) of BDC-NH₂ in 10 mL of DMF, with sonication until fully dissolved. Solution A was added to 20 mL of DMF and then heated to 80°C under stirring at 300-500 rpm until the set temperature was reached. Following this, solution B was added dropwise to the diluted solution A. The mixture was then sealed in a vial, covered with aluminum foil, and maintained at 80°C with continuous stirring until the solution became milky (the reaction was typically allowed to proceed overnight), indicating the formation of UiO-66-NH₂.

After the synthesis, the stirring and heating were switched off, and the vials were allowed to cool to room temperature. The MOF was then collected via centrifugation, washed three times with DMF, and subsequently three times with ethanol. The collected powder was soaked in ethanol for 24 hours and finally dried in an oven at 70°C.

7.2.2 Synthesis of Zr- and Hf-UiO-66-NH₂ thin films on different substrates

Zr- and Hf-UiO-66-NH₂ SURMOFs on FGCS were prepared using a flow cell system. First, metal ion (MI) and linker (L) solutions were prepared. The MI solution consisted of 90 mM of Zr(Hf)Cl₄ in 35 mL of DMF with 7 mL of HCl. The L solution was composed of 150 mM of NH₂-BDC dissolved in 40 mL of DMF. Pure DMF was used as the washing solution.

Next, all three solutions were filled into Teflon tubes using a peristaltic pump (Ismatec, Wertheim, Germany) controlled by MATLAB 2021B. The sample was

placed inside the cell, and the MI solution was introduced into the flow cell. The heating was switched on to reach 80 °C, allowing for a 20-minute reaction period between the MI solution and the functionalized surface.

A cycle started with a 20 second flow of fresh MI solution, and the reaction was maintained for 90 minutes. Then, the washing agent was introduced for 20 seconds to refill the cell and push out the MI solution. After that, the L solution was introduced for 20 seconds to fill the cell, and the reaction with the sample was maintained for 120 minutes. Following the interaction with the linker molecules, the cell was refilled with DMF. This process was repeated for 20-25 cycles to obtain the UiO-66-NH₂ SURMOF.

At the end of the synthesis, the flow cell was cooled to room temperature in air, the sample was taken out, and it was washed with ethanol six times, followed by immersion in ethanol for 24 hours. After the washing process, the samples were left to dry overnight in air. The entire synthesis process was managed using the MATLAB 2021B.

UiO-66-NH₂ thin film on functionalized membranes were prepared using two different methods: for Zr-based film LPE LbL method using dip-coating (see details in 4.2.1 Synthesis of UiO-66-NH₂ via dip-coating) was applied; while in case of Hf-based film flow cell method described above was employed. Similar to UiO-66-NH₂@ FGCS samples the membranes were washed six times with ethanol, followed by immersion in ethanol for 24 hours. After the washing process, the samples were left to dry overnight in air.

7.2.3 Chemical Stability Experiments of Hf-UiO-66-NH₂@gold in Acidic, Neutral and Alkaline Media

To evaluate the stability of Hf-UiO-66-NH₂ SURMOF films in different environments, the films were immersed in solutions with pH values of 2, 7.5 and 11. The pH of the different solutions was adjusted with distilled water using 1 M HCl for the acidic environments and 1 M NaOH for the basic environments.

Initially, a Hf-UiO-66-NH₂@gold sample was cut into three pieces (1 cm × 1 cm). Each piece was then subjected to specific pH conditions at room temperature as follows: the sample was first immersed in the solution for 1 minute, rinsed three times with ethanol, and dried with a stream of dry nitrogen. Subsequently, XRD was used to check for any changes in crystallinity. Based on the results, the same sample was then immersed for progressively longer durations (10 minutes, 20 minutes, 60 minutes, 120 minutes and one day), followed by the same rinsing and XRD characterization process. The pH of the solutions was also measured after immersion to ensure it remained unchanged upon contact with the sample.

7.3 Results and discussion

XRD analysis results show that the calculated XRD patterns for Zr- and Hf-UiO-66 (Figure 60) look very similar in terms of diffraction peak positions and relative intensities giving that the crystal structure is perfect with no metal nodes vacancies and all the pores are empty and the electron density distribution is uniform. This is due to the similarities between Zr and Hf ions and the identical arrangement of metal nodes inside UiO-66 structure. The primary difference between their XRD patterns is the slightly higher peak intensities ratio observed for Hf-UiO-66 due to higher electron density. However, subtle variations in peak positions and intensities might be observed in the experimental XRD patterns due to factors such as synthesis conditions or structural defects.

The calculated XRD pattern for Zr- and Hf-UiO-66 show two main diffraction orientation at (111) and (200), that correlates to the metal and linker arrangement within the UiO-66 structure (Figure 60 inset), with the corresponding second order plans (222) and (400), respectively, which have low intensity. In addition, several peaks for other diffraction plans can be observed. Crystal maker simulation software showed that Zr- and Hf-UiO-66 have the same powder XRD pattern in terms of peak positions but showed that the ratio between the (111) and (200) plans are slightly higher in the case of Hf-UiO-66. However,

the low difference between the peak intensities' ratio cannot be used to differentiate between Zr- and Hf-UiO-66 as multiple factors can affect the intensities in the case of experimental data such as the pore filling, the electron density distribution, and the metal vacancies leading to false identification of the structure.

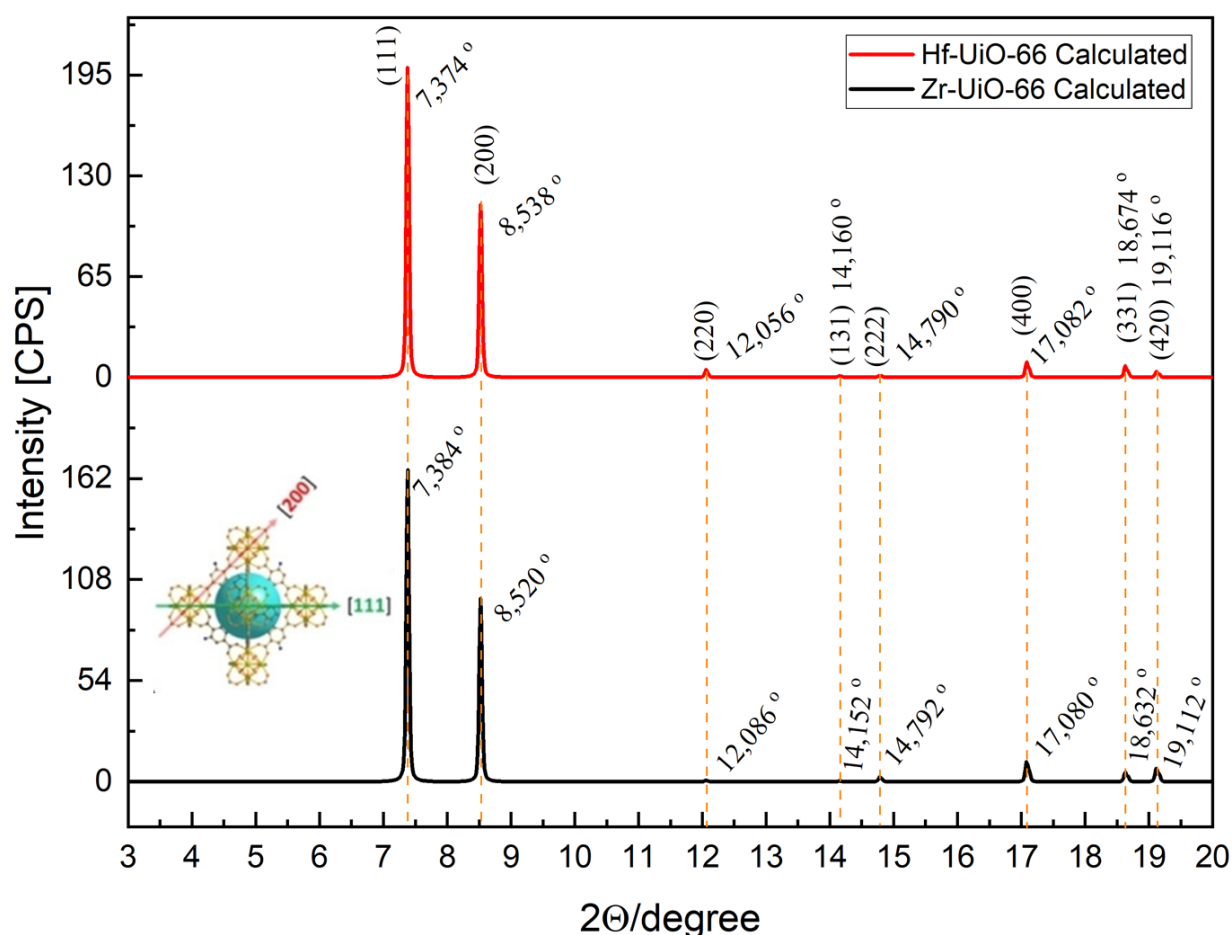


Figure 60 – Calculated XRD patterns for Zr- and Hf-UiO-66. The inset is from [100].
Copyright 2020 Wiley

LPE LbL flow-cell method was used to grow Zr(Hf)-UiO-66-NH₂ SURMOF on the FGCS. PXRD confirmed crystal structure of the resulting UiO-66-NH₂ (Figure 61). In the case of SURMOF it can be noticed that only two peaks for (111) and (200) appear which indicates the oriented growth of both MOFs. The main reason for the existence of two different crystal planes in the SURMOF XRD can be explained by the growth method of the SURMOF on the substrate

surface where two possible ways of growth happens at the same time in the (111) and (200) directions with small energy difference, however, the (111) plane is more energetically favorable. The low intensities of the corresponding second order plans in the calculated XRD (Figure 60) explains their absences from the experimental XRD patterns.

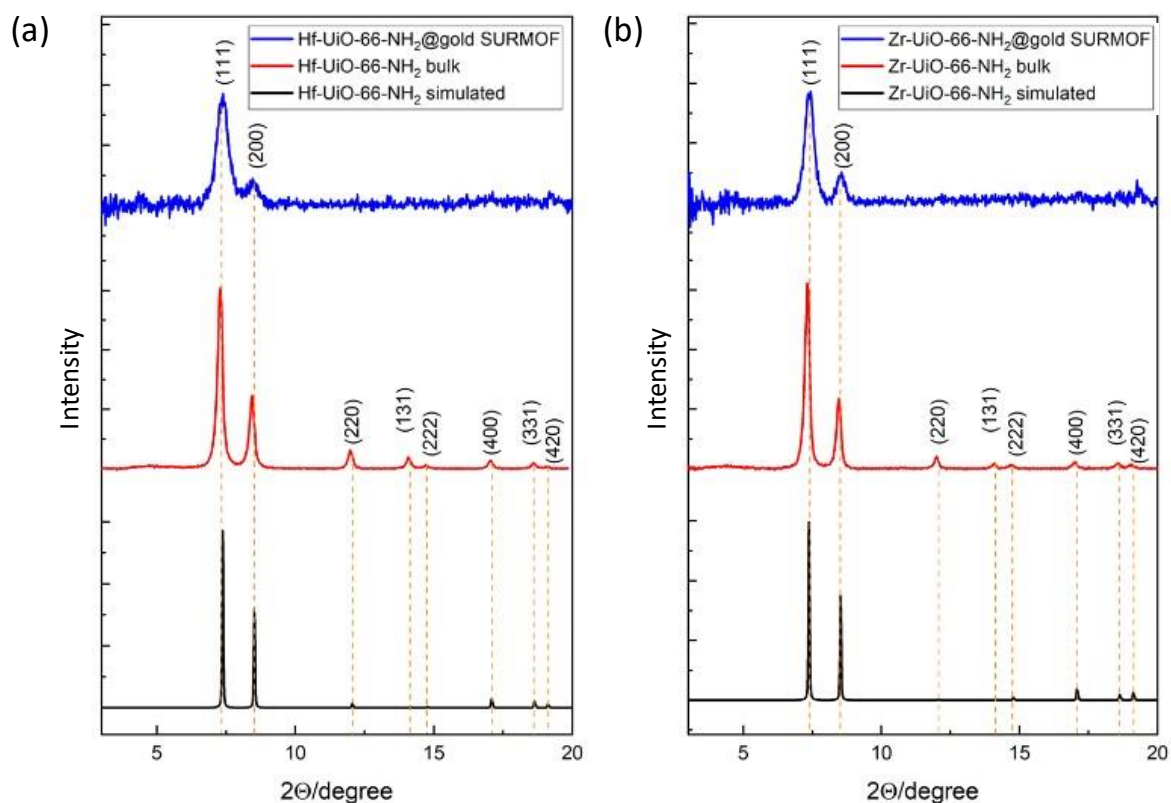


Figure 61 – XRD patterns of (a) Hf- and (b) Zr-UiO-66-NH₂

In the IRRA spectra (Figure 62 (a)), the main peaks characteristic of UiO-66-NH₂ were observed for both the Zr- and Hf-based MOF bulk and SURMOF. The carboxylate peaks from the linker appeared at 1576 cm⁻¹ and 1658 cm⁻¹, while the amino group vibrations were detected at 3390 cm⁻¹. SEM images (Figure 62 (b)) confirm homogeneous films of the SURMOFs.

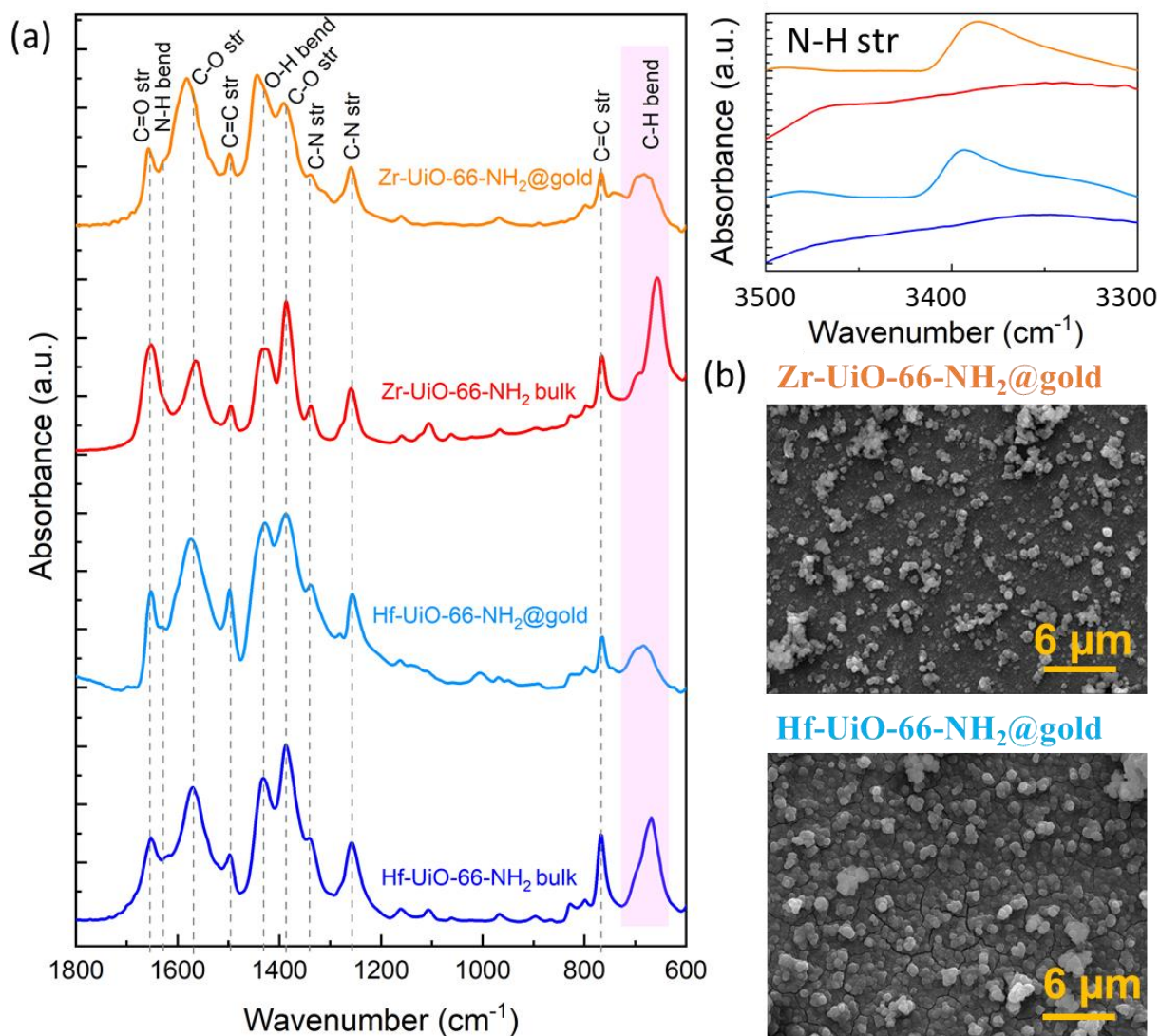


Figure 62 – (a) IRRA spectra and (b) SEM top-view images of Zr- and Hf-UiO-66-NH₂ SURMOF

The stability study of Hf-UiO-66-NH₂ SURMOFs showed that the Hf SURMOF exhibited impressive stability when exposed to both acidic (pH 2) and neutral (pH 7.5) conditions, as evidenced by the consistent diffraction peak intensity and unchanged crystal morphology even after immersion in different pH solutions for a day (Figure 63 (a, b, d)). However, immersion of the Hf-UiO-66-NH₂ SURMOF film in a pH 11 solution (Figure 63 (c, d)) resulted in significant degradation of the film within just one minute of immersion.

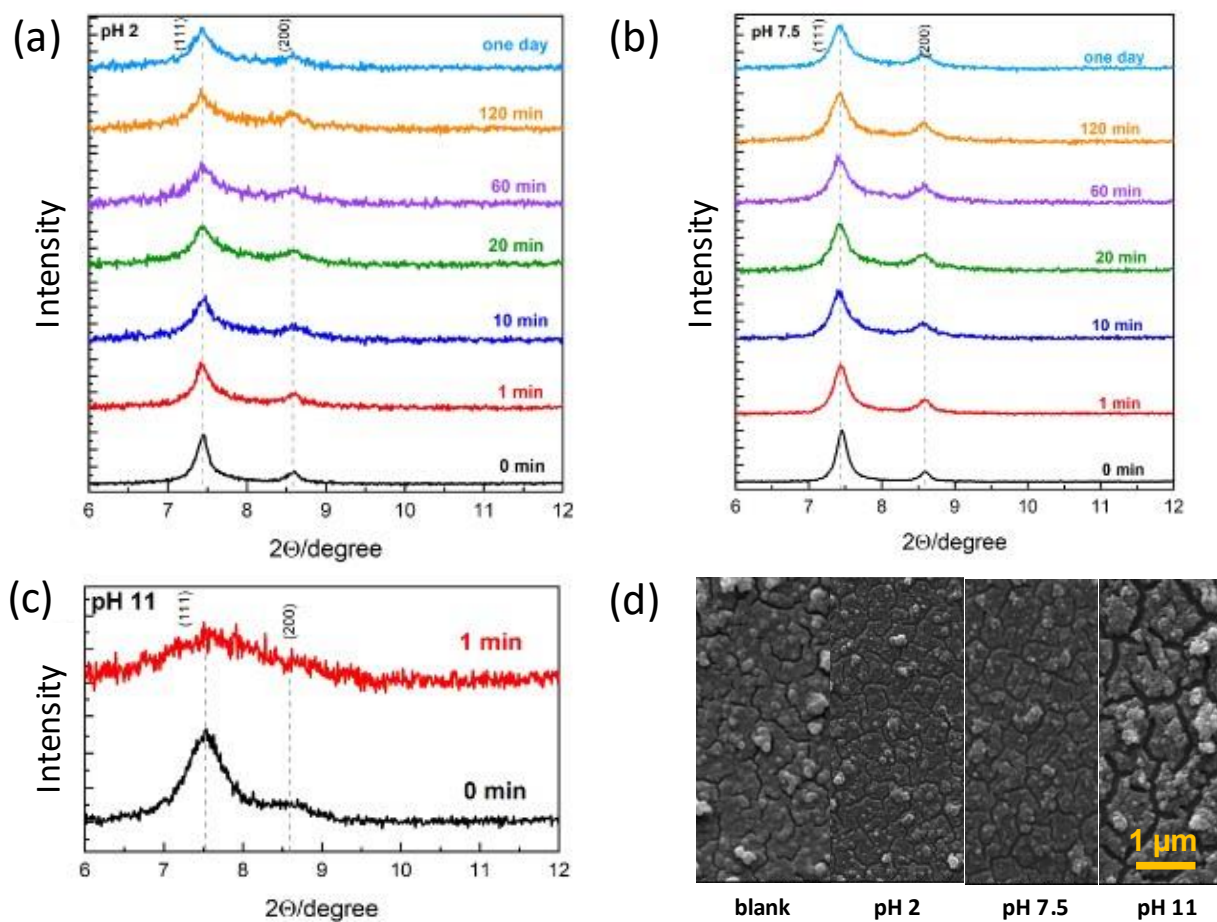


Figure 63 – XRD patterns of Hf-UiO-66-NH₂ SURMOF films immersed in a: (a) pH 2 solution, (b) pH 7.5 solution, and (c) pH 11 solution; and (d) SEM images before and after immersions

The obtained results align well with previous findings on Zr-UiO-66-NH₂@gold stability [117]. However, additional tests with pH 10 should be conducted for further confirmation of the similar behavior of Zr-UiO-66-NH₂ and Hf-UiO-66-NH₂ SURMOFs.

While this study primarily focuses on exploring homogeneous and stable films, it's worth noting that controlled SURMOF growth could offer advantages in various applications, including electrochemical, optical, electronic, sensing, and separation processes.

Additionally, to showcase the flexibility of the UiO-66-NH₂ deposition techniques discussed in this study, membranes were created through the LbL

process to deposit UiO-66-NH₂ thin film on a cellulose substrate. The successful formation of crystalline Zr(Hf)-UiO-66-NH₂ thin film was verified (Figure 64).

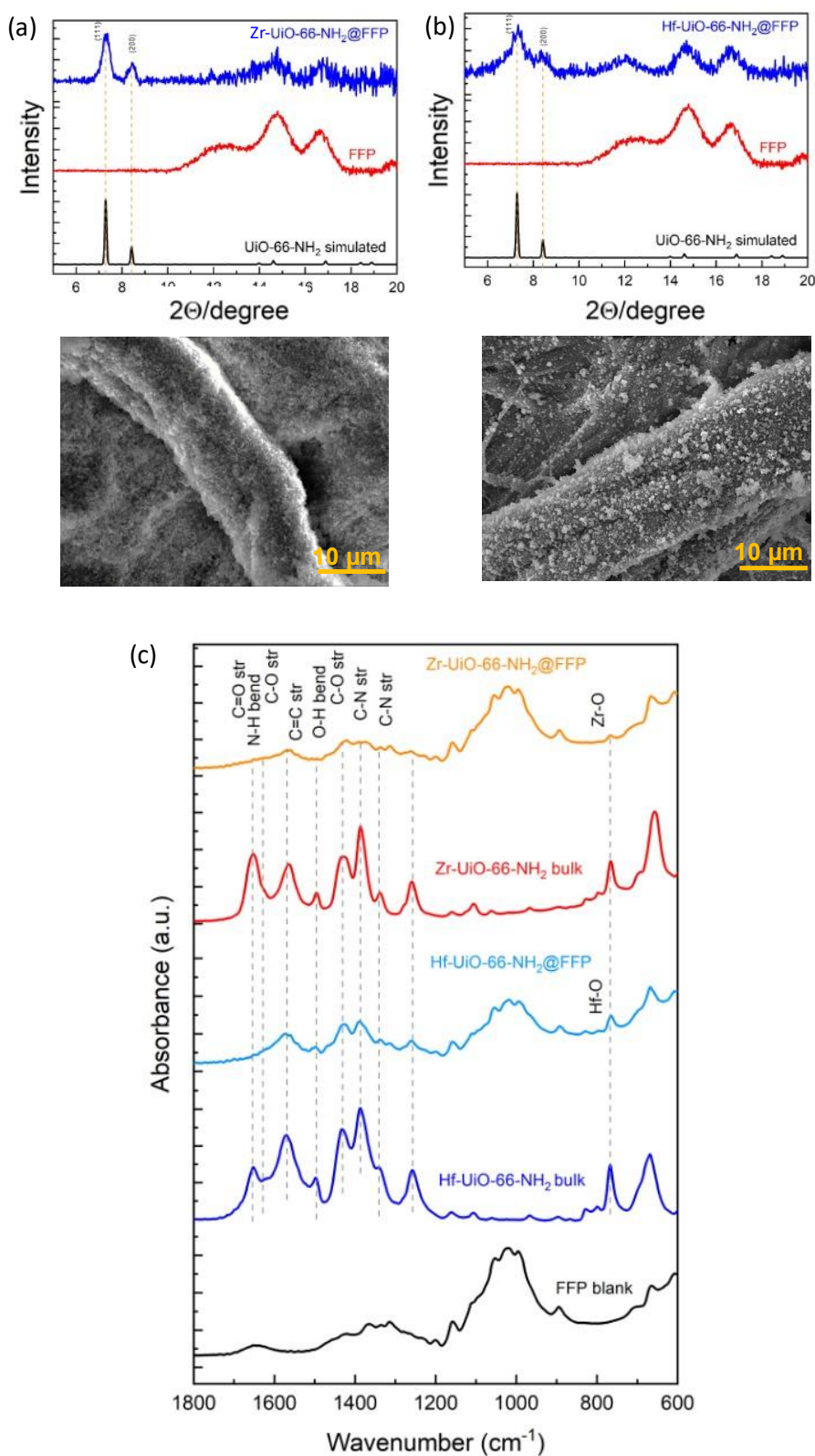


Figure 64 – XRD patterns and SEM images of (a) Zr- and (b) Hf-UiO-66-NH₂ SURMOF films; (c) IR-ATR spectra

The availability of monolithic, pinhole-free MOF coatings on different substrates is crucial for various membrane applications [100], including medical use, water treatment, gas separation as well as catalysis.

7.4 Conclusion

The flow cell synthesis method effectively produced Hf-UiO-66-NH₂ SURMOF on gold-coated Si substrates. The stability of these Hf-UiO-66-NH₂ SURMOF films was tested in various acidic and alkaline environments (pH 2, 7.5, and 11), showing consistency with previous findings for Zr-UiO-66-NH₂@gold SURMOF. The Hf-UiO-66-NH₂ films retained their highly crystalline structure after 24 hours in highly acidic (pH 2) and neutral (pH 7.5) conditions, but exhibited significant instability in a pH 11 basic solution.

Future research should address the need to examine the performance impact of MOF materials, beyond preserving crystallinity and morphology, by evaluating factors like adsorption behavior and surface area. Concurrently, the optimization of UiO-66-NH₂ SURMOF films' quality, especially in acidic and mildly basic conditions, should be pursued.

Zr- and Hf-UiO-66-NH₂ SURMOFs were successfully fabricated on cost-effective cellulose substrates using dip-coating and flow cell methods, respectively. These membranes present numerous potential applications, with water treatment, gas separation, and catalysis being particularly promising. Consequently, this study represents a significant advancement in the development and application of Zr- and Hf-SURMOF-based materials.

7.5 Outlook

Our further steps in this research are as follows:

1) Testing Dip-Coating Method for synthesis of Hf-UiO-66-NH₂ SURMOF: We aim to explore the dip-coating method for the preparation of Hf-

UiO-66-NH₂ SURMOF membranes. This method will be evaluated for its efficacy in achieving uniform and consistent coatings on larger substrates.

2) **Stability Testing of Hf-UiO-66-NH₂@Gold at pH 10:** We plan to test the stability of Hf-UiO-66-NH₂@gold samples under pH 10 conditions. The results will be compared with the previously published stability data of Zr-UiO-66-NH₂@gold membranes [117]. This comparative analysis will provide insights into the relative durability and performance of Hf-based UiO-66-NH₂ SURMOFs versus Zr-based ones in a milder (than pH 11) alkaline environment.

3) **Application Testing for Water Treatment:** Both Zr- and Hf-UiO-66-NH₂ membranes will be tested for water treatment applications. This involves evaluating their effectiveness in removing contaminants from water, assessing parameters such as selectivity, flux, and long-term operational stability. The outcomes will help determine the practical applicability of these MOF membranes in addressing water treatment challenges.

By pursuing these steps, we aim to enhance the synthesis, stability, and application potential of MOF-based membranes, contributing to advancements in membrane technology for environmental and industrial applications.

8 Chapter VIII. NU-1000 SURMOF/thin film for enzymes immobilization

8.1 Introduction

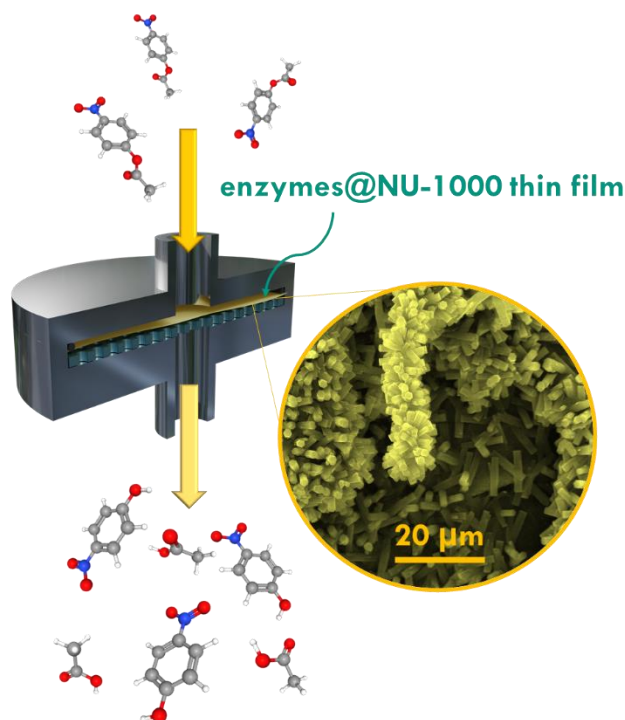
Enzymes are biological catalysts that accelerate chemical reactions by lowering the activation energy required. They are crucial in various biological processes and industrial applications, including pharmaceuticals, food processing, and biofuel production, due to their high specificity and efficiency. However, using enzymes in catalysis poses significant challenges, primarily due to their instability and difficulty in recovering and reusing them, which increases costs and limits their practical applications [271].

One effective way to address these limitations is through enzyme immobilization [272]. Immobilization involves attaching enzymes to a support material, which provides a stable environment for the enzymes to function effectively. Various materials such as natural polymers, synthetic polymers, inorganic materials, and hybrid materials can serve as scaffolds for enzyme immobilization.

Immobilization offers several advantages, including enhanced enzyme stability, improved functionality in extreme conditions, and the ability to recycle enzymes for repeated use in catalytic processes [273]. Among the various scaffolds available for enzyme immobilization, MOFs are particularly well-suited due to their tunable porosity, high surface area, and structural versatility. MOFs provide a stable environment for enzymes, protecting them from denaturation and enhancing their catalytic activity. Specifically, Zr-based MOFs have shown significant advantages in enzyme immobilization, offering high stability and efficient catalytic performance [274, 275].

Immobilization of enzymes into NU-1000 bulk MOF has demonstrated high catalytic efficiency and stability [274, 276]. Despite these promising results, further improvement could be achieved by using MOF thin film membranes instead of bulk materials (Scheme 17). Membranes can handle higher flow rates,

avoid issues like bed splitting and backpressure, and provide a highly oriented structure of NU-1000 crystals, which enhances the immobilization process. Additionally, customized membranes can be designed to accommodate different substrates, making the system more versatile and easier to operate.



Scheme 17 – Continuous flow reactor scheme for catalytic process using a membrane

In summary, NU-1000 thin film membranes for enzyme immobilization present a highly effective solution for continuous catalysis, combining the benefits of MOF stability and enzyme efficiency with the practical advantages of membrane systems. This approach holds significant promise for advancing industrial biocatalytic processes, making them more efficient, sustainable, and adaptable to a wide range of applications

Here, we present a successful method for growing NU-1000 SURMOF on solid substrates, including FGCS, QCM-D sensors, and α -alumina, as well as synthesizing NU-1000 thin films on cellulose membranes (functionalized filter paper, FFP). Additionally, we successfully immobilized enzymes into NU-1000@QCMs using solutions with varying enzyme concentrations.

8.2 Experimental section

8.2.1 Synthesis of NU-1000 SURMOF

NU-1000 SURMOF was prepared using the automated dip coating method using a silar coating system (Holmarc, HO-TH-03B1, India). Two different solutions were prepared. Solution A, the metal ion source, consisted of 37.6 mM (1.05 g) of ZrCl_4 dissolved in 120 mL DEF using an ultrasonicator. To this, 2.813 M (41.25 g) of benzoic acid was added, and the mixture was dissolved until clear using ultrasonication. The final clear mixture was incubated in an oven at 80 °C for 1 hour. Solution B, the organic linker source, consisted of 6.78 mM (0.60 g) H_4TBAPy dissolved in 120 mL DEF using ultrasonication. All solutions were heated to 80 °C and maintained at this temperature during all preparation steps.

Samples were immersed in Solution A for 30 minutes until the hotplates reached the set temperature. The immersion time in the metal ion and linker solutions was 30 minutes, and the washing time in pure solvent (DEF) was 2 minutes. Stirring was applied at each step at 300 rpm. Up to 50 cycles were applied. The resulting NU-1000 SURMOFs were washed with ethanol six times after cooling to room temperature. The samples were then immersed in ethanol for 24 hours. After the washing process, the samples were left to dry overnight in air.

8.2.2 Synthesis of NU-1000 thin films

Solvothermal one-pot synthesis was used (Figure 65). First, 38 mM (0.980 g) of $\text{ZrOCl}_2 \cdot 8\text{H}_2\text{O}$ was dissolved in 80 ml DMF using ultrasonicator. Then 2.76 M (27 g) of benzoic acid was added, and the solution was completely dissolved via ultrasonication. The resulting clear solution was incubated in an oven at 100 °C for 1 hour, then cooled back to room temperature. Functionalized substrates were fixed in a Teflon holder and placed in an autoclave filled with 40 mL of the metal

ion solution, and incubated in the oven at 100 °C for 1 hour. The autoclave was then cooled to room temperature.

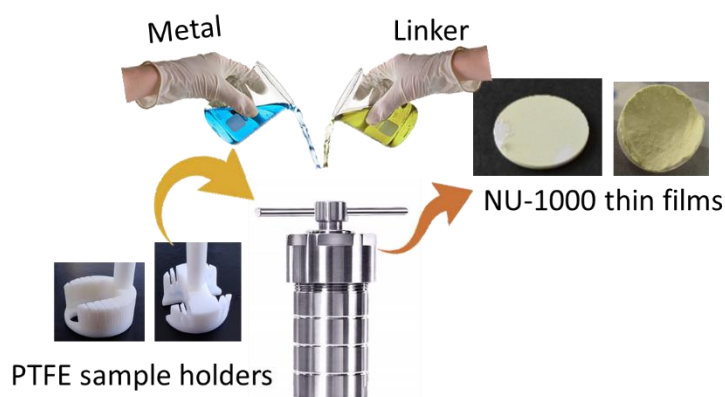


Figure 65 – The preparation process of NU-1000 thin films using custom-machined PTFE holder

Next, 12.18 mM (0.240 g) of H_4TBAPy was added to 60 mL of the second part of the metal ion solution, and the mixture was sonicated for 20 minutes. The metal ion solution from the substrates was disposed of, and the autoclave was filled with the resulting yellow solution and then heated in an oven at 120 °C for 24 hours. After cooling to room temperature, the yellow polycrystalline reaction product was separated by filtration and washed three times with DMF and ethanol. The NU-1000 thin films were immersed in ethanol several times to remove residuals of the NU-1000 bulk (Figure 66). The samples were then immersed in ethanol for 24 hours and dried overnight.

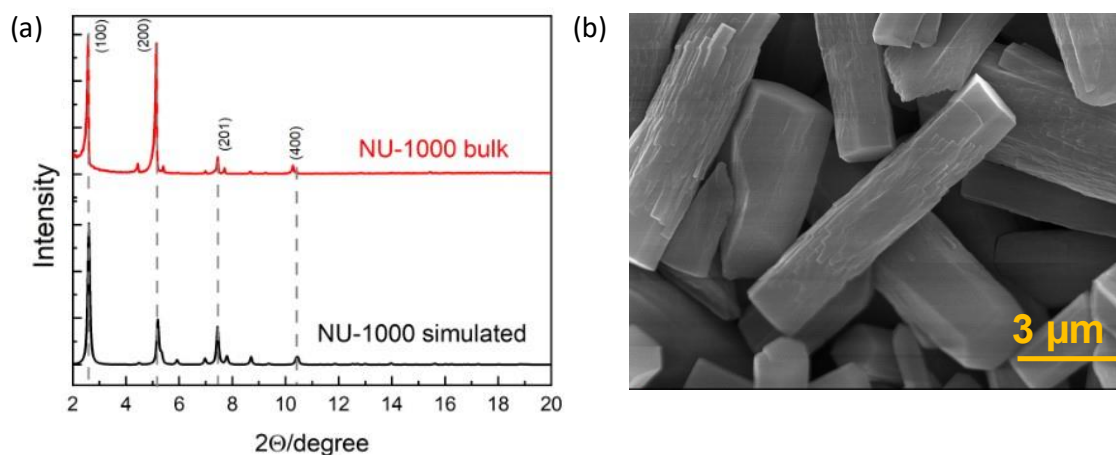


Figure 66 – (a) XRD pattern, (b) SEM image of NU-1000 bulk

8.2.3 Materials for enzyme immobilization

Enzymes were provided and purified by KIT, IBG. The esterase AaEST2-His (EC 3.1.1.1) was prepared as described in [276].

Tris(hydroxymethyl)aminomethane (Tris) and sodium chloride were purchased from Merck, Germany and used as received.

8.2.4 Enzyme immobilization into NU-1000@QCM-D

Operations and control using the openQCM system were performed by Dr. S. Okur (KIT, IFG).

The Teflon cells from the openQCM-D system were used for testing of immobilization of esterase into NU-1000 thin films (Figure 67). The openQCM teflon cell contained a QCM-D sensor with an NU-1000 thin film. Three solutions (water, Tris-buffer saline (TBS), and esterase in TBS) were introduced to the cell via a peristaltic pump, with water serving as a washing agent. Various concentrations of esterase (20 $\mu\text{g/mL}$, 80 $\mu\text{g/mL}$, and 200 $\mu\text{g/mL}$) were tested, and the mass of adsorbed enzymes was calculated using the Sauerbrey equation.

For each concentration, enzyme loading was performed at room temperature (25 °C) for 2 hours, followed by washing with water after each cycle for additional 2 hours. To assess repeatability, the adsorption and desorption cycles were repeated three to four times. A control experiment using TBS without enzymes was conducted to ensure that water effectively removed salts from the thin film surface.

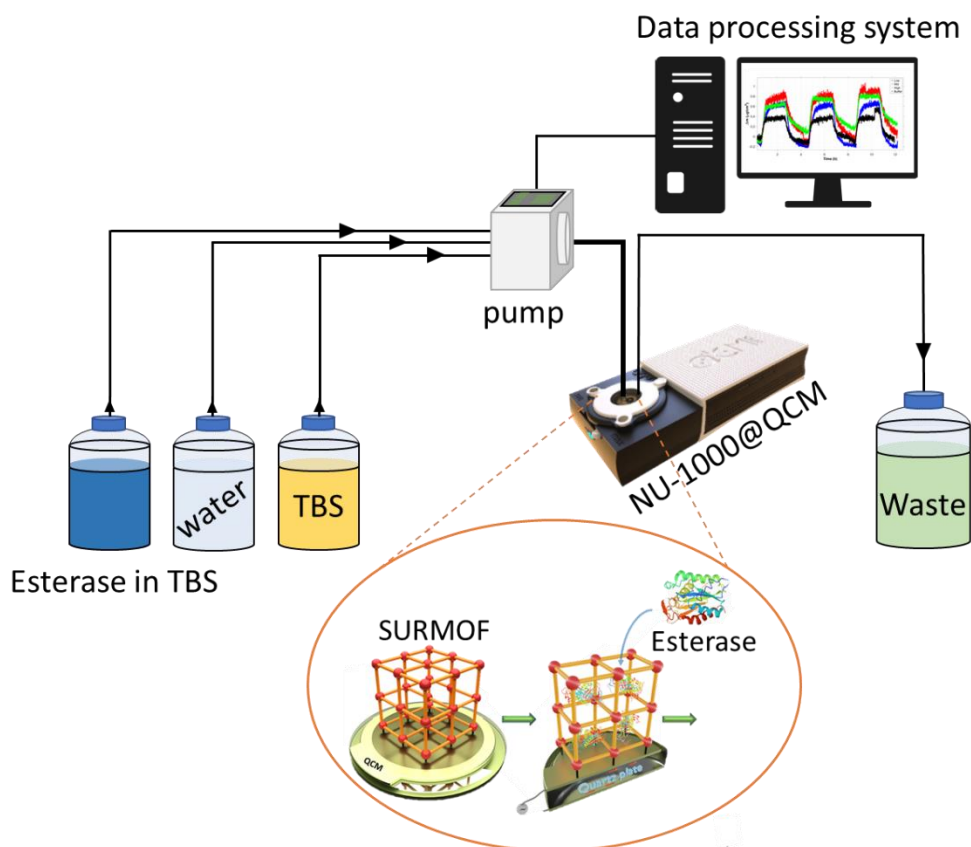


Figure 67 – QCM type experimental setup for enzyme immobilization

The entire setup, control, data acquisition, and analysis of enzyme immobilization data were managed using MATLAB 2021B.

8.3 Results and discussion

The LPE LbL dip-coating method was used to synthesize NU-1000 SURMOF on FGCS (Au-coated Si wafers and Au-coated QCM sensors) and α -alumina substrates, while successfully avoiding polymorphism (NU-901). Based on the analysis of XRD data (Figure 68 (a)) and SEM-results (Figure 68 (b)), showing only hexagonal rods with smooth surfaces), we conclude that the synthesized SURMOFs are exclusively NU-1000. When using FGCS substrates, a high degree of orientation is observed in the resulting films, likely due to the smooth and uniform surface of the gold, which promotes crystallite alignment. In contrast, a greater variety of crystallographic planes are detected on α -alumina

substrates. This difference can be attributed to the initial roughness and high porosity of the α -alumina surface, which disrupts uniform growth and leads to the exposure of multiple planes in the XRD patterns.

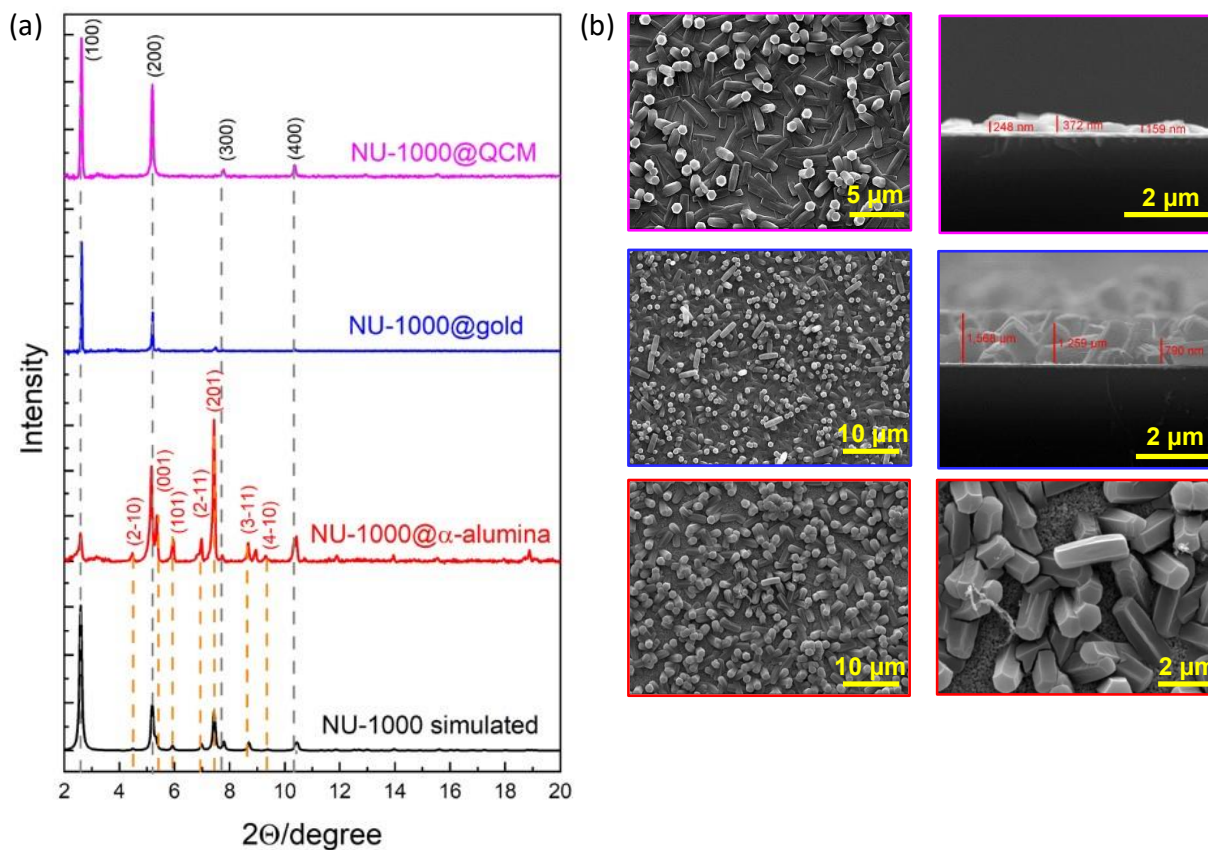


Figure 68 – (a) XRD patterns and (b) SEM images of NU-1000 SURMOFs

Moreover, NU-1000 thin films were grown on a cost-effective substrate, cellulose. Functionalized filter paper [123] was used as the cellulose substrate for better attachment. Resulting XRD, IR and SEM analysis confirmed synthesis of NU-1000 crystals on the cellulose substrate (Figure 69).

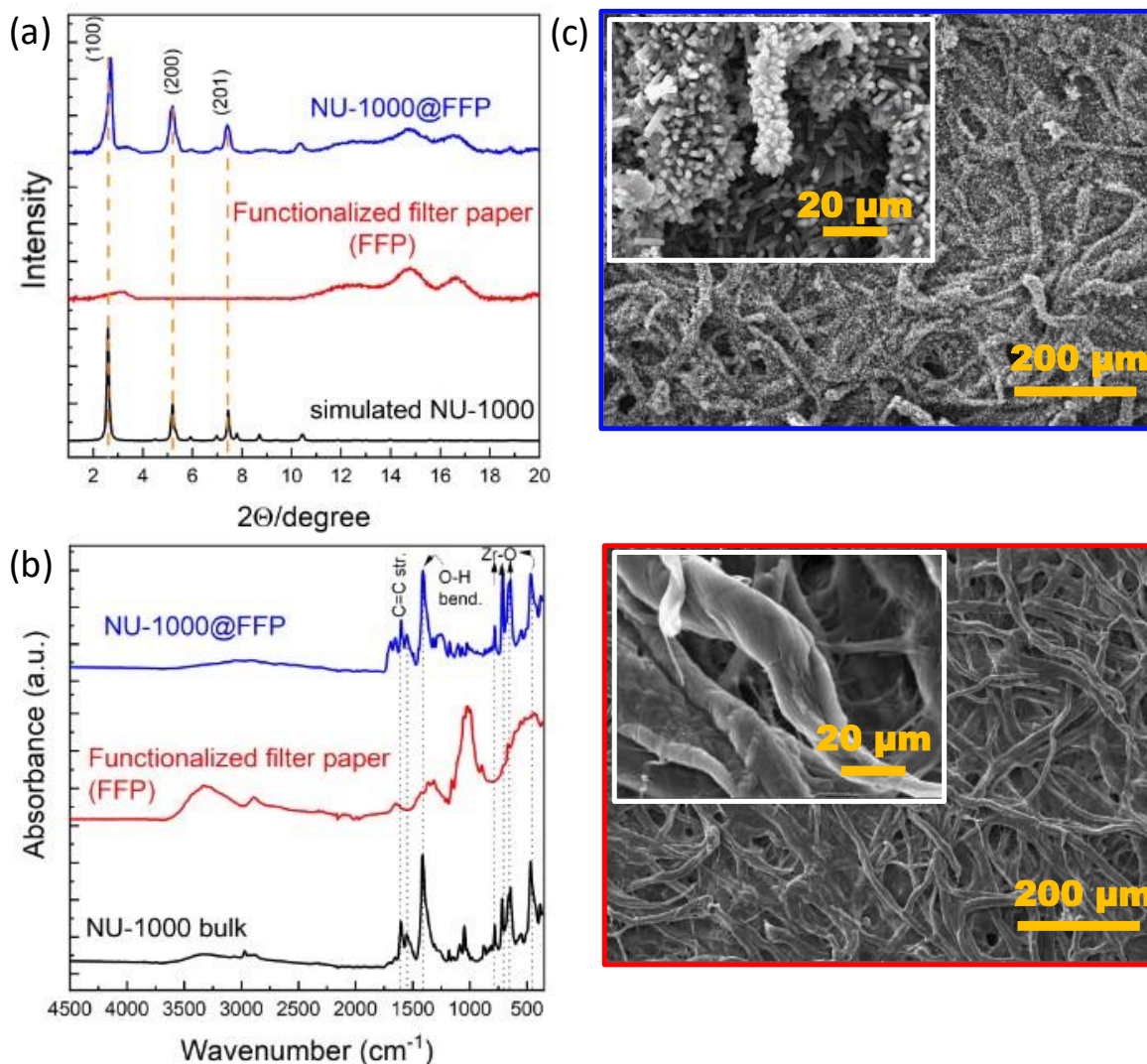


Figure 69 – (a) XRD, (b) IR and (c) SEM data of NU-1000 thin films on the cellulose substrate

In order to confirm possibility of enzymes immobilization into NU-1000@QCM films, an initial experiment was done using openQCM system. The recombinant esterase AaEST2 (molecular weight of 35 kDa), purified to at least 98%, was chosen for this study. PXRD confirmed crystallinity of NU-1000@QCM thin films (Figure 70).

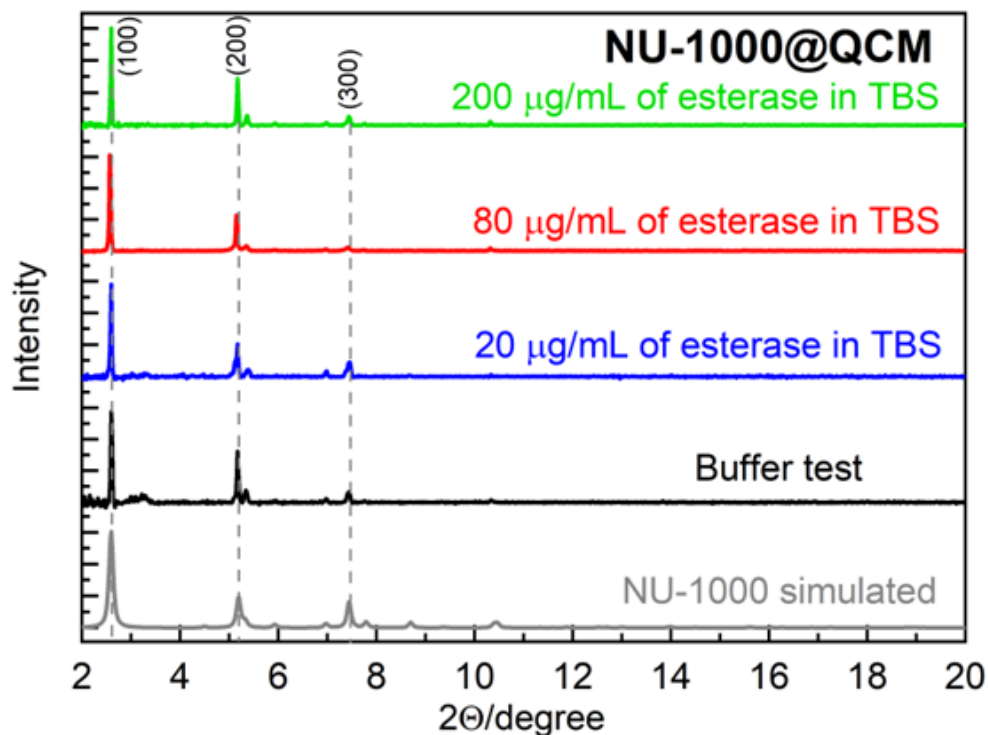


Figure 70 – PXRD data of NU-1000@QCM films before enzyme immobilization process

Initially, water was tested as a washing agent to confirm its effectiveness in removing salts from TBS and to ensure that the buffer itself did not affect mass uptake (Figure 71). Initially, the cell was filled with water to setup the baseline. Then, TBS was introduced into the openQCM cell to monitor mass uptake. After 2 h the cell was flushed with water in order to remove any molecules that might have adsorbed onto the surface of the sample. The graph returned to its initial values, confirming the efficiency of water as a washing agent. This process was repeated three times to ensure repeatability.

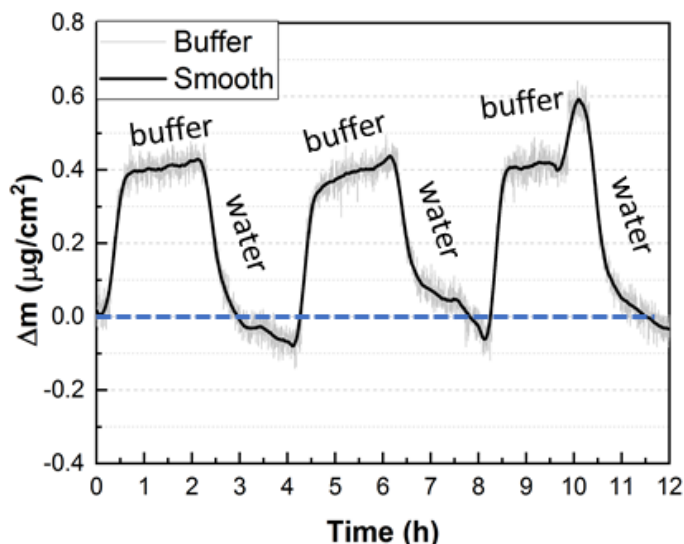


Figure 71 – Uptake results for TRIS buffer saline

Following this, enzyme immobilization was evaluated using three different concentrations (20 $\mu\text{g/mL}$, 80 $\mu\text{g/mL}$, and 200 $\mu\text{g/mL}$) (Figure 72 (a, b, c)). First, all samples were filled with water to establish a baseline. Then, TBS with esterase was introduced into the openQCM cell for 2 h to monitor mass uptake. Afterward, water was used to flush the cell. After washing process a mass uptake of esterase was observed, which might indicate the encapsulation of esterase into the pores of SURMOF. However, a more detailed study needs to be carried out to confirm this claim and demonstrate the actual distribution the enzyme inside the pores of the SURMOF or on the surface. This process was repeated 3-4 times. Since the primary goal of the experiment was to demonstrate enzyme encapsulation, the saturation point was not reached.

The mass uptakes for esterase concentrations of 20 $\mu\text{g/mL}$, 80 $\mu\text{g/mL}$, and 200 $\mu\text{g/mL}$ were 12 ng, 41 ng, and 201 ng, respectively, indicating a higher degree of enzyme immobilization with increasing enzyme concentration. It can be also stated that the increasing slope of the baseline with increasing enzyme concentration might also come from a thickness increase of a decorating enzyme layer and this why a more detailed study is required.

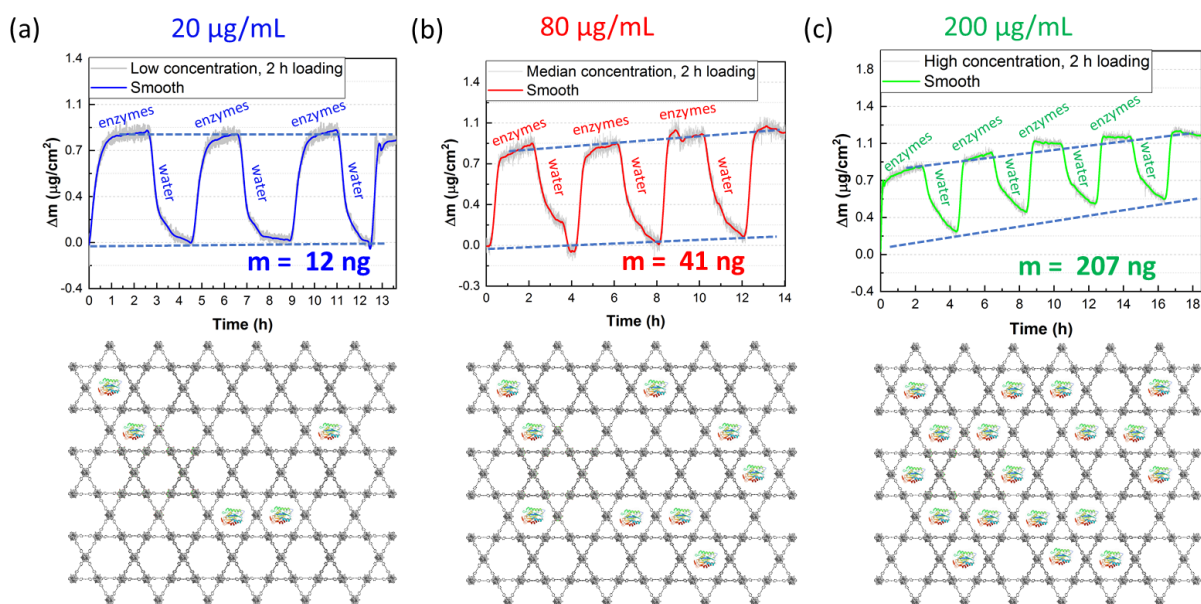


Figure 72 – **Top**: Uptake results for esterase immobilization at different concentrations: (a) 20 µg/mL, (b) 80 µg/mL, and (c) 200 µg/mL. **Bottom**: Schematic representation of MOF pores with varying percentages of pore filling by the immobilized enzyme

The amounts of immobilized esterase were calculated to be 2.07×10^{11} molecules, 7.04×10^{11} , and 3.56×10^{12} , respectively. Considering the dimensions of NU-1000 MOF (Figure 73) and the AaEST2 ($45 \times 32 \times 32 \text{ \AA}^3$) it was determined that at least 3 unit cells of NU-1000 are required to encapsulate a single esterase molecule. Given the working area of the QCM sensor (113.1 mm^2) and an approximate MOF thickness of 250 nm, the estimated volume of the MOF film on the substrate is 0.0283 mm^3 . The maximum amount of esterase that could be encapsulated in this volume is 232.4 ng, indicating that the different concentrations of esterase achieved approximately 5.2%, 17.6%, and 89.1%, of the maximum capacity, respectively.

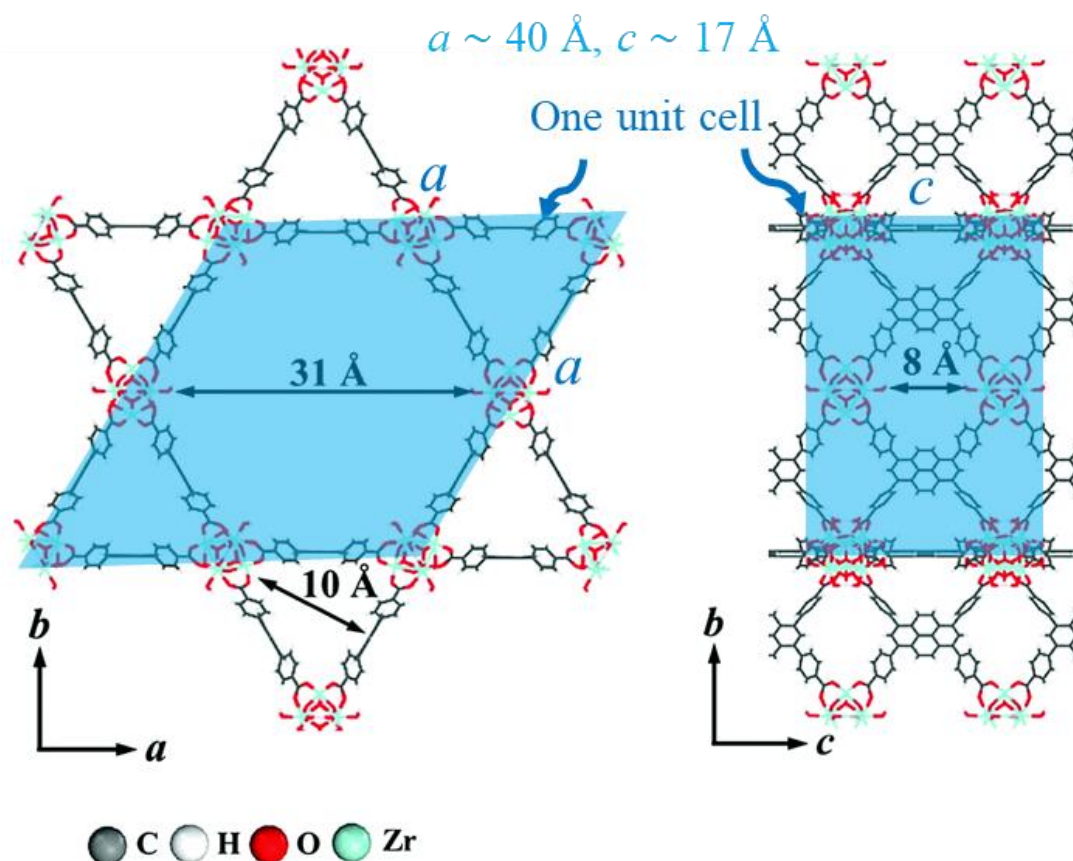


Figure 73 – The dimension of NU-1000: the hexagonal and triangular channels along the c direction (left), and the small pore connecting the ab layers along the c direction (right).
Edited from [277] with permission from the Royal Society of Chemistry

The results described above gives an initial description and rational of the immobilization of esterase into the NU-1000 SURMOF.

8.4 Conclusion

In summary, we successfully demonstrated the synthesis and application of NU-1000 SURMOF on various solid substrates, including Au-coated Si wafers, QCM-D sensors, and α -alumina substrates, as well as NU-1000 thin films on cellulose membranes. Our synthesis methods effectively prevented polymorphism, ensuring the exclusive formation of NU-1000 crystals.

Furthermore, our experiment showed that the successful immobilization of recombinant esterase AaEST2 into the NU-1000 MOF thin films could be done, but further confirmation experiments are required.

8.5 Outlook

Our further steps in this research are as follows:

1) **Repeating and Investigating the Immobilization of Esterase into NU-1000@QCM:** We will conduct additional experiments to refine the immobilization process, explore the detailed interaction mechanisms, and specifically investigate and confirm that the enzymes are immobilized within the pores of NU-1000, rather than merely adhering to the surface.

2) **Performing Continuous catalysis Tests for Membranes:** We will compare the results achieved using bulk and membrane technologies to evaluate the effectiveness of the membrane approach.

3) **Exploring Organic Solvent Stability:** Since encapsulation into MOF thin films is expected to enhance enzyme stability under harsh conditions, we will evaluate the performance of enzyme@NU-1000 membranes in various organic solvents. This will involve testing solvents such as ethanol, methanol, and acetone, and assessing the catalytic activity, stability, and reusability of the immobilized enzymes.

By pursuing these steps, we aim to improve the stability and application potential of enzyme@MOF thin film membranes, advancing biocatalysis and membrane technology for a range of industrial and environmental applications.

9 Chapter IX. Conclusion and Outlook

This study presents significant advancements in the synthesis, characterization, modification, and application of highly stable Zr(Hf)-based SURMOFs. The findings demonstrate the potential of these materials in various technical applications, from superhydrophobic substrates to gravimetric sensor platforms and selective QCM-sensor arrays.

The successful fabrication of low-roughness **superhydrophobic substrates** was achieved by grafting C18 hydrocarbon chains onto UiO-66-NH₂ SURMOFs. This post-functionalization transformed the initially wetting SURMOFs into superhydrophobic surfaces with water contact angles exceeding 150°. The remarkable water repellency was attributed to the high entropy state of the coiled C18 hydrocarbons, which was not observed in substrates functionalized with less flexible fluorinated compounds. Additionally, the roughness of the SURMOFs influenced water adhesion strength, with higher roughness reducing adhesion strength significantly. These findings suggest potential applications in creating self-cleaning surfaces due to the low adhesion strength of the superhydrophobic substrates.

A novel **gravimetric sensor platform** based on UiO-66-X SURMOFs was introduced, demonstrating exceptional stability and high accuracy in VOC detection under severe conditions. The sensor array, utilizing variations X = NH₂, Cl, and N₃, achieved near 100% discrimination accuracy at saturated vapor pressure and high accuracy (74.8%-99.9%) at lower concentrations. Detection limits varied between 19 and 440 ppm. The QCM-based sensors showcased versatility, with future potential in expanding detection capabilities by functionalizing the -NH₂ side groups in UiO-66-NH₂ SURMOF. This E-Nose platform represents a robust and sensitive method for VOC detection.

Moreover, the highly stable and functionalized **UiO-66-X SURMOF QCM-sensor array** highlighted its ability to accurately distinguish between various

liquids. The functionalized sensors demonstrated enhanced performance and stability in humid and acidic environments. The robustness and functionalizability of these SURMOFs make them ideal candidates for environmental monitoring, quality control in the food and beverage industries, and medical diagnostics. The integration with machine learning techniques further enhances the effectiveness and reliability of this E-Tongue system.

The LPE LbL dip coating and flow cell synthesis methods effectively produced **Zr- and Hf-UiO-66-NH₂ SURMOF films on different substrates** including membranes. The high stability of Hf-UiO-66-NH₂@gold was demonstrated in acidic and neutral environments, but instability was observed in basic conditions. The films retained their crystalline structure in pH 2 and 7.5 conditions. These results are consistent with those for Zr-UiO-66-NH₂@gold. This study represents significant advancements in the development and application of Zr- and Hf-SURMOF-based materials, with promising potential in water treatment, gas separation, and catalysis.

The synthesis of **NU-1000 thin films on various substrates** was successfully demonstrated, and an initial test of enzyme immobilization into NU-1000@QCM sensors showed promising results. However, more detailed analysis is required to confirm that the enzymes are immobilized within the pores. The achieved results provide a strong foundation for future research in enzyme immobilization within SURMOFs and the use of those immobilized enzymes in catalysis.

References

1. Yaghi OM, Kalmutzki MJ, Diercks CS. Introduction to reticular chemistry: metal-organic frameworks and covalent organic frameworks: John Wiley & Sons; 2019.
2. Yaghi OM, Li H. Hydrothermal synthesis of a metal-organic framework containing large rectangular channels. *Journal of the American Chemical Society*. 1995;117(41):10401-2.
3. Moghadam PZ, Li A, Liu X-W, Bueno-Perez R, Wang S-D, Wiggin SB, Wood PA, Fairen-Jimenez D. Targeted classification of metal-organic frameworks in the Cambridge structural database (CSD). *Chemical science*. 2020;11(32):8373-87.
4. Moosavi SM, Nandy A, Jablonka KM, Ongari D, Janet JP, Boyd PG, Lee Y, Smit B, Kulik HJ. Understanding the diversity of the metal-organic framework ecosystem. *Nature Communications*. 2020;11(1):1-10.
5. Kitagawa S. Metal-organic frameworks (MOFs). *Chemical Society Reviews*. 2014;43(16):5415-8.
6. Yaghi OM. Reticular Chemistry — Construction, Properties, and Precision Reactions of Frameworks. ACS Publications; 2016. p. 15507-9.
7. Yuan S, Qin J-S, Lollar CT, Zhou H-C. Stable metal-organic frameworks with group 4 metals: current status and trends. *ACS Central Science*. 2018;4(4):440-50.
8. Lu W, Wei Z, Gu Z-Y, Liu T-F, Park J, Park J, Tian J, Zhang M, Zhang Q, Gentle Iii T. Tuning the structure and function of metal-organic frameworks via linker design. *Chemical Society Reviews*. 2014;43(16):5561-93.
9. Furukawa H, Cordova KE, O'Keeffe M, Yaghi OM. The chemistry and applications of metal-organic frameworks. *Science*. 2013;341(6149):1230444.
10. Bae YS, Snurr RQ. Development and evaluation of porous materials for carbon dioxide separation and capture. *Angewandte Chemie International Edition*. 2011;50(49):11586-96.
11. Li H, Eddaoudi M, O'Keeffe M, Yaghi OM. Design and synthesis of an exceptionally stable and highly porous metal-organic framework. *Nature*. 1999;402(6759):276-9.
12. Baumann AE, Burns DA, Liu B, Thoi VS. Metal-organic framework functionalization and design strategies for advanced electrochemical energy storage devices. *Communications Chemistry*. 2019;2(1):86.
13. Bon V, Kavoosi N, Senkovska I, Müller P, Schaber J, Wallacher D, Többs DM, Mueller U, Kaskel S. Tuning the flexibility in MOFs by SBU functionalization. *Dalton Transactions*. 2016;45(10):4407-15.
14. Wang Z, Bilegsaikhani A, Jerozal RT, Pitt TA, Milner PJ. Evaluating the robustness of metal-organic frameworks for synthetic chemistry. *ACS Applied Materials & Interfaces*. 2021;13(15):17517-31.

15. Rubio-Martinez M, Avci-Camur C, Thornton AW, Imaz I, Maspoch D, Hill MR. New synthetic routes towards MOF production at scale. *Chemical Society Reviews*. 2017;46(11):3453-80.
16. Yitong H, Hong Y, Xinwen G. Synthesis methods and crystallization of MOFs. In: Riadh M, editor. *Synthesis Methods and Crystallization*. Rijeka: IntechOpen; 2020. p. Ch. 5.
17. Férey G. Hybrid porous solids: past, present, future. *Chemical Society Reviews*. 2008;37(1):191-214.
18. Kamal K, Bustam MA, Ismail M, Grekov D, Mohd Shariff A, Pré P. Optimization of washing processes in solvothermal synthesis of nickel-based MOF-74. *Materials*. 2020;13(12).
19. Ma D, Huang X, Zhang Y, Wang L, Wang B. Metal-organic frameworks: Synthetic methods for industrial production. *Nano Research*. 2023;16(5):7906-25.
20. Ni Z, Masel RI. Rapid production of metal-organic frameworks via microwave-assisted solvothermal synthesis. *Journal of the American Chemical Society*. 2006;128(38):12394-5.
21. Kong Y-R, Zhang R, Zhang J, Luo H-B, Liu Y, Zou Y, Ren X-M. Microwave-assisted rapid synthesis of nanoscale MOF-303 for hydrogel composites with superior proton conduction at ambient-humidity conditions. *ACS Applied Energy Materials*. 2021;4(12):14681-8.
22. Vaitsis C, Sourkouni G, Argirusis C. Metal organic frameworks (MOFs) and ultrasound: A review. *Ultrasonics Sonochemistry*. 2019;52:106-19.
23. Safarifard V, Morsali A. Applications of ultrasound to the synthesis of nanoscale metal-organic coordination polymers. *Coordination Chemistry Reviews*. 2015;292:1-14.
24. Liu Y, Wei Y, Liu M, Bai Y, Wang X, Shang S, Chen J, Liu Y. Electrochemical synthesis of large area two-dimensional metal-organic framework films on copper anodes. *Angewandte Chemie International Edition*. 2021;60(6):2887-91.
25. Wei J-Z, Wang X-L, Sun X-J, Hou Y, Zhang X, Yang D-D, Dong H, Zhang F-M. Rapid and large-scale synthesis of IRMOF-3 by electrochemistry method with enhanced fluorescence detection performance for TNP. *Inorganic Chemistry*. 2018;57(7):3818-24.
26. Tao C-A, Wang J-F. Synthesis of metal-organic frameworks by ball-milling. *Crystals*. 2021;11(1).
27. Ahmadi M, Ebrahimnia M, Shahbazi M-A, Keçili R, Ghorbani-Bidkorbeh F. Microporous metal-organic frameworks: synthesis and applications. *Journal of Industrial and Engineering Chemistry*. 2022;115:1-11.
28. Nalaparaju A, Jiang J. Metal-organic frameworks for liquid phase applications. *Advanced Science*. 2021;8(5):2003143.
29. Lu Z, Du L, Guo R, Zhang G, Duan J, Zhang J, Han L, Bai J, Hupp JT. Double-walled Zn₃₆@Zn₁₀₄ multicomponent senary metal-organic polyhedral

framework and its isorecticular evolution. *Journal of the American Chemical Society*. 2021;143(43):17942-6.

30. Hu J, Wang Y, Wu L. Selective separation of gases by metal organic framework Materials (MOFs). *Journal of Physics: Conference Series*. 2022;2194(1):012005.

31. Lin X, Jia J, Zhao X, Thomas KM, Blake AJ, Walker GS, Champness NR, Hubberstey P, Schröder M. High H₂ adsorption by coordination-framework materials. *Angewandte Chemie International Edition*. 2006;45(44):7358-64.

32. Gándara F, Furukawa H, Lee S, Yaghi OM. High methane storage capacity in aluminum metal–organic frameworks. *Journal of the American Chemical Society*. 2014;136(14):5271-4.

33. Luebbers MT, Wu T, Shen L, Masel RI. Trends in the adsorption of volatile organic compounds in a large-pore metal–organic framework, IRMOF-1. *Langmuir*. 2010;26(13):11319-29.

34. Li B, Wen H-M, Zhou W, Chen B. Porous metal–organic frameworks for gas storage and separation: What, how, and why? *The Journal of Physical Chemistry Letters*. 2014;5(20):3468-79.

35. Rodenas T, Luz I, Prieto G, Seoane B, Miro H, Corma A, Kapteijn F, Llabrés i Xamena FX, Gascon J. Metal–organic framework nanosheets in polymer composite materials for gas separation. *Nature Materials*. 2015;14(1):48-55.

36. Cheng Y, Datta SJ, Zhou S, Jia J, Shekhah O, Eddaoudi M. Advances in metal–organic framework-based membranes. *Chemical Society Reviews*. 2022;51(19):8300-50.

37. Lee J, Farha OK, Roberts J, Scheidt KA, Nguyen ST, Hupp JT. Metal–organic framework materials as catalysts. *Chemical Society Reviews*. 2009;38(5):1450-9.

38. Liu J, Chen L, Cui H, Zhang J, Zhang L, Su C-Y. Applications of metal–organic frameworks in heterogeneous supramolecular catalysis. *Chemical Society Reviews*. 2014;43(16):6011-61.

39. Gu Z-Y, Park J, Raiff A, Wei Z, Zhou H-C. Metal–organic frameworks as biomimetic catalysts. *ChemCatChem*. 2014;6(1):67-75.

40. Chen C, Fei L, Wang B, Xu J, Li B, Shen L, Lin H. MOF-based photocatalytic membrane for water purification: A review. *Small*. 2024;20(1):2305066.

41. Zhang H, Lou L-L, Yu K, Liu S. Advances in chiral metal–organic and covalent organic frameworks for asymmetric catalysis. *Small*. 2021;17(22):2005686.

42. Sun Y, Zheng L, Yang Y, Qian X, Fu T, Li X, Yang Z, Yan H, Cui C, Tan W. Metal–organic framework nanocarriers for drug delivery in biomedical applications. *Nano-Micro Letters*. 2020;12(1):103.

43. Zong Z, Tian G, Wang J, Fan C, Yang F, Guo F. Recent advances in metal–organic framework-based nanocarriers for controllable drug delivery and release. *Pharmaceutics*. 2022;14(12).
44. Cai M, Chen G, Qin L, Qu C, Dong X, Ni J, Yin X. Metal organic frameworks as drug targeting delivery vehicles in the treatment of cancer. *Pharmaceutics*. 2020;12(3).
45. Wu MX, Yang YW. Metal–organic framework (MOF)-based drug/cargo delivery and cancer therapy. *Advanced Materials*. 2017;29(23):1606134.
46. Rana A. Metal-organic frameworks for the removal of heavy metals from water. *Prayogik Rasayan*. 2020;4(3):20-3.
47. Agamendran N, Uddin M, Yesupatham MS, Shanmugam M, Augustin A, Kundu T, Kandasamy R, Sasaki K, Sekar K. Nanoarchitectonics design strategy of metal–organic framework and bio-metal–organic framework composites for advanced wastewater treatment through adsorption. *Langmuir*. 2024;40(7):3320-42.
48. Saravanan A, Kumar PS, Rangasamy G. Removal of toxic pollutants from industrial effluent: Sustainable approach and recent advances in metal–organic framework. *Industrial & Engineering Chemistry Research*. 2022;61(43):15754-65.
49. Shukla AK, Alam J, Alhoshan MS, Ali FAA, Mishra U, Hamid AA. Thin-film nanocomposite membrane incorporated with porous Zn-based metal–organic frameworks: Toward enhancement of desalination performance and chlorine resistance. *ACS Applied Materials & Interfaces*. 2021;13(24):28818-31.
50. Cao Z, Liu V, Barati Farimani A. Water desalination with two-dimensional metal–organic framework membranes. *Nano Letters*. 2019;19(12):8638-43.
51. Wang H-T, Ao D, Lu M-C, Chang N. Alteration of the morphology of polyvinylidene fluoride membrane by incorporating MOF-199 nanomaterials for improving water permeation with antifouling and antibacterial property. *Journal of the Chinese Chemical Society*. 2020;67(10):1807-17.
52. Xu W, Zhuang H, Xu Z, Huang M, Gao S, Li Q, Zhang G. Design and construction of Ag@MOFs immobilized PVDF ultrafiltration membranes with anti-bacterial and antifouling properties. *Advances in Polymer Technology*. 2020;2020:5456707.
53. Rojas S, Horcajada P. Metal–organic frameworks for the removal of emerging organic contaminants in water. *Chemical Reviews*. 2020;120(16):8378-415.
54. Liu K, Zhang S, Hu X, Zhang K, Roy A, Yu G. Understanding the adsorption of PFOA on MIL-101(Cr)-based anionic-exchange metal–organic frameworks: Comparing DFT calculations with aqueous sorption experiments. *Environmental Science & Technology*. 2015;49(14):8657-65.
55. Li R, Alomari S, Islamoglu T, Farha OK, Fernando S, Thagard SM, Holsen TM, Wriedt M. Systematic study on the removal of per- and polyfluoroalkyl

substances from contaminated groundwater using metal–organic frameworks. *Environmental Science & Technology*. 2021;55(22):15162-71.

56. Ondrušová S, Bůžek D, Kloda M, Rohlíček J, Adamec S, Pospíšil M, Janoš P, Demel J, Hynek J. Linker-functionalized phosphinate metal–organic frameworks: Adsorbents for the removal of emerging pollutants. *Inorganic Chemistry*. 2023;62(38):15479-89.

57. Stassen I, Burtch N, Talin A, Falcaro P, Allendorf M, Ameloot R. An updated roadmap for the integration of metal–organic frameworks with electronic devices and chemical sensors. *Chemical Society Reviews*. 2017;46(11):3185-241.

58. Stavila V, Talin AA, Allendorf MD. MOF-based electronic and optoelectronic devices. *Chemical Society Reviews*. 2014;43(16):5994-6010.

59. Wang H, Zhu Q-L, Zou R, Xu Q. Metal-organic frameworks for energy applications. *Chem*. 2017;2(1):52-80.

60. Qin M. Metal-organic frameworks (MOFs) for building applications: DTU Building Physics Research Report; 2020. 87 p.

61. Lugier O, Pokharel U, Castellanos S. Impact of synthetic conditions on the morphology and crystallinity of FDMOF-1(Cu) thin films. *Crystal Growth & Design*. 2020;20(8):5302-9.

62. Zacher D, Shekhah O, Wöll C, Fischer RA. Thin films of metal–organic frameworks. *Chemical Society Reviews*. 2009;38(5):1418-29.

63. Chen D-H, Gliemann H, Wöll C. Layer-by-layer assembly of metal-organic framework thin films: Fabrication and advanced applications. *Chemical Physics Reviews*. 2023;4(1):011305.

64. Zhuang J-L, Kind M, Grytz CM, Farr F, Diefenbach M, Tussupbayev S, Holthausen MC, Terfort A. Insight into the oriented growth of surface-attached metal–organic frameworks: Surface functionality, deposition temperature, and first layer order. *Journal of the American Chemical Society*. 2015;137(25):8237-43.

65. Shekhah O, Liu J, Fischer RA, Wöll C. MOF thin films: existing and future applications. *Chemical Society Reviews*. 2011;40(2):1081-106.

66. Liu J, Wöll C. Surface-supported metal–organic framework thin films: fabrication methods, applications, and challenges. *Chemical Society Reviews*. 2017;46(19):5730-70.

67. Zhuang J-L, Terfort A, Wöll C. Formation of oriented and patterned films of metal–organic frameworks by liquid phase epitaxy: A review. *Coordination Chemistry Reviews*. 2016;307:391-424.

68. Bradshaw D, Garai A, Huo J. Metal–organic framework growth at functional interfaces: thin films and composites for diverse applications. *Chemical Society Reviews*. 2012;41(6):2344-81.

69. Ohnsorg ML, Beaudoin CK, Anderson ME. Fundamentals of MOF thin film growth via liquid-phase epitaxy: investigating the initiation of deposition and the influence of temperature. *Langmuir*. 2015;31(22):6114-21.

70. Xiao Y-H, Gu Z-G, Zhang J. Surface-coordinated metal–organic framework thin films (SURMOFs) for electrocatalytic applications. *Nanoscale*. 2020;12(24):12712-30.
71. Self-Assembled monolayer Wikimedia Commons [updated 28.08.2023. Available from: https://commons.wikimedia.org/w/index.php?title=File:Self-assembled_monolayer.svg&oldid=796575576.
72. Mandemaker LDB, Jabbour C, Nikolopoulos N, Dorresteyn JM, Rivera-Torrente M, Weckhuysen BM. The growth of metal–organic framework films on calcium fluoride and their interaction with reactive molecules. *Advanced Materials Interfaces*. 2023;10(5):2201753.
73. Zhang B, Zhang J, Liu C, Sang X, Peng L, Ma X, Wu T, Han B, Yang G. Solvent determines the formation and properties of metal-organic framework. *RSC Adv*. 2015;5.
74. Shekhah O, Wang H, Kowarik S, Schreiber F, Paulus M, Tolan M, Sternemann C, Evers F, Zacher D, Fischer RA, Wöll C. Step-by-step route for the synthesis of metal–organic frameworks. *Journal of the American Chemical Society*. 2007;129(49):15118-9.
75. Gu Z-G, Zhang J. Epitaxial growth and applications of oriented metal–organic framework thin films. *Coordination Chemistry Reviews*. 2019;378:513-32.
76. Shekhah O. Layer-by-layer method for the synthesis and growth of surface mounted metal-organic frameworks (SURMOFs). *Materials*. 2010;3(2):1302-15.
77. Fischer RA, Wöll C. Layer-by-layer liquid-phase epitaxy of crystalline coordination polymers at surfaces. *Angewandte Chemie International Edition*. 2009;48(34):6205-8.
78. Wang Z, Wöll C. Fabrication of metal–organic framework thin films using programmed layer-by-layer assembly techniques. *Advanced Materials Technologies*. 2019;4(5):1800413.
79. Heinke L, Wöll C. Surface-mounted metal–organic frameworks: crystalline and porous molecular assemblies for fundamental insights and advanced applications. *Advanced Materials*. 2019;31(26):1806324.
80. Munuera C, Shekhah O, Wang H, Wöll C, Ocal C. The controlled growth of oriented metal–organic frameworks on functionalized surfaces as followed by scanning force microscopy. *Physical Chemistry Chemical Physics*. 2008;10(48):7257-61.
81. Gu Z-G, Pfriem A, Hamsch S, Breitwieser H, Wohlgemuth J, Heinke L, Gliemann H, Wöll C. Transparent films of metal-organic frameworks for optical applications. *Microporous and Mesoporous Materials*. 2015;211:82-7.
82. Delen G, Ristanović Z, Mandemaker LDB, Weckhuysen BM. Mechanistic insights into growth of surface-mounted metal-organic framework films resolved by infrared (nano-) spectroscopy. *Chemistry – A European Journal*. 2018;24(1):187-95.

83. Arslan HK, Shekhah O, Wohlgemuth J, Franzreb M, Fischer RA, Wöll C. High-throughput fabrication of uniform and homogenous MOF coatings. *Advanced Functional Materials*. 2011;21(22):4228-31.
84. Hurre S, Friebe S, Wohlgemuth J, Wöll C, Caro J, Heinke L. Sprayable, large-area metal–organic framework films and membranes of varying thickness. *Chemistry – A European Journal*. 2017;23(10):2294-8.
85. Chernikova V, Shekhah O, Eddaoudi M. Advanced fabrication method for the preparation of MOF thin films: Liquid-phase epitaxy approach meets spin coating method. *ACS Applied Materials & Interfaces*. 2016;8(31):20459-64.
86. Monjezi BH, Okur S, Limbach R, Chandresh A, Sen K, Hashem T, Schwotzer M, Wondraczek L, Wöll C, Knebel A. Fast dynamic synthesis of MIL-68 (In) thin films in high optical quality for optical cavity sensing. *ACS Nano*. 2023;17(6):6121-30.
87. Qin P, Okur S, Jiang Y, Heinke L. A MOF-based electronic nose for carbon dioxide sensing with enhanced affinity and selectivity by ionic-liquid embedment. *Journal of Materials Chemistry A*. 2022;10(47):25347-55.
88. Bétard A, Fischer RA. Metal–organic framework thin films: from fundamentals to applications. *Chemical Reviews*. 2012;112(2):1055-83.
89. Liu B, Fischer RA. Liquid-phase epitaxy of metal organic framework thin films. *Science China Chemistry*. 2011;54(12):1851-66.
90. Mazel A, Rocco L, Penin N, Rougier A. Oriented surface-anchored metal–organic frameworks (SurMOFs) as electrochromic thin films. *Advanced Optical Materials*. 2023;11(9):2202939.
91. Yuan S, Feng L, Wang K, Pang J, Bosch M, Lollar C, Sun Y, Qin J, Yang X, Zhang P. Stable metal–organic frameworks: design, synthesis, and applications. *Advanced Materials*. 2018;30(37):1704303.
92. Cavka JH, Jakobsen S, Olsbye U, Guillou N, Lamberti C, Bordiga S, Lillerud KP. A new zirconium inorganic building brick forming metal organic frameworks with exceptional stability. *Journal of the American Chemical Society*. 2008;130(42):13850-1.
93. Schaate A, Roy P, Godt A, Lippke J, Waltz F, Wiebcke M, Behrens P. Modulated synthesis of Zr-based metal–organic frameworks: From nano to single crystals. *Chemistry – A European Journal*. 2011;17(24):6643-51.
94. Lam ITY, Choi S-J, Lu D, Kim Y. Functionalized metal–organic frameworks for heavy metal ion removal from water. *Nanoscale*. 2023;15(24):10189-205.
95. Yaghi OM, Li G, Li H. Selective binding and removal of guests in a microporous metal–organic framework. *Nature*. 1995;378(6558):703-6.
96. Jakobsen S, Gianolio D, Wragg DS, Nilsen MH, Emerich H, Bordiga S, Lamberti C, Olsbye U, Tilset M, Lillerud KP. Structural determination of a highly stable metal-organic framework with possible application to interim radioactive waste scavenging: Hf-UiO-66. *Physical Review B*. 2012;86(12):125429.

97. Mondloch JE, Bury W, Fairen-Jimenez D, Kwon S, DeMarco EJ, Weston MH, Sarjeant AA, Nguyen ST, Stair PC, Snurr RQ, Farha OK, Hupp JT. Vapor-phase metalation by atomic layer deposition in a metal–organic framework. *Journal of the American Chemical Society*. 2013;135(28):10294-7.
98. Furukawa H, Gándara F, Zhang Y-B, Jiang J, Queen WL, Hudson MR, Yaghi OM. Water adsorption in porous metal–organic frameworks and related materials. *Journal of the American Chemical Society*. 2014;136(11):4369-81.
99. Beyzavi H, Klet RC, Tussupbayev S, Borycz J, Vermeulen NA, Cramer CJ, Stoddart JF, Hupp JT, Farha OK. A hafnium-based metal–organic framework as an efficient and multifunctional catalyst for facile CO₂ fixation and regioselective and enantioselective epoxide activation. *Journal of the American Chemical Society*. 2014;136(45):15861-4.
100. Hashem T, Sánchez EPV, Weidler PG, Gliemann H, Alkordi MH, Wöll C. Liquid-phase quasi-epitaxial growth of highly stable, monolithic UiO-66-NH₂ MOF thin films on solid substrates. *ChemistryOpen*. 2020;9(5):515.
101. Matemb Ma Ntep TJ, Reinsch H, Schlüsener C, Goldman A, Breitzke H, Moll B, Schmolke L, Buntkowsky G, Janiak C. Acetylenedicarboxylate and in situ generated chlorofumarate-based hafnium (IV)–metal–organic frameworks: Synthesis, structure, and sorption properties. *Inorganic Chemistry*. 2019;58(16):10965-73.
102. Waitschat S, Fröhlich D, Reinsch H, Terraschke H, Lomachenko KA, Lamberti C, Kummer H, Helling T, Baumgartner M, Henninger S, Stock N. Synthesis of M-UiO-66 (M = Zr, Ce or Hf) employing 2,5-pyridinedicarboxylic acid as a linker: defect chemistry, framework hydrophilisation and sorption properties. *Dalton Transactions*. 2018;47(4):1062-70.
103. Bon V, Senkovskyy V, Senkovska I, Kaskel S. Zr(IV) and Hf(IV) based metal–organic frameworks with reo-topology. *Chemical Communications*. 2012;48(67):8407-9.
104. Bon V, Senkovska I, Baburin IA, Kaskel S. Zr- and Hf-based metal–organic frameworks: Tracking down the polymorphism. *Crystal Growth & Design*. 2013;13(3):1231-7.
105. Chen Y-C, Chiang W-H, Kurniawan D, Yeh P-C, Otake K-i, Kung C-W. Impregnation of graphene quantum dots into a metal–organic framework to render increased electrical conductivity and activity for electrochemical sensing. *ACS Applied Materials & Interfaces*. 2019;11(38):35319-26.
106. Maksimchuk NV, Lee JS, Solovyeva MV, Cho KH, Shmakov AN, Chesalov YA, Chang J-S, Kholdeeva OA. Protons make possible heterolytic activation of hydrogen peroxide over Zr-based metal–organic frameworks. *ACS Catalysis*. 2019;9(11):9699-704.
107. Hu Z, Kundu T, Wang Y, Sun Y, Zeng K, Zhao D. Modulated hydrothermal synthesis of highly stable MOF-808(Hf) for methane storage. *ACS Sustainable Chemistry & Engineering*. 2020;8(46):17042-53.

108. Micero A, Hashem T, Gliemann H, Léon A. Hydrogen separation performance of UiO-66-NH₂ membranes grown via liquid-phase epitaxy layer-by-layer deposition and one-pot synthesis. *Membranes*. 2021;11(10).
109. Hu Z, Nalaparaju A, Peng Y, Jiang J, Zhao D. Modulated hydrothermal synthesis of UiO-66(Hf)-type metal–organic frameworks for optimal carbon dioxide separation. *Inorganic Chemistry*. 2016;55(3):1134-41.
110. Teplensky MH, Fantham M, Li P, Wang TC, Mehta JP, Young LJ, Moghadam PZ, Hupp JT, Farha OK, Kaminski CF, Fairen-Jimenez D. Temperature treatment of highly porous zirconium-containing metal–organic frameworks extends drug delivery release. *Journal of the American Chemical Society*. 2017;139(22):7522-32.
111. Lin S, Zhao Y, Yun Y-S. Highly effective removal of nonsteroidal anti-inflammatory pharmaceuticals from water by Zr(IV)-based metal–organic framework: Adsorption performance and mechanisms. *ACS Applied Materials & Interfaces*. 2018;10(33):28076-85.
112. Rameesha L, Rana D, Nagendran A. Poly(vinylidene fluoride) ultrafiltration membranes tailored with zirconium-based MOF-801 for water treatment applications. *Polymer International*. 2024;73(5):368-77.
113. Wang B, Lv X-L, Feng D, Xie L-H, Zhang J, Li M, Xie Y, Li J-R, Zhou H-C. Highly stable Zr(IV)-based metal–organic frameworks for the detection and removal of antibiotics and organic explosives in water. *Journal of the American Chemical Society*. 2016;138(19):6204-16.
114. Mohamed A, Sanchez EPV, Bogdanova E, Bergfeldt B, Mahmood A, Ostvald RV, Hashem T. Efficient fluoride removal from aqueous solution using zirconium-based composite nanofiber membranes. *Membranes*. 2021;11(2):147.
115. Wu H, Yildirim T, Zhou W. Exceptional mechanical stability of highly porous zirconium metal–organic framework UiO-66 and its important implications. *The Journal of Physical Chemistry Letters*. 2013;4(6):925-30.
116. Kandiah M, Nilsen MH, Usseglio S, Jakobsen S, Olsbye U, Tilset M, Larabi C, Quadrelli EA, Bonino F, Lillerud KP. Synthesis and stability of tagged UiO-66 Zr-MOFs. *Chemistry of Materials*. 2010;22(24):6632-40.
117. Hashem T, Sanchez EPV, Bogdanova E, Ugodchikova A, Mohamed A, Schwotzer M, Alkordi MH, Wöll C. Stability of monolithic mof thin films in acidic and alkaline aqueous media. *Membranes*. 2021;11(3):207.
118. Xydias P, Spanopoulos I, Klontzas E, Froudakis GE, Trikalitis PN. Drastic enhancement of the CO₂ adsorption properties in sulfone-functionalized Zr- and Hf-UiO-67 MOFs with hierarchical mesopores. *Inorganic Chemistry*. 2014;53(2):679-81.
119. Hu Z, Castano I, Wang S, Wang Y, Peng Y, Qian Y, Chi C, Wang X, Zhao D. Modulator effects on the water-based synthesis of Zr/Hf metal–organic frameworks: Quantitative relationship studies between modulator, synthetic condition, and performance. *Crystal Growth & Design*. 2016;16(4):2295-301.

120. Cohen SM. Postsynthetic methods for the functionalization of metal–organic frameworks. *Chemical Reviews*. 2012;112(2):970-1000.
121. Garibay SJ, Cohen SM. Isorecticular synthesis and modification of frameworks with the UiO-66 topology. *Chemical Communications*. 2010;46(41):7700-2.
122. Planas N, Mondloch JE, Tussupbayev S, Borycz J, Gagliardi L, Hupp JT, Farha OK, Cramer CJ. Defining the proton topology of the Zr6-based metal–organic framework NU-1000. *The Journal of Physical Chemistry Letters*. 2014;5(21):3716-23.
123. Hashem T, Ibrahim AH, Wöll C, Alkordi MH. Grafting zirconium-based metal–organic framework UiO-66-NH₂ nanoparticles on cellulose fibers for the removal of Cr(VI) ions and methyl orange from water. *ACS Applied Nano Materials*. 2019;2(9):5804-8.
124. Ali A, Chiang YW, Santos RM. X-ray diffraction techniques for mineral characterization: a review for engineers of the fundamentals, applications, and research directions. *Minerals*. 2022;12(2).
125. John F. Wager RH. Thin, fast, and flexible semiconductors 2011 16.07.2024. Available from: <https://spectrum.ieee.org/thin-fast-and-flexible-semiconductors>.
126. Hammond C. The basics of crystallography and diffraction: Oxford University Press; 2015.
127. Waseda Y, Matsubara E, Shinoda K. X-ray diffraction crystallography: introduction, examples and solved problems: Springer Science & Business Media; 2011.
128. Mourdikoudis S, Pallares RM, Thanh NTK. Characterization techniques for nanoparticles: comparison and complementarity upon studying nanoparticle properties. *Nanoscale*. 2018;10(27):12871-934.
129. Authier A. Dynamical theory of X-ray diffraction. *International Tables for Crystallography*. 2006:534-51.
130. Reynolds RC. Modern powder diffraction. In: Bish DL, Post JE, editors.: De Gruyter; 1989. p. 1-18.
131. Harrington GF, Santiso J. Back-to-basics tutorial: X-ray diffraction of thin films. *Journal of Electroceramics*. 2021;47(4):141-63.
132. Biemmi E, Scherb C, Bein T. Oriented growth of the metal organic framework Cu₃(BTC)₂(H₂O)₃·xH₂O tunable with functionalized self-assembled monolayers. *Journal of the American Chemical Society*. 2007;129(26):8054-5.
133. Dutta A. Chapter 4 - Fourier transform infrared spectroscopy. In: Thomas S, Thomas R, Zachariah AK, Mishra RK, editors. *Spectroscopic Methods for Nanomaterials Characterization*: Elsevier; 2017. p. 73-93.
134. Kitagawa S, Suga R, Araki K, Hashimoto O, editors. Active absorption/transmission FSS using diodes. 2015 IEEE International Symposium on Electromagnetic Compatibility (EMC); 2015 16-22 Aug. 2015.

135. Dufour É. Chapter 1 - Principles of infrared spectroscopy. In: Sun D-W, editor. *Infrared Spectroscopy for Food Quality Analysis and Control*. San Diego: Academic Press; 2009. p. 1-27.
136. Theophile T. Introduction to infrared spectroscopy. In: Theophile T, editor. *Infrared Spectroscopy*. Rijeka: IntechOpen; 2012. p. Ch. 0.
137. Why Infrared? : Ceramicx. Infrared for industry; [Figure of electromagnetic spectrum]. Available from: <https://turkish.ceramicx.com/information/teknik-destek/why-infrared/>.
138. Stuart BH. *Infrared spectroscopy: fundamentals and applications*: John Wiley & Sons; 2004.
139. Entropy Changes and the Third Law of Thermodynamics. In: CHEM 2000: Chemistry for Engineers (Sinex). LibreTexts: LibreTexts. Available from: [https://chem.libretexts.org/Courses/Prince_Georges_Community_College/CHEM_2000%3A_Chemistry_for_Engineers_\(Sinex\)/Unit_6%3A_Thermo_and_Electrochemistry/Chapter_16%3A_Entropy_and_Free_Energy/Chapter_16.2%3A_Entropy_Changes_and_the_Third_Law_of_Thermodynamics](https://chem.libretexts.org/Courses/Prince_Georges_Community_College/CHEM_2000%3A_Chemistry_for_Engineers_(Sinex)/Unit_6%3A_Thermo_and_Electrochemistry/Chapter_16%3A_Entropy_and_Free_Energy/Chapter_16.2%3A_Entropy_Changes_and_the_Third_Law_of_Thermodynamics).
140. Roche C, Ven M, Planche J-P, Van den bergh W, Grenfell J, Gabet T, Mouillet V, Porot L, Farcas F, Ruot C. Hot pecycling of bituminous mixtures. 2013. p. 361-428.
141. Spitsyn AN, Utkin DV, Kuznetsov OS, Erokhin PS, Osina NA, Kochubei VI. Application of optical techniques to investigation and identification of microorganisms: a review. *Optics and Spectroscopy*. 2021;129(1):135-48.
142. Kattner J, Hoffmann H. External reflection spectroscopy of thin films on dielectric substrates. *Handbook of Vibrational Spectroscopy*. 2006.
143. Kaliva M, Vamvakaki M. Chapter 17 - Nanomaterials characterization. In: Narain R, editor. *Polymer Science and Nanotechnology*: Elsevier; 2020. p. 401-33.
144. Electron-matter interaction volume and various types of signal generated: Wikimedia Commons; 2023 [updated 24.02.2023. Available from: https://commons.wikimedia.org/w/index.php?title=File:Electron-matter_interaction_volume_and_various_types_of_signal_generated_-_v2.svg&oldid=735478301.
145. Abd Mutalib M, Rahman MA, Othman MHD, Ismail AF, Jaafar J. Chapter 9 - Scanning electron microscopy (SEM) and energy-dispersive X-ray (EDX) spectroscopy. In: Hilal N, Ismail AF, Matsuura T, Oatley-Radcliffe D, editors. *Membrane Characterization*: Elsevier; 2017. p. 161-79.
146. Agarwal DH, Bhatt PM, Pathan AM, Patel H, Joshi US. Development of portable experimental set-up for AFM to work at cryogenic temperature. *AIP Conference Proceedings*. 2012;1447(1):531-2.
147. Aguilar Meza IB, Ortiz Ortega E, Hosseinian H, Rodríguez Vera A, Rosales López MJ, Hosseini S. Characterization techniques for wettability analysis. In: Ortiz Ortega E, Hosseinian H, Aguilar Meza IB, Rosales López MJ,

- Rodríguez Vera A, Hosseini S, editors. Material Characterization Techniques and Applications. Singapore: Springer Singapore; 2022. p. 181-93.
148. Fearn S. An Introduction to Time-of-Flight Secondary Ion Mass Spectrometry (ToF-SIMS) and its Application to Materials Science: Morgan & Claypool Publishers; 2015. Available from: <https://dx.doi.org/10.1088/978-1-6817-4088-1>.
149. Instruments n. Quartz crystal microbalance (QCM) 2024 [Available from: <https://www.nanoscience.com/techniques/quartz-crystal-microbalance/>].
150. Sauerbrey G. Use a quartz vibration form weigh thin films on a microbalance. Z Phys. 1959;155:206-10.
151. Reviakine I, Johannsmann D, Richter RP. Hearing what you cannot see and visualizing what you hear: Interpreting quartz crystal microbalance data from solvated interfaces. Analytical Chemistry. 2011;83(23):8838-48.
152. Lu C, Czanderna AW. Applications of piezoelectric quartz crystal microbalances: Elsevier; 2012.
153. Bundschuh S, Kraft O, Arslan H, Gliemann H, Weidler P, Wöll C. Mechanical properties of metal-organic frameworks: An indentation study on epitaxial thin films. Applied Physics Letters. 2012;101(10):101910.
154. Mensink LI, de Beer S, Snoeijer JH. The role of entropy in wetting of polymer brushes. Soft Matter. 2021;17(5):1368-75.
155. Zhao CY, Tao YB, Wang WY. Shell effect on microstructure and diffusion in interface region of nanoencapsulated phase change material: A molecular dynamics simulation. Journal of Molecular Liquids. 2022;354:118872.
156. Abbaspour M, Jorabchi MN, Akbarzadeh H, Ebrahimnejad A. Investigation of the thermal properties of phase change materials encapsulated in capped carbon nanotubes using molecular dynamics simulations. RSC Advances. 2021;11(40):24594-606.
157. Geyer F, D'Acunzi M, Sharifi-Aghili A, Saal A, Gao N, Kaltbeitzel A, Sloot TF, Berger R, Butt HJ, Vollmer D. When and how self-cleaning of superhydrophobic surfaces works. Science Advances. 2020;6(3).
158. Bhadra P, Siu SWI. Comparison of biomolecular force fields for alkanethiol self-assembled monolayer simulations. The Journal of Physical Chemistry C. 2017;121(47):26340-9.
159. Boyd PG, Moosavi SM, Witman M, Smit B. Force-field prediction of materials properties in metal-organic frameworks. The Journal of Physical Chemistry Letters. 2017;8(2):357-63.
160. Li Z, Xiao Y, Xue W, Yang Q, Zhong C. Ionic liquid/metal-organic framework composites for H₂S removal from natural gas: A computational exploration. The Journal of Physical Chemistry C. 2015;119(7):3674-83.
161. Vazquez M, Liu M, Zhang Z, Chandresh A, Kanj AB, Wenzel W, Heinke L. Structural and dynamic insights into the conduction of lithium-ionic-liquid mixtures in nanoporous metal-organic frameworks as solid-state electrolytes. ACS Applied Materials & Interfaces. 2021;13(18):21166-74.

162. Dodda LS, Cabeza de Vaca I, Tirado-Rives J, Jorgensen WL. LigParGen web server: an automatic OPLS-AA parameter generator for organic ligands. *Nucleic acids research*. 2017;45(W1):W331-W6.
163. Iannuzzi M, Laio A, Parrinello M. Efficient exploration of reactive potential energy surfaces using car-parrinello molecular dynamics. *Physical Review Letters*. 2003;90(23):238302.
164. Prieve DC, Russel WB. Simplified predictions of Hamaker constants from Lifshitz theory. *Journal of Colloid and Interface Science*. 1988;125(1):1-13.
165. Hoover WG. Canonical dynamics: Equilibrium phase-space distributions. *Physical review A*. 1985;31(3):1695.
166. Andersen H. Molecular dynamics at constant temperature and/or pressure. *J Chem Phys*. 1980;72:2384.
167. Stewart JJ. Optimization of parameters for semiempirical methods VI: more modifications to the NDDO approximations and re-optimization of parameters. *Journal of Molecular Modeling*. 2013;19(1):1-32.
168. Li H, Yan T, Fichthorn KA, Yu S. Dynamic contact angles and mechanisms of motion of water droplets moving on nanopillared superhydrophobic surfaces: a molecular dynamics simulation study. *Langmuir*. 2018;34(34):9917-26.
169. Lu H, Zeysing D, Kind M, Terfort A, Zharnikov M. Structure of self-assembled monolayers of partially fluorinated alkanethiols with a fluorocarbon part of variable length on gold substrate. *The Journal of Physical Chemistry C*. 2013;117(37):18967-79.
170. Arnold R, Terfort A, Wöll C. Determination of molecular orientation in self-assembled monolayers using IR absorption intensities: the importance of grinding effects. *Langmuir*. 2001;17(16):4980-9.
171. Lee DT, Zhao J, Oldham CJ, Peterson GW, Parsons GN. UiO-66-NH₂ metal-organic framework (MOF) nucleation on TiO₂, ZnO, and Al₂O₃ atomic layer deposition-treated polymer fibers: Role of metal oxide on MOF growth and catalytic hydrolysis of chemical warfare agent simulants. *ACS Applied Materials & Interfaces*. 2017;9(51):44847-55.
172. Kind M, Wöll C. Organic surfaces exposed by self-assembled organothiol monolayers: Preparation, characterization, and application. *Progress in Surface Science*. 2009;84(7-8):230-78.
173. Pensa E, Vericat C, Grumelli D, Salvarezza RC, Park SH, Longo GS, Szleifer I, De Leo LPM. New insight into the electrochemical desorption of alkanethiol SAMs on gold. *Physical Chemistry Chemical Physics*. 2012;14(35):12355-67.
174. Tian L, Fan A, Yu X, Hu W. Achieving high-performance molecular rectification through fast screening alkanethiol carboxylate-metal complexes electroactive units. *CCS Chemistry*. 2023;5(4):902-14.

175. Lundy R, Byrne C, Bogan J, Nolan K, Collins MN, Dalton E, Enright R. Exploring the role of adsorption and surface state on the hydrophobicity of rare earth oxides. *Acs Applied Materials & Interfaces*. 2017;9(15):13751-60.
176. Colorado R, Lee TR. Wettabilities of self-assembled monolayers on gold generated from progressively fluorinated alkanethiols. *Langmuir*. 2003;19(8):3288-96.
177. Mouterde T, Raux PS, Clanet C, Quéré D. Superhydrophobic frictions. *Proceedings of the National Academy of Sciences of the United States of America*. 2019;116(17):8220-3.
178. Reyssat M, Richard D, Clanet C, Quéré D. Dynamical superhydrophobicity. *Faraday Discussions*. 2010;146:19-33.
179. Dhar M, Kara UI, Das S, Xu Y, Mandal S, Dupont RL, Boerner EC, Chen B, Yao Y, Wang X, Manna U. Design of a self-cleanable multilevel anticounterfeiting interface through covalent chemical modulation. *Materials Horizons*. 2023;10(6):2204-14.
180. Feng L, Li SH, Li YS, Li HJ, Zhang LJ, Zhai J, Song YL, Liu BQ, Jiang L, Zhu DB. Super-hydrophobic surfaces: From natural to artificial. *Advanced Materials*. 2002;14(24):1857-60.
181. Bittoun E, Marmur A. The role of multiscale roughness in the lotus effect: Is it essential for super-hydrophobicity? *Langmuir*. 2012;28(39):13933-42.
182. Miwa M, Nakajima A, Fujishima A, Hashimoto K, Watanabe T. Effects of the surface roughness on sliding angles of water droplets on superhydrophobic surfaces. *Langmuir*. 2000;16(13):5754-60.
183. Bhushan B, Jung YC, Koch K. Self-cleaning efficiency of artificial superhydrophobic surfaces. *Langmuir*. 2009;25(5):3240-8.
184. Wang M, Zi Y, Zhu J, Huang W, Zhang Z, Zhang H. Construction of super-hydrophobic PDMS@MOF@Cu mesh for reduced drag, anti-fouling and self-cleaning towards marine vehicle applications. *Chemical Engineering Journal*. 2021;417.
185. Zhao Y, Hu J-M. Double immobilized superhydrophobic and lubricated slippery surface with antibacterial and antifouling properties. *ACS Applied Bio Materials*. 2023;6(8):3341-50.
186. Wang D, Sun Q, Hokkanen MJ, Zhang C, Lin F-Y, Liu Q, Zhu S-P, Zhou T, Chang Q, He B, Zhou Q, Chen L, Wang Z, Ras RHA, Deng X. Design of robust superhydrophobic surfaces. *Nature*. 2020;582(7810):55-9.
187. Telmenbayer L, Ramu AG, Yang D, Choi D. Development of mechanically robust and anticorrosion slippery PEO coating with metal-organic framework (MOF) of magnesium alloy. *Chemical Engineering Journal*. 2023;458.
188. Bechler SL, Lynn DM. Reactive polymer multi layers fabricated by covalent layer-by-layer assembly: 1,4-conjugate addition-based approaches to the design of functional biointerfaces. *Biomacromolecules*. 2012;13(5):1523-32.

189. Li X, Li B, Li Y, Sun J. Nonfluorinated, transparent, and spontaneous self-healing superhydrophobic coatings enabled by supramolecular polymers. *Chemical Engineering Journal*. 2021;404.
190. Lepikko S, Jaques YM, Junaid M, Backholm M, Lahtinen J, Julin J, Jokinen V, Sajavaara T, Sammalkorpi M, Foster AS, Ras RHA. Droplet slipperiness despite surface heterogeneity at molecular scale. *Nature Chemistry*. 2024;16(4).
191. Zhao X, Park DS, Choi J, Park S, Soper SA, Murphy MC. Robust, transparent, superhydrophobic coatings using novel hydrophobic/hydrophilic dual-sized silica particles. *Journal of Colloid and Interface Science*. 2020;574:347-54.
192. Nakajima A, Fujishima A, Hashimoto K, Watanabe T. Preparation of transparent superhydrophobic boehmite and silica films by sublimation of aluminum acetylacetonate. *Advanced Materials*. 1999;11(16):1365-8.
193. Wang D, Zhang Z, Li Y, Xu C. Highly transparent and durable superhydrophobic hybrid nanoporous coatings fabricated from polysiloxane. *Acs Applied Materials & Interfaces*. 2014;6(13):10014-21.
194. Singh V, Men XH, Tiwari MK. Transparent and robust amphiphobic surfaces exploiting nanohierarchical surface-grown metal–organic frameworks. *Nano Letters*. 2021;21(8):3480-6.
195. Victor JF, D.; Palumbo, G.; Erb, U. . Biology inspired superhydrophobic surfaces. *Advanced Materials Research, Trans Tech Publ*. 2012:814-9
196. Ulman A, Tillman N. Self-assembling double-layers on gold surfaces - the merging of 2 chemistries. *Langmuir*. 1989;5(6):1418-20.
197. Stenger DA, Pike CJ, Hickman JJ, Cotman CW. Surface determinants of neuronal survival and growth on self-assembled monolayers in culture. *Brain Research*. 1993;630(1-2):136-47.
198. Kim JY, Lee EK, Jung J, Lee DW, Yun Y, Chung JW, Park JI, Kim JJ. Densely cross-linked polysiloxane dielectric for organic thin-film transistors with enhanced electrical stability. *Journal of Materials Chemistry C*. 2019;7(19):5821-9.
199. Harsch A, Calderon J, Timmons R, Gross G. Pulsed plasma deposition of allylamine on polysiloxane: A stable surface for neuronal cell adhesion. *Journal of Neuroscience Methods*. 2000;98(2):135-44.
200. Lin G, Zhang X, Kumar SR, Mark JE. Modification of polysiloxane networks for biocompatibility. *Molecular Crystals and Liquid Crystals*. 2010;521(1):56-71.
201. Sun Z, Liu B, Huang S, Wu J, Zhang Q. Facile fabrication of superhydrophobic coating based on polysiloxane emulsion. *Progress in Organic Coatings*. 2017;102:131-7.
202. Gao ML, Zhao SY, Chen ZY, Liu L, Han ZB. Superhydrophobic/superoleophilic MOF composites for oil-water separation. *Inorganic Chemistry*. 2019;58(4):2261-4.

203. Chen S, Wang J, Ma T, Chen D. Molecular dynamics simulations of wetting behavior of water droplets on polytetrafluorethylene surfaces. *The Journal of Chemical Physics*. 2014;140(11):114704.
204. Schertel A, Hahner G, Grunze M, Wöll C. Near edge x-ray absorption fine structure investigation of the orientation and thermally induced order-disorder transition in thin organic films containing long chain hydrocarbons. *Journal of Vacuum Science & Technology a-Vacuum Surfaces and Films*. 1996;14(3):1801-6.
205. Saitoh T, Hoshino H, Yotsuyanagi T. Volume constraint effect on solute partitioning to Triton X-100 micelles in water. *Journal of the Chemical Society, Faraday Transactions*. 1994;90(3):479-86.
206. Jonas AM, Hu ZJ, Glinel K, Huck WTS. Chain entropy and wetting energy control the shape of nanopatterned polymer brushes. *Macromolecules*. 2008;41(19):6859-63.
207. Binder K, Milchev A. Polymer brushes on flat and curved surfaces: How computer simulations can help to test theories and to interpret experiments. *Journal of Polymer Science Part B-Polymer Physics*. 2012;50(22):1515-55.
208. Bico J, Marzolin C, Quéré D. Pearl drops. *Europhysics Letters*. 1999;47(2):220-6.
209. Ueda E, Levkin PA. Emerging applications of superhydrophilic-superhydrophobic micropatterns. *Advanced Materials*. 2013;25(9):1234-47.
210. Zhang LS, Zhou AG, Sun BR, Chen KS, Yu HZ. Functional and versatile superhydrophobic coatings via stoichiometric silanization. *Nature Communications*. 2021;12(1).
211. Bon V, Brunner E, Pöpl A, Kaskel S. Unraveling structure and dynamics in porous frameworks via advanced in situ characterization techniques. *Advanced Functional Materials*. 2020;30(41):1907847.
212. Gandara-Loe J, Pastor-Perez L, Bobadilla LF, Odriozola JA, Reina TR. Understanding the opportunities of metal–organic frameworks (MOFs) for CO₂ capture and gas-phase CO₂ conversion processes: a comprehensive overview. *Reaction Chemistry & Engineering*. 2021;6(5):787-814.
213. von Helden G, van Heijnsbergen D, Meijer G. Resonant ionization using IR light: A new tool to study the spectroscopy and dynamics of gas-phase molecules and clusters. *The Journal of Physical Chemistry A*. 2003;107(11):1671-88.
214. Silva P, Vilela SMF, Tomé JPC, Almeida Paz FA. Multifunctional metal–organic frameworks: from academia to industrial applications. *Chemical Society Reviews*. 2015;44(19):6774-803.
215. Wang C, Liu D, Lin W. Metal–organic frameworks as a tunable platform for designing functional molecular materials. *Journal of the American Chemical Society*. 2013;135(36):13222-34.
216. Eddaoudi M, Moler DB, Li H, Chen B, Reineke TM, O'Keeffe M, Yaghi OM. Modular chemistry: Secondary building units as a basis for the design of

highly porous and robust metal–organic carboxylate frameworks. *Accounts of Chemical Research*. 2001;34(4):319-30.

217. Altaf A, Hassan S, Pejcic B, Baig N, Hussain Z, Sohail M. Recent progress in the design, synthesis and applications of chiral metal-organic frameworks. *Front Chem*. 2022;10:1014248.

218. Lee T, Liu ZX, Lee HL. A biomimetic nose by microcrystals and oriented films of luminescent porous metal–organic frameworks. *Crystal Growth & Design*. 2011;11(9):4146-54.

219. Qin L, Wang X, Liu Y, Wei H. 2D-metal–organic framework-nanozyme sensor arrays for probing phosphates and their enzymatic hydrolysis. *Analytical Chemistry*. 2018;90(16):9983-9.

220. Campbell MG, Liu SF, Swager TM, Dincă M. Chemiresistive sensor arrays from conductive 2D metal–organic frameworks. *Journal of the American Chemical Society*. 2015;137(43):13780-3.

221. Hu W, Wan L, Jian Y, Ren C, Jin K, Su X, Bai X, Haick H, Yao M, Wu W. Electronic Noses: From advanced materials to sensors aided with data processing. *Advanced Materials Technologies*. 2019;4(2):1800488.

222. Yang X-L, Zang R-B, Shao R, Guan R-F, Xie M-H. Chiral UiO-MOFs based QCM sensors for enantioselective discrimination of hazardous biomolecule. *Journal of Hazardous Materials*. 2021;413:125467.

223. Wang L. Metal-organic frameworks for QCM-based gas sensors: A review. *Sensors and Actuators A: Physical*. 2020;307:111984.

224. Okur S, Zhang Z, Sarheed M, Nick P, Lemmer U, Heinke L. Towards a MOF e-Nose: A SURMOF sensor array for detection and discrimination of plant oil scents and their mixtures. *Sensors and Actuators B: Chemical*. 2020;306:127502.

225. Okur S, Qin P, Chandresh A, Li C, Zhang Z, Lemmer U, Heinke L. An enantioselective e-Nose: An array of nanoporous homochiral MOF films for stereospecific sensing of chiral odors. *Angewandte Chemie International Edition*. 2021;60(7):3566-71.

226. Qin P, Okur S, Li C, Chandresh A, Mutruc D, Hecht S, Heinke L. A photoprogrammable electronic nose with switchable selectivity for VOCs using MOF films. *Chemical Science*. 2021;12(47):15700-9.

227. Zhang LT, Zhou Y, Han ST. The role of metal–organic frameworks in electronic sensors. *Angewandte Chemie*. 2021;133(28):15320-40.

228. Feng L, Wang K-Y, Day GS, Ryder MR, Zhou H-C. Destruction of metal–organic frameworks: positive and negative aspects of stability and lability. *Chemical Reviews*. 2020;120(23):13087-133.

229. Binaeian E, El-Sayed E-SM, Khanpour Matikolaei M, Yuan D. Experimental strategies on enhancing toxic gases uptake of metal–organic frameworks. *Coordination Chemistry Reviews*. 2021;430:213738.

230. Younas M, Rezakazemi M, Daud M, Wazir MB, Ahmad S, Ullah N, Inamuddin, Ramakrishna S. Recent progress and remaining challenges in post-

combustion CO₂ capture using metal-organic frameworks (MOFs). *Progress in Energy and Combustion Science*. 2020;80:100849.

231. Tzoulaki D, Heinke L, Lim H, Li J, Olson D, Caro J, Krishna R, Chmelik C, Kärger J. Assessing surface permeabilities from transient guest profiles in nanoporous host materials. *Angewandte Chemie International Edition*. 2009;48(19):3525-8.

232. Nijem N, Fürsich K, Kelly ST, Swain C, Leone SR, Gilles MK. HKUST-1 thin film layer-by-layer liquid phase epitaxial growth: Film properties and stability dependence on layer number. *Crystal Growth & Design*. 2015;15(6):2948-57.

233. Shultz AM, Sarjeant AA, Farha OK, Hupp JT, Nguyen ST. Post-synthesis modification of a metal-organic framework to form metallosalen-containing MOF materials. *Journal of the American Chemical Society*. 2011;133(34):13252-5.

234. Okur S, Hashem T, Bogdanova E, Hodapp P, Heinke L, Bräse S, Wöll C. Optimized detection of volatile organic compounds utilizing durable and selective arrays of tailored UiO-66-X SURMOF sensors. *ACS Sensors*. 2024;9(2):622-30.

235. Sandmeyer T. Ueber die ersetzung der amidgruppe durch chlor in den aromatischen substanzen. *Berichte der Deutschen Chemischen Gesellschaft*. 1884;17(2):1633-5.

236. Sandmeyer T. Ueber die ersetzung der amid-gruppe durch chlor, brom und cyan in den aromatischen substanzen. *Berichte der Deutschen Chemischen Gesellschaft*. 1884;17(2):2650-3.

237. Hodgson HH. The Sandmeyer reaction. *Chemical Reviews*. 1947;40(2):251-77.

238. Thomson GW. The Antoine equation for vapor-pressure data. *Chemical Reviews*. 1946;38(1):1-39.

239. Okur S, Qin P, Chandresh A, Li C, Zhang Z, Lemmer U, Heinke L. An enantioselective e-nose: an array of nanoporous homochiral MOF films for stereospecific sensing of chiral odors. *Angewandte Chemie International Edition*. 2021;60(7):3566-71.

240. Okur S, Sarheed M, Huber R, Zhang Z, Heinke L, Kanbar A, Wöll C, Nick P, Lemmer U. Identification of mint scents using a QCM based e-Nose. *Chemosensors*. 2021;9(2):31.

241. Okur S, Li C, Zhang Z, Vaidurya Pratap S, Sarheed M, Kanbar A, Franke L, Geislhöringer F, Heinke L, Lemmer U, Nick P, Wöll C. Sniff species: SURMOF-based sensor array discriminates aromatic plants beyond the genus level. *Chemosensors*. 2021;9(7):171.

242. Armbruster DA, Pry T. Limit of blank, limit of detection and limit of quantitation. *Clin Biochem Rev* (0159-8090 (Print)).

243. Zhan K, Qin P, Jiang Y, Chen Y, Heinke L. Optical sensor array of metal-organic-framework-based inverse opal films for the detection and identification of various alcohols. *Sensors and Actuators B: Chemical*. 2023;393:134271.
244. Mahendran V, Philip J. A methanol sensor based on stimulus-responsive magnetic nanoemulsions. *Sensors and Actuators B: Chemical*. 2013;185:488-95.
245. Naik AD, Robeyns K, Meunier CF, Léonard AF, Rotaru A, Tinant B, Filinchuk Y, Su BL, Garcia Y. Selective and reusable iron (II)-based molecular sensor for the vapor-phase detection of alcohols. *Inorganic Chemistry*. 2014;53(3):1263-5.
246. Wang F, Zhu Z, Xue M, Xue F, Wang Q, Meng Z, Lu W, Chen W, Qi F, Yan Z. Cellulose photonic crystal film sensor for alcohols. *Sensors and Actuators B: Chemical*. 2015;220:222-6.
247. Ruminski AM, King BH, Salonen J, Snyder JL, Sailor MJ. Porous silicon-based optical microsensors for volatile organic analytes: effect of surface chemistry on stability and specificity. *Advanced Functional Materials*. 2010;20(17):2874-83.
248. Davydovskaya P, Ranft A, Lotsch BV, Pohle R. Analyte detection with Cu-BTC metal-organic framework thin films by means of mass-sensitive and work-function-based readout. *Analytical Chemistry*. 2014;86(14):6948-58.
249. Yu H, Wang J, Yao C, Zhang H, Yu Y. Quality grade identification of green tea using E-nose by CA and ANN. *LWT - Food Science and Technology*. 2008;41(7):1268-73.
250. Wilson AD, Baietto M. Applications and advances in electronic-Nose technologies. *Sensors*. 2009;9(7):5099-148.
251. Saraoğlu HM, Edin B. E-Nose system for anesthetic dose level detection using artificial neural network. *Journal of Medical Systems*. 2007;31(6):475-82.
252. Devaraj NK, Finn MG. Introduction: click chemistry. *Chemical Reviews*. 2021;121(12):6697-8.
253. Kumar GS, Lin Q. Light-triggered click chemistry. *Chemical Reviews*. 2021;121(12):6991-7031.
254. Moharramnejad M, Ehsani A, Shahi M, Gharanli S, Saremi H, Malekshah RE, Basmenj ZS, Salmani S, Mohammadi M. MOF as nanoscale drug delivery devices: Synthesis and recent progress in biomedical applications. *Journal of Drug Delivery Science and Technology*. 2023;81:104285.
255. Qin P, Day BA, Okur S, Li C, Chandresh A, Wilmer CE, Heinke L. VOC mixture sensing with a MOF film sensor array: Detection and discrimination of xylene isomers and their ternary blends. *ACS Sensors*. 2022;7(6):1666-75.
256. Krantz-Rülcker C, Stenberg M, Winquist F, Lundström I. Electronic tongues for environmental monitoring based on sensor arrays and pattern recognition: a review. *Analytica Chimica Acta*. 2001;426(2):217-26.
257. Vlasov YG, Legin AV, Rudnitskaya AM, D'Amico A, Di Natale C. «Electronic tongue» — new analytical tool for liquid analysis on the basis of non-

- specific sensors and methods of pattern recognition. *Sensors and Actuators B: Chemical*. 2000;65(1):235-6.
258. Deisingh AK, Stone DC, Thompson M. Applications of electronic noses and tongues in food analysis. *International Journal of Food Science & Technology*. 2004;39(6):587-604.
259. Legin A, Rudnitskaya A, Vlasov Y, Di Natale C, Mazzone E, D'Amico A. Application of Electronic Tongue for Quantitative Analysis of Mineral Water and Wine. *Electroanalysis*. 1999;11(10-11):814-20.
260. Garcia-Breijo E, Peris RM, Pinatti CO, Fillol MA, Civera JI, Prats RB. Low-cost electronic tongue system and its application to explosive detection. *IEEE Transactions on Instrumentation and Measurement*. 2012;62(2):424-31.
261. Tuantranont A, Wisitsora-at A, Sritongkham P, Jaruwongrunsee K. A review of monolithic multichannel quartz crystal microbalance: A review. *Analytica Chimica Acta*. 2011;687(2):114-28.
262. Ha D, Sun Q, Su K, Wan H, Li H, Xu N, Sun F, Zhuang L, Hu N, Wang P. Recent achievements in electronic tongue and bioelectronic tongue as taste sensors. *Sensors and Actuators B: Chemical*. 2015;207:1136-46.
263. Ciosek P, Wróblewski W. Sensor arrays for liquid sensing – electronic tongue systems. *Analyst*. 2007;132(10):963-78.
264. Aydemir F, Ebeoğlu MA. A QCM sensor array-based electronic tongue with the optimized oscillator circuit using FPGA. *IEEE Transactions on Instrumentation and Measurement*. 2017;67(2):431-8.
265. Kaneda H, Takashio M, Okahata Y. Development of Beer Taste Sensor Using a Lipid-Coated Quartz-Crystal Microbalance. *Journal of the American Society of Brewing Chemists*. 2005;63(3):89-95.
266. Kaneda H, Kobayashi N, Watari J, Shinotsuka K, Takashio M, Okahata Y. A New Taste Sensor for Evaluation of Beer Body and Smoothness Using a Lipid-Coated Quartz Crystal Microbalance. *Journal of the American Society of Brewing Chemists*. 2002;60(2):71-6.
267. Aoki PHB, Volpati D, Cabrera FC, Trombini VL, Riul A, Constantino CJL. Spray layer-by-layer films based on phospholipid vesicles aiming sensing application via e-tongue system. *Materials Science and Engineering: C*. 2012;32(4):862-71.
268. Hashem T, Valadez Sánchez EP, Weidler PG, Gliemann H, Alkordi MH, Wöll C. Liquid-Phase Quasi-Epitaxial Growth of Highly Stable, Monolithic UiO-66-NH₂ MOF thin Films on Solid Substrates. *ChemistryOpen*. 2020;9(5):524-7.
269. Kanazawa KK, Gordon JG. Frequency of a quartz microbalance in contact with liquid. *Analytical Chemistry*. 1985;57(8):1770-1.
270. Faria RG, Julião D, Balula SS, Cunha-Silva L. Hf-based UiO-66 as adsorptive compound and oxidative catalyst for denitrogenation processes. *Compounds*. 2021;1(1):3-14.

271. Wu S, Snajdrova R, Moore JC, Baldenius K, Bornscheuer UT. Biocatalysis: Enzymatic synthesis for industrial applications. *Angewandte Chemie International Edition*. 2021;60(1):88-119.
272. Datta S, Christena LR, Rajaram YRS. Enzyme immobilization: an overview on techniques and support materials. *3 Biotech*. 2013;3(1):1-9.
273. Wong JX, Ogura K, Chen S, Rehm BHA. Bioengineered polyhydroxyalkanoates as immobilized enzyme scaffolds for industrial applications. *Frontiers in Bioengineering and Biotechnology*. 2020;8.
274. Li P, Modica Justin A, Howarth Ashlee J, Vargas L E, Moghadam Peyman Z, Snurr Randall Q, Mrksich M, Hupp Joseph T, Farha Omar K. Toward design rules for enzyme immobilization in hierarchical mesoporous metal–organic frameworks. *Chem*. 2016;1(1):154-69.
275. Li P, Chen Q, Wang TC, Vermeulen NA, Mehdi BL, Dohnalkova A, Browning ND, Shen D, Anderson R, Gómez-Gualdrón DA, Cetin FM, Jagiello J, Asiri AM, Stoddart JF, Farha OK. Hierarchically engineered mesoporous metal–organic frameworks toward cell-free immobilized enzyme systems. *Chem*. 2018;4(5):1022-34.
276. Greifenstein R, Ballweg T, Hashem T, Gottwald E, Achauer D, Kirschhöfer F, Nusser M, Brenner-Weiß G, Sedghamiz E, Wenzel W, Mittmann E, Rabe KS, Niemeyer CM, Franzreb M, Wöll C. MOF-hosted enzymes for continuous flow catalysis in aqueous and organic solvents. *Angewandte Chemie International Edition*. 2022;61(18):e202117144.
277. Kinik FP, Ortega-Guerrero A, Ongari D, Ireland CP, Smit B. Pyrene-based metal organic frameworks: from synthesis to applications. *Chemical Society Reviews*. 2021;50(5):3143-77.

List of Abbreviations

AFM – Atomic-Force Microscopy
ATR – Attenuated Total Reflection
ATR-IR – Attenuated total reflection infrared spectroscopy
BET – Brunauer, Emmett and Teller (theory)
BSE – backscattered electrons
DEF – diethylformamide
DFT – density functional theory
DMF – dimethylformamide
EDX – energy dispersive X-ray analysis
ESEM – environmental scanning electron microscope
FEG – field emission guns
FE-SEM – Field Emission Scanning Electron Microscopy
FFP – functionalized filter paper
FGCS – functionalized gold-coated substrate
FT-IR – Fourier Transform Infrared Spectroscopy
H₂BDC – 1,4-benzene-dicarboxylate
IR – Infrared
IRRAS – infrared reflection-absorption spectroscopy
k-NN – k-nearest neighbor
L – linker
LbL – Layer-by-layer
LDA – linear discriminant analysis
LMIG/S – liquid metal ion gun/source
LOD – limits of detection
LPE – Liquid-Phase epitaxial
MCT – mercury-cadmium-telluride
MD – molecular dynamics

MI – metal ion
ML – machine learning
MOF – Metal-Organic Frameworks
NNA – neural network analysis
NU – Northwestern University
PCN – Porous Coordination Network
pNP – 4-nitrophenol
pNPA – 4-nitrophenyl acetate
PSM – post-synthetic modification
PXRD – powder X-ray diffraction
QCM – Quartz Crystal Microbalance
ReLU – rectified linear unit
SAM – Self-Assembled Monolayers
SBU – secondary building unit
SE – secondary electrons
SEM – Scanning Electron Microscopy
SIMS – Secondary Ion Mass Spectrometry
SPM – scanning probe microscopy
SURMOF – Surface-Anchored Metal-Organic Frameworks
TBAPy – 1,3,6,8-tetrakis(p-benzoate)pyrene
TBS – Tris-buffer saline
TEA – Triethylamine
THF – tetrahydrofuran
TIR – total internal reflection
ToF-SIMS – Time of Flight Secondary Ion Mass Spectrometry
UiO – University of Oslo
VOCs – volatile organic compounds
WCA – Water Contact Angle
XRD – X-Ray Diffraction

List of Figures

Figure 1 – Structure of MOF	20
Figure 2 – Examples of inorganic secondary building units (A) and organic linkers (B). From [9]. Reprinted with permission from AAAS.....	21
Figure 3 – Timeline of the most common synthesis approaches for MOFs [15]. Reproduced with permission from Royal Society of Chemistry	23
Figure 4 – Components of SAMs [71].....	33
Figure 5 – Timeline of development of stable Zr(Hf)-based MOFs and SURMOFs. Edited from [94]; Copyright 2023 RSC. MOF from [95]; Copyright 1995 Springer Nature. Zr based UiO-66, UiO-67, and UiO-68 from [92]; Copyright 2008 American Chemical Society. Hf-UiO-66 from [96]; Copyright 2012 American Chemical Society. Zr-NU-1000 from [97]; Copyright 2013 American Chemical Society. MOF-808 from [98]; Copyright 2014 American Chemical Society. Hf-NU-1000 from [99]; Copyright 2014 American Chemical Society. Zr-UiO-66-NH ₂ SURMOF from [100]; Copyright 2020 Wiley.	43
Figure 6 – XRD patterns and SEM images of UiO-66-NH ₂ SURMOF films immersed in a: (A) pH 2 solution, (B) pH 7 solution, (C) pH 10 solution, and (D) pH 11 solution [117]	46
Figure 7 – (a) One unit cell of copper drawn to scale with: (b) Zr–MOF with 1,4-benzene-dicarboxylate (BDC) as linker, UiO-66, (c) Zr–MOF with 4,4' biphenyl-dicarboxylate (BPDC) as linker, UiO-67, (d) Zr–MOF with terphenyl dicarboxylate (TPDC) as linker, UiO-68 [92]. Reproduced with permission from American Chemical Society.	47
Figure 8 – Postsynthetic ligand and cation exchange in robust MOFs [91]. Reproduced with permission from Wiley	49
Figure 9 – (a) 1,3,6,8-Tetrakis(p-benzoic acid)pyrene linker, TBAPy ⁴⁻ and (b) the [Zr ₆ (μ ₃ -O) ₈ (O) ₈] ⁸⁻ node of the (c and d) Zr ₆ -based framework NU-1000. Note that the linkers are not shown in the representation of the node, and the hydrogens	

are not shown in the framework representations for clarity [122]. Reproduced with permission from American Chemical Society	50
Figure 10 – Solid phases [125]	54
Figure 11 – Visualization of the Bragg’s Law.....	55
Figure 12 – Components of a diffractometer [131]. Reproduced with permission from Springer Nature	57
Figure 13 – X-ray diffraction patterns (background corrected) of thin films of $\text{Cu}_3(\text{BTC})_2$ on functionalized gold surfaces, compared with a randomly oriented $\text{Cu}_3(\text{BTC})_2$ powder sample measurement. Each pattern is normalized to the most intensive reflection [132]. Reproduced with permission from American Chemical Society	58
Figure 14 – Infrared radiation: absorption and transmission [134]. Reproduced with permission from IEEE	59
Figure 15 – Electromagnetic spectrum, highlighting the visible and IR regions [137]	60
Figure 16 – (a) Three common forms of motions in a molecule [139] and (b) Vibrational bond alignments.....	61
Figure 17 – Michelson interferometer [140]. Reproduced with permission from Springer Nature	62
Figure 18 – Beam geometry and polarization of IR radiation at the interface between two optically different media [142]. Reproduced with permission from Wiley	64
Figure 19 – IRRAS spectra of different cycles of $\text{Zn}_x(\text{bdc})_y$ MOF grown on a MHDA SAM [76]	65
Figure 20 – Electron – matter interactions: the different types of signals generated [144]	67
Figure 21 – FE-SEM instrument illustration with all major components	69

Figure 22 – Illustration of three-phase contact line, where γ_{lv} , γ_{sv} and γ_{sl} represent the liquid-vapor, solid-vapor and solid-liquid intermolecular tension, and Θ_γ is the contact angle [147]. Reproduced with permission from Springer Nature	74
Figure 23 – Graphical illustration of sessile drop technique. The camera takes images of the droplet, while the light is in the background and the contact angle is assessed by the software [147]. Reproduced with permission from Springer Nature	76
Figure 24 – The steps needed to obtain mass spectra and ion images [148]. (a) A short pulse from the primary ion beam irradiates a spot and sputters secondary ions. (b) These are collected in the analyser, and separated according to (m/z). (c) The process is repeated on the neighboring pixel, until a specified area has been analysed. (d) Mass spectra are produced as the detector collects the sputtered secondary ions. (e) By selecting specific peaks from the mass spectrum, (f) the spatial distribution of the selected peaks can be generated to give ion images as the spatial co-ordinates for the secondary ion signals are known. Reproduced with permission from Morgan & Claypool Publishers	80
Figure 25 – Design of quartz crystal (grey) with electrodes (yellow); (a) top view (b) bottom view. (c) A schematic illustration of the strain induced in an AT cut crystal on application of AC voltage. (d) A schematic illustration of how amplitude of vibration ($A(r)$) varies with the distance (r) from the center of the sensor. The area of vibration is called the active surface area and is sensitive to mass changes [149].	83
Figure 26 – ToF-SIMS results for pristine UiO-66-NH ₂ SURMOF (blank sample in black) and its surface-modified counterpart (modified samples in blue and red), demonstrating (a-b) the high prevalence of Zr ⁴⁺ and Cl ⁻ in the blank sample before modification, which are washed away with (c) higher appearance of amino groups in the blank sample, followed by (d) concurrent appearance of amino and amido groups in the modified samples in addition to (e) full proof of the amidation reaction by the existence of the residual part of stearic acid chloride.	93

Figure 27 – AFM comparison of UiO-66-NH₂, UiO-66-C18F and UiO-66-C18 SURMOFs.....94

Chemotion IDs: pw9911-291-1, pw9911-291-2, pw9911-291-3

Figure 28 – SEM images and WCA of UiO-66-NH₂, UiO-66-C18F and UiO-66-NH-C18.....95

Chemotion IDs: pw9911-291-1, pw9911-291-2, pw9911-291-3

Figure 29 – The stretching of hydrocarbon chains in the dry conditions for (a) SAM@Au, (b) C18F@SURMOF, and (c) C18@SURMOF. The substrates are aligned, marked by the orange dotted line across the three systems, whereas the distinguished thicknesses between C18F@SURMOF and C18@SURMOF are illustrated by orange arrows. This difference in chain stretching is measured at 0.4 nm due to the stronger repulsion among fluorine atoms in CF chains, exemplifying a lower entropy in CF chains. The fluorine atoms are explicitly shown in bright yellow, whereas hydrogen atoms on hydrocarbon chains are omitted for clarity.....96

Figure 30 – Water contact angles in the wetting simulations for (a) SAM@Au, (b) SURMOF, (c) C18F@SURMOF, and (d) C18@SURMOFs. The substrates are aligned, marked by the orange dotted line across the four systems. The water contact angles are marked by orange dotted lines. Particularly, in the case of C18F@SURMOF and C18@SURMOFs, the water droplet cannot react to the reference surface on the substrate, where additional baselines are indicated by horizontal orange dotted lines. For better clarity, MOF linkers are shown in light gray.....97

Figure 31 – Ramachandran plots for the torsional angles of the C-C backbone in the dry conditions for (a) SAM@Au, (b) C18F@SURMOF, and (c) C18@SURMOF. Color-coded is the occurrence frequencies of individual states. The SAM is in all-trans states where the torsional angles are constrained to the π - π corners in all quadrants, whereas for C18F@SURMOF and C18@SURMOF, there exist numerous gauche defects. The entropy calculated based on the state

occurrence frequencies ranks the SAM as the least entropic at 5.3, the C18F@SURMOF in the middle with an entropy reference at 6.47, and C18@SURMOF with the highest entropy at 6.97. In dry conditions, the number of gauche defects per chain is 0.04 for SAM, 1.42 for C18F@SURMOF, and 2.89 for C18@SURMOF98

Figure 32 – IRRAS data of UiO-66-NH₂, C18@SURMOF and C18F@SURMOF99

Chemotion IDs: pw9911-291-1, pw9911-291-2, pw9911-291-3

Figure 33 – DFT optimized molecular geometries and corresponding calculated IR spectra for isolated chains.100

Figure 34 – (a) XRD patterns and (b) IRRAS data for the pristine SURMOF UiO-66-NH₂ and the modified UiO-66-NH-C18.....102

Chemotion IDs: pw9911-285-1, pw9911-285-2

Figure 35 – The IRRAS results demonstrate the shift in the CH-region of self-assembled monolayers (SAM@Au) and C18@SURMOF. The spectrum shows a noticeable shift in the CH stretching vibration for both samples, confirm the disorder of the C18 on the surface of C18@SURMOF.....103

Chemotion IDs: pw9911-285-1, pw9911-396-2

Figure 36 – Static water contact angle, snapshots taken from equilibrated MD-simulations for water droplets and enlarged structure of UiO-66-NH₂. **Top:** Static water contact angle of (a) pristine UiO-66-NH₂ SURMOF, (b) SURMOF grafted with perfluorinated chains, UiO-66-NH-CF and (c) SURMOF grafted with C18 hydrocarbon chains from the experiment and the simulation. **Center:** Snapshots taken from equilibrated MD-simulations for water droplets on pristine (a) UiO-66-NH₂ SURMOF, (b) SURMOF grafted with perfluorinated hydrocarbon chains, and (c) SURMOF grafted with C18 hydrocarbon chains. **Bottom:** Enlarged structure of UiO-66-NH₂ (C₄₈H₃₄N₆O₃₂Zr₆) SURMOF, formed by linking Zr-clusters (Zr₆O₄(OH)₄) with organic linkers BDC-NH₂ (C₈H₇NO₄). Explicit hydrogen atoms are omitted for clarity.104

Chemotion IDs: pw9911-291-1; pw9911-291-2; pw9911-291-3

Figure 37 – (a) AFM images comparing the surface roughness of two different SURMOF surfaces. (b) Sequential images showing static and receding water contact angles on C18@SURMOF with arithmetic average roughness (R_a) of 31.4 nm. (c) Sequential images showing receding contact angle and sliding angle on C18@SURMOF with R_a of 62.4 nm. (d) Adhesion force measurement of the water droplet on adhesive and non-adhesive superhydrophobic surfaces. (e) High-speed images depict the bouncing behavior of a water droplet dropped on the non-adhesive superhydrophobic SURMOF surface. (b)-(e) results were obtained by Dr. U. Manna and Dr. A. Borbora (IITG)..... 105

Chemotion IDs: pw9911-297-1; pw9911-297-2

Figure 38 – Snapshot of conformations of the water droplets on the grafted SURMOF with (a) perfluorinated hydrocarbons and (b) C18 hydrocarbons. The dashed region corresponding to the wetting on perfluorinated hydrocarbons exhibits pin-and-plug patterns, mixing with CF chains, whereas in the case of CH chains, the water droplet maintains its spherical shape. 109

Figure 39 – (a) XRD patterns and (b) WCA data for the pristine SURMOF UiO-66-NH₂ and the modified UiO-66-NH-C18 on α -alumina substrate..... 112

Chemotion IDs: pw9911-285-3; pw9911-285-4

Figure 40 – QCM type E-Nose experimental setup for VOC measurements with three functionalized UiO-66-X SURMOFs (X: NH₂, N₃, and Cl). Reprinted with permission from [234]. Copyright 2024 American Chemical Society 119

Figure 41 – Typical temperature and time-dependent synthesis kinetics of UiO-66-NH₂ SURMOF films with the LBL method using a high-temperature QCM-D liquid cell. Reprinted with permission from [234]. Copyright 2024 American Chemical Society 122

Figure 42 – The structural analysis: (a) XRD pattern, (b) SEM surface topography, and (c) SEM cross section of the functional UiO-66-X after post-

modification process. Reprinted with permission from [234]. Copyright 2024 American Chemical Society123

Chemotion IDs: pw9911-121; pw9911-122; pw9911-123

Figure 43 – IRRAS data of UiO-66-NH₂, UiO-66-N₃ and UiO-66-Cl. Reprinted with permission from [234]. Copyright 2024 American Chemical Society124

Chemotion IDs: pw9911-121; pw9911-122; pw9911-123

Figure 44 – Ethanol uptake results (a) before and (b) after saturated hot water vapor at relative humidity conditions at 90 °C. XRD results of UiO-66-X (c) before and (d) after a high-humidity test (100% RH at 90 °C). Reprinted with permission from [234]. Copyright 2024 American Chemical Society125

Chemotion IDs: pw9911-121; pw9911-122; pw9911-123

Figure 45 – Uptake results at saturated hot water vapor at relative humidity conditions between 25 and 90 °C for (a) UiO-66-NH₂, (b) UiO-66-Cl, (c) UiO-66-N₃. XRD results of (d) UiO-66-NH₂@QCM sensor after high humidity/HCl test. Reprinted with permission from [234]. Copyright 2024 American Chemical Society126

Chemotion IDs: pw9911-121

Figure 46 – Negative QCM frequency changes observed due to mass uploads on three functional UiO-66-X SURMOF sensors with X = NH₂ (a), X = Cl (b), and X = N₃ (c) when exposed to VOCs. The radar plot (d) illustrates the maximum sensor responses against each VOC gas. Reprinted with permission from [234]. Copyright 2024 American Chemical Society127

Figure 47 – QCM responses of three functional UiO-66-X with X=NH₂, X=Cl, and X=N₃, against p-xylene (a-c), water (d-f), toluene (g-i), ethanol (j-l), 2-propanol (m-o), n-hexane (p-r), cyclohexane (s-u), and methanol (v-x) at different low concentrations between 10 and 100 ppm. Reprinted with permission from [234]. Copyright 2024 American Chemical Society130

Figure 48 – E-Nose analysis results. (a) Two-dimensional plot of LDA with a 95% confidence ellipse of eight VOCs, including water, at their saturated vapor

pressure concentrations. The confusion matrix results of the (b) LDA, (c) k-NN, and (d) NNA models. True classes (Y-axis) represent the already trained (labeled) values introduced to the models and predicted classes (X-axis) are the calculated results by the model. The discrimination accuracy is 100% for all three models. Reprinted with permission from [234]. Copyright 2024 American Chemical Society134

Figure 49 – E-Nose analysis results at 25 ppm concentrations. (a) Two-dimensional plot of LDA with a 95% confidence ellipse of eight VOCs, including water. The confusion matrix results of (b) LDA model with 88.7% discrimination accuracy, (c) k-NN model with 96.1% test discrimination accuracy, and (d) NNA model with 96.2% test discrimination accuracy. Reprinted with permission from [234]. Copyright 2024 American Chemical Society135

Figure 50 – E-Nose analysis results at 100 ppm. (a) Two-dimensional plot of LDA with a 95% confidence ellipse of eight VOCs, including water. The confusion matrix results of (b) LDA model with 90% discrimination accuracy, (c) k-NN model with 99.9% test discrimination accuracy, and (d) NNA model with 99.6% test discrimination accuracy. Reprinted with permission from [234]. Copyright 2024 American Chemical Society136

Figure 51 – Change in the discrimination accuracy of LDA, k-NN, and NNA models with increasing concentration from 10 to 100 ppm. Reprinted with permission from [234]. Copyright 2024 American Chemical Society137

Figure 52 – Possible postmodification of UiO-66-NH₂ to add different functional groups. Reprinted with permission from [234]. Copyright 2024 American Chemical Society138

Figure 53 – Structural analysis of the functional UiO-66-X following the post-modification process: (a) XRD pattern, (b) SEM surface topography, and (c) SEM cross-section.....143

Chemotion IDs: pw9911-150; pw9911-151; pw9911-152

Figure 54 – Changes in resonance frequency of (a) the bare QCM as compared to UiO-66-NH ₂ @QCM, indicating enhanced response for the MOF-coated QCM towards all the liquids tested; (b) the bare QCM and the three different UiO-66-X@QCM sensors	145
Figure 55 – Frequency difference for the UiO-66-NH ₂ @QCM sample and the bare QCM sample using ethanol as a baseline	146
Figure 56 –Response to varying concentrations of 2-isopropanol and n-hexane with ethanol as a baseline for (a) bare QCM and UiO-66-NH ₂ @QCM; (b) all four sensors: bare QCM, UiO-66-NH ₂ , UiO-66-Cl, and UiO-66-N ₃	147
Figure 57 – Response to varying concentrations of 2-isopropanol and n-hexane with toluene as a baseline, demonstrating sensitivity, stability and repeatability	148
Figure 58 – The liquid phase test results for the (a) UiO-66-X for X=NH ₂ , (b) X=Cl and (c) X=N ₃ for 36% HCl, water, n-hexane, 2-isopropanol, toluene, and p-xylene with respect to pure ethanol in liquid form as a reference solution...	149
Figure 59 – E-Tongue analysis results: (a) Two-dimensional plot of LDA with a 95% confidence ellipse of six different liquid, e.g. n-hexane, 2-isopropanol, toluene, p-xylene, including water and 36% HCl; (b) the confusion matrix results of LDA model with 99.6% discrimination accuracy, (c) the confusion matrix results of k-NN model with 99.5% test discrimination accuracy; (d) the confusion matrix results of NNA model with 99.9% test discrimination accuracy.	151
Figure 60 – Calculated XRD patterns for Zr- and Hf-UiO-66. The inset is from [100]. Copyright 2020 Wiley	158
Figure 61 – XRD patterns of (a) Hf- and (b) Zr-UiO-66-NH ₂	159
<i>Chemotion ID: pw9911-404-1, pw9911-407</i>	
Figure 62 – (a) IRRA spectra and (b) SEM top-view images of Zr- and Hf-UiO-66-NH ₂ SURMOF.....	160
<i>Chemotion ID: pw9911-404-1, pw9911-407</i>	

Figure 63 – XRD patterns of Hf-UiO-66-NH ₂ SURMOF films immersed in a: (a) pH 2 solution, (b) pH 7.5 solution, and (c) pH 11 solution; and (d) SEM images before and after immersions.....	161
Figure 64 – XRD patterns and SEM images of (a) Zr- and (b) Hf-UiO-66-NH ₂ SURMOF films; (c) IR-ATR spectra.....	162
<i>Chemotion ID: pw9911-404-2, pw9911-427</i>	
Figure 65 – The preparation process of NU-1000 thin films using custom-machined PTFE holder	168
Figure 66 – (a) XRD pattern, (b) SEM image of NU-1000 bulk.....	168
Figure 67 – QCM type experimental setup for enzyme immobilization.....	170
Figure 68 – (a) XRD patterns and (b) SEM images of NU-1000 SURMOFs..	171
<i>Chemotion IDs: pw9911-413-1; pw9911-413-2; pw9911-416</i>	
Figure 69 – (a) XRD, (b) IR and (c) SEM data of NU-1000 thin films on the cellulose substrate	172
<i>Chemotion ID: pw9911-418</i>	
Figure 70 – PXRD data of NU-1000@QCM films before enzyme immobilization process.....	173
<i>Chemotion ID: pw9911-424-1, pw9911-424-2, pw9911-424-3, pw9911-424-4</i>	
Figure 71 – Uptake results for TRIS buffer saline.....	174
Figure 72 – Top: Uptake results for esterase immobilization at different concentrations: (a) 20 µg/mL, (b) 80 µg/mL, and (c) 200 µg/mL. Bottom: Schematic representation of MOF pores with varying percentages of pore filling by the immobilized enzyme	175
Figure 73 – The dimension of NU-1000: the hexagonal and triangular channels along the c direction (left), and the small pore connecting the ab layers along the c direction (right). Edited from [277] with permission from the Royal Society of Chemistry.....	176

List of Schemes

Scheme 1 – Schematic diagram for the step-by-step approach for the growth of the MOFs on substrates functionalized with SAMs [76].....	35
Scheme 2 – Dip-coating approach for SURMOFs synthesis [78]. Reproduced with permission from Wiley	35
Scheme 3 – Setup employed for the fabrication of MOF thin films with the spray method: (1) Gas supply, (2) gas flow controller (3) three-way valve gas distributor (4) (A, B, C) solutions storage containers (5) sample holder (6) dosing valves, (7) spray chamber, (8) PC [83]. Reproduced with permission from Wiley	36
Scheme 4 –Spin Coating approach for SURMOFs synthesis. Reprinted with permission from [85]. Copyright 2016 American Chemical Society.....	38
Scheme 5 – Pump approach for SURMOFs synthesis	39
Scheme 6 – Flow cell approach for SURMOFs synthesis.....	40
Scheme 7 – Schematic illustration of the ATR -FTIR system [141]. The infrared beam passes through the ATR crystal covered on the top by the sample. The damping wave penetrates into the sample and is absorbed by the sample. The polarizer generates parallel and perpendicular polarized incident beam. Reproduced with permission from Springer Nature	63
Scheme 8 – Schematic of AFM imaging technique [146]. Reproduced with permission from AIP Publishing.....	72
Scheme 9 – Schematic representation of different measured contact angles where less than 90° surface is hydrophilic and more than 90 ° surface is hydrophobic [147]. Reproduced with permission from Springer Nature	75
Scheme 10 – Schematic representation of the collision of a primary ion (grey) with a sample surface (red). Energy is transferred onto the surface and distributed through several atoms (grey lines) until a secondary ion (blue) is ejected [148]. Reproduced with permission from Morgan & Claypool Publishers	77

Scheme 11 – Schematic representation of the main components of dual-beam time-of-flight secondary mass spectrometer. Secondary ions are sputtered from a target/sample by primary ion gun. The sputtered secondary ions are extracted by an extraction potential into the flight tube and detector electronically, typically with a microchannel plate. Depending on the mode of operation of the instrument, a range of signal outputs can be obtained: mass spectra, ion images, depth profiles and 3D analyses [148]. Reproduced with permission from Morgan & Claypool Publishers	78
Scheme 12 – Schematic representation of the three main steps used in depth profile ToF-SIMS [148]. (a) A high energy sputter beam is rastered over the sputter area. (b) The analytical beam is applied to the analysis area which is centered within the sputter area. (c) The secondary ions generated by the analysis beam are collected and accelerated into the analyser, and a mass spectrum produced. (d) By selecting certain peaks a depth profile of the species can be obtained (e). Reproduced with permission from Morgan & Claypool Publishers	82
Scheme 13 – The WCA on a hydrocarbon monolayer is shown to be substantially increased when instead of the normal close packing (left) the chains adopt a brush-like structure (right). The C18 hydrocarbon chains have an end-to-end distance of ~2 nm [155, 156], which is much larger than the separation of grafting sites in the SURMOF grid (~0.8 nm), such that the grafted hydrocarbons form a polymer brush.	86
Scheme 14 – Schematic diagram for the synthesis of UiO-66-NH ₂ SURMOF through LPE using dip-coating. Edited from [100] with permission from Wiley	88
Scheme 15 – Schematic illustration of perfluorooctadecanoyl chloride preparation.....	89

Scheme 16 – A schematic illustration of the working principle of the one-channel openQCM for SURMOF synthesis. Reprinted with permission from [234]. Copyright 2024 American Chemical Society	117
Scheme 17 – Continuous flow reactor scheme for catalytic process using a membrane	166

List of Tables

Table 1 – Different synthetic methods for MOF synthesis [19]. <i>Reproduced with permission from Springer Nature</i>	24
Table 2 – Zr-MOFs [91]. Reproduced with permission from Wiley.....	44
Table 3 – WCA comparisons for hydrophobic thin films. WCA colored in red correspond to mediocrehydrophobicity and the rest corresponds to superhydrophobicity [184-194]	106
Table 4 – Calculated concentrations under saturated pressures of eight VOCs used for gas adsorption measurements at room temperature (25 °C)	120
Table 5 – The sensor names, the calculated sensitivity (a), and limit of detections (b) of individual sensors.....	130
Table 6 – Comparison of LOD of the present sensor with some published sensors for alcohol vapors.....	132
Table 7 – Viscosity values of liquids.....	149

Acknowledgements

First of all, all praises and thanks be to Allah: “All praise is for Allah, to Whom belongs whatever is in the heavens and whatever is on the earth. And praise be to Him in the Hereafter. He is the All-Wise, All-Aware.” (Quran, 34:1). I extend my sincere gratitude to my Lord for His guidance and blessings throughout the journey of completing this PhD thesis and in all aspects of my life.

I express my deepest gratitude to **Prof. Dr. Christof Wöll** for the opportunity to work at IFG and for supervising my PhD thesis.

A special thanks to **Dr. Tawheed Hashem** for giving me the chance to realize my potential in his group; for providing me with many skills and much knowledge; for entrusting me with many exciting projects, and for his mentoring and guidance throughout.

I would like to thank **Dr. Salih Okur, Dr. Patrick Hodapp, Dr. Modan Liu, Dr. Angana Borbora, Dr. Uttam Manna, André Jung, Zheqin Dong, Dr. Raphael Greifenstein, Dr. Alexander Welle**, and other colleagues, whose collaboration significantly contributed to this thesis.

Thank you to **Prof. Dr. Stefan Bräse** for kindly accepting to be the co-referee of my thesis.

Thanks to the heads of the department: **Dr. Hartmut Gliemann** and **Dr. Peter Weidler** for their support and assistance.

I am grateful to **Stefan Heissler** and **Peter Krolla** for teaching me IR and AFM characterization techniques, respectively.

I extend my gratitude to **Prof. Dr. Mattias Franzreb, Tim Ballweg, Ulrich Thiele, Dr. Meike König, Dr. Muhammad Haseeb Iqbal, Dr. Mohamed Alkordi, Prof. Dr. Andreas Gerdes, Jonas Kaltenbach, and Japsimar Kaur** for collaboration in other projects. Moreover, I thank **Prof. Dr. Andreas Gerdes** for his kind support and for offering new opportunities to enhance my professional skills.

Thanks to other colleagues and IFG members, especially **Dr. Alexei Nefedov, Dr. Sarah Moulai, Lachlan Caulfield, Dr. Lena Pilz, Ana Claudia Fingolo, Dr. Chatrawee Scheiger and Zairan Yu** for their help, assistance, and for fostering a friendly environment.

I am deeply thankful to my friends who supported me and helped me to “stay on board.” Special thanks to **Amine Kamri**, whose belief in me and prayers helped me navigate through difficulties. I am also very grateful to **Dr. Anemar Bruno Kanj** and **Taher Al-Najjar**, who became my closest companions during the toughest times and provided valuable support, care, and encouragement throughout this journey. Thanks to them for bringing light into the darkest moments. Particularly, I want to thank **Taher Al-Najjar** for his unwavering support, invaluable research and life advice, and for being a constant source of strength and care during the most challenging times. I also wish to thank my dear friend and colleague **Zhiyun Xu** for her constant help and support.

Lastly, I would like to express my deepest gratitude to my parents, who are my best friends and main advisors, and who motivated me to complete this PhD. Without them, none of this would have been possible.

I also extend my heartfelt thanks to my other family members and friends for their care, for helping shape my personality, for encouraging my pursuit of science, and for their unwavering support and advice along the way.

Curriculum Vitae (CV)

Personal data

Name: Evgenia Bogdanova
Title: M.Eng.
Date of birth: 05.11.1997
Place of birth: Zheleznogorsk, Krasnoyarskiy kray, Russia
Nationality: Russian

Educational steps

Karlsruhe Institute of Technology Karlsruhe - Germany

Institute of Functional Interfaces (IFG)

July 2021 - Jul 2024

- Dr.rer.nat.
- Field of study: Physical chemistry
- Topic of the thesis: «*Highly stable Zr(Hf)-based Surface-anchored Metal-Organic Frameworks (SURMOFs) for technical application*»
- Supervisor: Prof. Dr. Christof Wöll
- Secondary Supervisor: Dr. Tawheed Hashem
- Graduation defense in October 2024
- Overall mark: “Very good” (magna cum laude)

National Research Tomsk Polytechnic University Tomsk - Russia

School of Nuclear Science & Engineering

Sep 2015 - Feb 2021

- Specialist’s degree diploma with honours
- Qualification: Chemical Engineer
- Specialty: Chemical technology of modern energy materials

- GPA: 4.75/5.00
- Final Qualification Project (Diploma paper): *«Design of a Water Treatment Plant for the Storage of Spent Nuclear Fuel with Capacity of 150 cubic meters per hour»*
- Supervisor: Associate Prof. Dr. Roman Ostwald

Secondary School No. 95

Zheleznogorsk - Russia

Sep 2004 - Jun 2015

- Certificate of Basic General Education with Honours
- GPA: 5.00/5.00

List of Publications

From this thesis

1. Okur S, Hashem T, **Bogdanova E**, Hodapp P, Heinke L, Bräse S, Wöll C. Optimized Detection of Volatile Organic Compounds Utilizing Durable and Selective Arrays of Tailored UiO-66-X SURMOF Sensors. ACS Sensors. 2024; 9(2):622-630.
2. **Bogdanova E**, Liu M, Hodapp P, Borbora A, Wenzel W, Bräse S, Jung A, Dong Z, Levkin P, Manna U, Hashem T, Wöll C. Functionalization of Monolithic MOF Thin Films with Hydrocarbon Chains to Achieve Superhydrophobic Surfaces with Tunable Water Adhesion Strength. Materials Horizons, 2025; 12(4):1274-1281.
3. Okur S, **Bogdanova E**, Hodapp P, Bräse S, Wöll C, Hashem T. SURMOF e-Tongue: Highly Stable Functionalized UiO-66-X Sensor Array for liquid Discrimination. (*in preparation*)
4. **Bogdanova E**, Hashem T. Liquid-Phase Quasi-Epitaxial Layer-by-layer growth of Highly Stable, Monolithic Zr and Hf-based Surface-Anchored Metal-Organic Frameworks (SURMOF) UiO-66-NH₂ using closed cell. (*in preparation*)
5. **Bogdanova E**, Okur S., Greifenstein R., Franzreb M..... Hashem T. NU-1000 Thin Films Growth on Diverse Substrates: Insights into Crystallite Orientation and Film Homogeneity (*in preparation*)